IntechOpen

Phonons in Low Dimensional Structures

Edited by Vasilios N. Stavrou

PHONONS IN LOW DIMENSIONAL STRUCTURES

Edited by **Vasilios N. Stavrou**

Phonons in Low Dimensional Structures
http://dx.doi.org/10.5772/intechopen.74693
Edited by Vasilios N. Stavrou

Contributors

Punit Suthar, Pierre Deymier, Jerome Vasseur, Keith Runge, Pierre Lucas, Takahiro Yamamoto, Kenji Sasaoka, Kwadwo Dompreh, Jose Alarco, Ian Mackinnon, Bao Jingfu, Muhammad Ammar Khan, Aleksandr Maslov, Olga Proshina, Rita Iotti, Fausto Rossi

Notice

First published in London, United Kingdom, 2018 by IntechOpen
eBook (PDF) Published by IntechOpen, 2019
IntechOpen is the global imprint of INTECHOPEN LIMITED, registered in England and Wales, registration number: 11086078, The Shard, 25th floor, 32 London Bridge Street
London, SE19SG – United Kingdom
Printed in Croatia

British Library Cataloguing-in-Publication Data
A catalogue record for this book is available from the British Library

Additional hard and PDF copies can be obtained from orders@intechopen.com

Phonons in Low Dimensional Structures
Edited by Vasilios N. Stavrou

p. cm.

Print ISBN 978-1-78984-626-3

Online ISBN 978-1-78984-627-0

eBook (PDF) ISBN 978-1-83881-803-6

Meet the editor

Dr. V. N. Stavrou is currently an adjunct member at the Hellenic Naval Academy, Piraeus, Greece. He received an MSc and PhD in Theoretical Solid State Physics from the University of Essex in England in 1995 and 1999, respectively. He has held postdoctoral positions at the following research institutions: Deutsche Forschungsanstalt fuer Luft und Raumfahrt e.V (German Aerospace Research Center) in Germany, Helsinki University of Technology, State University of New York (SUNY) at Buffalo, USA, and University of Iowa, USA. He is specifically interested in searching the electronic, optical, and lattice properties of semiconducting low-dimensional structures (quantum dots and quantum wells among others). These properties are of special importance for quantum computing architecture and laser technology. He has published his research work in reputable journals related, among others, to quantum computing, spintronics, decoherence in quantum dots, diluted magnetic semiconductors, and phonon models in low-dimensional structures.

Contents

Preface

In solid-state structures, phonons are important pseudoparticles that can be used to describe characteristic properties of matter such as electrical conductivity, thermal conductivity, superconductivity, carrier scattering, and light scattering by solids, among others. Phonons are quantized modes of vibration occurring in a crystal lattice, such as the atomic lattice of a solid. When the unit cell contains more than one atom, the crystal will exhibit two types of phonons: acoustic and optical phonons. Acoustic phonons can describe properties associated with small energies and optical phonons are responsible for most optical behaviors of solids. During the last four decades or so, low-dimensional structures have been theoretically and experimentally researched. Theoretical research concerns itself with models such as the bulk phonon model, the dielectric continuum model, the hydrodynamic phonon model, and the hybrid model, among others. The aforementioned models have been used to calculate the phonon modes for heterostructures such as quantum wells, quantum wires, quantum dots, nanotubes, etc. The vibration modes of the solid-state structures have been observed by using spectroscopic techniques such as Raman and infrared spectroscopy.

The first part of the book includes chapters related to semiconductor devices and metallic glasses devices. More precisely, topics related to interface phonons and polaron states, carrier-phonon non-equilibrium dynamics, directional projection of elastic waves in parallel array of N elastically coupled waveguides, collective dynamics for longitudinal and transverse phonon modes, and elastic properties for bulk metallic glasses are included. The second part of the book contains, among others, topics related to superconductor devices, phononic crystal devices, carbon nanotube devices such as phonon dispersion calculations using density functional theory for a range of superconducting materials, phononic crystal-based MEMS resonators, absorption of acoustic phonons in the hyper-sound regime in fluorine-modified carbon nanotubes and single-walled nanotubes, phonon transport in carbon nanotubes, quantization of phonon thermal conductance, and phonon Anderson localization.

As an editor of this book, I would like to express my gratitude to all authors for their contributions and their high research standards and constructive feedback. Lastly, I would like to express my gratitude to the IntechOpen team for their support during the preparation of this book.

Dr. Vasilios N. Stavrou
Hellenic Naval Academy
Greece

Section 1

Semicoductor and Metallic Devices

Chapter 1

Interface Phonons and Polaron States in Quantum Nanostructures

Aleksandr Yu Maslov and Olga V. Proshina

Additional information is available at the end of the chapter

http://dx.doi.org/10.5772/intechopen.80403

Abstract

The interface optical phonons arise near the hetero-interface of a quantum nanostructure. Moreover, its spectrum and dispersion laws may differ from ones for excitations arising in the bulk materials. The study of such excitations can give fundamentally new information about the optical and transport properties of nanostructures. The interaction of charged particles with polar optical phonons can lead to the large radius polaron creation in the materials with high ionicity. This chapter deals with the results of our theoretical investigations of the polaron states in quantum wells, quantum wires, and quantum dots. The charged particle and exciton interaction with both bulk and interface optical phonons are taken into account. The original method has been developed taking into consideration an interface phonon influence. The enhancement conditions are found for both strong and weak interactions. It is established that the barrier material dielectric properties give a decisive contribution to the polaron binding energy value for strong electron-phonon interaction. The manifestation of strong polaron effects is a pronounced demonstration of the interface optical phonon influence on optical and transport properties of nanostructures.

Keywords: interface optical phonons, quantum well, quantum wire, quantum dot, electron-phonon interaction, polaron

1. Introduction

The electron-phonon interaction proves to be rather weak for most of the phonon branches. Such interaction can be taken into account in the framework of perturbation theory. The interaction of charged particles with polar optical phonons turns out to be fundamentally different [1]. The effective constant of the electron-phonon interaction may exceed unity in

materials with high ionicity. Moreover, the formation of a new type of elementary excitations, which is a bound state of charged particles and polar optical phonons, is possible even in bulk materials. This is the so-called large-radius polaron. The conditions for the appearance of such polaron are most favorable in quantum-dimensional structures. First, the additional branches of polar optical phonons, which are the interface phonons, appear in such structures. Second, the effective interaction of charged particles with polar optical phonons increases with the decreasing structure dimensionality. This significantly expands the range of materials for the nanostructure design where the large-radius polaron formation is possible. The large-radius polaron appearance significantly changes the optical and transport properties of nanostructures. Even the manifestation of polaron superconductivity may take place [2]. Available theoretical studies of large radius polaron in quantum nanostructures consider the charged particle interaction with only one polar phonon mode [2–10]. This approach seems to be inconsistent for us. The phonon spectrum modification turns out to be very significant in quantum nanostructures. Therefore, it is necessary to take into account the interaction with all phonon branches in the large-radius polaron investigations.

In this chapter, conditions of strong electron-phonon interaction observation are investigated theoretically in the quantum well, quantum wire, and quantum dot. Particular attention is paid to the theory of charged particle interaction with interface optical phonons playing a decisive role in quantum wells and quantum wires. The contribution of interface phonons to the interaction energy value turns out to be comparable with that of bulk phonons in the quantum dot case. The conditions necessary for the strong electron-phonon interaction are obtained for all types of nanostructures. Analytic expressions for the polaron binding energy are found for nanostructures considered. In some cases, the results for the weak electron-phonon interaction are discussed. This helps to understand better the interaction in a region of intermediate values of the coupling constant where obtaining the analytical result is impossible.

The total Hamiltonian of the system is given by:

$$\hat{H} = \hat{H}_e + \hat{H}_{ph} + \hat{H}_{e-ph,} \tag{1}$$

where the electron Hamiltonian $\hat{H}_e$ describes charged particle interaction with nanostructure potential; $\hat{H}_{ph}$ contains the energies of all optical phonon branches; and $\hat{H}_{e-ph}$ is the electron-phonon interaction Hamiltonian. The expressions for these operators will be given below. The wave functions and energies corresponding to the Hamiltonian from Eq. (1) can be found both for the strong and for the weak electron-phonon interaction. Strong interaction is implemented under the condition:

$$E_{pol} \gg \hbar\omega_0. \tag{2}$$

Here $\hbar\omega_0$ is the optical phonon energy and E_{pol} is the polaron binding energy. Weak interaction corresponds to the inverse inequality:

$$\hbar\omega_0 \gg E_{pol}. \tag{3}$$

In this case, the contribution of the electron-phonon interaction can be taken into account by perturbation theory.

The adiabatic approximation turned out to be an effective method for solving the problem in the case of a strong electron-phonon interaction. Within the framework of this approach, the motion of the charged particles (electrons and holes) is considered to be fast, and vibrations of the atoms of the crystal lattice are supposed to be slow. The Hamiltonian from Eq. (1) can be averaged over the wave function of fast motion Ψ_m. The averaged Hamiltonian $\hat{H}_{av}$ can be written in the form:

$$\hat{H}_{av} = E_m\{\Psi_m\} + \hat{H}_{ph} + \hat{H}_{e-ph,av}. \tag{4}$$

Eq. (4) contains the energy of charged particles $E_m\{\Psi_m\}$, which is the functional of the wave function in a general case. Here $\hat{H}_{e-ph,av}$ is the Hamiltonian of electron-phonon interaction averaged over the wave function Ψ_m. In what follows, we will use the standard expression for $\hat{H}_{ph}$:

$$\hat{H}_{ph} = \sum_{r,n} \hbar\omega_{r,n} a^+_{r,n} a_{r,n}, \tag{5}$$

where the index r denotes different phonon branches; n is the quantum number that takes various values for the different nanostructures; $a^+_{r,n}$ and $a_{r,n}$ are the phonon creation and annihilation operators, respectively. Averaged Hamiltonian of electron-phonon interaction $\hat{H}_{e-ph,av}$ can be written as:

$$\hat{H}_{e-ph,av} = \sum_{r,n} \alpha(r,n)\left[a^+_{r,n} + a_{r,n}\right]. \tag{6}$$

Here the interaction parameters $\alpha(r,n)$ must be defined for all phonon branches in each nanostructure type. Eq. (4) is reduced to a diagonal form with respect to the phonon variables by using the unitary transformation $e^{-U}\hat{H}_{av}e^{U}$, where

$$U = \sum_{r,n} \alpha(r,n)\left[a_{rn} - a^+_{rn}\right]. \tag{7}$$

As a result, we get

$$e^{-U}\hat{H}_{av}e^{U} = E_{pol}\{\Psi_m\} + \hat{H}_{ph}. \tag{8}$$

As follows from Eq. (8), the spectrum of all phonon branches remains unchanged in the adiabatic approximation. The value $E_{pol}\{\Psi_m\}$ has the meaning of the binding energy of a large-radius polaron. This energy depends on the charge particle interaction parameters for all branches of the polar optical phonon spectrum. It is also a functional of the electron wave function Ψ_m that is used in the averaging procedure. The explicit form of this wave function Ψ_m is determined from the condition for the minimum of the polaron energy E_{pol}. This solution scheme is used below to find the polaron binding energy in various nanostructures.

2. Symmetric quantum well

In general, for the case of a quantum well, the interaction of charged particles with the phonons of the well, barriers, and interface phonons must be taken into account. Let us consider

the case of complete localization of charged particles within a quantum well. In this case, the interaction of such particles with barrier material phonons can be neglected. Nevertheless, the effect of barriers is very important. This is determined by the structure and properties of interface phonon spectrum. To describe the properties of interface phonons, we will use the continuum model proposed in [11]. The spectrum of the symmetric mode of interface phonons is determined from the solution of the following equation:

$$\varepsilon^{(w)}(\omega) th\left(\frac{qL}{2}\right) + \varepsilon^{(b)}(\omega) = 0, \tag{9}$$

where L is the quantum well characteristic size; q is two-dimensional wave vector; $\varepsilon^{(w)}(\omega)$ and $\varepsilon^{(b)}(\omega)$ are the dielectric functions of the quantum well and barriers, respectively. The frequency dispersion of the dielectric function in the phonon frequency region is determined as follows:

$$\varepsilon(\omega) = \varepsilon_{\infty} \frac{\omega^2 - \omega_{LO}^2}{\omega^2 - \omega_{TO}^2}. \tag{10}$$

Here ω_{LO} and ω_{TO} are the frequencies of longitudinal and transverse optical phonons, respectively, and ε_{∞} is the high-frequency dielectric constant. The expression Eq. (10) means that we use the approximation of dispersionless modes for bulk optical phonons. It is in this approximation interface, and bulk phonon modes can be considered independently [12]. The contribution of the antisymmetric mode of interface phonons vanishes when the Hamiltonian is averaged over the wave function of the charged particle localized in a symmetric quantum well. Let us start with the electron polaron. The amplification of the electron-phonon interaction occurs in fairly narrow quantum wells having a width L that is less than the polaron radius a_0:

$$L < a_0. \tag{11}$$

The exact definition of the polaron radius a_0 will be given below.

When the inequality from Eq. (11) is satisfied, the electron wave function $\Psi_m^{(e)}(\mathbf{r})$ can be represented as a product:

$$\Psi_m^{(e)}(\mathbf{r}) = \phi_m(z)\, \chi_m(\mathbf{r}_{\parallel}), \tag{12}$$

where $\phi_m(z)$ is the transverse motion wave function that is determined by the quantum well potential; $\mathbf{r}_{\parallel}$ is the two-dimensional plane well coordinate; and $\chi_m(\mathbf{r}_{\parallel})$ is yet unknown two-dimensional wave function that is determined by electronic localization in a self-consistent well created by polar optical phonons.

The electron-phonon interaction parameters $\alpha(r, n)$ from Eq. (6) are given in [11, 13]. For further discussion, we will use an explicit form of these coefficients for the symmetric interface mode and an even part of the interaction with the localized phonons of the quantum well. Performing the aforementioned procedure allows us to get the polaron binding energy $E_{pol,well}$

from Eq. (8) as a functional of the wave function $\chi_n(\mathbf{r}_\parallel)$ for the quantum well case. It can be defined from the condition of minimum for this functional [13]:

$$-\frac{\hbar^2}{2m_e}\nabla^2\chi_m(\mathbf{r}_\parallel)-\frac{e^2}{\varepsilon_{opt}^{(b)}}\int d^2\mathbf{r}_\parallel\frac{\left|\chi_m(\mathbf{r}_\parallel)\right|^2}{\left|\mathbf{r}_\parallel-\mathbf{r}_\parallel\right|}\chi_m(\mathbf{r}_\parallel)=\left(E_m-E_{pol,well}^{(e)}\right)\chi_m(\mathbf{r}_\parallel). \tag{13}$$

Here $E_{pol,well}^{(e)}$ is the electron polaron binding energy; $\varepsilon_{opt}^{(b)}$ from $\frac{1}{\varepsilon_{opt}^{(b)}}=\frac{1}{\varepsilon_\infty^{(b)}}-\frac{1}{\varepsilon_0^{(b)}}$ is the optical dielectric function of the barriers; and E_m is the size quantization level energy. Eq. (13) formally coincides with the equation for two-dimensional polaron [3–6, 14]. However, it should be noted that Eq. (13) involves the electron mass within the quantum well and the optical barrier dielectric constant. This combination of parameters appears because the major contribution to the polaron binding energy is given by interaction with interface optical phonons. In accordance with Eq. (13), the polaron binding energy in the quantum well is:

$$E_{pol,well}^{(e)}=-C_1\frac{m_e e^4}{\left(\varepsilon_{opt}^{(b)}\right)^2\hbar^2}, \tag{14}$$

where $C_1\cong 0.4$ is the numerical coefficient. Its value is determined by the integral of two-dimensional polaron dimensionless wave function $\chi_m(\mathbf{r}_\parallel)$ given in [14]. In this case, the radius of the electron polaron state $a_0^{(e)}$ is:

$$a_0^{(e)}=\frac{\hbar^2\varepsilon_{opt}^{(b)}}{m_e e^2}. \tag{15}$$

It is this quantity from Eq. (11) on which the adiabatic approximation used in our work is based. In the next order in the parameter from Eq. (11), some corrections to polaron binding energy Eq. (14) appear. These corrections can be expressed in terms of the dimensionless wave function of two-dimensional polaron $\chi_0(\mathbf{r}_\parallel)$ known from [14]. The calculations give the following:

$$\Delta E_{pol,well}=E_{pol,well}^{(e)}\frac{L}{a_0^{(e)}}\left(D_V+D_S\right)C_2, \tag{16}$$

where $C_2=0.07$ is the numerical factor that was calculated in [3]. The dimensionless coefficients D_V and D_S are determined by fairly complex combinations of the phonon frequencies in the quantum well and barrier materials and are found in [13]. It turns out that the corrections to the binding energy of a polaron are related to the interaction with both bulk and interface phonons. According to the expressions for D_V and D_S received in [13], these corrections may have different signs. The total value of the binding energy depends essentially on the dielectric properties of both the quantum well and the barrier materials. We note that the main contribution to polaron binding energy from Eq. (14) coincides with our result obtained earlier in [15] by means of an approximate method for calculating the phonon fields. However, the accurate inclusion of corrections to $E_{pol,well}^{(e)}$ in this approximate approach is impossible. Obtaining a quantity $\Delta E_{pol,well}$ from Eq. (16) requires taking into account the phonon spectrum of the system.

A similar consideration can be repeated for a hole polaron. The main contribution to the binding energy of a hole polaron is determined by an expression analogous to Eq. (14). It looks like this:

$$E_{pol,well}^{(h)} = -C_1 \frac{m_h e^4}{\hbar^2 \left(\varepsilon_{opt}^{(b)}\right)^2}. \tag{17}$$

Usually, for semiconductor materials, the hole mass m_h is much larger than the electron mass m_e, then the binding energy of the hole polaron from Eq. (17) is much larger than the energy of the electron polaron from Eq. (14). In this case, the localization region for a hole polaron $a_0^{(h)}$ turns out to be smaller than that for an electron polaron $a_0^{(e)}$:

$$a_0^{(h)} = \frac{m_e}{m_h} a_0^{(e)} << a_0^{(e)}. \tag{18}$$

The condition from Eq. (18) plays an important role in the study of a polaron exciton. The interaction of an exciton with optical phonons has a number of additional features. Polarization of the medium, created by an electron and a hole, partially compensates each other. The degree of this compensation essentially depends on the ratio of the radii of the electron and hole polarons, $a_0^{(e)}$ and $a_0^{(h)}$, respectively, and the exciton radius $a_0^{(ex)}$. In this case, the influence of the barrier dielectric properties on the exciton state must be taken into account in narrow quantum wells. Without allowance for the electron-phonon interaction, such influence was considered in [16]. In these articles, it was shown that the exciton binding energy in narrow symmetric quantum wells has the form:

$$E_{ex,well} = \frac{2\mu e^4}{\left(\varepsilon_0^{(b)}\right)^2 \hbar^2}. \tag{19}$$

Here μ is the reduced mass of the electron and hole in the quantum well. The radius of such quasi-two-dimensional exciton $a_0^{(ex)}$ also depends on the barrier dielectric constant $\varepsilon_0^{(b)}$. It is equal to:

$$a_0^{(ex)} = \frac{\hbar^2 \varepsilon_0^{(b)}}{\mu e^2}. \tag{20}$$

Eqs. (19) and (20) are valid for narrow quantum wells, the width of which satisfies the inequality

$$L < a_0^{(ex)}. \tag{21}$$

The possibility of strong coupling of an exciton with polar optical phonons depends on the relationship between $a_0^{(ex)}$ and $a_0^{(h)}$. It is seen from Eqs. (15) and (20) that the electron polaron radius is always greater than the exciton one, that is $a_0^{(e)} > a_0^{(ex)}$. If also $a_0^{(h)} > a_0^{(ex)}$, then the medium polarization created by the electron and hole largely compensates each other. In this case, for the exciton, the condition of strong coupling with phonons, as a rule, is not realized.

When the opposite relationship is satisfied, that is

$$a_0^{(h)} < a_0^{(ex)}, \tag{22}$$

the strong exciton-phonon interaction is possible. The main contribution to the polaron exciton binding energy is due to the localization of the hole in the polaron well. Its size is determined by the radius of the hole polaron $a_0^{(h)}$. The motion of an electron occurs in a larger region of space. The medium polarization created by the electron compensates partially the polarization created by the hole. If we take into account the largest contributions with respect to the parameters of Eqs. (11) and (22) only, then the polaron exciton binding energy is equal to:

$$E_{ex,well} = C_1 \frac{m_h e^4}{\hbar^2 \left(\varepsilon_{opt}^{(b)}\right)^2} - 2\frac{m_e e^4}{\hbar^2 \left(\varepsilon_{\infty}^{(b)}\right)^2}. \tag{23}$$

The second contribution in Eq. (23) is small, compared to the first one in the parameter $m_e/m_h \ll 1$. It can be seen from Eq. (23) that the possibility of strong coupling of an exciton with optical phonons depends on parameters of both the quantum well and barrier materials. The appearance of a polaron exciton requires a significant difference between the effective masses of an electron and a hole in a quantum well. In addition, the presence of barriers made of high ionicity materials is necessary. In this case, the polarization properties of the quantum well material do not play an essential role.

For most II–VI compounds, the exciton radius $a_0^{(ex)}$ from Eq. (20) is in the range 20–40 $\mathring{A}$. The electron polaron radius $a_0^{(e)}$ (Eq. (15)) falls within the range 50–100 $\mathring{A}$, and hole polaron one $a_0^{(h)}$ (Eq. (18)) is approximately 10–20 $\mathring{A}$. Therefore, the strong exciton-phonon interaction condition from Eq. (22) can be satisfied. This means that the quasi-two-dimensional polaron formation is possible in sufficiently narrow quantum wells of width $L < 20$ $\mathring{A}$.

The heterovalent quantum wells based on II–VI/III–V materials are more promising target for the experimental study of polaron effects in the case of strong electron-phonon interaction. For such structures, growth technologies have been developing successfully in recent times [17]. In the III–V compounds, effective masses of quantum well carriers are small. The optical dielectric function of the barriers based on II–VI materials is also rather small. Thus, given above values of exciton and polaron radii increase by 2 – 3 times. Hence, a quasi-two-dimensional polaron in heterovalent quantum wells can be observed for the well widths $L \leq 50$ $\mathring{A}$. Quantum wells of more complex configuration (e.g., I–VII/III–V) can also become a promising object for the polaron study when strong electron-phonon interaction takes place.

3. Cylindrical quantum wire

In the quantum wires under consideration, the spectrum of interface phonons depends on the one-dimensional wave vector $\mathbf{q}$ directed along the wire axis. Using the same Eq. (10) for the dielectric functions of wire and barrier materials, we obtain the interface phonon spectrum equation in the context of the continuum approximation:

$$\frac{I_m'(q\,\rho_0)}{I_m(q\,\rho_0)}\,\varepsilon^{(b)}(\omega) \;=\; \frac{K_m'(q\,\rho_0)}{K_m(q\,\rho_0)}\,\varepsilon^{(w)}(\omega). \tag{24}$$

Here I_m is the m-th order modified Bessel function of the first kind; K_m is the m-th order modified Bessel function of the second kind; and ρ_0 is the quantum wire radius. The interface phonon spectrum is determined by solution of Eq. (24). The wave vector dependences of interface phonon frequencies are shown in **Figure 1**. These dependences are calculated for the quantum wire based on *CdSe*, surrounded by *ZnSe* barriers for $m = 0$ in Eq. (24). The compound parameters are taken from [18].

The adiabatic parameter of this problem is the ratio between the quantum wire radius ρ_0 and the polaron radius a_0:

$$\rho_0 \ll a_0. \tag{25}$$

Below, an exact analytic expression is obtained for determining the polaron radius. The inequality Eq. (25) means that the main contribution to the binding energy of a polaron is determined by the wave vector values which are small as:

$$q\,\rho_0 < 1. \tag{26}$$

According to Eq. (25), the electron wave function for n-th size quantization level can be written as:

$$\Psi^{(e)}(\mathbf{r}) \;=\; \phi(n^{(e)}; m^{(e)}; \boldsymbol{\rho})\chi(n^{(e)}; m^{(e)}; z)\, e^{im^{(e)}\phi}. \tag{27}$$

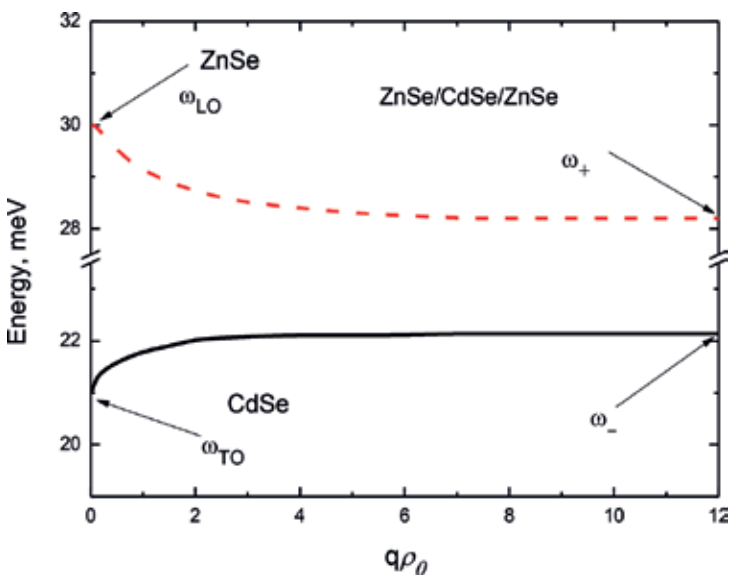

Figure 1 . Wave vector dependencies of interface optical phonon energies for *ZnSe/CdSe/ZnSe* quantum wire; $m = 0$.

Here $n^{(e)}$ is size quantization level number and $\phi(n^{(e)}, m^{(e)}, \boldsymbol{\rho})$ is the wave function of two-dimensional electron motion. The electron-phonon interaction does not affect this motion, which occurs within a quantum wire. The wave function $\chi(n^{(e)}, m^{(e)}, z)$ describes the electron localization in phonon self-consistent potential well. Not disturbed electron states in the quantum wire are defined by the quantum numbers $n^{(e)}$ and $m^{(e)}$. In the case of total electron localization inside the cylindrical quantum wire, the wave function $\phi(n^{(e)}, m^{(e)}, \boldsymbol{\rho})$ has the form:

$$\phi(n^{(e)}, m^{(e)}, \boldsymbol{\rho}) = J_{m^{(e)}}\left[\mu_{n^{(e)}}(m^{(e)})\frac{\rho}{\rho_0}\right], \tag{28}$$

where $\mu_{n^{(e)}}(m^{(e)})$ is $n^{(e)}$-th root of $m^{(e)}$-th order Bessel function, $\chi(n^{(e)}, m^{(e)}, z)$ is the wave function which may be obtained after solving the self-consistent problem. Thus, the total wave function from Eq. (27) must be normalized.

Generally, the value of polaron binding energy $\Delta E_{pol,wire}$ is determined by the optical phonon spectrum properties and depends on electron size-quantization level number. It is necessary to take into account the optical phonons localized both inside the quantum wire and at the hetero-interface. We obtain this energy after the angle averaging procedure expressible in explicit form:

$$\Delta E_{pol,wire} = -\sum_{n,q}\frac{\alpha^2(0,n,q)}{\hbar\omega_0} - \sum_{q}\frac{\alpha^2(0,q)}{\hbar\omega_S}. \tag{29}$$

Here $\alpha(0, n, q)$ and $\alpha(0, q)$ are the coefficients defined in Eq. (6). The value of $\Delta E_{pol,wire}$ from Eq. (29) is defined by the interaction of an electron with phonon modes for which $m = 0$ and contains the contribution caused by interaction with both confined and interface phonons for all size-quantization levels. Eq. (29) can be used for numerical analysis of electron-phonon interaction characteristic properties for the quantum wires of various symmetry. At the same time, the electron energy and wave function are obtained analytically when the inequality from Eq. (26) is satisfied.

The interaction of an electron with interface phonon mode of the frequency close to barrier frequency $\omega_{LO}^{(b)}$ gives the most significant contribution to the polaron binding energy in the parameter Eq. (26). It has the form:

$$\Delta E_{pol,wire} = \frac{e^2}{2\varepsilon_{opt}^{(b)}}\sum_{q}\left|\int|\chi(z)|^2\exp[iqz]dz\right|^2\ln(q\rho_0). \tag{30}$$

Eq. (30) contains the optical dielectric function of the barriers $\varepsilon_{opt}^{(b)}$. In other words, the polaron states arise independently of the quantum wire material dielectric properties. Contribution due to these properties can be obtained in higher orders in the parameter from Eq. (26). It can be seen from Eq. (30) that phonon wave vector q characteristic values that determine the electron-phonon interaction are inversely proportional to the polaron radius magnitude, that is $q \simeq 1/a_0$. In this region, the logarithmic function changes slightly, and we can obtain the energy $\Delta E_{pol,wire}$ with the same accuracy in parameter from Eq. (26):

$$\Delta E_{pol,wire} = \frac{e^2}{2\varepsilon_{opt}^{(b)}} \ln\left(\frac{\rho_0}{a_0}\right) \sum_q \left| \int |\chi(z)|^2 \exp[iqz] dz \right|^2. \tag{31}$$

The electron polaron binding energy as the functional of unknown yet wave function $\chi(z)$ can be obtained by substituting Eq. (31) into the average Hamiltonian from Eq. (4) and by variational method:

$$-\frac{\hbar^2}{2m_e}\frac{d^2\chi(z)}{dz} - \left(\frac{e^2}{\varepsilon_{opt}^{(b)}} \ln\left(\frac{a_0}{\rho_0}\right)\right) \chi^3(z) = E_{pol}^{(e)} \chi(z). \tag{32}$$

The solution of nonlinear Eq. (32) has the form:

$$\chi(z) = \frac{1}{\sqrt{2a_0}} \frac{1}{ch(z/a_0)}. \tag{33}$$

By substituting the wave function from Eq. (33) into Eq. (32), we obtain the polaron binding energy as:

$$E_{pol,wire}^{(e)} = -\frac{Me^4}{\hbar^2 \left(\varepsilon_{opt}^{(b)}\right)^2} \ln^2\left(\frac{a_0}{\rho_0}\right). \tag{34}$$

Thus, the polaron radius a_0 contains the adiabatic parameter from Eq. (25) and is equal to:

$$a_0 = \frac{\hbar^2 \varepsilon_{opt}^{(b)}}{m_e e^2 \ln\left(\frac{a_0}{\rho_0}\right)}. \tag{35}$$

The substitution of the material parameters [18] for *ZnSe*/*CdSe*/*ZnSe* quantum wire into Eq. (35) leads one to expect that the strong polaron effects should be observed at a wire radius $\rho_0 < 40\ \mathring{A}$.

The condition for polaron exciton appearance in a quantum wire is analogous to that considered above for a quantum well, Eq. (18). The basic requirement is a significant difference between the hole and the electron masses. If the radius of a quantum wire corresponds to the conditions from Eqs. (21) and (22), a complete compensation of the contributions from the electron and hole does not occur, and a strong electron-phonon interaction is possible.

4. Spherical quantum dot

In this chapter, we study the structures in which the quantum dot and matrix materials have different phonon modes and its dielectric functions are described by Eq. (10). We have used the approximation presented in [19], where the interface phonon spectrum is described by the following equation:

$$l\,\varepsilon^{(d)}(\omega) + (l+1)\,\varepsilon^{(m)}(\omega) = 0, \tag{36}$$

where $\varepsilon^{(d)}(\omega)$ and $\varepsilon^{(m)}(\omega)$ are the dielectric functions of the quantum dot and matrix materials, respectively; l is the number of the spherical harmonic for corresponding interface vibration. If $l = 0$, there is only one solution, which coincides with ω_{LO} in the matrix material. For $l \neq 0$, there are two solutions for the interface phonon frequencies.

For our problem, the coefficients $\alpha(r, n)$ from Eq. (6) have the form [19]:

$$\alpha(v, nlm) = \hbar\,\omega_{LO}^{(m)}\,\rho(nlm)\left(\frac{4\pi e^2}{r_0\,\mu_{nl}^2\,j_{l+1}^2(\mu_{nl})\,\varepsilon_{opt}^{(m)}}\right)^{1/2} \tag{37}$$

for the bulk phonons and

$$\alpha(s, l) = -\left(\frac{2\pi e^2}{\omega^2 r_0}\right)^{1/2}\left[\varepsilon_\infty^{(d)}\frac{\omega_{LO,d}^2-\omega_{TO,d}^2}{\left(\omega^2-\omega_{TO,d}^2\right)^2}\,l+\varepsilon_\infty^{(d)}\frac{\omega_{LO,m}^2-\omega_{TO,m}^2}{\left(\omega^2-\omega_{TO,m}^2\right)^2}(l+1)\right]^{-1/2}\cdot\hbar\,\omega_s\,\rho_s(lm) \tag{38}$$

for the interface phonons. Here r_0 is the quantum dot radius; j_l are the spherical Bessel functions; and $j_l(\mu_{nl}) = 0$. The quantities $\rho(nlm)$ and $\rho_s(lm)$ are the bulk and interface phonons densities, respectively, which have the form:

$$\rho(nlm) = j_l\left(\mu_{nl}\frac{r}{r_0}\right)Y_{lm}(\theta,\phi), \tag{39}$$

$$\rho_s(lm) = \left(\frac{r}{r_0}\right)^l Y_{lm}(\theta,\phi), \tag{40}$$

where $Y_{lm}(\theta,\phi)$ are the spherical wave functions. After the averaging procedure over the electron wave function $\Psi(\mathbf{r})$, the values of the densities from the equations should be replaced by its average values:

$$\rho_{av} = \int d^3 r\,|\Psi(\mathbf{r})|^2\,\rho(nlm), \tag{41}$$

$$\rho_{s,av} = \int d^3 r\,|\Psi(\mathbf{r})|^2\,\rho_s(lm). \tag{42}$$

In this case, the energy of electron size quantization level polaron shift has the form:

$$\Delta E_{pol,dot} = -\sum_{n,l,m}\hbar\,\omega_{LO}\,|\alpha(v, nl)|^2\,|\rho_{av}|^2-\sum_{l,m}\hbar\omega(l)\,|\alpha(s, l)|^2\,|\rho_{s,av}|^2. \tag{43}$$

As follows from Eq. (43), the bulk and interface phonon contributions to the polaron binding energy are summed. It will be seen from the further consideration that the interface phonon contribution can exceed the surface phonon one under certain conditions. The results obtained make it possible to calculate the polaron shifts for any size quantization level. Consider a polaron shift for a particle with a spherical wave function. For example, it could be an electron in the ground state. The polaron shift can be obtained analytically [20] and is equal to:

$$E_{pol,dot}^{(e)} = -\frac{e^2}{r_0}\left(\frac{0.39}{\varepsilon_{opt}^{(d)}} + \frac{0.5}{\varepsilon_{opt}^{(m)}}\right). \tag{44}$$

It follows from Eq. (44) that taking into account matrix polarization leads to an increase in the polaron effect. It should be noted that there is a noticeable polaron shift even for quantum dots based on a nonpolar material. This is due to the presence of interface phonons that create the polarization in surrounding matrix. Note also that for the quantum dot case, the contributions of charged particle interaction with bulk and interface phonons are of the same order of magnitude in the adiabatic parameter.

$$r_0 \ll a_0. \tag{45}$$

This is the main difference between this problem and the quantum well and quantum wire considered earlier. For these structures, the largest contribution in the adiabatic parameters from Eq. (11) and Eq. (25) is caused by the interface phonons. The inequality (45) is satisfied, for example, for *CdSe* quantum dots in a *ZnSe* matrix when the dot radius $r_0 < 30\ \mathring{A}$.

Another significant feature of the polaron in quantum dots is a significant suppression of the polaron exciton state. The exciton polaron shift turns out to be zero for the localization of the electron and hole with wave functions of the same symmetry inside the quantum dot. The nonzero interaction of an exciton with polar optical phonons arises for different symmetries of the electron and hole wave functions only. This is possible if the quantum dot is made of a material where interband transitions are forbidden (e.g., CuO_2) or if the valence band complex spectrum is taken into account. The latter is typical for most III–V and II–VI semiconductor compounds. It is shown in [20] that taking into account the valence band degeneracy in the Luttinger Hamiltonian model leads to a noticeable difference between the polaron shift for the electron and hole. In this case, the exciton-phonon interaction can turn out to be strong at the quantum dot.

5. Weak electron: phonon interaction

The interaction of charge particles with polar optical phonons can be weak in nanostructures based on materials with low ionicity. When the condition Eq. (3) is satisfied, the electron-phonon interaction described by the Hamiltonian $\hat{H}_{e-ph}$ can be taken into account by the perturbation theory [21]. In the bulk crystals with weak electron-phonon interaction, the position of the ground electronic state level is shifted, and the electron effective mass increases [22]. Our calculations have shown that similar effects arise in a quantum well, and they are mainly due to the interaction of charge carriers with interface optical phonons. The level position displacement corresponds to the renormalization of the forbidden band width. When the electron-phonon interaction is weak, this effect is rather small. Therefore, the main attention will focus to polaron effect on the charged carrier effective mass change. This change for an electron depends on the material dielectric properties of both the quantum well and barriers. A quasi-two-dimensional analog of known results for bulk materials [22] is obtained in the sufficiently narrow quantum well for which the size quantization energy ΔE_m exceeds the quantum well localized optical phonon energy $\hbar\omega^{(w)}(\mathbf{q})$ and interface optical phonon energy

$\hbar\omega^{(s)}(\mathbf{q})$. The main contribution to the electron ground state energy correction with respect to parameter $\Delta E_m/\hbar\omega^{(w)}(\mathbf{q})$ has the form:

$$\Delta E_m = \frac{\pi}{2}\alpha_{eff}\hbar\omega^{(b)} + \frac{p^2}{2m^*}. \tag{46}$$

The frequency from Eq. (46) is $\omega^{(b)} = \omega^{(s)}(0)$. The polaron mass is equal to:

$$m_{pol} = \frac{m^{(w)}}{1 - \pi\alpha_{eff}/8}. \tag{47}$$

Eqs. (46) and (47) are similar to the known results from two-dimensional polaron theory [14]. However, the effective coupling constant is equal to:

$$\alpha_{eff} = \frac{e^2}{2\hbar\omega^{(b)}}\left(\frac{2m^{(w)}\omega^{(b)}}{\hbar}\right)^{1/2}\left(\frac{1}{\varepsilon_\infty^{(b)}} - \frac{1}{\varepsilon_0^{(b)}}\right). \tag{48}$$

It is seen from Eq. (48) that, just as in the case of a strong-coupling polaron, the effective electron-phonon interaction constant is determined by the effective electron mass inside the quantum well and the barrier material dielectric properties. This value is analogous to the Frohlich constant, but it is not a characteristic of any particular material and is determined by the quantum well properties. In a specific approximation, when the condition $q \ll 1/L$ is satisfied, the charge particle interaction with polar optical phonons is defined by the interface phonon spectrum. The interface phonon frequencies in the same approximation are close to ones for the barrier optical phonons and can differ markedly from the quantum well optical phonon frequencies. This may explain the discrepancy between the experimental and theoretical values of the effective polaron mass for the *ZnO-ZnMgO* quantum well, obtained in [23]. In estimating the effective mass, the authors of [23] have used the Frohlich constant for *ZnO* instead of the effective constant from Eq. (48). Using the effective constants of Eq. (48) greatly improves the agreement between theory and experimental data.

6. Conclusions

It is shown that the interface phonons play an important role in the polaron state formation in quantum nanostructures. In quantum wells and quantum wires, the polaron binding energy is determined mainly by the interaction of charged particles with interface optical phonons. In the quantum dots, the contribution due to the interaction with interface phonons is additive with the energy of interaction with bulk phonons. Moreover, for nanostructures based on the same materials, the polaron binding energy increases with the structure dimensionality reduction.

Thus, the results obtained show that the barrier material ionicity degree plays a fundamental role for forming the large radius polarons in quantum wells and quantum wires. Meanwhile, the quantum well itself can be based on low ionicity material. The interaction of charged particles with interface optical phonons is the reason that the polaron effects are enhanced significantly.

The condition for observing a polaron exciton is the essential difference between the electron and hole effective masses. In this case, only partial compensation of the phonon interaction with charged particles occurs, and the achievement of a strong electron-phonon interaction is possible.

Thus, the appearance of strong polaron effects is a clear demonstration of the interface phonon influence on optical and transport properties of nanostructures.

Author details

Aleksandr Yu Maslov* and Olga V. Proshina

*Address all correspondence to: maslov.ton@mail.ioffe.ru

Ioffe Institute, Saint Petersburg, Russia

References

[1] Pekar SI. Untersuchungen uber die electronentheorie kristalle. Berlin: Akademie Verlag; 1954. p. 184

[2] Alexandrov AS, Devreese JT. Advances in Polaron Physics. Berlin Heidelberg: Springer-Verlag; 2010. p. 165. DOI: 10.1007/978-3-642-01896-1

[3] Ipatova IP, Maslov AY, Proshina OV. Polaron in quantum nanostructures. Surface Science. 2002;**507-510**:598-602. DOI: 10.1016/S0039-6028(02)01321-3

[4] Pokatilov EP, Klimin SW, Fomin VM, Devreese JT, Wise FW. Multiphonon Raman scattering in semiconductor nanocrystals: Importance of nonadiabatic transitions. Physical Review B. 2002;**65**:075316. DOI: 10.1103/PhysRevB.65.075316

[5] Verzelen O, Ferreira R, Bastard G. Excitonic polaron in semiconductor quantum dot. Physical Review Letters. 2002;**88**:146803. DOI: 10.1103/PhysRevLett.88.146803

[6] Vasilevsky MI, Anda EV, Makler SS. Electron-phonon interaction effects in semiconductor quantum dots: A nonperturabative approach. Physical Review B. 2004;**70**:035318. DOI: 10.1103/PhysRevB.70.035318

[7] Asatryan AL, Vartanian AL, Kirakosyan AA, Vardanyan LA. Electric field and image charge effects on impurity-bound polarons in a CdS colloidal quantum dot embedded in organic matrices. Physica B: Condensed Matter. 2016;**503**:70-74. DOI: 10.1016/j.physb.2016.09.020

[8] Yeranosyan MA, Vartanian AL, Vardanyan KA. Influence of spin–orbit interactions on the polaron properties in wurtzite semiconductor quantum well. Physica E: Low-dimensional Systems and Nanostructures. 2016;**75**:330-335. DOI: 10.1016/j.physe.2015.09.034

[9] Vartanian A, Kirakosyan A, Vardanyan K. Fröhlich polaron in nanowire with Rashba and Dresselhaus spin-orbit couplings. Superlattices and Microstructures. 2017;**109**:655-661. DOI: 10.1016/j.spmi.2017.05.057

[10] Miyata K, Meggiolaro D, Trinh MT, Joshi PP, Mosconi E, et al. Large polarons in lead halide perovskites. Science Advances. 2017;**3**:e1701217. DOI: 10.1126/sciadv.1701217

[11] Mori M, Ando T. Electron–optical-phonon interaction in single and double heterostructures. Physical Review B. 1989;**40**:6175. DOI: 10.1103/PhysRevB.40.6175

[12] Ridley BK. Hybrid Phonons in Nanostructures. Oxford, New York: Oxford University Press; 2017. p. 192. DOI: 10.1093/acprof:oso/9780198788362.001.0001

[13] Maslov AY, Proshina OV. The role of interface phonons in the formation of polaron states in quantum wells. Semiconductors. 2010;**44**:189-193. DOI: 10.1134/S1063782610020090

[14] Wu H, Peeters FM, Devreese JT. Exact and approximate results for the ground state energy of a Fröhlich polaron in two dimensions. Physical Review B. 1985;**31**:3420. DOI: 10.1103/PhysRevB.31.3420

[15] Maslov AY, Proshina OV, Rusina AN. Interface phonon effect on optical spectra of quantum nanostructures. Journal of Luminescence. 2009;**129**:1934-1936. DOI: 10.1016/j.jlumin.2009.01.032

[16] Keldysh LV. Excitons in semiconductor-dielectric nanostructures. Physica Status Solidi. 2001;**164**:3-12. DOI: 10.1002/1521-396X(199711)164:1<3::AID-PSSA3>3.0.CO;2-S

[17] Lassise MB, Wang P, Tracy BD, Chen G, Smith DJ, Zhang YH. Growth of II-VI/III-V heterovalent quantum structures. Journal of Vacuum Science and Technology B: Nanotechnology and Microelectronics. 2018;**36**:02D110. DOI: 10.1116/1.5017972

[18] Madelung O, editor. Landolt-Bornstein, Numerical data and functional relationships in science and technology. In: Physics of II-VI and I-VII Compounds. Vol. 17b. New York: Springer-Verlag Berlin Heidelberg; 1982. DOI: 10.1002/crat.2170231029

[19] Melnikov DV, Fowler WB. Electron-phonon interaction in a spherical quantum dot with finite potential barriers: The Fröhlich Hamiltonian. Physical Review B. 2001;**64**:245320. DOI: 10.1103/PhysRevB.64.245320

[20] Maslov AY, Proshina OV, Rusina AN. The role of surface phonons in the formation of the spectrum of polaron states in quantum dots. Semiconductors. 2007;**41**:822-827. DOI: 10.1134/S1063782607070093

[21] Maslov AY, Proshina OV. Polaron mass of charge carriers in semiconductor quantum wells. Semiconductors. 2015;**49**:1344-1347. DOI: 10.1134/S1063782615100152

[22] Madelung O. Introduction to solid-state theory. In: Springer Series in Solid-State Sciences. Stuttgart: Springer-Verlag Berlin Heidelberg; 1978. p. 491. DOI: 10.1007/978-3-642-61885-7

[23] Imanaka Y, Takamasu T, Tampo H, Shibata H, Niki S. Two-dimensional polaron mass in ZnO quantum Hall systems. Physica Status Solidi C. 2010;**7**:1599-1601. DOI: 10.1002/pssc.200983242

Chapter 2

Monte Carlo Kinetic Modeling of the Combined Carrier-Phonon Nonequilibrium Dynamics in Semiconductor Heterostructure Devices

Rita C. Iotti and Fausto Rossi

Additional information is available at the end of the chapter

http://dx.doi.org/10.5772/intechopen.80447

Abstract

Electron-phonon interaction is a key mechanism for charge and heat transport in both bulk materials as well as in state-of-the-art electronic and optoelectronic solid-state devices. Indeed, that of an effective heat dissipation, at the diverse design levels, has always been a primary issue in device operation and performances. In various circumstances, the charge carrier subsystem happens to be coupled to a significant nonequilibrium optical phonon population. This regime may be particularly pronounced in new-generation quantum emitters based on semiconductor heterostructures and operating both in the mid-infrared as well as in the terahertz region of the electromagnetic spectrum. In this chapter, we review a global kinetic approach based on a Monte Carlo simulation technique that we have recently proposed for the modeling of the combined carrier-phonon nonequilibrium dynamics in realistic unipolar multisubband device designs. Results for the case of a prototypical resonant-phonon terahertz emitting quantum cascade laser are shown and discussed.

Keywords: electronic transport theory, carrier-phonon scattering, nanoelectronic devices, density matrix, Monte Carlo simulation

1. Introduction

Electron-phonon scattering is a main mechanism behind the charge carrier dynamics in solid-state materials and devices. Its simplest treatment assumes to consider the phonon subsystem as characterized by a huge number of degrees of freedom in comparison to the electron one. The former, in other words, behaves as a thermal bath, being always in thermal equilibrium

and not crucially perturbed by the dynamics of the latter. This premise is however unconvincing for many new-generation devices, involving ultrafast and/or high-field-transport phenomena in nanomaterials and nanostructures. In these cases, the carrier-quasiparticle treatment has to be extended to properly account for phonon nonequilibrium regimes as well [1].

In general terms, the latter may be subdivided into two classes: one including coherent phenomena, where the quasiparticle nondiagonal density matrix elements play a crucial role —a typical example being that of the so-called coherent phonons—, and one in which, even in the absence of such phase-coherence effects, the quasiparticle diagonal density matrix terms significantly deviate from the equilibrium Bose distribution—a typical case being that of the so-called hot phonon effects—.[1]

A paradigmatic example within this second class of nonequilibrium phenomena is represented by quantum cascade lasers (QCLs). In the core region of these devices, the carrier dynamics in general, and the population inversion regime in particular, are not only unavoidably affected but in fact intentionally controlled through the electron-phonon interaction. This strategy was the key to success for the pioneering mid-infrared emitting devices [2], but comes out to have a crucial role also for terahertz operating structures, where the closeness of the photon and longitudinal-optical (LO) phonon energy initially oriented toward alternative, and less intuitive, designs [3, 4].

QCLs are unipolar coherent light sources whose basic principle of operation may be declined in a variety of specific—and often rather complex—designs, guided by the requested/desired output and performances [5, 6]. For the purposes of the present review, it will suffice to focus on their core region. The latter is basically a semiconductor multiquantum-well heterostructure consisting of a periodic repetition of identical stages, each made up of an active region sandwiched between an electron-injecting and an electron-collecting region. When a proper bias is applied, each collecting region behaves as an injection one for the subsequent stage, and an "electron cascade" takes place along the energy-level staircase in which the conduction band is split due to quantum confinement. Since their first demonstration, the potentialities of band-gap engineering and molecular beam epitaxy have been inspiring several successful QCL designs for both the active region and the injector/collector part. In particular, the key issue of establishing and maintaining the gain regime in the active region can be accomplished by means of a proper tailoring of electron energy relaxation dynamics, resulting in a selective depopulation of the diverse subband states. Both conventional mid-infrared as well as so-called THz resonant-phonon designs [7] are devised in such a way that the separation between the lower lasing subband and the ground one within each period matches the LO phonon energy. This allows one to maximize carrier relaxation out of the former into the latter via LO phonon emission.

As a by-product, a LO phonon population significantly out of equilibrium is expected within the core region of the running device when—as it often happens—their generation rate is

[1] Nonequilibrium electrons and phonons are sometimes referred to as 'hot electrons' and 'hot phonons', respectively. Although such a terminology seems to suggest thermalized distributions, it is worth noting that this does not need to be —and usually is not—the case.

higher than the one describing their anharmonic decay into acoustic phonon modes. Actually, if one compares the LO phonon energy with the potential energy drop allowing for the essential subband alignment along the growth direction, it comes out that, while cascading along the succession of equal stages, each electron generates at least one optical phonon per period. State-of-the-art designs may include from several tens up to more than 100 stages. It therefore easily appears how these devices are not only reliable and robust infrared light sources but also rather effective LO phonon generators; this poses severe heat-removal issues especially in high-performance device architectures [8, 9]. Already at the drawing board stage, it is evident that the combined effect of high LO phonon generation rates and limited thermal conductivity requires a realistic description of charge transport in these devices which goes beyond the thermal bath picture, taking into account the carrier interaction with a nonequilibrium phonon subsystem. In particular, while simplified multilevel rate-equation models may offer a computationally light picture of the electronic cascade in the active region [10], their quantitative/predictive value is limited and does for sure greatly benefit from the inputs offered by the more exhaustive three-dimensional multisubband kinetic picture.

In the past, several theoretical schemes have been proposed to model the impact that nonequilibrium phonon effects may have on the electron relaxation dynamics, and therefore on the performances of QCLs: Monte Carlo (MC) kinetic approaches restricted to a subgroup of subbands [11–13], within a prototypical Krönig-Penney model [12, 13] or partially refined implementations [14]. From the experimental point of view, various studies have highlighted peculiar nonequilibrium phonon features both in mid-infrared [15] as well as in THz QCLs [16, 17]; in particular, a significant heating of both the electronic and the lattice subsystem has been observed [18]. Motivated also by these evidences, we have recently addressed the issue of developing a theoretical model suitable for the microscopic simulation of realistic devices [19, 20], proposing an MC-based global kinetic approach [21]. In particular, our analysis has allowed to include on equal footing the fully three-dimensional nature of the multiband electronic structure as well as of the phonon degrees of freedom and is therefore able to overcome significant limitations affecting some of the MC techniques previously cited.

In the present chapter, we are presenting a review of the above-mentioned global MC approach. In particular, in Section 2 we shall describe the general coupled carrier-phonon model and the kinetic approach based on the MC sampling of the closed set of dynamical equations for the corresponding distribution functions; in Section 3, we will apply our model and method to a prototypical resonant-phonon THz QCL design, highlighting the interplay between the nonequilibrium electron and phonon populations; finally, in Section 4, we shall summarize and draw a few concluding remarks.

2. Physical model and kinetic description

First of all, to provide quantitative and predictive insight into the details of the carrier dynamics in unipolar multisubband devices such as QCLs, a proper treatment of the fully three-dimensional

nature of the problem is mandatory [22]. In most configurations of practical interest, the description of the coupled electron-phonon nonequilibrium dynamics may safely be limited to a semiclassical approach for both subsystems. Within this scheme, the kinetic variables of interest are the electron and phonon distribution functions. The latter obey a coupled set of nonlinear equations of motion which may be formally derived in the framework of the quantum-kinetic theory, following a conventional single-particle correlation expansion procedure and neglecting all nondiagonal carrier and quasiparticle density matrix elements [23]. Coherent phonons and electron phase-coherence effects, which may show up within the transient ultrafast timescale [22], are indeed expected to play a minor role in the device's steady-state operation regime considered here. Even though the system under investigation is spatially inhomogeneous, the LO phonon subsystem may be described in terms of a density matrix diagonal in q, parametrized by a meso/macroscopic spatial coordinate related to the thermal-transport space-scale. In other words, it could still be a good approximation to assume the phonon modes and interaction potentials of the host bulk material.

In principle, the proper treatment of the steady-state properties of our prototypical device should therefore be based on the set of coupled electron and phonon Boltzmann equations. This task is quite demanding, since it requires, for the latter, the inclusion of both acoustic and optical modes, ideally with finite size and quantization effects [12]. A simpler, though reasonable, starting point suggests to focus on the main physical aspects of the energy redistribution between charge carriers and lattice degrees of freedom. The basic idea is then to consider the full electron subsystem (i.e., the complete set of active region and injector subbands within each period) coupled via Frölich interaction with bulk LO phonon modes, and to include the decay of the latter into acoustic modes (lattice thermal bath at temperature T_L) via a phenomenological lifetime τ in their dynamical equation. The role of electron-acoustic phonon scattering is expected to be minor, due to the much lower rates, and for this reason it is not included in the present model.

In other words, energy dissipation is modeled—and basically occurs—as a two-step process: first, the carrier subsystem transfers a significant amount of energy to the LO phonon one; then, the latter transfers its excess energy to additional degrees of freedom (acoustic phonons) that are not taken into account dynamically and are characterized by a much larger heat capacity. This second step is described via a standard relaxation-time approximation. The structure of the closed set of coupled equations corresponding to the above-described dynamics is then the following:

$$\frac{\mathrm{d}f_{\nu\mathbf{k}_\parallel}}{\mathrm{d}t} = \left.\frac{\mathrm{d}f_{\nu\mathbf{k}_\parallel}}{\mathrm{d}t}\right|_{\mathrm{e-LO}} + \left.\frac{\mathrm{d}f_{\nu\mathbf{k}_\parallel}}{\mathrm{d}t}\right|_{\mathrm{s}} \tag{1}$$

$$\frac{\mathrm{d}n_{\mathbf{q}}}{\mathrm{d}t} = \left.\frac{\mathrm{d}n_{\mathbf{q}}}{\mathrm{d}t}\right|_{\mathrm{e-LO}} + \left.\frac{\mathrm{d}n_{\mathbf{q}}}{\mathrm{d}t}\right|_{\mathrm{loss}}, \tag{2}$$

where $f_{\nu\mathbf{k}_\parallel}$ is the carrier distribution function corresponding to the single-particle state in subband ν and with in-plane wavevector $\mathbf{k}_\parallel$, while $n_{\mathbf{q}}$ is the average phonon occupation number of a single LO phonon mode with wavevector $\mathbf{q}$.

Starting with the first term on the right-hand side of Eq. (1), in the framework of the Fermi's golden rule approximation, the electron-phonon (e-LO) coupling hamiltonian produces the typical Boltzmann scattering structure. In particular, the latter consists of the following in- and out-scattering terms, coming from LO phonon emission and absorption processes:

$$\frac{\mathrm{d}}{\mathrm{d}t} f_{\nu\mathbf{k}_\parallel}\big|_{\mathrm{e}\text{-}LO} = \sum_{\mathbf{q}^\pm} \left(n_\mathbf{q} + \frac{1}{2} \pm \frac{1}{2} \right) \sum_{\nu'\mathbf{k}'_\parallel} \left[\left(1 - f_{\nu\mathbf{k}_\parallel} \right) P^{\mathbf{q}^\pm}_{\nu\mathbf{k}_\parallel, \nu'\mathbf{k}'} f_{\nu'\mathbf{k}'_\parallel} - \left(1 - f_{\nu'\mathbf{k}'_\parallel} \right) P^{q^\pm}_{\nu'\mathbf{k}'_\parallel, \nu\mathbf{k}} f_{\nu\mathbf{k}_\parallel} \right]. \tag{3}$$

Here

$$P^{\mathbf{q}^\pm}_{\nu\mathbf{k}_\parallel, \nu'\mathbf{k}'_\parallel} = \frac{2\pi}{\hbar} \left| g^\pm_{\nu\mathbf{k}_\parallel, \nu'\mathbf{k}'_\parallel; \mathbf{q}} \right|^2 \delta\left(\varepsilon_{\nu\mathbf{k}_\parallel} - \varepsilon_{\nu'\mathbf{k}'_\parallel} \pm \varepsilon_\mathbf{q} \right), \tag{4}$$

where $g^\pm_{\nu\mathbf{k}_\parallel, \nu'\mathbf{k}'_\parallel; \mathbf{q}}$ are the matrix elements of the $\mathbf{q}$-dependent carrier-LO phonon coupling coefficients within the considered multisubband electronic basis $\nu\mathbf{k}_\parallel$; the sign + (−) refers to phonon emission (absorption) processes.

The second term, labeled with s, at the right-hand side of Eq. (1), generally accounts for further scattering mechanisms, of both intrinsic and extrinsic types, that may affect the carrier dynamics. Within the first sort of processes, for the kind of devices we are interested in, the electron-electron interaction has proven to generally play a significant role [3] and should be included in any realistic analysis (as will be done for the results presented in the next section). Regarding extrinsic mechanisms, such as, for example, interface roughness and electron-impurity scattering, they should be considered if one is interested in analyzing the behavior of a specific device. Indeed, such processes do not significantly modify the trend of the current-voltage characteristics since they have, unlike carrier-LO phonon scattering, a threshold-less nature and do poorly depend on the applied bias. On the contrary, they are strongly device/sample-dependent and their implementation therefore inevitably requires a phenomenological treatment. For these reasons, they will not be considered in the following.

The structure of Eq. (1) would allow for a self-consistent charge-conserving MC electron transport simulation on the condition that the phonon distribution $n_\mathbf{q}$ was known [22]. This typically occurs when the latter may be reasonably well approximated by the $\mathbf{q}$-independent Bose-Einstein term corresponding to a given (quasi)equilibrium temperature. However, this is not the case we are presently interested in since the interplay between electron and phonon dynamics is here expected to significantly drive the LO phonon distribution out of equilibrium while the device is in operation. When nonequilibrium phonons are considered, their occupation numbers $n_\mathbf{q}$ are no longer $\mathbf{q}$ independent and have to be obtained by solving the corresponding dynamical equation, Eq. (2).

The Boltzmann transport equation for the electron subsystem, Eq. (1), with the previously described contribution in Eq. (3), goes then together with the phonon counterpart in Eq. (2). The two quantities at the right-hand side of the latter can be explicitly written as

$$\left.\frac{\mathrm{d}n_\mathbf{q}}{\mathrm{d}t}\right|_{\mathrm{e}\text{-}\mathrm{LO}} = \sum_\pm \pm \left(n_\mathbf{q} + \frac{1}{2} \pm \frac{1}{2} \right) \sum_{\nu\mathbf{k}_\parallel, \nu'\mathbf{k}'_\parallel} \left(1 - f_{\nu\mathbf{k}_\parallel} \right) P^{\mathbf{q}^\pm}_{\nu\mathbf{k}_\parallel, \nu'\mathbf{k}'} f_{\nu'\mathbf{k}'_\parallel}, \tag{5}$$

$$\left.\frac{\mathrm{d}n_{\mathbf{q}}}{\mathrm{d}t}\right|_{\mathrm{loss}} = -\frac{n_{\mathbf{q}} - n_{\mathbf{q}}^{\mathrm{th}}}{\tau}, \tag{6}$$

with the $-\frac{n_{\mathbf{q}}-n_{\mathbf{q}}^{\mathrm{th}}}{\tau}$ term accounting for loss processes from the LO phonon subsystem due to anharmonic decay into acoustic modes, $n_{\mathbf{q}}^{\mathrm{th}}$ being the Bose-Einstein distribution at the lattice (acoustic) bath temperature T_L.

The structure of the coupled set of sections, Eqs. (1) and (2), allows us to simulate both the electron and phonon dynamics by means of a MC particle-like technique. In particular, the latter consists of a generalized simulation approach suitable to describe a fixed number of electrons and a variable number of phonons, and can therefore be implemented in state-of-the-art MC simulation tools [22, 24, 25]. Technically, the $\mathbf{q}$ dependency of the phonon occupation numbers $n_{\mathbf{q}}$ can be managed by means of a combined self-scattering and rejection technique. In addition, the previously discussed symmetry-by-design of the device core region allows us to evaluate the device performances within a "closed-circuit" picture. More specifically, a periodic boundary condition scheme may be adopted in which the simulation/solution for the electron dynamics is limited to a single stage only. As described in detail in Ref. [24], every time an electron undergoes an inter-stage scattering process, it is properly re-injected into the simulated region and the corresponding charge contributes to the current through the device. This charge-conserving scheme allows for a purely kinetic evaluation of the device performances such as the gain spectrum or the current-voltage characteristics. The current density across the whole structure, for example, results as a pure output of the simulation just by a proper counting of the in- and out-stage scattering processes.

Within the above-described simulation framework, the LO phonon lifetime, τ, and the lattice temperature, T_L, are the only free parameters. Realistic values for the former in bulk materials are in the range 6–9 ps [26], while the latter may be accessed by means of state-of-the-art microprobe band-to-band photoluminescence experiments, [17, 18].

3. Application to a prototypical THz coherent light source

As anticipated in the previous section, heating is a serious aspect generally affecting electronic and optoelectronic device performances at diverse stages. For the case of typical mid-infrared as well as THz resonant-phonon QCLs, a significant amount of LO phonons is generated in the core region during operation and a considerable amount of energy is dissipated in the device via Joule effect. Moreover, the combination of high LO phonon generation rates and limited thermal conductivity may cause a significant—and, in principle, detrimental—feedback on the electron relaxation kinetics and therefore on the device performances.

In recent years, experimental evidences highlighted the need for a deeper and more quantitative insight into the impact of hot-phonon phenomena on the nonequilibrium electron dynamics in THz QCL emitters [19, 20]. Motivated by these reasons, we have developed the global

kinetic approach described in Section 2 [21]. In particular, the resonant-phonon device proposed in Ref. [27] appeared to be an interesting candidate deserving further investigation that will be reviewed here. As a starting point, besides the evident carrier-LO phonon scattering, also carrier-carrier interaction should be included in the electron dynamical equation, Eq. (1). This can be done employing the well-established time-dependent static-screening model which is commonly adopted in two-dimensional systems [28]. Regarding Eq. (2), the lifetime τ appearing there is set to the constant value of 6 ps throughout the whole simulated device operation range. This is a realistic guess based on the lower bound value in bulk materials [26] that allows us to investigate the relevance of nonequilibrium LO phonon effects already in the less favorable situation corresponding to their fastest decay into thermalized acoustic modes. Concerning the latter, the values for the input temperature parameter, T_L, may be directly extracted from microprobe band-to-band photoluminescence analysis on the operating device. In particular, the experimental data evidence a significant device heating, with T_L being bias dependent and locally higher than the cryostat temperature (100–180 K—varying with the applied bias—vs. 80 K) [19].

The global and three-dimensional kinetic approach reviewed here has the key feature of directly accessing the distribution functions of the electrons in the various subbands: these data are a straightforward output of the MC simulation. In other words, there is no a priori assumption of carrier intrasubband thermalization. The latter, instead, may or may not eventually show up because of the complex and sinergistic interplay between two-particle (carrier-carrier) and single-particle (carrier-LO phonon) interactions. It turns out that for the device that we are considering here [21], the nonequilibrium electron distributions do show a typical heated Maxwellian form. The corresponding subband effective temperatures are higher than the lattice ones, in good agreement with experimental findings [19]. As will be discussed later, a quite different scenario appears on the side of the LO phonon subsystem.

A key question when investigating and exploring novel QCL designs concerns the feedback that the nonequilibrium phonon dynamics has on the device gain performances. Since the electron cascading dynamics is strategically tailored and controlled by LO phonon emission processes, a gain reduction could be a reasonable expectation. However, any reliable/quantitative answer does require all the power and flexibility of our MC-based approach. In fact, a peculiar feature of MC simulations is that of allowing for truly simulated experiments, in which the diverse contributions to the dynamical equations may be selectively switched on and off, thus highlighting both their individual and synergistic roles. For the case of the prototypical THz QCL device considered here, when hot phonon effects are taken into account we indeed found a population inversion amounting to approximately 85% of the value corresponding to the ideal case in which the carrier subsystem interacts with a thermalized LO phonon population at the cryostat temperature [19]. A closer look at the subband population dynamics shows that this is in fact a "thermal backfilling" effect. More specifically, there is a significant reduction of the extraction efficiency out of the lower laser subband into the ground injector one, while the thermally activated depopulation of the upper laser states remains marginal. The presence of a nonequilibrium phonon population translates into an enhancement of the phonon absorption rates and this reduces the net energy relaxation/loss for the electrons [29].

Figure 1 shows the simulated current-voltage characteristics of the prototypical device we are considering. Indeed, results obtained from diverse MC simulated experiment—at diverse levels of description—are compared. The first set of data (triangles) corresponds to the plainest case, that is the one in which the complete (acoustic and optical) phonon subsystem is at equilibrium and behaves as a thermal bath at the cryostat (80 K) temperature. The other two datasets describe the electron transport performance when LO phonon nonequilibrium phenomena are dynamically taken into account and the acoustic phonon bath is at equilibrium either at the cryostat temperature (squares) or at higher (experimentally measured) ones (discs). All the three cases show the typical QCL behavior: as long as the injector and upper laser subbands remain aligned, the current density increases on increasing the bias; a negative differential resistance region then shows up at higher fields. When comparing the more realistic results (discs) with the other two, one finds out that the above-mentioned reduction in the electron cooling process out of the lower laser subband has a beneficial effect on the global transport dynamics across the device core region. Thermal backfilling actually prevents the accumulation of charge carriers in the injector ground subband, which is less efficiently coupled to the upper laser one, and forces electrons to follow alternative relaxation paths. Indeed, the resulting current increment may amount to more than 60% with respect to the equilibrium LO phonon case (triangles) and this is again a hot-phonon effect in the broader sense. Nonequilibrium LO phonon phenomena at the bare cryostat temperature for the acoustic phonon bath (squares) actually only account for a small fraction of the above-discussed findings.

A closer inspection of the current-voltage profiles allows for further remarks. In particular, the quantitative impact of the nonequilibrium phonon dynamics occurs at diverse levels, the most

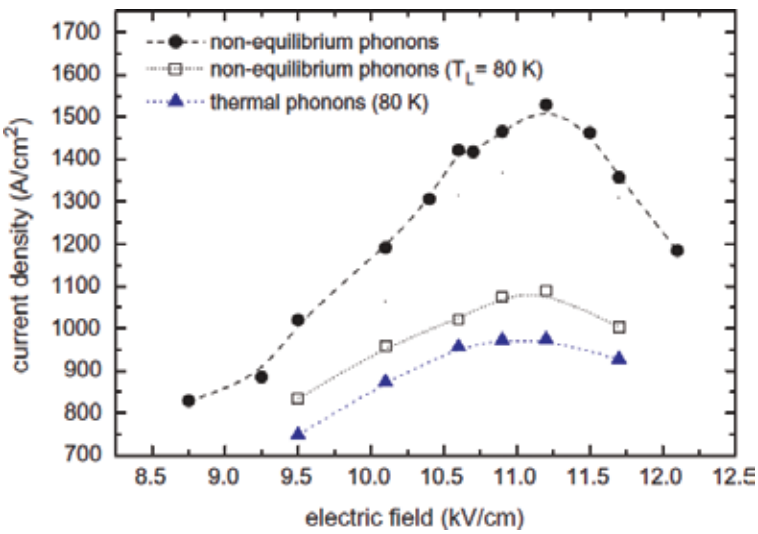

Figure 1. Simulated current density versus applied field characteristics, obtained under diverse conditions for the LO phonon subsystem and the acoustic phonon bath temperature. Triangles: LO and acoustic phonons at equilibrium at the cryostat (80 K) temperature; squares: nonequilibrium LO phonons and cryostat temperature for the acoustic phonon bath; discs: nonequilibrium LO phonons and measured T_L for the acoustic phonon bath. Lines are a guide to the eye. Reprinted from [21].

http://dx.doi.org/10.5772/intechopen.80447

relevant being the specific device design and the particular operation condition, that is, the applied bias. From the theoretical modeling point of view, it follows that it is not possible to assume an a priori heated-phonon approximation parametrized by an effective temperature: the latter will unavoidably be device and bias dependent, and therefore fully equivalent to an a posteriori fitting parameter with no predictive added value.

The current density across the device, being a global quantity, somehow averages over the phonon distribution. In this respect, it does not unambiguously allow to discriminate between the effects of a quasiequilibrium population (thermal, though heated) and a nonthermal one. Indeed, the assessment of a nonequilibrium LO phonon population can and should be acknowledged by looking at the solution of Eq. (2). **Figure 2** shows the $n_{\mathbf{q}}$ values obtained from the MC simulation, as a function of the in-plane modulus $q = |\mathbf{q}_{\text{in plane}}|$. In particular, the plotted quantity is obtained averaging over the dependence on the out-of-plane wavevector component within the superlattice Brillouin minizone. These data (solid line) are compared with the thermal, **q**-independent, Bose distribution at the temperature T_L (dashed line). Actually, the strictly quantitative values for the former and the latter depend on the applied bias; the qualitative behaviors at diverse bias show, however, a common feature: the build-up of a significant amount of small-**q** LO phonons within the core region of the operating device. This is indeed a characteristic fingerprint of the polar phonon emission process: the latter, whose rate decays as $1/q^2$, privileges, at resonance, **q** wavevectors in the proximity of the zone center.

The above-described nonthermal phonon population scenario has been recently probed and confirmed by microRaman spectroscopy studies. In particular, an extremely good agreement between simulated and measured data has been observed [20].

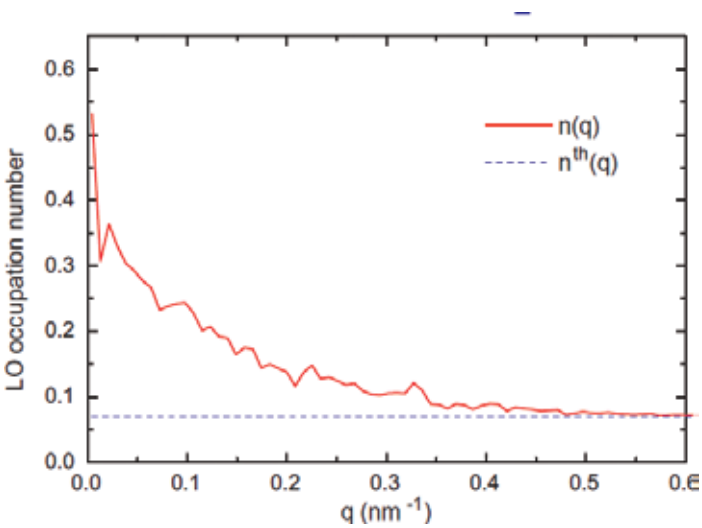

Figure 2. Longitudinal optical-phonon occupation number (solid line) as a function of the in-plane wavevector modulus, for the operating THz QCL device considered in the text. The thermal Bose-Einstein distribution at the bias-dependent temperature T_L is also shown for comparison (dashed line). Reprinted from [21].

4. Summary and conclusions

In state-of-the-art nanomaterials and related optoelectronic nanodevices, the excited (i.e., nonequilibrium) charge carrier dynamics often involves the emission of a significant amount of phonons. As a consequence, the population of the latter may therefore be accordingly driven out of equilibrium as well. This is distinctly noticeable in new-generation device designs where relaxation via LO phonon emission is deliberately exploited as the key mechanism to achieve and maintain the desired transport/gain performances. In this contribution, we have analyzed hot electron versus hot phonon effects in a prototypical THz resonant-phonon QCL structure. In particular, we have reviewed a recently proposed MC-based global kinetic approach describing the entire interacting electron subsystem (i.e., the complete set of active region and injector subbands), coupled to a bulk LO phonon subsystem, whose decay into acoustic modes is modeled by a phenomenological lifetime. Energy dissipation occurs then via a two-step process: first, the strongly biased electron subsystem conveys a conspicuous amount of energy into the LO phonon one; then, the latter transfers the excess energy to additional degrees of freedom, having a much larger heat capacity. The results of our MC simulations are in very good agreement with measured data and highlight how and to what extent the nonequilibrium phonon dynamics may affect the electrooptical device performances.

The simulation scheme reviewed here may be extended to account for a more refined modeling of the LO phonon subsystem as well as to include a more realistic description of their decay into acoustic phonon modes and of the heat transport dynamics. Indeed, it is worth noting that the analysis presented so far, in principle, quantitatively applies only to a specific part of the device, the one whose T_L temperature is selectively accessed and sampled by means of appropriate experimental techniques. Actually, mainly due to their multiinterface structure, the cross-plane thermal conductivity of these devices is greatly reduced with respect to the bulk materials, resulting in a nonuniform heating along the growth direction. The measured T_L values are therefore local quantities that may show significant variations in the direction of the applied bias. A possible way to include in the proposed model these thermal resistance effects consists in assuming the value of T_L—which is an input parameter—to be position dependent and set it from an experimental device temperature mapping.

Author details

Rita C. Iotti* and Fausto Rossi

*Address all correspondence to: rita.iotti@polito.it

Department of Applied Science and Technology, Politecnico di Torino, Torino, Italy

References

[1] Rossi F. Theory of Semiconductor Quantum Devices. Berlin-Heidelberg: Springer; 2011. 382p. DOI: 10.1007/978-3-642-10556-2

[2] Faist J, Capasso F, Sivco DL, Sirtori C, Hutchinson AL, Cho AY. Quantum cascade laser. Science. 1994;**264**:553-556. DOI: 10.1126/science.264.5158.553

[3] Köhler R, Iotti RC, Tredicucci A, Rossi F. Design and simulation of terahertz quantum cascade lasers. Applied Physics Letters. 2001;**79**:3920-3922. DOI: 10.1063/1.1423777

[4] Köhler R, Tredicucci A, Beltram F, Beere HE, Linfield EH, Davies AG, Ritchie DA, Iotti RC, Rossi F. Terahertz semiconductor-heterostructure laser. Nature. 2002;**417**:156-159. DOI: 10.1038/417156a

[5] Gmachl C, Capasso F, Sivco DL, Cho AY. Recent progress in quantum cascade lasers and applications. Reports on Progress in Physics. 2001;**64**:1533-1601. DOI: 10.1088/0034-4885/64/11/204

[6] Belkin MA, Capasso F. New frontiers in quantum cascade lasers: High performance room temperature terahertz sources. Physica Scripta. 2015;**90**:118002. DOI: 10.1088/0031-8949/90/11/118002

[7] Williams BS, Callebaut H, Kumar S, Hu Q, Reno JL. 3.4-THz quantum cascade laser based on longitudinal-optical-phonon scattering for depopulation. Applied Physics Letters. 2003;**82**:1015-1017. DOI: 10.1063/1.1554479

[8] Bai Y, Slivken S, Kuboya S, Darvish SR, Razeghi M. Quantum cascade lasers that emit more light than heat. Nature Photonics. 2010;**4**:99-102. DOI: 10.1038/nphoton.2009.263

[9] Zhou W, Slivken S, Razeghi M. Phase locked, high power, mid-infrared quantum cascade laser arrays. Applied Physics Letters. 2018;**112**:181106. DOI: 10.1063/1.5028281

[10] Yousefvand HR. Equivalent circuit-level model of quantum cascade lasers with integrated hot-electron and hot-phonon effects. Quantum Electronics. 2017;**47**:992-999. DOI: 0.1070/QEL16401

[11] Paulaviciŭs G, Mitin V, Stroscio MA. Hot-optical-phonon effects on electron relaxation in an AlGaAs/GaAs quantum cascade laser structure. Journal of Applied Physics. 1998;**84**:3459-3466. DOI: 10.1063/1.368520

[12] Compagnone F, Manenti M, Di Carlo A, Lugli P. Hot electrons and hot phonons in quantum cascade lasers. Physica B. 2002;**314**:336-340

[13] Jirauschek C, Lugli P. MC simulation of double-resonant-phonon depopulation THz QCLs for high operating temperatures. Journal of Computational Electronics. 2008;**7**:436-439. DOI: 10.1007/s10825-008-0232-4

[14] Lü JT, Cao JC. Monte Carlo simulation of hot phonon effects in resonant-phonon-assisted terahertz quantum-cascade lasers. Applied Physics Letters. 2006;**88**:061119. DOI: 10.1063/1.2172225

[15] Spagnolo V, Scamarcio G, Troccoli M, Capasso F, Gmachl C, Sergent AM, Hutchinson AL, Sivco DL, Cho AY. Nonequilibrium optical phonon generation by steady-state electron transport in quantum-cascade lasers. Applied Physics Letters. 2002;**80**:4303-4305. DOI: 10.1063/1.1481186

[16] Spagnolo V, Vitiello MS, Scamarcio G, Williams BS, Kumar S, Hu Q, Reno JL. Hot-phonon generation in THz quantum cascade lasers. Journal of Physics: Conference Series. 2007;**92**:012018. DOI: 10.1088/1742-6596/92/1/012018

[17] Scamarcio G, Vitiello MS, Spagnolo V, Kumar S, Williams BS, Hu Q. Nanoscale heat transfer in quantum cascade lasers. Physica E. 2008;**40**:1780-1784. DOI: 10.1016/j.physe.2007.09.168

[18] Vitiello MS, Scamarcio G, Spagnolo V, Williams BS, Kumar S, Hu Q, Reno JL. Measurement of subband electronic temperatures and population inversion in THz quantum-cascade lasers. Applied Physics Letters. 2005;**86**:111115. DOI: 10.1063/1.1886266

[19] Iotti RC, Rossi F, Vitiello MS, Scamarcio G, Mahler L, Tredicucci A. Impact of nonequilibrium phonons on the electron dynamics in terahertz quantum cascade lasers. Applied Physics Letters. 2010;**97**:033110. DOI: 10.1063/1.3464977

[20] Vitiello MS, Iotti RC, Rossi F, Mahler L, Tredicucci A, Beere HE, Ritchie DA, Hu Q, Scamarcio G. Non-equilibrium longitudinal and transverse optical phonons in terahertz quantum cascade lasers. Applied Physics Letters. 2012;**100**:091101. DOI: 10.1063/1.3687913

[21] Iotti RC, Rossi F. Coupled carrier-phonon nonequilibrium dynamics in terahertz quantum cascade lasers: A Monte Carlo approach. New Journal of Physics. 2013;**15**:075027. DOI: 10.1088/1367-2630/15/7/075027

[22] Iotti RC, Rossi F. Nature of charge transport in quantum-cascade lasers. Physical Review Letters. 2001;**87**:146603. DOI: 10.1103/PhysRevLett.87.146603

[23] Rossi F, Kuhn T. Theory of ultrafast phenomena in photoexcited semiconductors. Reviews of Modern Physics. 2002;**74**:895-950. DOI: 10.1103/RevModPhys.74.895

[24] Iotti RC, Rossi F. Microscopic theory of semiconductor-based optoelectronic devices. Reports on Progress in Physics. 2005;**68**:2533-2571. DOI: 10.1088/0034-4885/68/11/R02

[25] Borowik P, Thobel J-L, Adamowicz L. Monte Carlo modeling applied to studies of quantum cascade lasers. Optical and Quantum Electronics. 2017;**49**:96. DOI: 10.1007/s11082-017-0931-9

[26] Shah J. Ultrafast Spectroscopy of Semiconductors and Semiconductor Nanostructures. Berlin: Springer-Verlag; 1998. 446p. DOI: 10.1007/978-3-662-03770-6

[27] Kumar S, Williams BS, Kohen S, Hu Q, Reno JL. Continuous-wave operation of terahertz quantum-cascade lasers above liquid-nitrogen temperature. Applied Physics Letters. 2001; **84**:2494-2496. DOI: 10.1063/1.1695099

[28] Goodnick SM, Lugli P. Effect of electron–electron scattering on nonequilibrium transport in quantum-well systems. Physical Review B. 1988;**37**:2578-2588. DOI: 10.1103/PhysRevB.37.2578

[29] Lugli P, Goodnick SM. Nonequilibrium longitudinal-optical phonon effects in GaAs-AlGaAs quantum wells. Physical Review Letters. 1987;**59**:716-719. DOI: 10.1103/PhysRevLett.59.716

Chapter 3

Separability and Nonseparability of Elastic States in Arrays of One-Dimensional Elastic Waveguides

Pierre Alix Deymier, Jerome Olivier Vasseur,
Keith Runge and Pierre Lucas

Additional information is available at the end of the chapter

http://dx.doi.org/10.5772/intechopen.77237

Abstract

We show that the directional projection of longitudinal waves propagating in a parallel array of N elastically coupled waveguides can be described by a nonlinear Dirac-like equation in a 2^N dimensional exponential space. This space spans the tensor product Hilbert space of the two-dimensional subspaces of N uncoupled waveguides grounded elastically to a rigid substrate (called φ-bits). The superposition of directional states of a φ-bit is analogous to that of a quantum spin. We can construct tensor product states of the elastically coupled system that are nonseparable on the basis of tensor product states of N φ-bits. We propose a system of coupled waveguides in a ring configuration that supports these nonseparable states.

Keywords: one-dimensional elastic waveguides, nonseparability, elastic waves, elastic pseudospin, coupled waveguides

1. Introduction

Quantum bit-based computing platforms can capitalize on exponentially complex entangled states which allow a quantum computer to simultaneously process calculations well beyond what is achievable with serially interconnected transistor-based processors. Ironically, a pair of classical transistors can emulate some of the functions of a qubit. While current manufacturing can fabricate billions of transistors on a chip, it is inconceivable to connect them in the exponentially complex way that would be required to achieve nonseparable quantum superposition analogues. In contrast, quantum systems possess such complexity through the nature of the quantum world. Outside the quantum world, the notion of classical nonseparability [1–3] has been receiving a lot of attention from the theoretical and experimental point of views

in the field of optics. Degrees of freedom of photon states that span different Hilbert spaces can be made to interact in a way that leads to local correlations. Correlation has been achieved between degrees of freedom that include spin angular momentum and orbital angular momentum (OAM) [4–9], OAM, polarization and radial degrees of freedom of a beam of light [10] as well as propagation direction [11, 12]. Recently, we have extended this notion to correlation between directional and OAM degrees of freedom in elastic systems composed of arrays of elastic waveguides [13]. This classical nonseparability lies only in the tensor product Hilbert space of the subspaces associated with these degrees of freedom. This Hilbert space does not possess the exponential complexity of a multiqubit Hilbert space, for instance. It has been suggested theoretically and experimentally that classical systems coupled via nonlinear interactions may have computational capabilities approaching that of quantum computers [14–16].

We demonstrated in Ref. [17] that nonlinear elastic media can be used to produce phonons that can be correlated simultaneously in time and frequency. We have also shown an analogy between the propagation of elastic waves on elastically coupled one-dimensional (1D) wave guides and quantum phenomena [18–21]. More specifically, the projection on the direction of propagation of elastic waves in an elastic system composed of a 1D waveguide grounded to a rigid substrate (denoted φ-bit) is isomorphic to the spin of a quantum particle. The pseudospin states of elastic waves in these systems can be described via a Dirac-like equation and possess 2×1 spinor amplitudes. Unlike the quantum systems, these amplitudes are, however, measurable through the measurement of transmission coefficients. The notion of measurement is an important one as it has been realized that separability is relative to the choice of the partitioning of a multipartite system. Indeed, it is known that given a multipartite physical system, whether quantum or classical, the way to subdivide it into subsystems is not unique [22, 23]. For instance, the states of a quantum system may not appear entangled relative to some decomposition but may appear entangled relative to another partitioning. The criterion for that choice may be the ability to perform observations and measurements of some degrees of freedom of the subsystems [23].

The objective of this paper is to investigate the notion of separability and nonseparability of multipartite classical mechanical systems supporting elastic waves. These systems are composed of 1D elastic waveguides that are elastically coupled along their length to each other and/or to some rigid substrate. The 1D waveguides support spinor-like amplitudes in the two-dimensional (2D) subspace of directional degrees of freedom. The amplitudes of N coupled waveguides span an N-dimensional subspace. Subsequently, the Hilbert space spanned by the elastic modes is a $2N$-dimensional space, comprised of the tensor product of the directional and waveguides subspaces. This representation is isomorphic to the degrees of freedom of photon states in a beam of light. While beams of light cannot be decomposed into subsystems, an elastic system composed of coupled 1D waveguides can. Indeed, the elastic system considered here forms a multipartite system composed of N 1D waveguide subsystems. We show that, since each waveguide possesses two directional degrees of freedom, one can represent the elastic states of the N-waveguide system in the 2^N dimensional tensor product Hilbert space of N 2D spinor subspaces associated with individual waveguides. The elastic modes in this representation obey a 2^N dimensional nonlinear Dirac-like equation. These modes span the same space as that of uncoupled waveguides grounded to a rigid substrate, i.e., N φ-bits. However, the modes' solutions of the nonlinear Dirac equation cannot be expressed as tensor products of the states of N uncoupled grounded waveguides, i.e., φ-bit states.

http://dx.doi.org/10.5772/intechopen.77237

In Section 2 of this chapter, we introduce the mathematical formalism that is needed to demonstrate the nonseparability of elastic states of coupled elastic waveguides in an exponentially complex space. Throughout this section, we use illustrations of the concepts in the case of systems composed of small numbers of waveguides. However, the approach is fully scalable and can be generalized to any large number of coupled waveguides. In Section 3, we draw conclusions concerning the applicability of this approach to solve complex problems.

2. Models and methods

We have previously considered systems constituted of N one-dimensional (1D) waveguides coupled elastically along their length [13]. In this section, we summarize the results of these previous investigations to develop a formalism to address our current considerations. The parallelly coupled waveguides can be arranged in any desired way. The propagation of elastic modes is limited to longitudinal modes along the waveguides in the long wavelength limit, i.e., the continuum limit. We consider the representations of the modes of the coupled waveguide systems in two spaces. The first space scales linearly with N. The second space scales as 2^N and leads to a description of the elastic system with exponential complexity. The linear representation enables us to operate easily on the states in the exponential space.

2.1. Representation of elastic states in a space scaling linearly with *N*

A compact form for the equations of motion of the N coupled waveguides is:

$$\left\{H.I_{N\times N} + \alpha^2 M_{N\times N}\right\} u_{N\times 1} = 0 \tag{1}$$

Here, the propagation of elastic waves in the direction x along the waveguides is modeled by the dynamical differential operator, $H = \frac{\partial^2}{\partial t^2} - \beta^2 \frac{\partial^2}{\partial x^2}$. The parameter β is proportional to the speed of sound in the medium constituting the waveguides and the parameter α^2 characterizes the strength of the elastic coupling between them (here, we consider that the strength is the same for all coupled waveguides). $u_{N\times 1}$ is a vector with components, $u_i, (i = 1, N)$, representing the displacement of the ith waveguide. The coupling matrix operator $M_{N\times N}$ describes the elastic coupling between waveguides which, in the case of N = 3 parallel waveguides in a closed ring arrangement with first neighbor coupling, takes the form:

$$M_{N=3\times N=3} = \begin{pmatrix} 2 & -1 & -1 \\ -1 & 2 & -1 \\ -1 & -1 & 2 \end{pmatrix} \tag{2}$$

Eq. (1) takes the form of a generalized Klein-Gordon (KG) equation and its Dirac factorization introduces the notion of the square root of the operator $\left\{H.I_{N\times N} + \alpha^2 M_{N\times N}\right\}$. In this factorization, the dynamics of the system are represented in terms of first derivatives with respect to time, t, and position along the waveguides, x. There are two possible Dirac equations:

$$\left\{U_{N\times N}\otimes\sigma_x\frac{\partial}{\partial t}+\beta U_{N\times N}\otimes\left(-i\sigma_y\right)\frac{\partial}{\partial x}\pm i\alpha U_{2N\times 2N}\sqrt{M_{N\times N}}\otimes\sigma_x\right\}\Psi_{2N\times 1}=0 \tag{3}$$

In Eq. (3), $U_{N\times N}$ and $U_{2N\times 2N}$ are antidiagonal matrices with unit elements. $\sigma_x=\begin{pmatrix}0&1\\1&0\end{pmatrix}$ and $\sigma_y=\begin{pmatrix}0&i\\-i&0\end{pmatrix}$ are two of the Pauli matrices. $\Psi_{2N\times 1}$ is a $2\ N$ dimensional vector which represents the modes of vibration of the N waveguides projected in the two possible directions of propagation (forward and backward) and $\sqrt{M_{N\times N}}$ is the square root of the coupling matrix. The square root of a matrix is not unique but we will show later that we can pick any form without loss of generality.

We choose components of the $\Psi_{2N\times 1}$ vector in the form of plane waves $\psi_I=a_I e^{ikx}e^{i\omega t}$ with $I=1,\ldots,2N$ and k and ω being the wave number and angular frequency, respectively, Eq. (3) becomes:

$$\left\{\omega A_{2N\times 2N}+\beta kB_{2N\times 2N}\pm\alpha C_{2N\times 2N}\right\}a_{2N\times 1}=0 \tag{4}$$

where

$$A_{2N\times 2N}=I_{N\times N}\otimes I_{2\times 2} \tag{5a}$$

$$B_{2N\times 2N}=I_{N\times N}\otimes\left(-\sigma_z\right) \tag{5b}$$

$$C_{2N\times 2N}=\sqrt{M_{N\times N}}\otimes\sigma_x \tag{5c}$$

In Eqs. (4) and (5), $\sigma_z=\begin{pmatrix}1&0\\0&-1\end{pmatrix}$ is the third Pauli matrix, $I_{N\times N}$ is the identity matrix of order N and $a_{2N\times 1}$ is a $2\ N$ dimensional vector whose components are the amplitudes a_I. In obtaining Eq. (4), we have multiplied all terms in Eq. (3) on the left by $U_{2N\times 2N}$.

Writing Eq. (4) as a linear combination of tensor products of $N\times N$ and 2×2 matrix operators:

$$\left\{I_{N\times N}\otimes\left[\omega I_{2\times 2}-\beta k\sigma_z\right]\pm\alpha\sqrt{M_{N\times N}}\otimes\sigma_x\right\}a_{2N\times 1}=0 \tag{6}$$

we seek solutions in the form of tensor products:

$$a_{2N\times 1}=E_{N\times 1}\otimes s_{2\times 1} \tag{7}$$

While the degrees of freedom associated with $E_{N\times 1}$ span an N dimensional Hilbert subspace, the degrees of freedom associated with $s_{2\times 1}$ span a 2D space.

Replacing $a_{2N\times 1}$ from Eq. (7) in Eq. (6) yields:

$$\left\{\left(I_{N\times N}E_{N\times 1}\right)\otimes\left(\left[\omega I_{2\times 2}-\beta k\sigma_z\right]s_{2\times 1}\right)\pm\alpha\left(\sqrt{M_{N\times N}}E_{N\times 1}\right)\otimes\left(\sigma_x s_{2\times 1}\right)\right\}=0. \tag{8}$$

Choosing $E_{N\times 1}$ to be an eigenvector, e_n, of the matrix $\sqrt{M_{N\times N}}$ with eigen value λ_n Eq. (8) reduces to:

$$e_n \otimes \left\{ \left(\left[\omega I_{2\times 2} - \beta k \sigma_z \right] \pm \alpha \lambda_n \sigma_x \right) s_{2\times 1} \right\} = 0 \tag{9}$$

For nontrivial eigenvectors e_n, the problem in the space of the directions of propagation reduces to finding solutions of

$$\left(\left[\omega I_{2\times 2} - \beta k \sigma_z \right] \pm \alpha \lambda_n \sigma_x \right) s_{2\times 1} = 0 \tag{10}$$

In obtaining Eq. (9), we have also used the fact that e_n is an eigen vector of $I_{N\times N}$ with eigen value 1 and we note that Eq. (9) is the 1D Dirac equation for an elastic system which solutions, $s_{2\times 1}$, have the properties of Dirac spinors [18–21]. The components of the spinor represent the amplitude of the elastic waves in the positive and negative directions along the waveguides, respectively.

Eq. (10), now written in the matrix form, can now be solved for a given λ_n;

$$\begin{pmatrix} \omega_n - \beta k & \pm \alpha \lambda_n \\ \pm \alpha \lambda_n & \omega_n + \beta k \end{pmatrix} \begin{pmatrix} s_1 \\ s_2 \end{pmatrix} = 0 \tag{11}$$

This eigen equation gives the dispersion relation $\omega_n^2 = \left(\beta k\right)^2 + \left(\alpha \lambda_n\right)^2$ (*vide infra*) and the following eigen vectors projected into the space of directions of propagation:

$$s_{2\times 1} = s_0 \begin{pmatrix} \sqrt{\omega_n + \beta k} \\ \pm \sqrt{\omega_n - \beta k} \end{pmatrix} \tag{12}$$

To determine the eigen vectors of $\sqrt{M_{N\times N}}$, we note that they are identical to the eigen vectors of the coupling matrix $M_{N\times N}$ and the eigen values of $M_{N\times N}$ are also λ_n^2. These properties indicate that we do not have to determine the square root of the coupling matrix to find the solutions $a_{2N\times 1}$. All that is required is to calculate the eigen vectors and the eigen values of the coupling matrix. Hence, the nonuniqueness of $\sqrt{M_{N\times N}}$ does not introduce difficulties in determining the elastic modes of the coupled system in the Dirac representation.

In the case of the coupling matrix, $M_{3\times 3}$, presented in Eq. (2), the eigen values and real eigen vectors are obtained as $\lambda_0^2 = 0,\ \lambda_1^2 = \lambda_2^2 = 3,$ and

$$e_0 = \frac{1}{\sqrt{3}} \begin{pmatrix} 1 \\ 1 \\ 1 \end{pmatrix}, e_1 = \frac{\sqrt{2}}{\sqrt{3}} \begin{pmatrix} 1 \\ \frac{-1}{2} \\ \frac{-1}{2} \end{pmatrix} \text{ and } e_2 = \frac{\sqrt{2}}{\sqrt{3}} \begin{pmatrix} \frac{-1}{2} \\ 1 \\ \frac{-1}{2} \end{pmatrix} \tag{13}$$

Eq. (3) being linear, its solutions can be written as linear combinations of elastic wave functions in the form:

$$\Psi_{2N\times 1}(n,k) = e_n(N) \otimes s_{2\times 1}(k)\, e^{ikx} e^{i\omega_n(k)t} \tag{14}$$

In Eq. (14), we have expressed the dependencies on the wave number k and the number of waveguides N. The eigen vectors $e_n(N)$ depend on the connectivity of the N waveguides. The space spanned by these solutions scales linearly with the number of waveguides, i.e., as $2N$.

2.2. Representation of elastic states in a space scaling as 2^N

We first illustrate the notion of exponential space in the case of three waveguides. Each guide is connected to a rigid substrate and therefore constitutes a φ-bit. The waveguides are not coupled to each other. The dynamics of the system can be described by a *single* equation which is constructed as follows:

$$\left[\sigma_x \otimes \sigma_x \otimes \sigma_x \frac{\partial}{\partial t} + i\beta\sigma_y \otimes \sigma_x \otimes \sigma_x \frac{\partial}{\partial x_1} + i\beta\sigma_x \otimes \sigma_y \otimes \sigma_x \frac{\partial}{\partial x_2} + i\beta\sigma_x \otimes \sigma_x \otimes \sigma_y \frac{\partial}{\partial x_3} \pm i\alpha I_{2\times 2} \otimes \sigma_x \right.$$
$$\left. \otimes \sigma_x \pm i\alpha\sigma_x \otimes I_{2\times 2} \otimes \sigma_x \pm i\alpha\sigma_x \otimes \sigma_x \otimes I_{2\times 2}\right]\Psi_{8\times 1} = 0 \tag{15}$$

In Eq. (15), we are now defining a positional variable for each waveguide, namely, x_1, x_2, x_3. The quantity α is a measure of the strength of the elastic coupling to the rigid substrate. The solutions are the 8×1 vectors $\Psi_{8\times 1} = \begin{pmatrix} \Psi_1 \\ \Psi_2 \\ \Psi_3 \\ \Psi_4 \\ \Psi_5 \\ \Psi_6 \\ \Psi_7 \\ \Psi_8 \end{pmatrix}$. When seeking solutions in the form of tensor products of spinor solutions for the three waveguides (as indicated by the upper scripts)

$$\Psi_{8\times 1} = \psi^{(1)} \otimes \psi^{(2)} \otimes \psi^{(3)} = \begin{pmatrix} \psi_1^{(1)} \\ \psi_2^{(1)} \end{pmatrix} \otimes \begin{pmatrix} \psi_1^{(2)} \\ \psi_2^{(2)} \end{pmatrix} \otimes \begin{pmatrix} \psi_1^{(3)} \\ \psi_2^{(3)} \end{pmatrix} = \begin{pmatrix} \psi_1^{(1)}\psi_1^{(2)}\psi_1^{(3)} \\ \psi_1^{(1)}\psi_1^{(2)}\psi_2^{(3)} \\ \psi_1^{(1)}\psi_2^{(2)}\psi_1^{(3)} \\ \psi_1^{(1)}\psi_2^{(2)}\psi_2^{(3)} \\ \psi_2^{(1)}\psi_1^{(2)}\psi_1^{(3)} \\ \psi_2^{(1)}\psi_1^{(2)}\psi_2^{(3)} \\ \psi_2^{(1)}\psi_2^{(2)}\psi_1^{(3)} \\ \psi_2^{(1)}\psi_2^{(2)}\psi_2^{(3)} \end{pmatrix} \tag{16}$$

it is straightforward to show that one recovers from Eq. (15), the six Dirac equations of Eq. (3) with $\sqrt{M_{N=3\times N=3}} = I_{3\times 3}$. The solutions of Eq. (16) are obtained from the spinor solution for individual waveguides (j):

$$\psi^{(j)} = s_0 \begin{pmatrix} \sqrt{\omega + \beta k} \\ \pm\sqrt{\omega - \beta k} \end{pmatrix} e^{ikx} e^{i\omega t} \tag{17}$$

The Hilbert space spanned by the solutions of Eq. (15) is the product space of the three 2D subspaces associated with each waveguide. The states of a system composed of N φ-bits span a space when dimension is 2^N.

The question that arises then concerns the possibility of writing an equation in the exponential Hilbert space for N waveguides coupled to each other. For instance, we wish to obtain the states of the system composed of three waveguides coupled in a ring arrangement from an equation of the form:

$$\left[\sigma_x \otimes \sigma_x \otimes \sigma_x \frac{\partial}{\partial t} + i\beta\sigma_y \otimes \sigma_x \otimes \sigma_x \frac{\partial}{\partial x_1} + i\beta\sigma_x \otimes \sigma_y \otimes \sigma_x \frac{\partial}{\partial x_2} + i\beta\sigma_x \otimes \sigma_x \otimes \sigma_y \frac{\partial}{\partial x_3} \pm i\alpha\varepsilon_{8\times 8}\right]\Psi_{8\times 1} = 0 \quad (18)$$

The matrix $\alpha\varepsilon_{8\times 8}$ represents the coupling between the waveguides in the $2^{N=3}$ space. We are still seeking solutions in the form of tensor products (Eq. (16)). After a lengthy algebraic manipulation, we find that we can reproduce Eq. (3) with the coupling matrix of Eq. (2) if one chooses $\varepsilon_{ij} = 0$ excepting

$$\begin{aligned}
&\varepsilon_{14} = \varepsilon_{41} = \varepsilon_{23} = \varepsilon_{31} = \frac{2\psi_1^{(1)} - \psi_1^{(2)} - \psi_1^{(3)}}{\psi_1^{(1)}}; \varepsilon_{16} = \varepsilon_{61} = \varepsilon_{25} = \varepsilon_{52} = \frac{2\psi_1^{(2)} - \psi_1^{(1)} - \psi_1^{(3)}}{\psi_1^{(2)}};\\
&\varepsilon_{17} = \varepsilon_{71} = \varepsilon_{35} = \varepsilon_{53} = \frac{2\psi_1^{(3)} - \psi_1^{(1)} - \psi_1^{(2)}}{\psi_1^{(3)}}; \varepsilon_{28} = \varepsilon_{82} = \varepsilon_{46} = \varepsilon_{64} = \frac{2\psi_2^{(3)} - \psi_2^{(1)} - \psi_2^{(2)}}{\psi_2^{(3)}};\\
&\varepsilon_{38} = \varepsilon_{83} = \varepsilon_{47} = \varepsilon_{74} = \frac{2\psi_2^{(2)} - \psi_2^{(1)} - \psi_2^{(3)}}{\psi_2^{(2)}}; \varepsilon_{58} = \varepsilon_{85} = \varepsilon_{67} = \varepsilon_{76} = \frac{2\psi_2^{(1)} - \psi_2^{(2)} - \psi_2^{(3)}}{\psi_2^{(1)}}
\end{aligned} \quad (19)$$

The Dirac equation of the three coupled waveguides in the exponential space is therefore nonlinear. Generalization to N coupled chains will result in the following nonlinear equation:

$$\left[(\sigma_x)^{\otimes N}\frac{\partial}{\partial t} + i\beta\sigma_y \otimes (\sigma_x)^{\otimes N-1}\frac{\partial}{\partial x_1} + i\beta\sigma_x \otimes \sigma_y \otimes (\sigma_x)^{\otimes N-2}\frac{\partial}{\partial x_2} + \ldots + i\beta(\sigma_x)^{\otimes N-1} \otimes \sigma_y \frac{\partial}{\partial x_N} \pm i\alpha\varepsilon_{2^N\times 2^N}\right]\Psi_{2^N\times 1} = 0 \quad (20)$$

where nonzero components of $\varepsilon_{2^N\times 2^N}$ depend on the $\psi_i^{(j)}, i = 1, 2; j = 1, N$ that appear in the solution $\Psi_{2^N\times 1} = \psi^{(1)} \otimes \psi^{(2)} \otimes \ldots \otimes \psi^{(N)}$. The solutions of the nonlinear Dirac equation for the coupled waveguides span the same space as that of the system of φ-bits, i.e., uncoupled waveguides connected to rigid substrates. The next subsection addresses the question of separability of the coupled waveguide system into a system of uncoupled φ-bits.

2.3. Elastic states in the exponential space

For a system of waveguides that are not coupled, the elastic states, solutions of linear equations of the form of Eq. (15), are tensor products but also linear combinations of tensor products of spinor solution for individual waveguides (see Eq. (17)). It is therefore possible to construct nonseparable states in the exponential space for systems of uncoupled

waveguides. For example, if we consider a system of two uncoupled waveguides, a possible state of the system in the 2^2 space can be constructed in the form of the following linear combination of tensor products:

$$\Psi_{4\times1} = (s_0)^2 \begin{pmatrix} \sqrt{\omega+\beta k} \\ \pm\sqrt{\omega-\beta k} \end{pmatrix} \otimes \begin{pmatrix} \sqrt{\omega+\beta k} \\ \pm\sqrt{\omega-\beta k} \end{pmatrix} e^{i2kx} e^{i2\omega t} - \left(s_0'\right)^2 \begin{pmatrix} \sqrt{\omega-\beta k} \\ \pm\sqrt{\omega+\beta k} \end{pmatrix} \otimes \begin{pmatrix} \sqrt{\omega-\beta k} \\ \pm\sqrt{\omega+\beta k} \end{pmatrix} e^{-i2kx} e^{i2\omega t} \tag{21}$$

Choosing $s_0 = s_0'$ and writing Eq. (21) at the location $x = 0$, one gets:

$$\Psi_{4\times1}(x=0) = \left\{ \begin{pmatrix} \sqrt{\omega+\beta k}\sqrt{\omega+\beta k} \\ \pm\sqrt{\omega+\beta k}\sqrt{\omega-\beta k} \\ \pm\sqrt{\omega-\beta k}\sqrt{\omega+\beta k} \\ \sqrt{\omega-\beta k}\sqrt{\omega-\beta k} \end{pmatrix} - \begin{pmatrix} \sqrt{\omega-\beta k}\sqrt{\omega-\beta k} \\ \pm\sqrt{\omega-\beta k}\sqrt{\omega+\beta k} \\ \pm\sqrt{\omega+\beta k}\sqrt{\omega-\beta k} \\ \sqrt{\omega+\beta k}\sqrt{\omega+\beta k} \end{pmatrix} \right\} e^{i2\omega t} \tag{22}$$

The bracket takes the form:

$$\left(\sqrt{\omega+\beta k}\sqrt{\omega+\beta k} - \sqrt{\omega-\beta k}\sqrt{\omega-\beta k}\right) \begin{pmatrix} 1 \\ 0 \\ 0 \\ -1 \end{pmatrix} \tag{23}$$

The vector $\begin{pmatrix} 1 \\ 0 \\ 0 \\ -1 \end{pmatrix}$ is not separable into a tensor product of two 2×1 vectors. Considering on the basis $|0\rangle = \begin{pmatrix} 1 \\ 0 \end{pmatrix}$ and $|1\rangle = \begin{pmatrix} 0 \\ 1 \end{pmatrix}$, one can write the state given in Eq. (22) in the form of the nonseparable Bell state:

$$\Psi_{4\times1}(x=0) = \left(\sqrt{\omega+\beta k}\sqrt{\omega+\beta k} - \sqrt{\omega-\beta k}\sqrt{\omega-\beta k}\right)(|0\rangle \otimes |0\rangle - |1\rangle \otimes |1\rangle) e^{i2\omega t} \tag{24}$$

Since the waveguides are not coupled, it is, however, not possible to manipulate the state of one of the waveguides by manipulating the state of the other one. Simultaneous manipulation of the state of waveguides in the exponential space requires coupling. We now address elastic states in the coupled waveguides system.

For a system of N coupled waveguides, we construct a solution of Eq. (3) that takes the form of a linear combination of solutions given in Eq. (14):

http://dx.doi.org/10.5772/intechopen.77237

$$\Psi_{2N\times1}(n,n',k,,k') = \chi_n e_n(N)\otimes s_{2\times1}(k)e^{ikx}e^{i\omega_n(k)t} + \chi_{n'}e_{n'}(N)\otimes s_{2\times1}(k')\, e^{ik'x}e^{i\omega_{n'}(k')t} \tag{25}$$

The n and n' correspond to two different nonzero eigen values, λ_n and $\lambda_{n'}$, i.e., they correspond to two different dispersion relations $\omega_n(k)$ and $\omega_{n'}(k)$. We also choose the wave number k' such that $\omega_{n'}(k') = \omega_n(k) = \omega_0$. These modes are illustrated in **Figure 1** in the case of an N = 9 waveguide system. χ_n and $\chi_{n'}$ are the coefficients of the linear combination.

With $e_n(N) = \begin{pmatrix} A_1 \\ A_2 \\ \vdots \\ A_N \end{pmatrix}$ and $e_{n'}(N) = \begin{pmatrix} A'_1 \\ A'_2 \\ \vdots \\ A'_N \end{pmatrix}$ where the specific values of the components A_I and A'_I are determined by the connectivity and coupling of the waveguides, the state of Eq. (25) can be rewritten as:

$$\Psi_{2N\times1}(n,n',k,,k') = \begin{pmatrix} \chi_n A_1\sqrt{\omega_0+\beta k}e^{ikx} + \chi_{n'}A'_1\sqrt{\omega_0+\beta k'}e^{ik'x} \\ \chi_n A_1\sqrt{\omega_0-\beta k}e^{ikx} + \chi_{n'}A'_1\sqrt{\omega_0-\beta k'}e^{ik'x} \\ \vdots \\ \chi_n A_N\sqrt{\omega_0+\beta k}e^{ikx} + \chi_{n'}A'_N\sqrt{\omega_0+\beta k'}e^{ik'x} \\ \chi_n A_N\sqrt{\omega_0-\beta k}e^{ikx} + \chi_{n'}A'_N\sqrt{\omega_0-\beta k'}e^{ik'x} \end{pmatrix} e^{i\omega_0 t} = \begin{pmatrix} \varphi_1^{(1)} \\ \varphi_2^{(1)} \\ \vdots \\ \varphi_1^{(N)} \\ \varphi_2^{(N)} \end{pmatrix} \tag{26}$$

Here, we have chosen, for the sake of simplicity, the $+$ of the $\pm$ in the $s_{2\times1}$ terms.

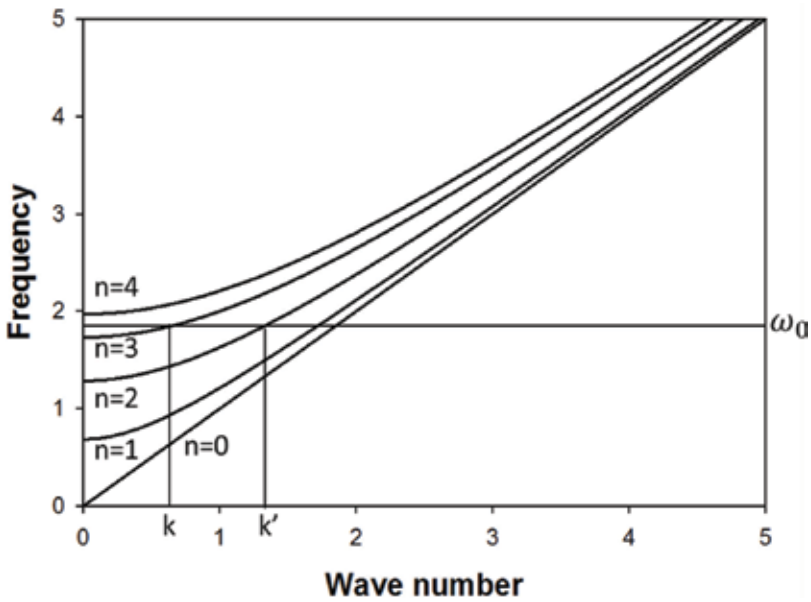

Figure 1. Schematic illustration of the band structure (circular frequency in rad s^{-1} versus the wave number in m^{-1}) for an array of nine elastically coupled waveguides arranged in a ring pattern. The four upper bands are doubly degenerate. We have taken $\beta = 1$ and $\alpha = 1$. The two modes with wave number k and k' ($n = 3$ and $n' = 2$) have the same frequency ω_0.

The first two terms in Eq. (26) form a 2×1 spinor, $\varphi^{(1)} = \begin{pmatrix} \varphi_1^{(1)} \\ \varphi_2^{(1)} \end{pmatrix}$, which corresponds to the first waveguide, the next two terms form a spinor $\varphi^{(2)}$ for the second waveguide, etc. We can then construct a solution of the nonlinear Dirac Eq. (20) in the exponential space as the tensor product:

$$\Phi_{2^N \times 1} = \varphi^{(1)} \otimes \varphi^{(2)} \otimes \ldots \otimes \varphi^{(N)} \tag{27}$$

Since Eq. (20) is nonlinear, linear combinations of tensor product solutions of the form above are not solutions. Solutions of the nonlinear Dirac equation always take the form of a tensor product when the spinor wave functions $\varphi^{(j)}$ are expressed on the basis of 2×1 vectors. $|0\rangle = \begin{pmatrix} 1 \\ 0 \end{pmatrix}$ and $|1\rangle = \begin{pmatrix} 0 \\ 1 \end{pmatrix}$. If one desires to express $\Phi_{2^N \times 1}$ as a nonseparable state, one has to define a new basis in which this wave function cannot be expressed as a tensor product. This is done in Section 2.5. However, prior to demonstrating this, we illustrate in the next subsection how one can manipulate states of the form $\Phi_{2^N \times 1}$ in the exponential space.

2.4. Operating on exponentially-complex tensor product elastic states

In this subsection, we expand tensor product states of the form given in Eq. (27) in linear combinations of tensor products of pure states in the exponential space. We illustrate this expansion in the case of three parallel waveguides elastically coupled to each other. Each waveguide is also coupled elastically to a rigid substrate. We treat the case where the strength of all the couplings is the same. In that case, the coupling matrix is:

$$M_{N=3 \times N=3} = \begin{pmatrix} 3 & -1 & -1 \\ -1 & 3 & -1 \\ -1 & -1 & 3 \end{pmatrix}$$

This matrix has three nonzero eigen values $\lambda_0^2 = 1,$ and $\lambda_1^2 = \lambda_2^2 = 4$ corresponding to two dispersion relations $\omega_n^2 = (\beta k)^2 + (\alpha \lambda_n)^2$ with cutoff frequencies. The second band is doubly degenerate. The eigen vectors are also given in Eq. (13). We now consider an elastic mode in the linear space that is a linear combination of these eigen modes (see Eq. (26)):

$$\Psi_{6\times1}(n, n', k, , k') = \begin{pmatrix} \varphi_1^{(1)} \\ \varphi_2^{(1)} \\ \varphi_1^{(2)} \\ \varphi_2^{(2)} \\ \varphi_1^{(3)} \\ \varphi_2^{(3)} \end{pmatrix} = \begin{pmatrix} \chi_n A_1 \sqrt{\omega_0 + \beta k} e^{ikx} + \chi_{n'} A_1' \sqrt{\omega_0 + \beta k'} e^{ik'x} \\ \chi_n A_1 \sqrt{\omega_0 - \beta k} e^{ikx} + \chi_{n'} A_1' \sqrt{\omega_0 - \beta k'} e^{ik'x} \\ \chi_n A_2 \sqrt{\omega_0 + \beta k} e^{ikx} + \chi_{n'} A_2' \sqrt{\omega_0 + \beta k'} e^{ik'x} \\ \chi_n A_2 \sqrt{\omega_0 - \beta k} e^{ikx} + \chi_{n'} A_2' \sqrt{\omega_0 - \beta k'} e^{ik'x} \\ \chi_n A_3 \sqrt{\omega_0 + \beta k} e^{ikx} + \chi_{n'} A_3' \sqrt{\omega_0 + \beta k'} e^{ik'x} \\ \chi_n A_3 \sqrt{\omega_0 - \beta k} e^{ikx} + \chi_{n'} A_3' \sqrt{\omega_0 - \beta k'} e^{ik'x} \end{pmatrix} e^{i\omega_0 t} \tag{28}$$

In Eq. (28), the A_I's can be the components of the eigen vector e_0 and the A_I''s can be linear combinations of the components of the eigen vectors e_1 and e_2. We can calculate the tensor product of the spinor components in the form of Eq. (27)

$$\Phi_{2^3\times 1} = \varphi^{(1)} \otimes \varphi^{(2)} \otimes \varphi^{(3)} \tag{29}$$

Eq. (29) can be rewritten after some algebraic manipulations in the form of the linear combination:

$$\begin{aligned}\Phi_{2^3\times 1} = \Bigg\{ &\begin{pmatrix}\zeta_1\\ \xi_1\end{pmatrix}\otimes\begin{pmatrix}\zeta_2\\ \xi_2\end{pmatrix}\otimes\begin{pmatrix}\zeta_3\\ \xi_3\end{pmatrix} + \begin{pmatrix}\zeta_1\\ \xi_1\end{pmatrix}\otimes\begin{pmatrix}\zeta_2\\ \xi_2\end{pmatrix}\otimes\begin{pmatrix}\zeta_3'\\ \xi_3'\end{pmatrix} + \begin{pmatrix}\zeta_1\\ \xi_1\end{pmatrix}\otimes\begin{pmatrix}\zeta_2'\\ \xi_2'\end{pmatrix}\otimes\begin{pmatrix}\zeta_3\\ \xi_3\end{pmatrix}\\ &+\begin{pmatrix}\zeta_1'\\ \xi_1'\end{pmatrix}\otimes\begin{pmatrix}\zeta_2\\ \xi_2\end{pmatrix}\otimes\begin{pmatrix}\zeta_3\\ \xi_3\end{pmatrix} + \begin{pmatrix}\zeta_1\\ \xi_1\end{pmatrix}\otimes\begin{pmatrix}\zeta_2'\\ \xi_2'\end{pmatrix}\otimes\begin{pmatrix}\zeta_3'\\ \xi_3'\end{pmatrix} + \begin{pmatrix}\zeta_1'\\ \xi_1'\end{pmatrix}\otimes\begin{pmatrix}\zeta_2\\ \xi_2\end{pmatrix}\otimes\begin{pmatrix}\zeta_3'\\ \xi_3'\end{pmatrix}\\ &+\begin{pmatrix}\zeta_1'\\ \xi_1'\end{pmatrix}\otimes\begin{pmatrix}\zeta_2'\\ \xi_2'\end{pmatrix}\otimes\begin{pmatrix}\zeta_3\\ \xi_3\end{pmatrix} + \begin{pmatrix}\zeta_1'\\ \xi_1'\end{pmatrix}\otimes\begin{pmatrix}\zeta_2'\\ \xi_2'\end{pmatrix}\otimes\begin{pmatrix}\zeta_3'\\ \xi_3'\end{pmatrix}\Bigg\} e^{i3\omega_0 t}\end{aligned} \tag{30}$$

In Eq. (30), we have defined

$$\begin{pmatrix}\zeta_I\\ \xi_I\end{pmatrix} = \chi_n A_I e^{ikx}\begin{pmatrix}\sqrt{\omega_0+\beta k}\\ \sqrt{\omega_0-\beta k}\end{pmatrix} = \chi_n A_I e^{ikx} s_{2\times 1} \tag{31a}$$

$$\begin{pmatrix}\zeta_I'\\ \xi_I'\end{pmatrix} = \chi_{n''} A_1' e^{ik'x}\begin{pmatrix}\sqrt{\omega_0+\beta k'}\\ \sqrt{\omega_0-\beta k'}\end{pmatrix} = \chi_{n''} A_1' e^{ik'x} s_{2\times 1}' \tag{31b}$$

The tensor product of Eq. (30) then reduces to

$$\begin{aligned}\Phi_{2^3\times 1} = \Big\{ &(\chi_n)^3 A_1A_2A_3 e^{i3kx} s_{2\times 1}\otimes s_{2\times 1}\otimes s_{2\times 1} + (\chi_n)^2\chi_{n'}A_1A_2A_3' e^{i2kx}e^{ik'x} s_{2\times 1}\otimes s_{2\times 1}\otimes s_{2\times 1}'\\ &+(\chi_n)^2\chi_{n'}A_1A_2'A_3 e^{i2kx}e^{ik'x} s_{2\times 1}\otimes s_{2\times 1}'\otimes s_{2\times 1} + (\chi_n)^2\chi_{n'}A_1'A_2A_3 e^{i2kx}e^{ik'x} s_{2\times 1}'\otimes s_{2\times 1}\otimes s_{2\times 1}\\ &+(\chi_{n'})^2\chi_n A_1A_2'A_3' e^{ikx}e^{i2k'x} s_{2\times 1}\otimes s_{2\times 1}'\otimes s_{2\times 1}' + (\chi_{n'})^2\chi_n A_1'A_2A_3' e^{ikx}e^{i2k'x} s_{2\times 1}'\otimes s_{2\times 1}\otimes s_{2\times 1}'\\ &+(\chi_{n'})^2\chi_n A_1'A_2'A_3 e^{ikx}e^{i2k'x} s_{2\times 1}'\otimes s_{2\times 1}'\otimes s_{2\times 1} + (\chi_{n'})^3 A_1'A_2'A_3' e^{i3k'x} s_{2\times 1}'\otimes s_{2\times 1}'\otimes s_{2\times 1}'\Big\} e^{i3\omega_0 t}\end{aligned} \tag{32}$$

The spinors $s_{2\times 1}$ and $s_{2\times 1}'$ can be expressed on the basis $|0\rangle = \begin{pmatrix}1\\0\end{pmatrix}$ and $|1\rangle = \begin{pmatrix}0\\1\end{pmatrix}$:

$$s_{2\times 1} = s_1|0\rangle + s_2|1\rangle \tag{33a}$$

$$s_{2\times 1}' = s_1'|0\rangle + s_2'|1\rangle \tag{33b}$$

With $s_1 = \sqrt{\omega_0+\beta k}$, $s_2 = \sqrt{\omega_0-\beta k}$, $s_1' = \sqrt{\omega_0+\beta k'}$ and $s_2' = \sqrt{\omega_0-\beta k'}$. Inserting Eqs. (33a) and (33b) into Eq. (32), we can express the tensor product $\Phi_{2^3\times 1}$ on the basis $\{|0\rangle|0\rangle|0\rangle, |0\rangle|0\rangle|1\rangle,$

$|0\rangle|1\rangle|0\rangle, |1\rangle|0\rangle|0\rangle, |0\rangle|1\rangle|1\rangle, |1\rangle|0\rangle|1\rangle, |1\rangle|1\rangle|0\rangle, |1\rangle|1\rangle|1\rangle\}$. In defining the basis vectors for the exponential space, we have omitted the symbols $\otimes$. It is also implicit that the left, middle, and right elements in the tensor product $|a\rangle|b\rangle|c\rangle$ correspond to the first, second, and third waveguides, respectively.

We find

$$\Phi_{2^3\times 1} = \{T_1|0\rangle|0\rangle|0\rangle + T_2|0\rangle|0\rangle|1\rangle + \ldots + T_8|1\rangle|1\rangle|1\rangle\}e^{i3\omega_0 t} \tag{34}$$

with

$$T_1 = Q_1 s_1 s_1 s_1 + Q_2 s_1 s_1 s_1' + Q_3 s_1 s_1' s_1 + Q_4 s_1' s_1 s_1 + Q_5 s_1 s_1' s_1' + Q_6 s_1' s_1 s_1' + Q_7 s_1' s_1' s_1 + Q_8 s_1' s_1' s_1' \tag{35a}$$

$$T_2 = Q_1 s_1 s_1 s_2 + Q_2 s_1 s_1 s_2' + Q_3 s_1 s_1' s_2 + Q_4 s_1' s_1 s_2 + Q_5 s_1 s_1' s_2' + Q_6 s_1' s_1 s_2' + Q_7 s_1' s_1' s_2 + Q_8 s_1' s_1' s_2' \tag{35b}$$

$$T_3 = Q_1 s_1 s_2 s_1 + Q_2 s_1 s_2 s_1' + Q_3 s_1 s_2' s_1 + Q_4 s_1' s_2 s_1 + Q_5 s_1 s_2' s_1' + Q_6 s_1' s_2 s_1' + Q_7 s_1' s_2' s_1 + Q_8 s_1' s_2' s_1' \tag{35c}$$

$$T_4 = Q_1 s_2 s_1 s_1 + Q_2 s_2 s_1 s_1' + Q_3 s_2 s_1' s_1 + Q_4 s_2' s_1 s_1 + Q_5 s_2 s_1' s_1' + Q_6 s_2' s_1 s_1' + Q_7 s_2' s_1' s_1 + Q_8 s_2' s_1' s_1' \tag{35d}$$

$$T_5 = Q_1 s_1 s_2 s_2 + Q_2 s_1 s_2 s_2' + Q_3 s_1 s_2' s_2 + Q_4 s_1' s_2 s_2 + Q_5 s_1 s_2' s_2' + Q_6 s_1' s_2 s_2' + Q_7 s_1' s_2' s_2 + Q_8 s_1' s_2' s_2' \tag{35e}$$

$$T_6 = Q_1 s_2 s_1 s_2 + Q_2 s_2 s_1 s_2' + Q_3 s_2 s_1' s_2 + Q_4 s_2' s_1 s_2 + Q_5 s_2 s_1' s_2' + Q_6 s_2' s_1 s_2' + Q_7 s_2' s_1' s_2 + Q_8 s_2' s_1' s_2' \tag{35f}$$

$$T_7 = Q_1 s_2 s_2 s_1 + Q_2 s_2 s_2 s_1' + Q_3 s_2 s_2' s_1 + Q_4 s_2' s_2 s_1 + Q_5 s_2 s_2' s_1' + Q_6 s_2' s_2 s_1' + Q_7 s_2' s_2' s_1 + Q_8 s_2' s_2' s_1' \tag{35g}$$

$$T_8 = Q_1 s_2 s_2 s_2 + Q_2 s_2 s_2 s_2' + Q_3 s_2 s_2' s_2 + Q_4 s_2' s_2 s_2 + Q_5 s_2 s_2' s_2' + Q_6 s_2' s_2 s_2' + Q_7 s_2' s_2' s_2 + Q_8 s_2' s_2' s_2' \tag{35h}$$

with

$$Q_1 = (\chi_n)^3 A_1 A_2 A_3 e^{i3kx}; \quad Q_2 = (\chi_n)^2 \chi_{n'} e^{i2kx} e^{ik'x} A_1 A_2 A_3'; \quad Q_3 = (\chi_n)^2 \chi_{n'} e^{i2kx} e^{ik'x} A_1 A_2' A_3;$$
$$Q_4 = (\chi_n)^2 \chi_{n'} e^{i2kx} e^{ik'x} A_1' A_2 A_3; \quad Q_5 = (\chi_{n'})^2 \chi_n e^{ikx} e^{i2k'x} A_1 A_2' A_3'; \quad Q_6 = (\chi_{n'})^2 \chi_n e^{ikx} e^{i2k'x} A_1' A_2 A_3';$$
$$Q_7 = (\chi_{n'})^2 \chi_n e^{ikx} e^{i2k'x} A_1' A_2' A_3; \quad Q_8 = (\chi_{n'})^3 A_1' A_2' A_3' e^{i3k'x}.$$

In a true quantum system composed of three spins for instance, states can be created in the form of linear combinations like $m_1|0\rangle|0\rangle|0\rangle + m_2|0\rangle|0\rangle|1\rangle + \ldots + m_8|1\rangle|1\rangle|1\rangle$. For the quantum system, the linear coefficients m_1, m_2,…, m_8 are independent. The classical elastic analogue, introduced here, states which are given in Eq. (34) possesses linear coefficients T_1,…, T_8 are

interdependent. While somewhat restrictive compared to true quantum systems, the coefficients T_I depend on an extraordinary number of degrees of freedom which allows exploration of a large volume of the exponential tensor product space. In the case of the three waveguides, these degrees of freedom include (a) the components (or linear combinations) of the eigen vectors of the coupling matrix through the choice of the eigen modes or the application of a rotational operation that creates cyclic permutations of the eigen vector components, (b) the linear coefficients χ_n and $\chi_{n'}$ used to form the multiband linear superposition of states in the linear space, (c) the frequency and therefore wave number which affect the spinor states and the phase factors e^{ikx} and $e^{ik'x}$, and (d) a phase added to the terms e^{ikx} and $e^{ik'x}$.

In the case of $N > 3$, Eq. (21) can be extended to linear combinations of more than two modes with the same frequency, leading to additional freedom in the control of the T_I. Furthermore, the elastic coefficients β of the waveguides and the coupling elastic coefficient α could also be modified by using constitutive materials with tunable elastic properties via, for instance, the piezoelectric, magneto-elastic or photoelastic effects [24–26]. Also note that in all the examples we considered, the coupling of the waveguides had the same strength. Tunability of the coupling elastic medium would lead to the ability to modify the connectivity of the waveguides and therefore the coupling matrix. Exploration of the elastic modes given in Eq. (34) can be realized by varying any number of these variables. We illustrate in **Figure 2** an example of operation in a very simple case. **Figure 2b** shows that by varying a single parameter one may achieve a wide variety of states. For instance, one can obtain states with $T_1 > 0$ and $T_2 > 0$ or $T_1 > 0$ and $T_2 = 0$ or $T_1 > 0$ and $T_2 < 0$ or $T_1 = 0$ and $T_2 = 0$. Another interesting example occurs at $\chi_{n'}$~0.6, there only T_5 and T_8 are different from zero. Then, $\Phi_{2^3\times 1} = \{T_5(0.6)|0\rangle|1\rangle|1\rangle + T_8(0.6)|1\rangle|1\rangle|1\rangle\}e^{i3\omega_0 t}$ can be written as the tensor product state $\{(T_5(0.6)|0\rangle + T_8(0.6)|1\rangle)|1\rangle|1\rangle\}e^{i3\omega_0 t}$. A similar state is also obtained for $\chi_{n'} \sim 0.25$. This is the state $\{(T_1(0.25)|0\rangle + T_4(0.25)|1\rangle)|0\rangle|0\rangle\}e^{i3\omega_0 t}$. Varying $\chi_{n'}$ can be visualized as a matrix operator. For example, in this latter case, one can define the operation:

$$\begin{pmatrix} q_{11} & 0 & 0 & 0 & 0 & 0 & 0 & 0 \\ 0 & 0 & 0 & 0 & 0 & 0 & 0 & 0 \\ 0 & 0 & 0 & 0 & 0 & 0 & 0 & 0 \\ 0 & 0 & 0 & q_{44} & 0 & 0 & 0 & 0 \\ 0 & 0 & 0 & 0 & 0 & 0 & 0 & 0 \\ 0 & 0 & 0 & 0 & 0 & 0 & 0 & 0 \\ 0 & 0 & 0 & 0 & 0 & 0 & 0 & 0 \\ 0 & 0 & 0 & 0 & 0 & 0 & 0 & 0 \end{pmatrix} \begin{pmatrix} T_1(\chi_{n'}) \\ T_2(\chi_{n'}) \\ T_3(\chi_{n'}) \\ T_4(\chi_{n'}) \\ T_5(\chi_{n'}) \\ T_6(\chi_{n'}) \\ T_7(\chi_{n'}) \\ T_8(\chi_{n'}) \end{pmatrix} = \begin{pmatrix} T_1(0.25) \\ T_2(0.25) \\ T_3(0.25) \\ T_4(0.25) \\ T_5(0.25) \\ T_6(0.25) \\ T_7(0.25) \\ T_8(0.25) \end{pmatrix} = \begin{pmatrix} T_1(0.25) \\ 0 \\ 0 \\ T_4(0.25) \\ 0 \\ 0 \\ 0 \\ 0 \end{pmatrix} \tag{36}$$

with $q_{11} = \frac{T_1(0.25)}{T_1(\chi_{n'})}$ and $q_{44} = \frac{T_4(0.25)}{T_4(\chi_{n'})}$. Another interesting state occurs at $\chi_{n'} = 0.5$. Here, we have $T_1 = T_5$, $T_2 = T_3$, $T_4 = T_8$ and $T_6 = T_7$. We also have $T_3 = -T_5$ and $T_4 = -T_6$ This state can be written as the tensor product $(T_1(0.5)|0\rangle - T_6(0.5)|1\rangle)(|0\rangle - |1\rangle)(|0\rangle - |1\rangle)$.

This simple example indicates the large variability in T_I's (i.e., of states) that we can achieve with a single variable. The large number of available variables will lead to even more flexibility in defining states and operators in the exponential tensor product space.

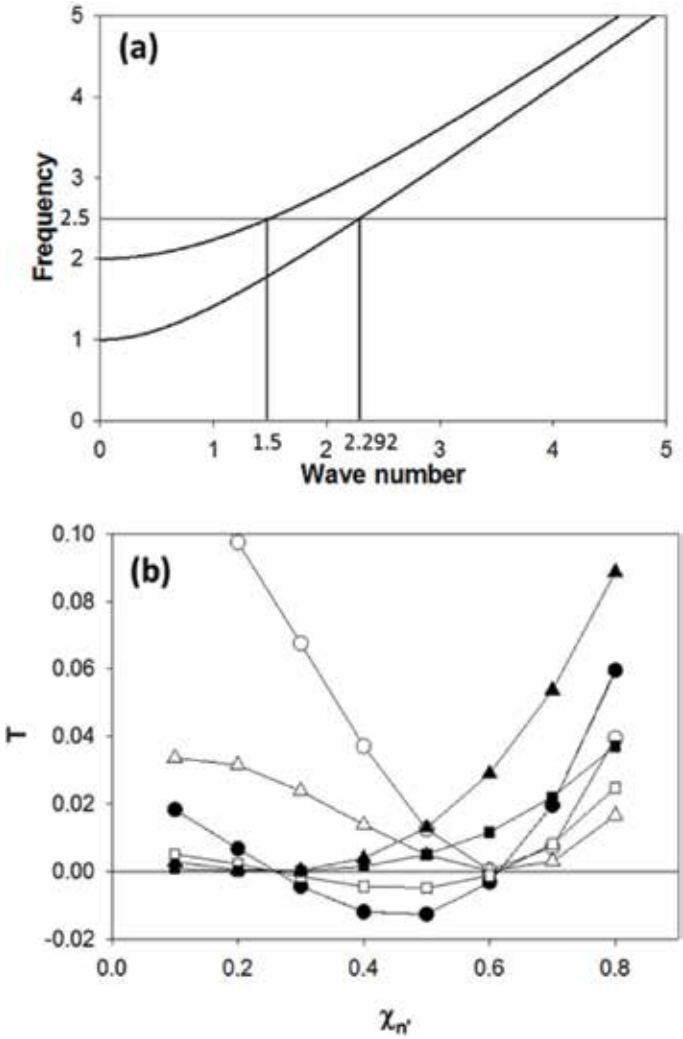

Figure 2. (a) Schematic illustration of the band structure for an array of three elastically coupled waveguides arranged in a ring pattern. Each of the waveguides is also grounded elastically to a rigid substrate. The upper band is doubly degenerate. We have taken $\beta = 1$ and $\alpha = 1$. We highlight the frequency $\omega_0 = 2.5$ corresponding to the wave numbers $k = 2.292$ and $k' = 1.5$. (b) Calculated values of T_1 (open circles), T_2 and T_3 (closed circles), T_4 (open triangles), T_5 (closed triangles), T_6 and T_7 (open squares) and T_8 (closed squares) as functions of $\chi_{n'}$ for $\chi_n = 0.4$. We have fixed $x = 0$.

2.5. Nonseparability of states in exponentially complex space

States given in Eq. (27) are tensor products on the basis $\{|0\rangle\ldots|0\rangle|0\rangle, |0\rangle\ldots|0\rangle|1\rangle, |0\rangle\ldots|1\rangle|0\rangle, \ldots, |1\rangle\ldots|1\rangle|1\rangle\}$. They are therefore always separable in that basis. Consequently these states cannot be written as nonseparable Bell states. However, we might be able to identify a basis in which Eq. (27) is not separable.

Since the Dirac equation (Eq. (15)) for the uncoupled waveguides is linear, its solutions can be a tensor product of a linear combination of N different individual spinors. For instance, we can write:

$$\Psi_{2^N\times 1} = \begin{pmatrix} \rho_1\sqrt{\omega_1+\beta k_1}e^{ik_1x} + \mu_1\sqrt{\omega_1-\beta k_1}e^{-ik_1x} \\ \rho_1\sqrt{\omega_1-\beta k_1}e^{ik_1x} + \mu_1\sqrt{\omega_1+\beta k_1}e^{-ik_1x} \end{pmatrix} e^{i\omega_1 t} \otimes \ldots \\ \otimes \begin{pmatrix} \rho_N\sqrt{\omega_N+\beta k_N}e^{ik_Nx} + \mu_N\sqrt{\omega_N-\beta k_N}e^{-ik_Nx} \\ \rho_N\sqrt{\omega_N-\beta k_N}e^{ik_Nx} + \mu_N\sqrt{\omega_N+\beta k_N}e^{-ik_Nx} \end{pmatrix} e^{i\omega_N t} \tag{37}$$

ρ_I and μ_I, $I = 1, \ldots, N$ are linear coefficients.

The state of the coupled waveguide system will be separable in the exponential space into the state of φ-bits if

$$\Phi_{2^N\times 1} = \Psi_{2^N\times 1} \tag{38}$$

A necessary condition for satisfying Eq. (38) is that $N\omega_0 = \omega_1 + \ldots + \omega_N$.

Furthermore, the first two terms in the column vector $\Phi_{2^N\times 1}$ of the coupled system are $\varphi_1^{(1)}\varphi_1^{(2)}\ldots\varphi_1^{(N)}$ and $\varphi_1^{(1)}\varphi_1^{(2)}\ldots\varphi_2^{(N)}$. Their ratio is simply equal to $r_N^c = \frac{\varphi_1^{(N)}}{\varphi_2^{(N)}}$. Similarly, the ratio of the first two terms in the vector $\Psi_{2^N\times 1}$ of the φ-bit system is given by $r_N^u = \frac{\rho_N\sqrt{\omega_N+\beta k_N}e^{ik_Nx}+\mu_N\sqrt{\omega_N-\beta k_N}e^{-ik_Nx}}{\rho_N\sqrt{\omega_N-\beta k_N}e^{ik_Nx}+\mu_N\sqrt{\omega_N+\beta k_N}e^{-ik_Nx}}$. Anecessary condition for Eq. (38) to be satisfied is that

$$r_N^C = r_N^u \tag{39}$$

This leads to

$$\frac{\chi_n A_N\sqrt{\omega_0+\beta k}e^{ikx} + \chi_{n'}A'_N\sqrt{\omega_0+\beta k'}e^{ik'x}}{\chi_n A_N\sqrt{\omega_0-\beta k}e^{ikx} + \chi_{n'}A'_N\sqrt{\omega_0-\beta k'}e^{ik'x}} = \frac{\rho_N\sqrt{\omega_N+\beta k_N}e^{ik_Nx} + \mu_N\sqrt{\omega_N-\beta k_N}e^{-ik_Nx}}{\rho_N\sqrt{\omega_N-\beta k_N}e^{ik_Nx} + \mu_N\sqrt{\omega_N+\beta k_N}e^{-ik_Nx}}$$

which can be rewritten as:

$$\frac{ue^{ikx} + u'e^{ik'x}}{ve^{ikx} + v'e^{ik'x}} = \frac{\gamma e^{ik_Nx} + \gamma' e^{-ik_Nx}}{\delta e^{ik_Nx} + \delta' e^{-ik_Nx}}$$

This condition takes the more compact form:

$$Pe^{i(k+k_N)x} + Qe^{i(k-k_N)x} + Re^{i(k'+k_N)x} + Se^{i(k'-k_N)x} = 0 \tag{40}$$

P, Q, R, S are real. Eq. (40) is true for all values of position x. At $x = 0$, we obtain the relation $P + Q + R + S = 0$. Inserting that relation into Eq. (27) and eliminating Q yields:

$$i2P\sin k_Nx = \{-(R+S)\cos k_Nx[\cos(k'-k)x - 1] + (R-S)\sin(k'-k)\sin k_Nx\} \\ + i\{(R+S)\sin(k'-k)x + \sin k_Nx[(R-S)\cos(k'-k)x + (R+S)]\}$$

For this condition to be satisfied, one needs the real part of the right-hand side of the equation to be equal to zero. This can be achieved for all x's by setting $k' = k$. In this case, equating the imaginary parts leads to $R = -P$. However, when $k' \neq k$, Eq. (39) and therefore Eq. (38) are not

satisfied. When $k' \neq k$ which corresponds to considering a linear combination of multiband states, $\Phi_{2^N\times 1}$ is not separable into the tensor product of individually uncoupled φ-bit waveguides. Therefore, we conclude that there are a large number of solutions of the nonlinear Dirac equation (Eq. (20)) representing states of arrangements of elastically coupled 1-D waveguides that are not separable in the 2^N dimensional tensor product Hilbert space of individual φ-bits.

We illustrate the notion of nonseparability of exponentially complex states of a coupled system composed of $N = 2$ waveguides on a basis in the exponential Hilbert space of two individual φ-bits. The waveguides are coupled to each other but also to a rigid substrate such that the coupling matrix, $M_{N\times N}$, takes the form:

$$M_{2\times 2} = \begin{pmatrix} 2 & -1 \\ -1 & 2 \end{pmatrix}$$

The eigen values and real eigen vectors of this coupling matrix are $\lambda_0^2 = 1,$ and $\lambda_1^2 = 3$ and

$$e_0 = \begin{pmatrix} A_1 \\ A_2 \end{pmatrix} = \frac{1}{\sqrt{2}}\begin{pmatrix} 1 \\ 1 \end{pmatrix}, e_1 = \begin{pmatrix} A_1' \\ A_2' \end{pmatrix} = \frac{1}{\sqrt{2}}\begin{pmatrix} 1 \\ -1 \end{pmatrix} \tag{41}$$

Following the procedure of Section 2.4, we construct a tensor product state in the 2^2 exponential space:

$$\begin{aligned}\Phi_{2^2\times 1} = \Big\{ &(\chi_n)^2 A_1 A_2 e^{i2kx} s_{2\times 1} \otimes s_{2\times 1} + \chi_n \chi_{n'} A_1 A_2' e^{ikx} e^{ik'x} s_{2\times 1} \otimes s'_{2\times 1} + \chi_{n'} \chi_n A_1' A_2 e^{ik'x} e^{ikx} s'_{2\times 1} \otimes s_{2\times 1} \\ &+ (\chi_{n'})^2 A_1' A_2' e^{i2k'x} s'_{2\times 1} \otimes s'_{2\times 1} \Big\} e^{i2\omega_0 t}\end{aligned} \tag{42}$$

Eq. (42) is equivalent to Eq. (32) but for two coupled waveguides.

On the basis, $\eta_1 = e^{i2\omega_0 t} e^{i2kx} s_{2\times 1} \otimes s_{2\times 1}$, $\eta_2 = e^{i2\omega_0 t} e^{ikx} e^{ik'x} s_{2\times 1} \otimes s'_{2\times 1}$, $\eta_3 = e^{i2\omega_0 t} e^{ik'x} e^{ikx} s'_{2\times 1} \otimes s_{2\times 1}$, and $\eta_4 = e^{i2\omega_0 t} e^{i2k'x} s'_{2\times 1} \otimes s'_{2\times 1}$, Eq. (42) can be rewritten as:

$$\Phi_{2^2\times 1} = \{a_{11}\eta_1 + a_{12}\eta_2 + a_{21}\eta_3 + a_{22}\eta_4\} \tag{43}$$

with $a_{11} = (\chi_n)^2 A_1 A_2 = \frac{1}{2}(\chi_n)^2$, $a_{12} = \chi_n \chi_{n'} A_1 A_2' = -\frac{1}{2}\chi_n \chi_{n'}$, $a_{21} = \chi_{n'} \chi_n A_1' A_2 = \frac{1}{2}\chi_{n'} \chi_n$, and $a_{22} = (\chi_{n'})^2 A_1' A_2' = -\frac{1}{2}(\chi_{n'})^2$. It is then easy to demonstrate that $\det\begin{pmatrix} a_{11} & a_{12} \\ a_{21} & a_{22} \end{pmatrix} = \begin{vmatrix} \frac{1}{2}(\chi_n)^2 & -\frac{1}{2}\chi_n\chi_{n'} \\ \frac{1}{2}\chi_{n'}\chi_n & -\frac{1}{2}(\chi_{n'})^2 \end{vmatrix} = 0$, which indicates that the state $\Phi_{2^2\times 1}$ is separable on the basis $\{\eta_1, \eta_2, \eta_3, \eta_4\}$. At this stage, there is nothing surprising as the state $\Phi_{2^2\times 1}$ was constructed as a tensor product. We now try to express the state given in Eq. (42) on a basis of two individually uncoupled φ-bits. Considering the Hilbert space of the first φ-bit, $H^{(1)}$, we use the spinor solutions for uncoupled waveguides given in Eq. (17) to construct the orthonormal basis

$$\psi_1^{(1)} = \frac{1}{\sqrt{2\omega_1}} \begin{pmatrix} \sqrt{\omega_1 + \beta_1 k_1} \\ \sqrt{\omega_1 - \beta_1 k_1} \end{pmatrix} e^{ik_1 x} e^{i\omega_1 t} = s_1^{(1)}(k_1) e^{ik_1 x} e^{i\omega_1 t} \tag{44a}$$

$$\psi_2^{(1)} = \frac{1}{\sqrt{2\omega_1}} \begin{pmatrix} \sqrt{\omega_1 - \beta_1 k_1} \\ -\sqrt{\omega_1 + \beta_1 k_1} \end{pmatrix} e^{-ik_1 x} e^{i\omega_1 t} = s_2^{(1)}(k_1) e^{-ik_1 x} e^{i\omega_1 t} \tag{44b}$$

Similarly, we define the orthonormal basis in the Hilbert space, $H^{(2)}$, of the second φ-bit,

$$\psi_1^{(2)} = \frac{1}{\sqrt{2\omega_2}} \begin{pmatrix} \sqrt{\omega_2 + \beta_2 k_2} \\ \sqrt{\omega_2 - \beta_2 k_2} \end{pmatrix} e^{ik_2 x} e^{i\omega_2 t} = s_1^{(2)}(k_2) e^{ik_2 x} e^{i\omega_2 t} \tag{45a}$$

$$\psi_2^{(2)} = \frac{1}{\sqrt{2\omega_2}} \begin{pmatrix} \sqrt{\omega_2 - \beta_2 k_2} \\ -\sqrt{\omega_2 + \beta_2 k_2} \end{pmatrix} e^{-ik_2 x} e^{i\omega_2 t} = s_2^{(2)}(k_2) e^{-ik_2 x} e^{i\omega_2 t} \tag{45b}$$

In these equations, we have used $s_1^{(1)}(k_1)$, $s_2^{(1)}(k_1)$, $s_1^{(2)}(k_2)$, and $s_2^{(2)}(k_2)$ as short-hands for the spinor parts of the basis functions.

The basis in the tensor product space $H^{(1)} \otimes H^{(2)}$ is given by the four functions:

$$\tau_1 = \psi_1^{(1)} \otimes \psi_1^{(2)}, \tau_2 = \psi_1^{(1)} \otimes \psi_2^{(2)}, \tau_3 = \psi_2^{(1)} \otimes \psi_1^{(2)}, \tau_4 = \psi_2^{(1)} \otimes \psi_2^{(2)} \tag{46}$$

We have

$$\tau_1 = s_1^{(1)}(k_1) \otimes s_1^{(2)}(k_2) e^{i(k_1+k_2)x} e^{i(\omega_1+\omega_2)t} \tag{47a}$$

$$\tau_2 = s_1^{(1)}(k_1) \otimes s_2^{(2)}(k_2) e^{i(k_1-k_2)x} e^{i(\omega_1+\omega_2)t} \tag{47b}$$

$$\tau_3 = s_2^{(1)}(k_1) \otimes s_1^{(2)}(k_2) e^{i(-k_1+k_2)x} e^{i(\omega_1+\omega_2)t} \tag{47c}$$

$$\tau_4 = s_2^{(1)}(k_1) \otimes s_2^{(2)}(k_2) e^{i(-k_1-k_2)x} e^{i(\omega_1+\omega_2)t} \tag{47d}$$

It is straightforward to show that $\{\tau_1, \tau_2, \tau_3, \tau_4\}$ form an orthogonal basis. That is, $\tau_i^\dagger \tau_j = 0$ if $i \neq j$, where $\tau_i^\dagger$ is the Hermitian conjugate of τ_i.

We want now to express the state $\Phi_{2^2 \times 1}$ in the τ basis:

$$\Phi_{2^2 \times 1} = \{b_{11}\tau_1 + b_{12}\tau_2 + b_{21}\tau_3 + b_{22}\tau_4\} \tag{48}$$

For this, we now need to expand the basis vectors $\{\eta_1, \eta_2, \eta_3, \eta_4\}$ on the basis $\{\tau_1, \tau_2, \tau_3, \tau_4\}$

We define the expansions:

$$\eta_1 = c_{11}\tau_1 + c_{12}\tau_2 + c_{13}\tau_3 + c_{14}\tau_4 \tag{49a}$$

$$\eta_2 = c_{21}\tau_1 + c_{22}\tau_2 + c_{23}\tau_3 + c_{24}\tau_4 \tag{49b}$$

$$\eta_3 = c_{31}\tau_1 + c_{32}\tau_2 + c_{33}\tau_3 + c_{34}\tau_4 \tag{49c}$$

$$\eta_4 = c_{41}\tau_1 + c_{42}\tau_2 + c_{43}\tau_3 + c_{44}\tau_4 \tag{49d}$$

Note that the c_{ij}'s are functions of $k_1, k_2, x,$ and t.

We can find the coefficients c_{ij} by exploiting the orthogonality of the $\tau_i's$. For instance, we can multiply Eq. (49a) to the left by the Hermitian conjugate $\tau_1^\dagger$, leading to

$$\tau_1^\dagger\eta_1 = c_{11}\tau_1^\dagger\tau_1 + c_{12}\tau_1^\dagger\tau_2 + c_{13}\tau_1^\dagger\tau_3 + c_{14}\tau_1^\dagger\tau_4 = c_{11}\tau_1^\dagger\tau_1 \tag{50}$$

or

$$\begin{aligned} c_{11}(k_1,k_2,x,t) = &\left(s_1^{(1)}(k_1)\otimes s_1^{(2)}(k_2)\right)^\dagger (s_{2\times1}\otimes s_{2\times1})e^{-i(k_1+k_2)x}e^{i2kx}e^{-i(\omega_1+\omega_2)t}e^{i2\omega_0 t}/ \\ &\left(s_1^{(1)}(k_1)\otimes s_1^{(2)}(k_2)\right)^\dagger \left(s_1^{(1)}(k_1)\otimes s_1^{(2)}(k_2)\right) \end{aligned} \tag{51}$$

We can obtain all other c_{ij}'s in a similar fashion. Eqs. (49a)–(49d) can be rewritten in the form:

$$\begin{pmatrix}\eta_1\\ \eta_2\\ \eta_3\\ \eta_1\end{pmatrix} = \eta_{4\times1} = \begin{pmatrix} c_{11} & c_{12} & c_{13} & c_{14}\\ c_{21} & c_{22} & c_{23} & c_{24}\\ c_{31} & c_{32} & c_{33} & c_{34}\\ c_{41} & c_{42} & c_{43} & c_{44}\end{pmatrix}\begin{pmatrix}\tau_1\\ \tau_2\\ \tau_3\\ \tau_4\end{pmatrix} = C_{4\times4}\tau_{4\times1} \tag{52}$$

The matrix $C_{4\times4}$ can be diagonalized. Let d_1, d_2, d_3, and d_4 be the four eigen values of $C_{4\times4}$ with their associated eigen vectors $\begin{pmatrix}v_{11}\\ v_{12}\\ v_{13}\\ v_{14}\end{pmatrix}$, $\begin{pmatrix}v_{21}\\ v_{22}\\ v_{23}\\ v_{24}\end{pmatrix}$, $\begin{pmatrix}v_{31}\\ v_{32}\\ v_{33}\\ v_{34}\end{pmatrix}$ and $\begin{pmatrix}v_{41}\\ v_{42}\\ v_{43}\\ v_{44}\end{pmatrix}$. We can construct the following matrix out of the four eigen vectors:

$$V_{4\times4} = \begin{pmatrix} v_{11} & v_{21} & v_{31} & v_{41}\\ v_{12} & v_{22} & v_{32} & v_{42}\\ v_{13} & v_{23} & v_{33} & v_{43}\\ v_{14} & v_{24} & v_{34} & v_{44}\end{pmatrix}$$

On the new basis $\{\tilde{\tau}_1, \tilde{\tau}_2, \tilde{\tau}_3, \tilde{\tau}_4\}$ constructed by using the relation $\tilde{\tau}_{4\times1} = V_{4\times4}^{-1}\tau_{4\times1}V_{4\times4}$, the matrix that couples the η basis and the τ basis takes the form: $\tilde{C}_{4\times4} = \begin{pmatrix} d_1 & 0 & 0 & 0\\ 0 & d_2 & 0 & 0\\ 0 & 0 & d_3 & 0\\ 0 & 0 & 0 & d_4\end{pmatrix}$ so $\eta_1 = d_1\tilde{\tau}_1$, $\eta_2 = d_2\tilde{\tau}_2$, $\eta_3 = d_3\tilde{\tau}_3$ and $\eta_4 = d_4\tilde{\tau}_4$. On the $\tilde{\tau}$ basis, Eq. (43) can be rewritten as

$$\Phi_{2^2\times1} = \{a_{11}d_1\tilde{\tau}_1 + a_{12}d_2\tilde{\tau}_2 + a_{21}d_3\tilde{\tau}_3 + a_{22}d_4\tilde{\tau}_4\} \tag{53}$$

Then on the basis $\tilde{\tau}$, we can investigate the separability or nonseparability of $\Phi_{2^2\times1}$ by calculating the determinant of the linear coefficients in Eq. (53), that is

$$\det\begin{pmatrix} a_{11}d_1 & a_{12}d_2 \\ a_{21}d_3 & a_{22}d_4 \end{pmatrix} = \begin{vmatrix} \frac{1}{2}(\chi_n)^2 d_1 & -\frac{1}{2}\chi_n\chi_{n'}d_2 \\ \frac{1}{2}\chi_{n'}\chi_n d_3 & -\frac{1}{2}(\chi_{n'})^2 d_4 \end{vmatrix} = -\frac{1}{4}(\chi_n)^2(\chi_{n'})^2[d_1d_4 - d_2d_3] \qquad (54)$$

Only in the unlikely event of degenerate eigen values, d_1, d_2, d_3, and d_4, would this determinant be equal to zero. A nonzero determinant given in Eq. (54) indicates that the state $\Phi_{2^2\times 1}$ is nonseparable on the basis $\{\tilde{\tau}_1, \tilde{\tau}_2, \tilde{\tau}_3, \tilde{\tau}_4\}$.

The existence of nonseparable solutions to the nonlinear Dirac equation raises the possibility of exploiting these solutions for storing and manipulating data within the 2^N dimensional tensor product Hilbert space. The exploration of algorithms for exploiting these solutions is beyond the scope of this chapter; however, we note that these solutions may well be observed in physical systems including elastic waveguides which are embedded in a coupling matrix. The manipulation of the system could be achieved either by externally altering the parameters of the system, i.e., the elastic properties of the waveguides, or by changing the frequency and wavenumber of input waves. These possibilities are illustrated for a five-waveguide system driven by transducers in Section 2.6.

2.6. Physical realization and actuation

Figure 3 illustrates a possible realization of a five waveguide system. The parallel elastic waveguides are embedded in an elastic medium which couples them elastically. The waveguides are arranged in a ring pattern.

Modes of the form given in Eq. (21) can be excited with N transducers attached to the input ends of the N waveguides and connected to N phase-locked signal generators to excite the appropriate eigen vectors e_n and $e_{n'}$. These modes can be excited by applying a superposition of signals on the transducers with the appropriate phase, amplitude and frequency relations. The frequencies $\omega_n(k)$ and $\omega_{n'}(k')$ are used to control the spinor parts of the wave functions

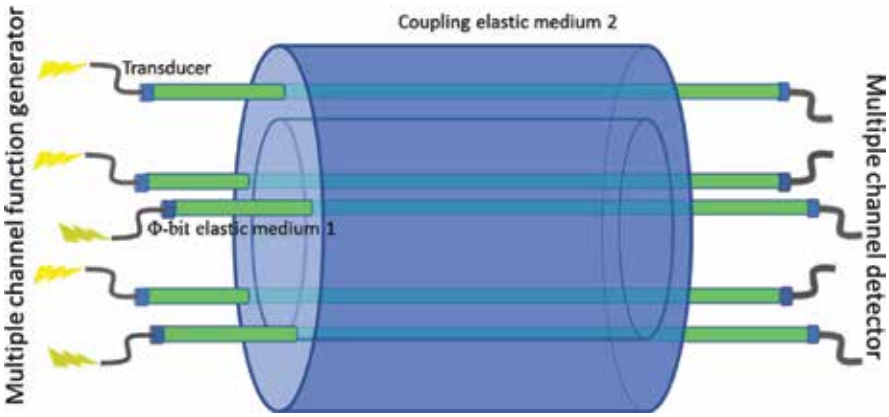

Figure 3. Schematic illustration of a five waveguide system. The waveguides are composed of an elastic medium 1 in which mass density and elastic stiffness determine the physical parameter β. The waveguides are embedded in an elastic medium 2 in which mass density and stiffness relate to the parameter α. The waveguides are actuated via transducers (see the text for details).

$s_{2\times1}(k)$ and $s_{2\times1}(k')$. The spinor components which represent a quasistanding wave can be quantified by measuring the transmission coefficient (normalized transmitted amplitude) along any one of the waveguides. It is then possible to operate on the eigen vectors e_n and $e_{n'}$ without affecting the spinor states or vice versa. For instance, one could apply a rotation that permutes cyclically the components of e_n by changing the phase of the signal generators. Such an operation could be quantified by measuring the phase of the transmission amplitude at the output end of the waveguides.

3. Conclusions

We have shown that the directional projection of elastic waves supported by a parallel array of N elastically coupled waveguides can be described by a nonlinear Dirac-like equation in a 2^N dimensional exponential space. This space spans the tensor product Hilbert space of the two-dimensional subspaces of N uncoupled waveguides grounded elastically to a rigid substrate (which we called φ-bits). We demonstrate that we can construct tensor product states of the elastically coupled system that are nonseparable on the basis of tensor product states of N uncoupled φ-bits. A φ-bit exhibits superpositions of directional states that are analogous to those of a quantum spin, hence it acts as a pseudospin. Since parallel arrays of coupled waveguides span the same exponentially complex space as that of uncoupled pseudospins, the type of elastic systems described here may serve as a simulator of interacting spin networks. The possibility of tuning the elastic coefficients and the elastic coupling constants of the waveguides would allow us to explore the properties of spin networks with variable connectivity and coupling strength. The mapping between the $2N$ dimensional and the 2^N dimensional representations of the elastic system leads to the capacity for exploring an exponentially scaling space by handling a linearly growing number of waveguides (i.e., preparation, manipulation, and measurement of these states). The scalability of the elastic system, the coherence of elastic waves at room temperature, and the ability to measure classical superpositions of states may offer an attractive way for addressing exponentially complex problem through the analogy with quantum systems.

Acknowledgements

We acknowledge the financial support of the W.M. Keck Foundation. We thank Saikat Guha and Zheshen Zhang for useful discussions.

Conflict of interest

The authors declare that they have no affiliations with or involvement in any organization or entity with any financial interest or nonfinancial interest in the subject matter or materials discussed in this manuscript.

Author details

Pierre Alix Deymier[1]*, Jerome Olivier Vasseur[2], Keith Runge[1] and Pierre Lucas[1]

*Address all correspondence to: deymier@email.arizona.edu

1 Department of Materials Science and Engineering, University of Arizona, Tucson, AZ, USA

2 CNRS, Centrale Lille, ISEN, Univ. Lille, Univ. Valenciennes, UMR 8520—IEMN, Lille, France

References

[1] Spreeuw RJ. A classical analogy of entanglement. Foundations of Physics. 1998;**28**:361

[2] Ghose P, Mukherjee A. Entanglement in classical optics. Reviews in Theoretical Science. 2014;**2**:274

[3] Karimi E, Boyd RW. Classical entanglement? Science. 2015;**350**:1172

[4] Chen L, She W. Single-photon spin-orbit entanglement violating a bell-like inequality. JOSA B. 2010;**27**:A7

[5] Borges C, Hor-Meyll M, Huguenin J, Khoury A. Bell-like inequality for the spin orbit separability of a laser beam. Physical Review A. 2010;**82**:033833

[6] Karimi E, Leach J, Slussarenko S, Piccirillo B, Marrucci L, Chen L, She W, Franke-Arnold S, Padgett MJ, Santamato E. Spin-orbit hybrid entanglement of photons and quantum contextuality. Physical Review A. 2010;**82**:022115

[7] Valles A, D'Ambrosio V, Hendrych M, Micuda M, Marrucci L, Sciarrino F, Torres JP. Generation of tunable entanglement and violation of a bell-like inequality between different degrees of freedom of a single photon. Physical Review A. 2014;**90**:052326

[8] Pereira LJ, Khoury AZ, Dechoum K. Quantum and classical separability of spin-orbit laser modes. Physical Review A. 2014;**90**:053842

[9] Qian X-F, Little B, Howell JC, Eberly JH. Shifting the quantum-classical boundary: Theory and experiment for statistically classical optical fields. Optica. 2015;**2**:611

[10] Rafsanjani SMH, Mirhosseini M, Magana-Loaiza OS, Boyd RW. State transfer based on classical nonseparability. Physical Review A. 2015;**92**:023827

[11] Michler M, Weinfurter H, Żukowski M. Experiments towards falsification of noncontextual hidden variable theories. Physical Review Letters. 2000;**84**:5457

[12] Gadway B, Galvez E, De Zela F. Bell-inequality violations with single photons entangled in momentum and polarization. Journal of Physics B: Atomic, Molecular and Optical Physics. 2008;**42**:015503

[13] Deymier PA, Runge K, Vasseur JO, Lucas P, Hladky A-C. Phonons with correlated directional and orbital angular momentum degrees of freedom. Journal of Physics B: Atomic, Molecular and Optical Physics. https://doi.org/10.1088/1361-6455/aac446

[14] Das A, Chakrabarti BK. Colloquium: Quantum annealing and analog quantum computation. Reviews of Modern Physics. 2008;**80**:1061

[15] Marandi A, Wang Z, Takata K, Byer RL, Yamamoto Y. Network of time-multiplexed optical parametric oscillators as a coherent Ising machine. Nature Photonics. 2014;**8**:837

[16] Santoro GE, Tosatti E. Quantum to classical and back. Nature Physics. 2007;**3**:593

[17] Dubus B, Swinteck N, Muralidharan K, Vasseur JO, Deymier PA. Nonlinear phonon modes in second-order anharmonic coupled monoatomic chains. Journal of Vibration and Acoustics. 2016;**138**:041016

[18] Deymier PA, Runge K, Swinteck N, Muralidharan K. Rotational modes in a phononic crystal with fermion-like behavior. Journal of Applied Physics. 2014;**115**:163510

[19] Deymier PA, Runge K, Swinteck N, Muralidharan K. Torsional topology and fermion-like behavior of elastic waves in phononic structures. Comptes Rendus Mécanique. 2015;**343**: 700-711

[20] Deymier PA, Runge K. One-dimensional mass-spring chains supporting elastic waves with non-conventional topology. Crystals. 2016;**6**:44

[21] Deymier PA, Runge K. Sound topology, duality, coherence and wave-mixing: An introduction to the emerging new science of sound. In: Springer Series in Solid State Sciences. Vol. 188. Berlin: Springer; 2017

[22] Zanardi P. Virtual quantum systems. Physical Review Letters. 2001;**87**:077901

[23] Zanardi P, Lidar DA, Lloyd S. Quantum tensor product structures are observable induced. Physical Review Letters. 2004;**92**:060402

[24] Croënne C, Vasseur JO, Bou Matar O, Ponge M-F, Deymier PA, Hladky-Hennion A-C, Dubus B. Brillouin scattering-like effect and non-reciprocal propagation of elastic waves due to spatio-temporal modulation of electrical boundary conditions in piezoelectric media. Applied Physics Letters. 2017;**110**:061901

[25] Bou Matar O, Robillard JF, Vasseur JO, Hladky-Hennion A-C, Deymier PA, Pernod P, Preobrazhensky V. Band gap tunability of magneto-elastic phononic crystal. Journal of Applied Physics. 2012;**111**:054901

[26] Swinteck N, Matsuo S, Runge K, Vasseur JO, Lucas P, Deymier PA. Bulk elastic waves with unidirectional backscattering-immune topological states in a time-dependent superlattice. Journal of Applied Physics. 2015;**118**:063103

Chapter 4

Phonon Modes and Elastic Properties of Zr-Based Bulk Metallic Glasses: A Pseudopotential Approach

Punitkumar Harshadbhai Suthar

Additional information is available at the end of the chapter

http://dx.doi.org/10.5772/intechopen.79568

Abstract

The collective dynamics for longitudinal and transverse phonon modes and elastic properties are studied for bulk metallic glasses (BMGs) using Hubbard-Beeby approach along with our well establishes model potential. The important ingredients in the present study are the pair-potential and local field correlation function. The local field correlation functions due to Hartree (H), Taylor (T), Ichimaru and Utsumi (IU), Farid et al. (F), Sarkar et al. (S) and Hubbard and Sham (HS) are employed to investigate the influence of the screening effects on the vibrational dynamics of Zr-Ti-Cu-Ni-Be, Zr-Cu-Ni-Al-Ta, Zr-Ti-Cu-Ni-Al and Zr-Al-Ni-Cu. The result for the elastic constants like bulk modulus B_T, rigidity modulus G, Poisson's ratio ξ, Young's modulus Y, Debye temperature Θ_D, the propagation velocity of elastic waves and dispersion curves are found to be in good agreement with experimental and other available data. The present results are consistent and confirm the applicability of model potential and self-consistent phonon theory for such studies.

Keywords: bulk metallic glass, pseudopotential, local field correction function, phonon modes, elastic properties

1. Introduction

Bulk metallic glass-forming liquids are alloys with typically three to five metallic components that have large atomic size mismatch and a composition close to a deep eutectic [1]. Metallic glasses have regained considerable interest due to the fact that new glass forming composition have been found that have a critical cooling rate of less than 100 K s^{-1} and can be made glassy with dimensions of 1 cm or more. The development of such alloys with a very high resistance to crystallization of the under cooled melt has opened new opportunities for the primary study

of both the liquid state and the glass transition. The ability of bulk specimens has enabled measurements of various physical, particularly mechanical, properties that were previously impossible. Furthermore, these alloys are progressively being used for engineering applications. This new class of material is normally referred to as "bulk metallic glasses." [1–10]

Bulk metallic glass an excellent glass forming ability and high thermal stability have attracted much attention in the recent years. It has also occupied an important position due to their unique physical properties and technological importance. Zr-based BMGs are the coming up candidates to replace the usual materials used in the industry as a result of their superior mechanical properties, for example strength, hardness, toughness and elasticity [2–10]. Recently formation of Zr-Ti-Cu-Ni-Be, Zr-Ti-Cu-Ni-Be, Zr-Cu-Ni-Al-Ta, Zr-Ti-Cu-Ni-Al and Zr-Al-Ni-Cu bulk metallic glass (BMGs) alloys distinguished itself from other metallic alloys by extraordinary glass forming ability (GFA) [4–9]. These alloys have opened the possibility to study the nature of glass transition in BMGs, offered the potential of BMGs as new generation engineering materials and controllable properties is one of the central issues in the condensed matter physics and material sciences [2–10]. Metallic glass alloys are normally regarded as elastically isotopic, and they behave as an elastic continuum at low temperatures, with well-defined dispersion relation so that ultrasonic waves propagated through it. Perker and Johnson [9] are made an important process of the design of the Zr–Ti–Cu–Ni–Be ($Zr_{41}Ti_{14}Cu_{12.5}Ni_{10}Be_{22.5}$, $Zr_{45.4}Ti_{9.6}Cu_{10.15}Ni_{8.6}Be_{26.25}$, and $Zr_{46.75}Ti_{8.25}Cu_{7.5}Ni_{10}Be_{27.5}$) five different concentration, Zr-Cu-Ni-Al glass-forming alloy family. This family has distinct glass transition, very high stability of supercooled liquid state and exhibits high thermal stability against crystallization. Dissolution of minute amount of metalloid elements into the Zr-base system can enlarge the thermal stability and hardness of the BMG. Zr-based BMGs are used in manufacturing of industrial production [4–9]. Recently, Agarwal has reported the phonon dispersion curves of Zr-Ti-Cu-Ni-Be BMGs using Bhatia and Singh (BS) approach [11]. Wang et al. [4–6] have represented elastic properties using ultrasonic method. In the present study, we have investigated theoretically, phonon dispersion curve and elastic properties of Zr-based [4–10] bulk metallic glasses with the help of pseudopotential formalism and along with Hubbard and Beeby [12] approach and employing pseudopotential formalism along with the five different local field correction functions due to Hartree [13], Taylor [14], Ichimaru and Utsumi [15], Farid et al. [16], Sarkar et al. [17].

2. Theory

There are three main theoretical approaches used to compute the phonon frequency of binary alloys: one is Hubbard and Beeby (HB) [12], second is Takeno and Goda (TG) [18], and last is Bhatia and Singh (BS) [11]. The HB approach is the random phase approximation according to this theory, a liquid random from a crystalline solid in two principal ways. Initially, the atoms in the metallic glasses do not form a regular array, i.e. they disordered. So the HB theoretical models have been employed to generate the phonon dispersion curve and their related properties of bulk metallic glass alloys in the present computation.

http://dx.doi.org/10.5772/intechopen.79568

The effective ion-ion interaction is given as

$$V(r) = \frac{Z^2 e^2}{r} + \frac{2}{\pi}\int dq F(q) \exp\left(-iq \cdot r\right) \tag{1}$$

where $F(q)$ is the characteristic energy wave number. The first and second terms in the above expression are due to the coulomb interaction between ion and indirect interaction through the conduction electrons, respectively; q is the q-space wave vector, e is the charge of an electron. In the present study, we have considered the effective atom approach to compute the phonon dispersion curve (PDC). For the present study, we have used the Jani et al. [19–21] model potential in q-space is given as,

$$W_B^{eff}(q) = -\frac{4\pi^2 e^2}{\Omega_0 q^2}\left(\cos\left(qr_c^{eff}\right) - \frac{\exp\left(-1\right)\ qr_c^{eff}}{1+\left(qr_c^{eff}\right)^2}\left(\sin\left(qr_c^{eff}\right) + qr_c^{eff}\cos\left(qr_c^{eff}\right)\right)\right) \tag{2}$$

The characteristic feature of this model potential is the single parametric nature. r_c^{eff} is the potential parameter. This determination of parameter is independent of any fitting procedure with the observed quantities. The energy wave number characteristics in expression (1) are given by [21–25]

$$F(q) = -\frac{\Omega_{0eff} q^2}{16\pi}\left|W_B^{eff}(q)\right|^2 \times \frac{\left[\varepsilon_H^{eff}(q) - 1\right]}{\left[1 + \left(\varepsilon_H^{eff}(q) - 1\right)\left(1 - f_{eff}(q)\right)\right]} \tag{3}$$

Here $W_B^{eff}(q)$ is the effective bare ion potential, $\varepsilon_{\mathrm{H}}^{\mathrm{eff}}(q)$is the Hartree dielectric response function and $f_{eff}(q)$ is the local field correction function (LFCF) due to the Hartree (H) [13], Taylor (T) [14], Ichimaru-Utsumi (IU) [15], Farid et al. (F) [16] and Sarkar et al. (S) [17] are used here to include the effect of screening on the collective modes of bulk metallic glasses Zr-Ti-Cu-Ni-Be BMG for five different concentration, Zr-Cu-Ni-Al-Ta BMG, Zr-Ti-Cu-Ni-Al BMG and Zr-Al--Ni-Cu BMG for three different concentration. Long-wavelength limits of the phonon modes are then used to investigate the elastic properties, viz. longitudinal sound velocity, transverse sound velocity, Debye temperature, isothermal bulk modulus, modulus of rigidity, Poisson's ratio and Young's modulus. Five different types of LFCF are employed here for the study of the effect of exchange and correlation on the aforesaid properties. Pair potential or effective interaction is realized through interatomic potential, ion-ion potential and electron-electron potential developed between two similar particles like atoms, ion and electrons. The pair-correlation function g(r) is equally important as the pair potential. It contains useful information about the inter particle radial correlation and structure which in turn decides the electrical thermodynamically and amorphous materials.

The effective potential and pair correlation function $g(r)$ are the used to calculate the longitudinal and transverse phonon frequencies. The product of the static pair-correlation function $g(r)$ and the second derivative of the interatomic potential $V_{eff}^{''}(r)$ are peaked at σ, which is the

hard sphere diameter. The longitudinal phonon frequency ω_l (q) and transverse phonon frequency ω_t(q) are given by the expression due to Hubbard and Beeby (HB).

$$\omega_l^2(q) = \omega_E^2\left[1 - \frac{3\sin(q\sigma)}{q\sigma} - \frac{6\cos(q\sigma)}{(q\sigma)^2} + \frac{6\sin(q\sigma)}{(q\sigma)^3}\right] \tag{4}$$

and

$$\omega_t^2(q) = \omega_E^2\left[1 + \frac{3\cos(q\sigma)}{(q\sigma)^2} - \frac{6\sin(q\sigma)}{(q\sigma)^3}\right] \tag{5}$$

where

$$\omega_E = \frac{4\pi n_{eff}}{3M_{eff}}\int_0^\infty g(r)r^2V_{eff}^{''}(r)dr \tag{6}$$

$$V_{eff}''(r) = \frac{4Z^2}{r^3} + \frac{\Omega_0}{\pi^2}\int_0^\infty F(q)q^2\left[\frac{2\sin(qr)}{qr^3} - \frac{2\cos(qr)}{r^2} - \frac{q\sin(qr)}{r}\right]dq, \tag{7}$$

and

$$g(r) = \exp\left[\left(\frac{-V_{eff}''(r)}{k_BT}\right) - 1\right] \tag{8}$$

Here, ρ is the number density, M is the atomic mass, g(r) is the pair correlation function, Ω_0 is the atomic volume, F(q) and S(q) be the energy wave number characteristic and the structure factor of the element, respectively.

In the long-wavelength limit, the phonon dispersion curve shows an elastic behavior. Hence, the longitudinal ν_l and transverse ν_t sound velocities are also calculated by [22–25]

$$\omega_L\ \alpha\ q \text{ and } \omega_T\ \alpha\ q, \therefore \omega_L = v_l q \text{ and } \omega_T = v_l q \tag{9}$$

Various elastic properties are determined by the longitudinal and transverse phonon frequencies.

The bulk modulus B, Poisson's ratio 'ξ', modulus of rigidity G, Young's modulus Y and the Debye temperature θ_D are calculated using the expression below [22–25]

$$B = \rho\left(v_l^2 - \frac{4}{3}v_t^2\right) \tag{10}$$

ρ is the isotropic density of the solid,

$$\xi = \frac{1 - 2\left(v_t^2/v_l^2\right)}{2 - 2\left(v_t^2/v_l^2\right)} \tag{11}$$

$$G = \rho\, v_t^2 \tag{12}$$

$$Y = 2G(\xi + 1) \tag{13}$$

and

$$\theta_D = \frac{h}{k_B}\left[\left(\frac{9\rho}{4\pi}\right)^{1/3}\left(\frac{1}{v_l^3}+\frac{2}{v_t^3}\right)^{-1/3}\right] \tag{14}$$

where 'h' is Plank constant and k_B is the Boltzmann constant.

3. Results and discussion

The input parameters and constants used in the present computation are shown in **Table 1**. Pair potential (**Figures 1(a)–10(a)**) and the phonon frequencies of longitudinal and transverse branch (**Figures 1(b)–10(b)**) of various bulk metallic glasses are shown in **Figures 1–10**. Our well-established model potential is used along with five different local field correction functions to computed form factors and thereby effective pair potentials. The phenomenological approach of Hubbard and Beeby [8, 12, 21–25] is used further to compute phonon frequencies. The longitudinal and transverse phonon frequencies show all broad features of collective excitations of all BMGs. It is seen from the results of phonon frequencies that the nature of peak positions are not much affected by different screening functions, but both the longitudinal and transverse frequencies show deviation for H, T and S functions with respect to IU and F screening function for present model potential. At large momentum, phonons from longitudinal branch are found responsible for momentum transfer. Phonons of transverse branch undergo large thermal modulation due to the anharmonicity of lattice vibrations in this branch. The first minimum in the longitudinal branch corresponds to umklapped scattering process. No experimental data of structure factor for these BMGs are available. In the long wavelength limit, the frequencies are elastic and allow us to computed elastic constants.

BMGs	Z_{eff}	Ω_{eff} (au)^3	r_c^{eff} (au)	M_{eff} (amu)	r_{seff} (au)
$Zr_{38.5}Ti_{16.5}Cu_{15.25}Ni_{9.75}Be_{20}$	3.100	115.447	1.0565	60.237	2.0716
$Zr_{41}Ti_{14}Cu_{12.5}Ni_{10}Be_{22.5}$	3.100	119.893	1.0699	59.945	2.0978
$Zr_{44}Ti_{11}Cu_{10}Ni_{10}Be_{25}$	3.100	119.809	1.0696	59.882	2.0974
$Zr_{45.4}Ti_{9.6}Cu_{10.15}Ni_{8.6}Be_{26.25}$	3.100	123.501	1.0805	59.875	2.1187
$Zr_{46.75}Ti_{8.25}Cu_{7.5}Ni_{10}Be_{27.5}$	3.100	124.510	1.0834	59.710	2.1245
$Zr_{52.25}Cu_{28.5}Ni_{4.75}Al_{9.5}Ta_5$	2.957	128.860	1.1133	80.173	2.1830
$Zr_{57}Ti_5Cu_{20}Ni_8Al_{10}$	3.040	127.676	1.0385	74.493	2.1560
$Zr_{61.88}Al_{10}Ni_{10.12}Cu_{18}$	3.056	127.039	1.0960	76.143	2.1459
$Zr_{64.13}Al_{10}Ni_{10.12}Cu_{15.75}$	3.124	130.140	1.0968	76.874	2.1505
$Zr_{65}Al_{10}Ni_{10}Cu_{15}$	3.150	135.985	1.1099	77.395	2.1762

Table 1. Input parameters and constants.

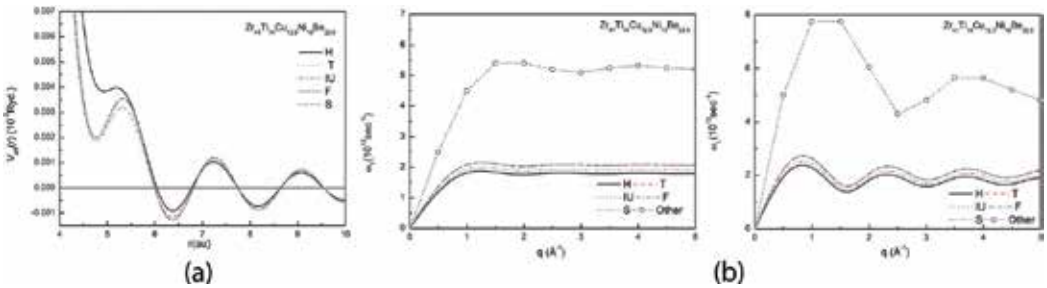

Figure 1. (a) Pair potential for $Zr_{41}Ti_{14}Cu_{12.5}Ni_{10}Be_{22.5}$ BMG. (b) Phonon dispersion curve (ω_L & ω_T) for $Zr_{41}Ti_{14}Cu_{12.5}Ni_{10}Be_{22.5}$ BMG along with other available data [8].

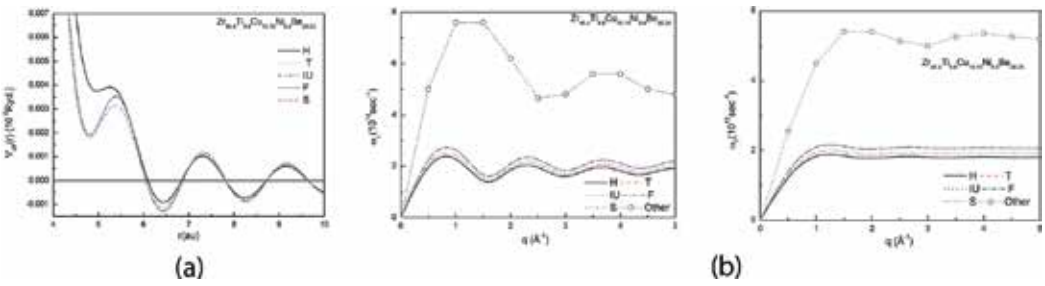

Figure 2. (a) Pair potential for $Zr_{45.4}Ti_{9.6}Cu_{10.15}Ni_{8.6}Be_{26.25}$ BMG. (b) Phonon dispersion curve (ω_L & ω_T) of $Zr_{45.4}Ti_{9.6}Cu_{10.15}Ni_{8.6}Be_{26.25}$ BMG along with other available data [8].

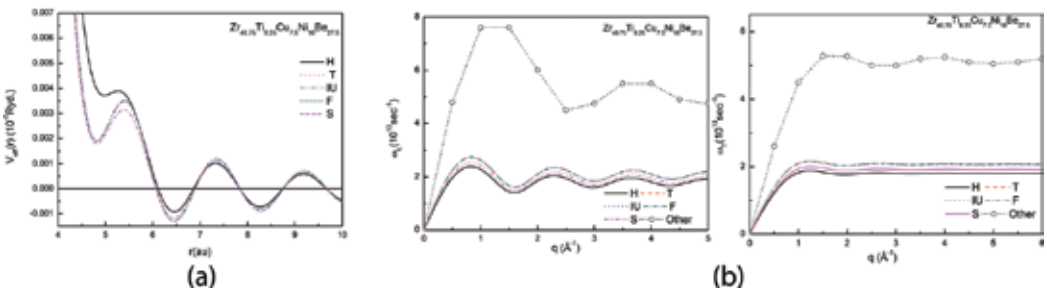

Figure 3. (a) Pair potential for $Zr_{46.75}Ti_{14}Cu_{12.5}Ni_{10}Be_{22.5}$ BMG. (b) Phonon dispersion curve (ω_L & ω_T) of $Zr_{46.75}Ti_{14}Cu_{12.5}Ni_{10}Be_{22.5}$ BMG, along with other available data [8].

3.1. Zr-Ti-Cu-Ni-Be BMG ($Zr_{41}Ti_{14}Cu_{12.5}Ni_{10}Be_{22.5}$, $Zr_{45.4}Ti_{9.6}Cu_{10.15}Ni_{8.6}Be_{26.25}$, $Zr_{46.75}Ti_{8.25}Cu_{7.5}Ni_{10}Be_{27.5}$, $Zr_{44}Ti_{11}Cu_{10}Ni_{10}Be_{25}$, $Zr_{38.5}Ti_{16.5}Ni_{9.75}Cu_{15.25}Be_{20}$)

Equation to compute phonon frequency and longitudinal and transverse sound velocity are taken from Thakore et al. [21, 23]. Pair potential and the phonon modes computed for $Zr_{41}Ti_{14}Cu_{12.5}Ni_{10}Be_{22.5}$ BMG, $Zr_{45.4}Ti_{9.6}Cu_{10.15}Ni_{8.6}Be_{26.25}$ BMG, $Zr_{46.75}Ti_{8.25}Cu_{7.5}Ni_{10}Be_{27.5}$

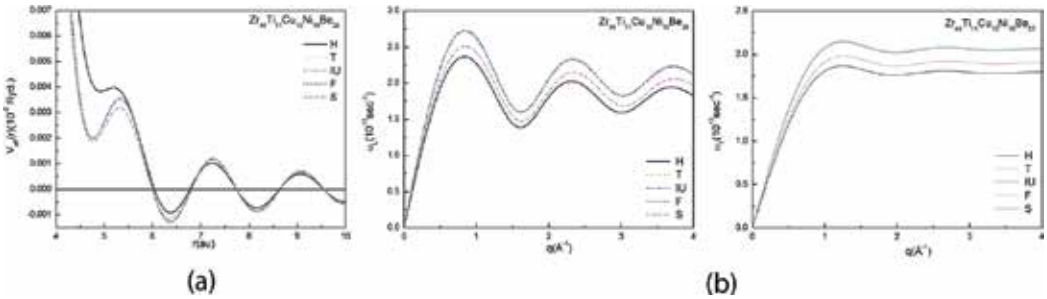

Figure 4. (a) Pair potential for $Zr_{44}Ti_{11}Cu_{10}Ni_{10}Be_{25}$ BMG. (b) Phonon dispersion curve (ω_L & ω_T) for $Zr_{44}Ti_{11}Cu_{10}Ni_{10}Be_{25}$ BMG.

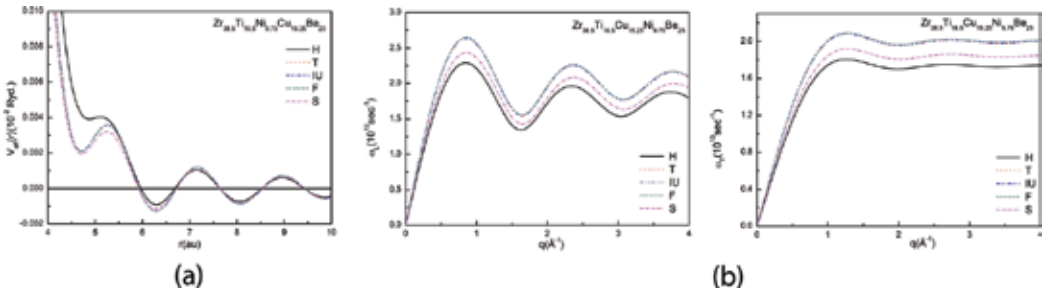

Figure 5. (a) Pair potential for $Zr_{38.5}Ti_{16.5}Cu_{15.25}Ni_{9.75}Be_{25}$ BMG. (b) Phonon dispersion curve (ω_L & ω_T) for $Zr_{38.5}Ti_{16.5}Cu_{15.25}Ni_{9.75}Be_{25}$ BMG.

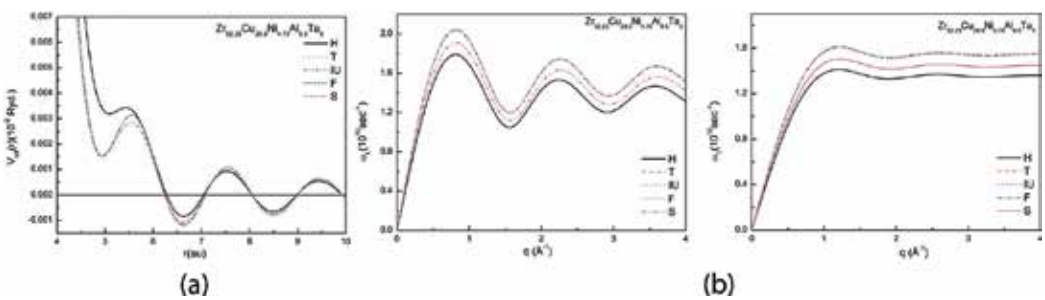

Figure 6. (a) Pair potential for $Zr_{52.25}Cu_{28.5}Ni_{4.75}Al_{9.5}Ta_5$ BMG. (b) Phonon dispersion curve (ω_L & ω_T) for $Zr_{52.25}Cu_{28.5}Ni_{4.75}Al_{9.5}Ta_5$ BMG.

BMG, $Zr_{44}Ti_{11}Cu_{10}Ni_{10}Be_{25}$ BMG, $Zr_{38.5}Ti_{16.5}Ni_{9.75}Cu_{15.25}Be_{20}$ BMG are shown in **Figures 1–5** respectively. It is observed that the study reveals the general trends of the pair potential for BMGs considered here, suggesting that the position of the first minima is affected by the type of screening functions. The maximum depth in the pair potential in the present study is obtained due to S screening function for $Zr_{41}Ti_{14}Cu_{12}Ni_{10}Be_{22.5}$, $Zr_{45.4}Ti_{9.6}Cu_{10.15}Ni_{8.6}Be_{26.25}$ and $Zr_{46.75}Ti_{8.25}Cu_{7.5}Ni_{10}Be_{27.5}$ BMGs. From **Figures 2–4** it is seen from the results of phonon frequencies that the general nature and peak positions are not affected very much by different

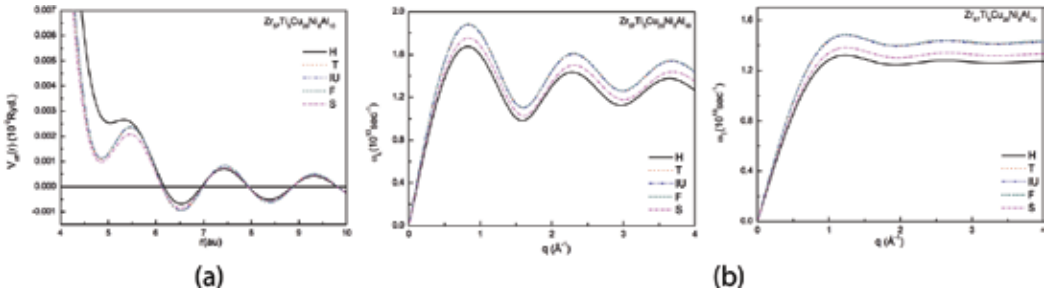

Figure 7. (a) Pair potential for $Zr_{57}Ti_5Cu_{20}Ni_8Al_{10}$ BMG. (b) Phonon dispersion curve (ω_L & ω_T)) for $Zr_{57}Ti_5Cu_{20}Ni_8Al_{10}$ BMG.

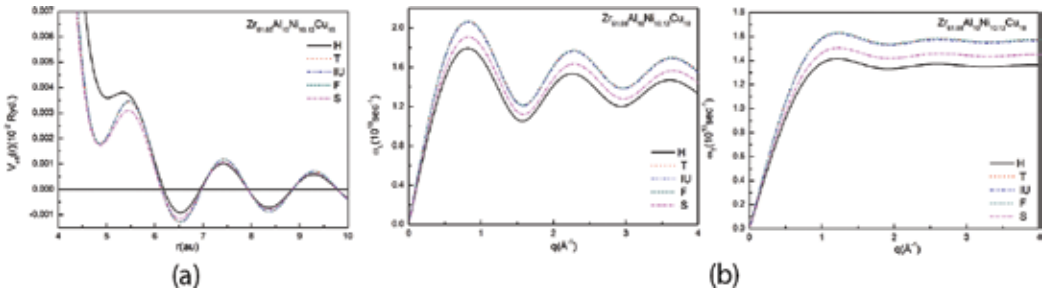

Figure 8. (a) Pair potential for $Zr_{61.88}Al_{10}Ni_{10.12}Cu_{18}$ BMG. (b) Phonon dispersion curve (ω_L & ω_T) for $Zr_{61.88}Al_{10}Ni_{10.12}Cu_{18}$ BMG.

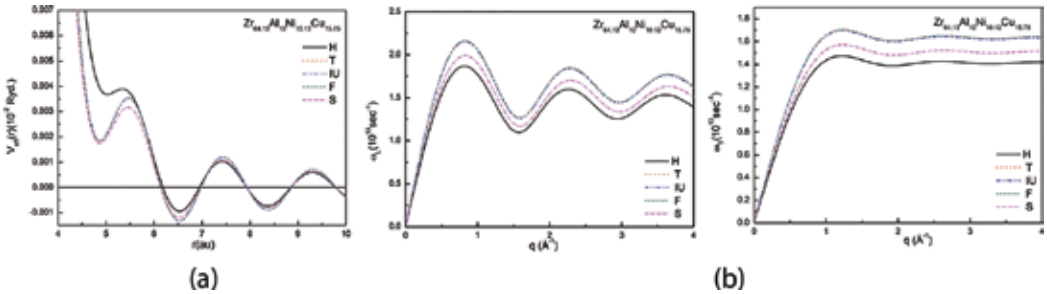

Figure 9. (a) Pair potential for $Zr_{64.13}Al_{10}Ni_{10.12}Cu_{15.75}$ BMG. (b) Phonon dispersion curve (ω_L & ω_T) for $Zr_{64.13}Al_{10}Ni_{10.12}Cu_{15.75}$ BMG.

screening functions, but magnitude of both the longitudinal and transverse frequencies show deviation with respect to screening function. From the **Figures 2–6** that the oscillations are prominent in the longitudinal mode as compared to transverse mode, which indicates that the collective excitations at larger wave vector transfer due to the dispersion of longitudinal excitation. The maximum and minimum percentile deviation for the elastic properties of bulk modulus, modulus of rigidity, Young modulus and Debye temperature with respect to the experimental data from **Tables 2–4**. For bulk modulus, the computed percentile maximum

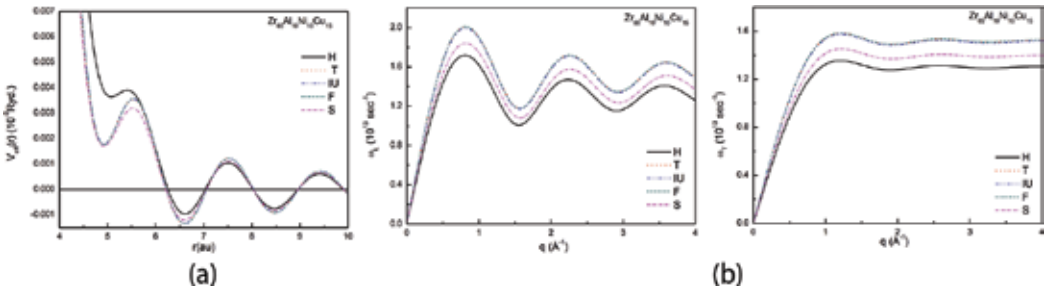

Figure 10. (a) Pair potential for $Zr_{65}Al_{10}Ni_{10}Cu_{15}$ BMG. (b) Phonon dispersion curve (ω_L & ω_T) for $Zr_{65}Al_{10}Ni_{10}Cu_{15}$ BMG.

Properties	H [13]	T [14]	IU [15]	F [16]	S [17]	Exp. [4–6]	Other [4–6]
$\upsilon_L \times 10^5$ (cm s^{-2})	4.553	5.177	5.176	5.203	4.776	—	5.174
$\upsilon_T \times 10^5$ (cm s^{-2})	2.629	2.989	2.988	3.004	2.757	—	2.472
$B_T \times 10^{12}$ (dyne/cm^2)	0.645	0.834	0.834	0.842	0.701	1.148 1.141	1.150
$G \times 10^{12}$ (dyne/cm^2)	0.387	0.501	0.500	0.505	0.426	0.374	0.471
ξ	0.25	0.25	0.25	0.25	0.25	0.35	0.352
$Y \times 10^{12}$ (dyne/cm^2)	0.966	1.251	1.251	1.263	1.065	1.013 1.012	1.055
θ_D (K)	333.0	378.7	378.7	380.6	349.4	—	327

Table 2. Elastic properties of $Zr_{41}Ti_{14}Cu_{12.5}Ni_{10}Be_{22.5}$ BMG.

Properties	H [13]	T [14]	IU [15]	F [16]	S [17]	Exp.	Other [4–6]
$\upsilon_L \times 10^5$ (cm s^{-2})	4.621	5.253	5.249	5.277	4.850	—	5.171
$\upsilon_T \times 10^5$ (cm s^{-2})	2.668	3.033	3.031	3.047	2.800	—	2.485
$B_T \times 10^{12}$ (dyne/cm^2)	0.644	0.833	0.832	0.840	0.709	—	1.119
$G \times 10^{12}$ (dyne/cm^2)	0.386	0.499	0.499	0.504	0.426	—	0.373
ξ	0.25	0.25	0.25	0.25	0.25	—	0.35
$Y \times 10^{12}$ (dyne/cm^2)	0.966	1.249	1.247	1.260	1.065	—	1.009
θ_D (K)	334.7	380.5	380.2	382.2	351.3	—	327

Table 3. Elastic properties for $Zr_{45.4}Ti_{9.6}Cu_{10.15}Ni_{8.6}Be_{26.25}$ BMG.

deviation with respect to experimental data is found in H functions, the values are 43.82, 42.42 and 43.48% and minimum deviation is found in F functions, the values are 26.69, 24.92 and 26.25% for $Zr_{41}Ti_{14}Cu_{12}Ni_{10}Be_{22.5}$, $Zr_{45.4}Ti_{9.6}Cu_{10.15}Ni_{8.6}Be_{26.25}$ and $Zr_{46.75}Ti_{8.25}Cu_{7.5}Ni_{10}Be_{27.5}$ BMGs respectively. The computed percentile deviation for modulus of rigidity with respect to experimental data, the maximum deviation is found to be 35.54, 35.12 and 42.55% of F

functions and minimum deviation is found in H function, the values are 3.47, 3.47 and 9.26% for $Zr_{41}Ti_{14}Cu_{12}Ni_{10}Be_{22.5}$, $Zr_{45.4}Ti_{9.6}Cu_{10.15}Ni_{8.6}Be_{26.25}$ and $Zr_{46.75}Ti_{8.25}Cu_{7.5}Ni_{10}Be_{27.5}$ BMGs respectively. For Young modulus, the computed percentile maximum deviation with respect to experimental data is found in F functions, the values are 24.72, 24.90 and 24.74% and minimum deviation is found in H functions, the values are 4.49, 4.22 and 7.47%, for $Zr_{41}Ti_{14}Cu_{12}Ni_{10}Be_{22.5}$, $Zr_{45.4}Ti_{9.6}Cu_{10.15}Ni_{8.6}Be_{26.25}$ and $Zr_{46.75}Ti_{8.25}Cu_{7.5}Ni_{10}Be_{27.5}$ BMGs respectively. Similarly for Debye temperature, the computed percentile maximum deviation with respect to experimental data is found in F function, the values are 16.39, 16.90 and 16.33% and minimum deviation is found in H function, the values are 1.86, 2.36 and 2.37%, for $Zr_{41}Ti_{14}Cu_{12}Ni_{10}Be_{22.5}$, $Zr_{45.4}Ti_{9.6}Cu_{10.15}Ni_{8.6}Be_{26.25}$ and $Zr_{46.75}Ti_{8.25}Cu_{7.5}Ni_{10}Be_{27.5}$ BMGs respectively.

Presently calculated elastic properties for $Zr_{44}Ti_{11}Cu_{10}Ni_{10}Be_{25}$ and $Zr_{38.5}Ti_{16.5}Cu_{15.25}Ni_{9.75}Be_{25}$ BMG are listed in **Tables 4** and **5** respectively. From this table, one can see that the results are obtained due to T, IU and F screening functions are very close to one another as compared to the H screening function. Due to lack of experimental data and other information of elastic

Properties	H [13]	T [14]	IU [15]	F [16]	S [17]	Exp. [5, 6]	Other [4–6]
$\upsilon_L \times 10^5$ (cm s^{-2})	4.634	5.266	5.265	5.294	4.866	—	5.182
$\upsilon_T \times 10^5$ (cm s^{-2})	2.675	3.040	3.0403	3.056	2.810	—	2.487
$B_T \times 10^{12}$ (dyne/cm^2)	0.641	0.828	0.828	0.836	0.707	1.134	1.137 1.119
$G \times 10^{12}$ (dyne/cm^2)	0.385	0.497	0.496	0.502	0.424	0.352	0.476 0.372
ξ	0.25	0.25	0.25	0.25	0.25	0.35	0.352
$Y \times 10^{12}$ (dyne/cm^2)	0.961	1.242	1.241	1.255	1.060	0.957	1.039 1.005
θ_D (K)	334.7	380.4	380.4	380.4	351.5	—	327

Table 4. Elastic properties for $Zr_{46.75}Ti_{14}Cu_{12.5}Ni_{10}Be_{22.5}$ BMG.

Properties	H [13]	T [14]	IU [15]	F [16]	S [17]	Exp.	Other
$\upsilon_L \times 10^5$ (cm s^{-2})	4.544	5.171	5.180	5.207	4.765	—	—
$\upsilon_T \times 10^5$ (cm s^{-2})	2.624	2.986	2.991	3.006	2.751	—	—
$B_T \times 10^{12}$ (dyne/cm^2)	0.643	0.832	0.835	0.843	0.706	—	—
$G \times 10^{12}$ (dyne/cm^2)	0.386	0.499	0.509	0.506	0.424	—	—
ξ	0.25	0.25	0.25	0.25	0.25	—	—
$Y \times 10^{12}$ (dyne/cm^2)	0.964	1.248	1.252	1.265	1.059	—	—
θ_D (K)	332.5	378.3	379.1	380.9	348.7	—	—

Table 5. Elastic properties of $Zr_{44}Ti_{11}Cu_{10}Ni_{10}Be_{25}$ BMG.

properties. So we do not offer any concrete remark at this stage, but it is sure that this data is very useful for the further investigation.

3.2. $Zr_{52.25}$-$Cu_{28.5}$-$Ni_{4.75}$-$Al_{9.5}$-Ta_5 BMG

Here, Our well established model potential is used along with five different types of local field correction functions due to H, T, IU, F and S for to generate the pair potential for $Zr_{52.25}Cu_{28.5}Ni_{4.75}Al_{9.5}Ta_5$ BMG [4] system. **Figure 5** shows the calculated pair potential for $Zr_{52.25}Cu_{28.5}Ni_{4.75}Al_{9.5}Ta_5$ BMG [4]. It is observed that the depth of the pair potential obtained using model potential is highly affected. This depth affects the height and peak of the pair correlation functions. This pair potential is helping to compute phonon frequencies of longitudinal and transverse branch and it is shown in **Figure 6(b)**. No experimental data and other available data are found for comparison for sound velocities. So, we do not put any concert comment on sound velocity at this point.

The absence of experimental data and other information on elastic properties like bulk modulus, Poisson ratio and Debye temperature, so that, present results are compared with calculated values and other available results [5]. From the **Table 7**, it is observed that F function is in good agreement with the calculated values and other available results [5]. On the other hand,

Properties	H [13]	T [14]	IU [15]	F [16]	S [17]	Exp.	Other
$\upsilon_L \times 10^5$ (cm s^{-2})	4.347	4.942	4.954	4.954	4.561	—	—
$\upsilon_T \times 10^5$ (cm s^{-2})	2.510	2.853	2.860	2.880	2.633	—	—
$B_T \times 10^{12}$ (dyne/cm^2)	0.614	0.793	0.797	0.805	0.675	—	—
$G \times 10^{12}$ (dyne/cm^2)	0.368	0.476	0.478	0.483	0.405	—	—
ξ	0.25	0.25	0.25	0.25	0.25	—	—
$Y \times 10^{12}$ (dyne/cm^2)	0.920	1.189	1.196	1.208	1.013	—	—
θ_D (K)	322.0	366.1	367.0	368.9	337.9	—	—

Table 6. Elastic properties of $Zr_{38.5}Ti_{16.5}Cu_{15.25}Ni_{9.75}Be_{25}$ BMG.

Properties	H [13]	T [14]	IU [15]	F [16]	S [17]	Exp.	Other [5]
$\upsilon_L \times 10^5$ (cm s^{-2})	3.5505	4.0124	4.0041	4.4025	3.7471	—	—
$\upsilon_T \times 10^5$ (cm s^{-2})	2.0499	2.3166	2.3118	2.324	2.1634	—	—
$B_T \times 10^{12}$ (dyne/cm^2)	0.4879	0.6230	0.6205	0.6271	0.5434	—	—
$G \times 10^{12}$ (dyne/cm^2)	0.2927	0.3738	0.3723	0.3762	0.3260	—	—
ξ	0.25	0.25	0.25	0.25	0.25	—	—
$Y \times 10^{12}$ (dyne/cm^2)	0.7317	0.9346	0.9307	0.9406	0.8151	—	0.90
θ_D (K)	253.57	286.56	285.97	287.48	267.61	—	—

Table 7. Elastic properties of $Zr_{52.25}Cu_{28.5}Ni_{4.75}Al_{9.5}Ta_5$ BMG.

Young modulus and Shear modulus using T, IU and S local field correction functions are in good agreement with the results mention in Ref. [5].

3.3. Zr_{57}-Ti_5-Cu_{20}-Ni_8-Al_{10} BMG

Here, it has been reported for the first time to generate the pair potential for the $Zr_{57}Ti_5Cu_{20}Ni_8Al_{10}$ BMG system. The computed pair potential is shown in **Figure 7(a)** using present model potentials. In this case, the computed pair potential is affected by type of screening used. The pair potential computed using model potential shows first positive minimum. The depth of this minimum is affected by type of screening used and almost at the r value where pair potential shows a positive minimum. The computed pair potential is greatly affected by model potential.

Using a pair potential it has been projected the longitudinal and transverse phonon frequencies for $Zr_{57}Ti_5Cu_{20}Ni_8Al_{10}$ BMG are shown in **Figure 7(b)**. From the **Figure 7(b)** it is understood from the results of phonon frequencies that the nature of peak positions are not much exaggerated by different screening functions, but both the longitudinal and transverse frequencies show small deviation for H, T and S functions with respect to IU and F screening function in **Figure 7(b)**.

On the other hand, the transverse modes undergo larger thermal modulation due to the anharmonicity of the vibrations in the BMGs. In the long wavelength limit, the dispersion curves are linear and confirming characteristics of elastic waves. The PDC for transverse phonons attain maxima at a higher q value than the longitudinal phonon curve. At present calculated elastic properties for $Zr_{57}Ti_5Cu_{20}Ni_8Al_{10}$ BMG are listed in **Table 8**. From **Table 8**, one can see that by using the T, IU and F screening functions, the results are very close to one another as compared to the H screening function. Modulus of rigidity 'G', Young modulus 'Y' and Debye temperature is showing the better agreement with experimental values [5, 6] computed using the T, IU and F screening while obtains due to H and S show the underestimate values than the experimental and other available data. We are sure that this data is very useful for the further investigation.

Properties	H [13]	T [14]	IU [15]	F [16]	S [17]	Exp. [4–6]	Other [4–6]
$\upsilon_L \times 10^5$ (cm s^{-2})	3.2622	3.6125	3.6212	3.6375	3.3707	4.623	—
$\upsilon_T \times 10^5$ (cm s^{-2})	1.8834	2.0857	2.0907	2.1001	1.9461	2.149	—
$B_T \times 10^{12}$ (dyne/cm^2)	0.3867	0.4738	0.47608	0.4804	0.4125	0.992	—
$G \times 10^{12}$ (dyne/cm^2)	0.2318	0.2843	0.2857	0.2882	0.2475	0.301	0.301
ξ	0.25	0.25	0.25	0.25	0.25	—	—
$Y \times 10^{12}$ (dyne/cm^2)	0.5795	0.7107	0.7141	0.7206	0.6188	0.82	0.82
θ_D (K)	233.70	258.79	259.92	260.58	241.47	270.3	270.1

Table 8. Elastic properties of $Zr_{57}Ti_5Cu_{20}Ni_8Al_{10}$ BMG.

3.4. Zr-Al-Ni-Cu BMG ($Zr_{61.88}Al_{10}Ni_{10.12}Cu_{18}$, $Zr_{64.13}Al_{10}Ni_{10.12}Cu_{15.15}$, $Zr_{65}Al_{10}Ni_{10}Cu_{15}$)

Our well recognized model potential is used along with five different local field correction function for the generate pair potential for $Zr_{61.88}Al_{10}Ni_{10.12}Cu_{18}$, $Zr_{64.13}Al_{10}Ni_{10.12}Cu_{15.75}$ and $Zr_{65}Al_{10}Ni_{10}Cu_{15}$ BMG system. From **Figures 8(a)**, **9(a)** and **10(a)** it is observed that the study reveals the general trends of the pair potential in all cases, suggesting that the position of the first minimum depth in the pair potential in the present study is obtained due to F screening function.

Using this pair potential it has been computed the longitudinal and transverse phonon frequency for $Zr_{61.88}Al_{10}Ni_{10.12}Cu_{18}$, $Zr_{64.13}Al_{10}Ni_{10.12}Cu_{15.75}$ and $Zr_{65}Al_{10}Ni_{10}Cu_{15}$ BMG are shown in **Figures 8(b)**, **9(b)** and **10(b)** respectively. Phonon mode graphs show that the nature of peak position is not much affected by different type of screening functions. The longitudinal and transverse frequencies show deviation for H, T and S functions with respect to F screening for Zr-Al-Ni-Cu BMG systems. It is obvious from the figures that the oscillations are protruding in the longitudinal mode as compared to transverse mode, which indicates that collective excitations at larger wave vector transfer due to the dispersion of longitudinal excitation. The influence of the results of phonon frequencies is clearly observed on the elastic constants, as we have calculated these elastic constants from the long wavelength limit of phonon frequencies.

From the **Tables 9–11** it is observed that sound velocity computed using present model potential along with T, IU and F functions are found to be very close to one another and calculated sound velocities using F screening function shows a good agreement with available data [4–6]. Computed bulk modulus using model potential along with all local field correction functions is underestimated as compared to the experimental [4] and other available data [5, 6]. Presently computed percentile deviation for modulus of rigidity with respect to available data. The maximum deviation is found in F screening function, the values are 25.5, 26.9 and 6.2% for $Zr_{61.88}Al_{10}Ni_{10.12}Cu_{18}$, $Zr_{64.13}Al_{10}Ni_{10.12}Cu_{15.75}$ and $Zr_{65}Al_{10}Ni_{10}Cu_{15}$ respectively, and minimum deviation is found for in H function, the values are found 2.57 and 4.0% for $Zr_{61.88}Al_{10}Ni_{10.12}Cu_{18}$ and $Zr_{64.13}Al_{10}Ni_{10.12}Cu_{15.75}$ respectively.

Presently calculated Young's modulus and Debye temperature using local model potential along with the S screening function is found in good agreement with available results for

Properties	H [13]	T [14]	IU [15]	F [16]	S [17]	Exp. [6]	Other [6]
$\upsilon_L \times 10^5$ (cm s^{-2})	3.6701	4.1883	4.1731	4.1990	3.8565	4.693	4.704
$\upsilon_T \times 10^5$ (cm s^{-2})	2.1189	2.4181	2.4043	2.4243	2.2265	2.046	2.092
$B_T \times 10^{12}$ (dyne/cm^2)	0.4975	0.6479	0.6432	0.6513	0.5493	1.077	1.083
$G \times 10^{12}$ (dyne/cm^2)	0.2985	0.3888	0.3899	0.3908	0.3296	0.293	0.291
ξ	0.25	0.25	0.25	0.25	0.25	0.375	0.37
$Y \times 10^{12}$ (dyne/cm^2)	0.7463	0.9719	0.9649	0.9769	0.8240	0.805	0.801
θ_D (K)	263.355	300.544	299.451	301.31	276.73	0.263	262.9

Table 9. Elastic properties of $Zr_{61.88}Al_{10}Ni_{10.12}Cu_{18}$ BMG.

Properties	H [13]	T [14]	IU [15]	F [16]	S [17]	Exp.	Other [6]
$\upsilon_L \times 10^5$ (cm s^{-2})	3.6694	3.4202	4.1873	4.2100	3.8666	—	4.679
$\upsilon_T \times 10^5$ (cm s^{-2})	2.1186	2.4262	2.4175	2.4306	2.2324	—	2.079
$B_T \times 10^{12}$ (dyne/cm^2)	0.4940	0.6479	0.6432	0.6502	0.5481	—	1.066
$G \times 10^{12}$ (dyne/cm^2)	0.2964	0.3887	0.3859	0.3901	0.5481	—	0.285
ξ	0.25	0.25	0.25	0.25	0.25	—	0.37
$Y \times 10^{12}$ (dyne/cm^2)	0.7410	0.9718	0.9649	0.9754	0.8227	—	0.785
θ_D (K)	261.2	299.1	298.06	299.68	275.24	—	259.2

Table 10. Elastic properties of $Zr_{64.13}Al_{10}Ni_{10.12}Cu_{15.75}$ BMG.

Properties	H [13]	T [14]	IU [15]	F [16]	S [17]	Exp. [4–6]	Other [4–6]
$\upsilon_L \times 10^5$ (cm s^{-2})	3.3964	3.9328	3.9199	3.9440	3.6025	—	5.050
$\upsilon_T \times 10^5$ (cm s^{-2})	1.9609	2.2706	2.2632	2.2771	2.0799	—	2.393
$B_T \times 10^{12}$ (dyne/cm^2)	0.4086	0.5478	0.5443	0.5510	0.4597	1.067	1.066 1.034 1.120
$G \times 10^{12}$ (dyne/cm^2)	0.2452	0.3267	0.3265	0.3306	0.2758	0.31	0.303 0.359
ξ	0.25	0.25	0.25	0.25	0.25	—	0.35
$Y \times 10^{12}$ (dyne/cm^2)	0.6129	0.8218	0.8164	0.8265	0.6895	0.791	0.83
θ_D (K)	238.2	275.9	274.9	276.6	252.7	267	267 292.9

Table 11. Elastic properties of $Zr_{65}Al_{10}Ni_{10}Cu_{15}$ BMG.

$Zr_{61.88}Al_{10}Ni_{10.12}Cu_{18}$, and $Zr_{64.13}Al_{10}Ni_{10.12}Cu_{15.75}$ and IU function is found in good agreement with experimental as well as other available results [6]. On the other hand, the calculated values of Young's modulus and Debye temperature using model potential along with T, IU and F screening functions are found very close to each other and good agreement with the other theoretical data for Zr-Al-Ni-Cu BMG system.

4. Conclusion

The dispersion of longitudinal phonon shows oscillatory behavior for the large q values while lack of thereof in the transverse phonons. The transverse phonon frequencies increase with wave number and get saturated at the first peak of $\omega_T \rightarrow q$ curves with small variations. The $\omega \rightarrow q$ curve for the transverse phonons achieves maxima at a higher q value than the longitudinal phonon curve. The peak heights of the longitudinal as well as transverse phonon frequencies of these BMGs are nearly the same. Thus, the dispersion curves of these BMGs are found to be similar.

It is apparent from the $\omega_L \rightarrow q$ curves of the glassy materials that they are screening sensitive in the low-momentum region. The difference in $\omega \rightarrow q$ relation begins right from the starting value of q and it's becomes maximum at the first peak of the $\omega_L \rightarrow q$ curve, again, it tends to decrease and both $\omega_L \rightarrow q$ relations seem to converge at the first minima of the $\omega_L \rightarrow q$ curve. The position of the first peak is independent of the screening functions. However, the height of the peak strongly depends on the type of screening employed in the present calculations. The phonon dispersion curve for the Zr-based bulk metallic glasses computed using the IU and F function give higher numerical values than other local field correction functions. Using H-function give the lowest values for the Zr-base bulk metallic glasses. Agarwal has done the longitudinal and transverse modes for the Zr-Ti-Cu-Ni-Be for three different concentrations using the BS-Method. When compared with our present approach, it is found that model potential gives underestimated results.

Presently calculated elastic properties for BMGs are listed in **Tables 2–11**. It is observed that the computed elastic properties using model potential are in excellent agreement with experimental and other available theoretical data. Among the five different screening functions T, IU and F functions show good agreement for present model potential. While due to H screening function than the other LFCF and computed values using S lying between the F and H screening function. For Zr-Ti-Cu-Ni-Be, Zr-Cu-Ni-Al-Ta, Zr-Ti-Cu-Ni-Al and Zr-Al-Ni-Al BMGs at different concentrations computed using model potential, it is observed that ν_l and ν_t, Young modulus, modulus rigidity, Debye temperature using the T, IU, F and S local field correction functions show the very good agreement with experimental and other available data. The Zr-based BMGs are observed that the present results obtained due to T, IU and F screening functions are in good agreement with available with other data. Present study clearly reveals that proper description of local field correction function is required for the study of phonon modes of bulk metallic glasses.

Overall, we stated that the phonon dispersion curve generated from the HB approach reproduces satisfactorily the general characteristic of dispersion curves. The well recognized Model potential along with IU, Farid et al. [F] and Sarkar-Sen et al. [S] local field correction functions generates consistent results. Hence, our Model-1 potential is suitable for the studying the phonon dynamics of bulk metallic glasses.

Author details

Punitkumar Harshadbhai Suthar

Address all correspondence to: sutharpunit@rediffmail.com

Department of Physics, CU Shah Science College, Ahmedabad, Gujarat, India

References

[1] Klement W, Willens RH, Duwez P. Non crystalline structure in solidified Gold-Silicon Alloy. Nature. 1960;**187**:869

[2] Johnson WL. Crystal to glass tranformation in metallic material. Progress in Materials Science. 1986;**30**:81

[3] Grrer AL. Metallic glasses. Current Opinion in Solid State & Materials Science. 1997;**2**:412

[4] Wang WH, Dong C, Shek CH. Bulk metallic glasses. Materials Science & Engineering R: Reports. 2004;**44**:45

[5] Wang WH. Correlation between elastic moduli and properties in bulk metallic glasses. Journal of Applied Physics. 2006;**99**:093506

[6] Wang WH. The elastic properties, elastic models and elastic perspectives of metallic glasses. Progress in Materials Science. 2012;**57**:487

[7] Hui X, Fang HZ, Chen GL, Shang SL, Wang Y, Liu ZK. Icosahedral ordring in $Zr_{41}Ti_{14}Cu_{12.5}Ni_{10}Be_{22.5}$ bulk metallic glass. Applied Physics Letters. 2008;**92**:201913

[8] Agarwal PC. Phonon dispersion in Zr-Ti-Cu-Ni-Be bulk metallic glasses. Physics B. 2006; **381**:239

[9] Perker A, Johnson WL. A highly processable metallic glass: $Zr_{41}Ti_{14}Cu_{12.5}Ni_{10}Be_{22.5}$. Applied Physics Letters. 1993;**63**:2342

[10] Jonson WL. Bulk Glass-Forming Metallic Alloys: Science and Technology. MRS Bulletin. 1999;**24**:42

[11] Bhatia AB, Singh RN. Phonon dispersion in metallic glass - A simple model. Physical Review B. 1985;**31**:4751

[12] Habbard J, Beeby JL. Collective motion in liquids. Journal of Physics C. 1971;**45**:331

[13] Harrison WA. Pseudopotential in the Theory of Metal. New York: W A Benamin Inc; 1966

[14] Taylor R. A simple, useful analytical form of static electron gas dielectric function. Journal of Physics F. 1981;**8**:1699

[15] Ichimaru S, Utsumi K. Analytic expression for the dielectric screening function of strongly coupled electron liquid at metallic and lower densities. Physics Review. 1978;**24**:3220

[16] Farid B, Heine V, Engel GE, Robertson IJ. Extremal properties of the Harris-Foulkes functional and improved screening caluation for the electron gas. Physical Review B. 1993; **48**:11602

[17] Sarkar A, Sen DS, Roy HD. Static local field factor for Dielectric screening function of electron gas at metallic and lower densities. Modern Physics Letters. 1998;**12**:639

[18] Takeno S, Goda M. A Theory of phonon-like excitations in non-crystalline solids and liquids. Progress in Theoretical Physics. 1971;**47**:790

[19] Jani AR, Gajjar PN, Patel HK. Suceptibility of some simple metals by local pesudopotentials. Physica Status Solidi B. 1991;**105**:169

[20] Thakor PB, Gajjar PN, Jani AR. Structure of some at Rare-Earth liquid metals - A charged hard sphere approach. Communications in Mathematical Physics. 2004;**14**:15

[21] Thakore BY, Gajjar PN, Jani AR. Collective modes in $Ca_{70}Mg_{30}$ Glass. Bulletin of Materials Science. 2000;**23**:5

[22] Suthar PH. Study of certain physical properties of some alkaline earth metals, some transition metals and their alloys and bulk metallic glasses using pseudopotential theory. [PhD thesis]. Sardar Patel University; 2012

[23] Thakore BY, Khambholja SG, Suthar PH, Bhatt NK, Jani AR. Collective modes and elastic constants of liquid $Al_{83}Cu_{17}$ binary alloy. Chinese Physics Letters. 2010;**27**(9):096203

[24] Suthar PH, Gajjar PN, Thakore BY, Jani AR. Study of phonon modes and elastic properties of $Sc_{36}Al_{24}Co_{20}Y_{20}$ and $Gd_{36}Al_{24}Co_{20}Y_{20}$ bulk metallic glasses. Journal of Physics: Conference Series. 2013;**423**(1):012030

[25] Suthar PH. Phonon dispersion relation of Mg-Cu-Gd bulk metallic glasses. AIP Conference Proceedings. 2016;**1728**:020599

Section 2

Superconductor, Phononic Crystal and Nanotube Devices

Chapter 5

Phonon Dispersions as Indicators of Dynamic Symmetry Reduction in Superconductors

Jose A. Alarco and Ian D.R. Mackinnon

Additional information is available at the end of the chapter

http://dx.doi.org/10.5772/intechopen.79216

Abstract

Strong correlations between phonon energies and superconducting transition temperatures can be extracted from phonon dispersion calculations using density functional theory for a range of superconducting materials. These correlations are robust and consistent with experimental data for key external conditions including isotope effects, elemental substitutions and pressure variations. Changes in the electronic band structure also correlate with transitions to/from superconductivity but, in general, are less sensitive and less obvious than phonon behaviour. A computational approach that considers both phonons and electrons and the presence or absence of a phonon anomaly works well for conventional superconducting materials with hexagonal, cubic or tetragonal symmetries. Superconductivity in these compounds often involves symmetry reduction in an original non-superconducting parent compound induced, for instance, by substitution or by a dynamic reduction in symmetry shown in electron density distributions and Raman spectra. Such symmetry reduction is effectively modelled with super-lattice constructs which link Raman spectra with key superconducting parameters.

Keywords: density functional theory, metal diboride, electronic band structure, phonon dispersion, phonon anomaly, Raman spectroscopy, superlattice, superconductivity, transition temperature, deformation potential, Fermi level

1. Introduction

When distant neutral atoms are brought together, they eventually come close enough to form solids. As the atoms approach, the initial gas-like behaviour of the neutral atoms, changes to a correlated atomic liquid-like behaviour first, and then, to more organised collective movements in the periodic, or aperiodic, solid. In a periodic solid, the electrons involved in the

ionic cores of the atoms retain much of their localised structure pertaining to their original neutral atoms, but the outer valence electron orbitals begin to overlap, forming bonds that stabilise the structure, if the right conditions are met [1]. Valence electrons also provide conduction electrons that can move around in the case of metals, and essentially, regulate overall collective behaviour [2]. In a metal, the valence electrons now become the entities with gas-like behaviour, following the Fermi-Dirac statistics for particles with spin ½ [3], instead of Maxwell-Boltzmann statistics [4].

The gas of valence electrons is not static and neutral; and is, in fact, more like a plasma, capable of collective motion to shield out variations in electrostatic potential caused by the motion of ions [5]. This behaviour is evident when the Born-Oppenheimer approximation is valid; a fundamental concept in density functional theory (DFT) [6, 7]. In this approximation, the positions or distributions of these outer electrons adjust very quickly in response to any ionic core movements [3, 8]. Furthermore, on the basis of Fermi-Dirac statistics and the exclusion principle, most of the electrons under the influence of external fields remain in the same states. Only a small fraction in the thermal layer (with energy k_BT from the Fermi energy E_F, where k_B is equal to the Boltzmann constant) are free to move [5], provided these electrons can find empty states to move to and that energy and momentum conservation laws are fulfilled.

1.1. Valence electrons

The movement of nearly free valence electrons in a metallic solid is generally well described by Bloch waves, which invoke periodicities in the crystal lattice. Again, this assertion is particularly true for systems subject to the Born-Oppenheimer approximation. The collection of energies of allowed quantized Bloch states is grouped together in the *electronic band structure*, which correspond to the solutions of Schrodinger's equation typically displayed in reciprocal space as a function of the wave vector k [3, 9]. Similarly, the equations for atomic or ionic core movements can be solved for the vibrational (or phonon) states and the allowed frequencies are grouped together in the *phonon dispersion*. In order to differentiate vibrational states from electronic states, the former and the latter are typically labelled with q and k, respectively. However, both q and k have the same formal periodic properties [9].

In the case of silicon or diamond, which have a two-atom basis in the lattice, or for more complex compounds with different atomic species, acoustic and optic branches evolve [3, 10]. The difference between acoustic and optic branches in phonon dispersions, particularly in monoatomic cases such as silicon or diamond, is quite similar to the difference between bonding and antibonding states in the electronic spectrum [9]. The frequencies in the phonon dispersion are related to the interatomic bonding forces or energies, and when the calculated phonon dispersions contain negative frequencies (or not), this can be considered an indicator of dynamic or structural stability or instability [7, 11, 12]. This indicator is particularly useful for analyses of situations that are difficult to replicate in the laboratory, such as for solids at very high pressures [7].

The Born-Oppenheimer approximation allows for the separation of variables in the equations of movement for electrons and for ionic cores [3, 8], and gives distinct electronic band structures and phonon dispersions. However, the two concepts are not completely independent, particularly for superconducting solids, such that the *electron–phonon interaction* often should be considered [3]. An electron–phonon coupling is dependent on the density of states in

proximity to the Fermi energy and is relatively strong for electronic bands with a high density of states adjacent to the Fermi energy [13]. Such coupling is important for explanations of a wide range of physical properties, including superconductivity [3] and especially that of the conventional Bardeen-Cooper-Schrieffer (BCS) type [14].

1.2. Lattice dynamics

Atoms in a crystal lattice participate in two types of oscillations of different nature [2]: (i) thermal oscillations, for which amplitudes and energy change with temperature become zero at T = 0 K; and (ii) zero oscillations, which exist even at T = 0 K and are of quantum mechanical origin related to Heisenberg's uncertainties. If the amplitude of zero oscillations are commensurate with the mean distance between atoms, then a crystalline structure cannot be formed at normal pressure, even at T = 0 K, and the substance will remain liquid [2]. Another important subset of the thermal oscillatory motion is given by the Debye temperature, Θ_D, which is determined by the ratio between the thermal and the bonding energies. At low temperatures (below Θ_D), the bonding energy promotes the coordinated motion of atoms and only the low frequency lattice waves are excited, while at higher temperatures (above Θ_D) the movement is more chaotic and all lattice waves are excited. In both cases, the equilibrium positions remain approximately in the same places [2, 15]. The concept of a high Θ_D has played a significant role in the historical understanding of superconductivity [16].

Raman spectroscopy of crystalline solids is one of the techniques that can provide direct estimates of the electron–phonon interactions, where an incident, monochromatic laser beam excites electrons, and as a result of interactions that are, in general with phonons, an inelastically scattered beam with a shifted frequency or wavenumber is detected. The Raman activity of phonon modes can be determined with reference to group symmetry analyses for the periodic crystal [10, 17]. Although, in fact, the structure of a crystalline compound is not strictly periodic in each given instant of time because of the oscillating motion of ions [2].

DFT offers the capability to calculate electronic bands and phonon dispersions with great accuracy and, more recently, within viable computation time given rapid progress with software codes and computer hardware. As a result, DFT is now an essential tool to assist with interpretation of experimental results. With continued success and more rigorous agreement between experimental and calculated results, DFT is now established as a reliable tool for accurate prediction of material properties. Furthermore, DFT is an effective computational technique for *ab initio* prediction of a new material's stability and of the potential to engender key properties such as superconductivity.

Of perhaps greater importance is the potential to predict the superconducting transition temperature, T_c, in anticipation of experimental measurement. We will demonstrate that this capacity is inherent in the fundamental attributes of DFT and that the practice is readily applied. We will use examples of existing materials to demonstrate the approach and provide reference to predicted "new superconducting materials" that are yet to be synthesised. Determination of a value for T_c is not only important to minimise the disappointment of synthesising an infertile haystack to find the elusive needle but also to plan for practical evaluations of superconducting applications. However, perhaps of even greater significance is the exceptional value of insight into the mechanisms and underlying interactions from which superconductivity emerges [18, 19].

For simple structures, the Eliashberg theory—modified via the McMillan or Allen-Dynes equations—determines T_c from electron–phonon couplings using normal state parameters [20] reasonably well. Given this, it should be possible for standard DFT models to provide all the necessary superconducting characteristics of a material from a knowledge of the crystal structure. In this chapter, we explore how Raman spectroscopy can reveal the dynamic symmetry of superconducting materials, and how consideration of lower symmetry superlattice modes provides clues to materials behaviour. We will show how the energy of key phonon modes shows strong correlation with the value of T_c for MgB_2, the archetype superconducting metal diboride, as well as for compositional analogues in the symmetry group.

2. MgB_2: unique characteristics

Magnesium diboride, MgB_2, is an electron–phonon coupled BCS-type superconductor with the highest superconducting transition temperature T_c for this structure type at ~40 K [21]. The material is a simple compound with only three atoms (two boron and one magnesium) in an hexagonal unit cell with P6/mmm symmetry and lattice parameters a = 3.086A and c = 3.524A [21, 22]. This simple structure with atoms in the second row of the Periodic Table and extensive microstructural and physical property characterisation, makes MgB_2 ideal for DFT calculations that can be experimentally validated [23, 24].

A wide variety of microstructural, chemical and physical properties of MgB_2 have been thoroughly investigated and the reader is referred to example review papers on the topic [24]. Investigations on MgB_2 include studies using high quality crystals and polycrystalline materials, on isotopic effects ([25, 26], and references there in), on hydrostatic pressure effects ([11, 27, 28], and references there in), on a variety of metal substituted forms ([29–33], and references there in), and other similar structures that do not superconduct or that have T_c values different to MgB_2. This significant body of work presents experimental data that can be compared with outcomes from DFT calculations [11, 19, 25, 29, 30, 34, 35] and provides validation of structure–property interpretations. **Figure 1** displays a schematic of the MgB_2 structure emphasising the layered nature of the compound.

2.1. Electronic properties

Figure 2a displays the electronic band structure (EBS) of MgB_2 along representative reciprocal space directions for the P6/mmm group symmetry, for the reduced Brillouin zone scheme [9, 36]. The EBS of MgB_2 contains two characteristic approximate parabolas centred at **Γ**, with a common vertex at about 0.4 eV above the Fermi energy, inverted and with different curvatures each of which represents different effective masses (see **Figure 2a**). These parabolas correspond to the σ heavy and light hole bands along the **Γ–K** and **Γ–M** reciprocal directions and are associated with electronic conduction or metallic behaviour in the plane of the boron atoms [37, 38]. Two parallel degenerate lines with low dispersion along the **Γ–A** direction, also associated with the σ bands, is another characteristic feature of the MgB_2 EBS. These σ bands are known to couple strongly with the important E_{2g} vibration modes that correspond to in-plane B–B atom movements and are key to superconductivity in MgB_2. Other bands, not identified as σ bands, are primarily π bands and relate to three-dimensional movement of electrons [37, 38].

http://dx.doi.org/10.5772/intechopen.79216

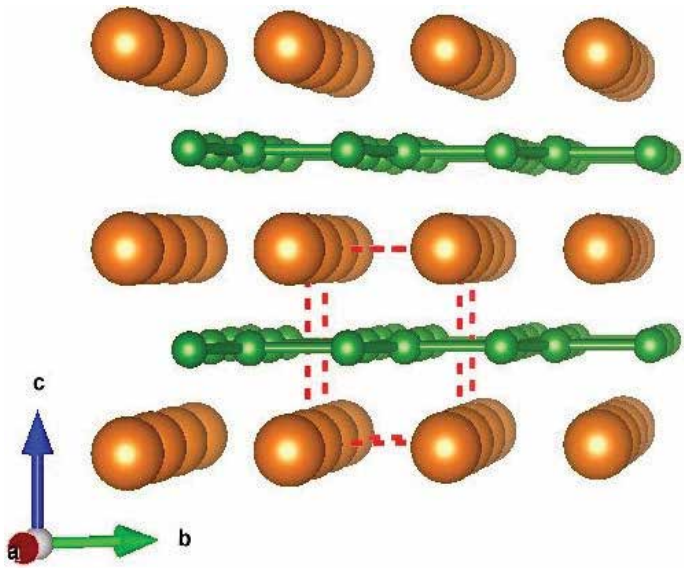

Figure 1. Schematic of the MgB_2 crystal structure in perspective view showing the layered nature of the compound. Metal atoms are gold colour and boron atoms are green; red dotted lines outline a unit cell.

The σ band parabolas at **Γ**, after folding from the extended Brillouin zones back into the reduced zone scheme are identified schematically in **Figure 2a** as red and blue lines. This folding of one suite of bands around **Γ** is exemplified in **Figure 2a** as extended orange dotted lines and, for more generic bands, is recognised in a number of key publications [39, 40]. The nature of these bands, and the observation that after folding the bands are nearly full, is a strong indication that the Fermi energy is large (compared with other AlB_2-type structures) and that valence electrons associated with these bands completely fill the first Brillouin zone.

The coexistence in MgB_2 of inverted, approximate parabolic σ bands and low dispersive bands in the **Γ–M** and **Γ–A** directions, respectively, results in approximately coaxial, parallel σ warped tubes for the Fermi surface when represented in the reduced zone scheme and as shown in **Figure 2b**. These parallel tubes correspond to hole carriers, that is, outside and inside are filled and empty, respectively, with electrons. This creates an inter-tubular volume in the reduced zone scheme, which is filled with respect to the inner tube and empty with respect to the outer tube [35]. This concept is awkward for physical interpretation in reciprocal, let alone real, space and can be more easily reconciled by assuming an extended zone scheme with separate inner or outer diameter tubes at alternating and adjacent reciprocal space points [11, 35]. Thus, the nature of the Fermi surface in MgB_2 with parallel sections in close proximity intrinsically implies resonant behaviour of electrons and phonons.

Calculating the difference in kinetic Fermi energies for the adjacent σ bands, using the respective Fermi vectors and effective masses, results in a value of phonon energy equivalent to approximately twice the energy gap of MgB_2 [38]. Such an energy gap corresponds to a frequency approximating 1/5, or 20%, of the frequency of the E_{2g} mode [25, 34]. This value of vibration frequency is a Raman active mode (after folding the Brillouin zone boundaries to the **Γ** point) for a reduced P6/mmm symmetry for MgB_2 (e.g. the space group $P6_3mc$). A reduced

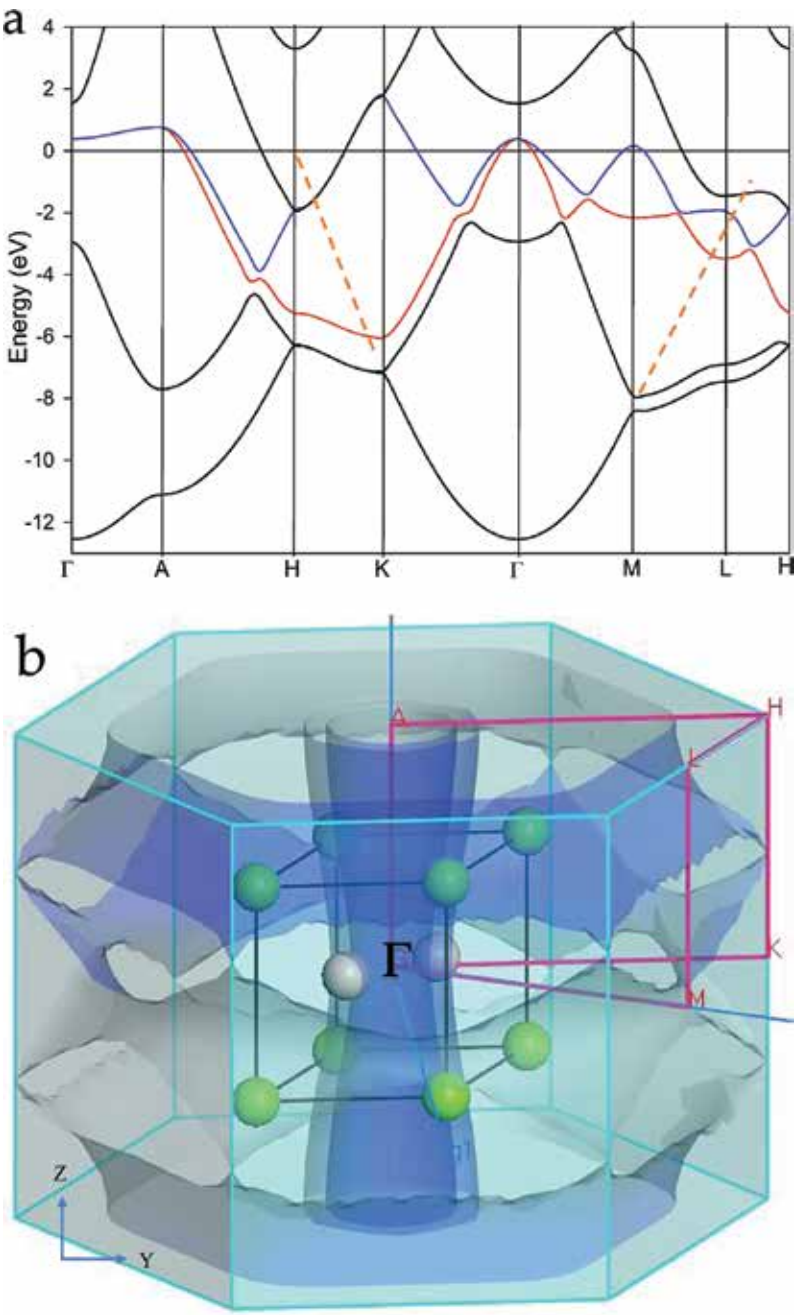

Figure 2. DFT calculated features of MgB_2 using the LDA functional and $\Delta k = 0.02A^{-1}$ showing (a) EBS highlighting the two characteristic parabolas (red and blue lines) centred around **Γ**. The folded nature of the parabolic σ bands identified by the orange dotted lines is discussed in the text; (b) a section of the Fermi surface showing tubular σ surfaces (light and dark blue) vertical segments coaxial with the *c*-axis.

symmetry configuration is readily represented by a superlattice along the *c*-axis direction [34]. Such low frequency vibrations have been observed in experimental Raman spectra of MgB_2 ([34], and references there in) which also varies commensurate with the isotope effect [25].

2.2. Vibrational properties

Figure 3 displays the calculated phonon dispersion (PD) for MgB_2 at atmospheric pressure (0 GPa hydrostatic stress). The PD branches for optical phonons are labelled at the **Γ** point. The important E_{2g} modes intersect the **Γ** point at about 550 cm^{-1} wavenumber. The "W shaped" region around the E_{2g} mode at **Γ** below the highest adjacent frequency B_{1g} is called a *phonon dispersion anomaly*. This feature was originally described by Kohn [41] after whom it is named and, for MgB_2, verified experimentally using inelastic X-ray scattering (IXS) [42, 43]. Hence, this "W shaped" feature is not an artefact of the DFT calculations.

As we will indicate later, there are important relationships between features in the EBS and PD of MgB_2 that are perhaps critical to the "tuning" of a structure to induce or enhance superconductivity. We show that the Kohn anomaly is an indicator of superconductivity in—to date—BCS materials [11, 19, 25, 29, 30, 34, 35]. Other features may also be important indicators of resonant behaviour. For example, we note above that the two characteristic parabolas centred at **Γ** show a common vertex at ~0.4 eV above the Fermi energy (**Figure 2a**). In the PD, the Kohn anomaly is also centred at **Γ** with degenerate E_{2g} modes. Of further interest, two other parabolas centred on **A** and **M** above the Fermi level in the EBS also show degenerate E_{2g} modes at the same reciprocal lattice boundaries in the PD. These characteristics imply, *a priori*, that symmetry plays a role in the real space moderation, or distribution, of electrons and phonons in superconducting materials.

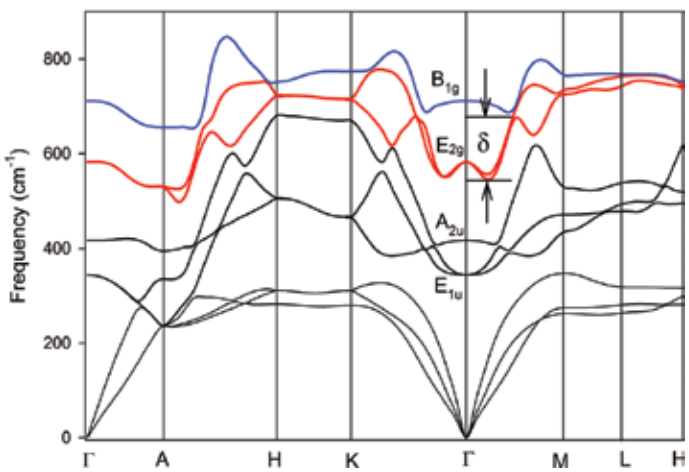

Figure 3. DFT calculated phonon dispersion for MgB_2 at atmospheric pressure. The parameter δ is an important indicator of the phonon anomaly thermal energy.

A temperature, T_δ can be extracted from measurement of the depth of the anomaly (i.e. a value in cm^{-1} for δ in **Figure 3**) [29, 30, 34]. The value for T_δ is strongly correlated with the superconducting transition temperature T_c. The correlation is robust and consistent with experiments under a wide range of external conditions including isotopic [25, 34] and metal substituted compositions of MgB_2 [29, 30], a wide range of hydrostatic pressures [11] as well as for isostructural compounds in the silicate system [30]. In addition, for MgB_2 we have shown that the depth of the anomaly is strongly correlated to the inter-tubular Fermi surface volume [11, 35] and to electron density variations along B–B bonds in response to movement of B atoms linked to the dominant E_{2g} vibration modes [35].

To model phonon dispersions, a practical computational consideration is that the virtual crystal approximation (VCA) is not implemented for plane waves in Materials Studio CASTEP [44]. Therefore, an alternative to representation of atom substitutions in a reduced unit cell structure is to use larger unit cells with substituent atoms in respective proportions. This approach results in a need to construct superlattices to describe metal substitution in MgB_2, albeit the principle may apply to many layered structures.

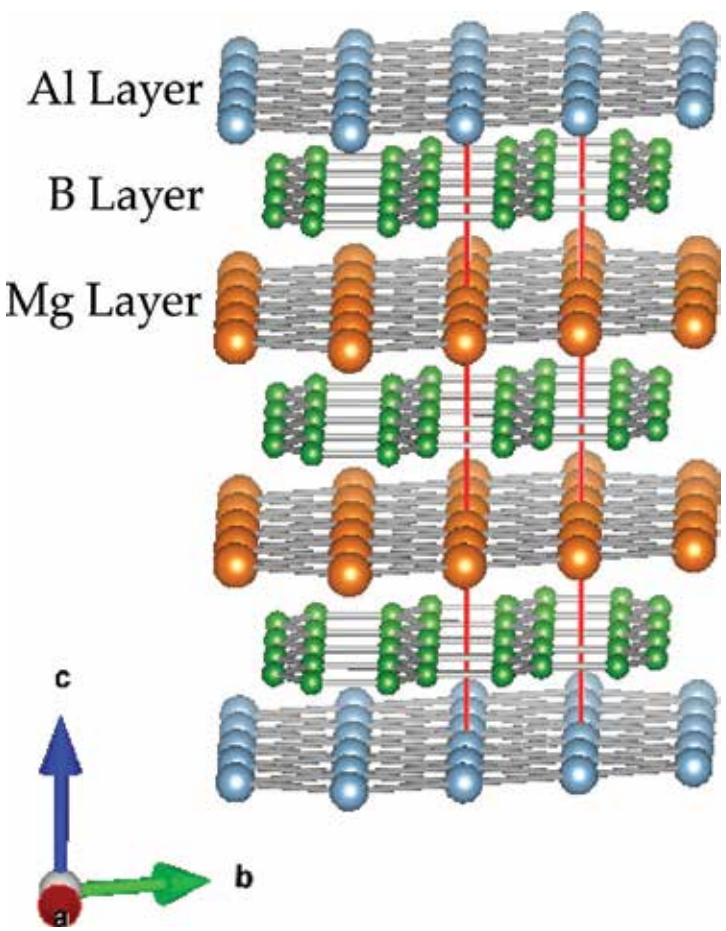

Figure 4. Superlattice construct for Mg_2AlB_6 (Mg:Al::2:1) representing $Mg_{0.67}Al_{0.33}B_2$.

For Al-substituted MgB_2, superlattices in the *c*-axis direction are well described using a range of diffraction and microscopy techniques [29, 45–47] (and references therein). Thus, we use superlattice constructs to describe intermediate compositions of metal-substituted MgB_2 to configure models for band structure and phonon dispersion DFT calculations. **Figure 4** shows a schematic of a superlattice for 0.33 atoms of Al substitution per Mg atom in MgB_2. This principle of a superlattice construct is also used for all other types of metals substituted into the MgB_2 structure in the examples to follow. This approach, when combined with a converged PD calculation, presents an *a priori* validation of potential for phase stability of the specific composition. However, this validation does not infer solubility of the substituted metal in the MgB_2 structure [30].

3. Transition metal diborides

As noted in Section 2, the electronic band structure and phonon dispersion of MgB_2 display unique characteristics that are not necessarily present in other metal diborides except for some metal substituted variations of MgB_2. We will now compare fundamental characteristics of MgB_2 with other diborides containing metal atoms with different valence states and orbital characteristics. **Figure 5** shows the region of the Periodic Table we systematically investigate using DFT calculations of both electronic band structures and phonon dispersions. In this

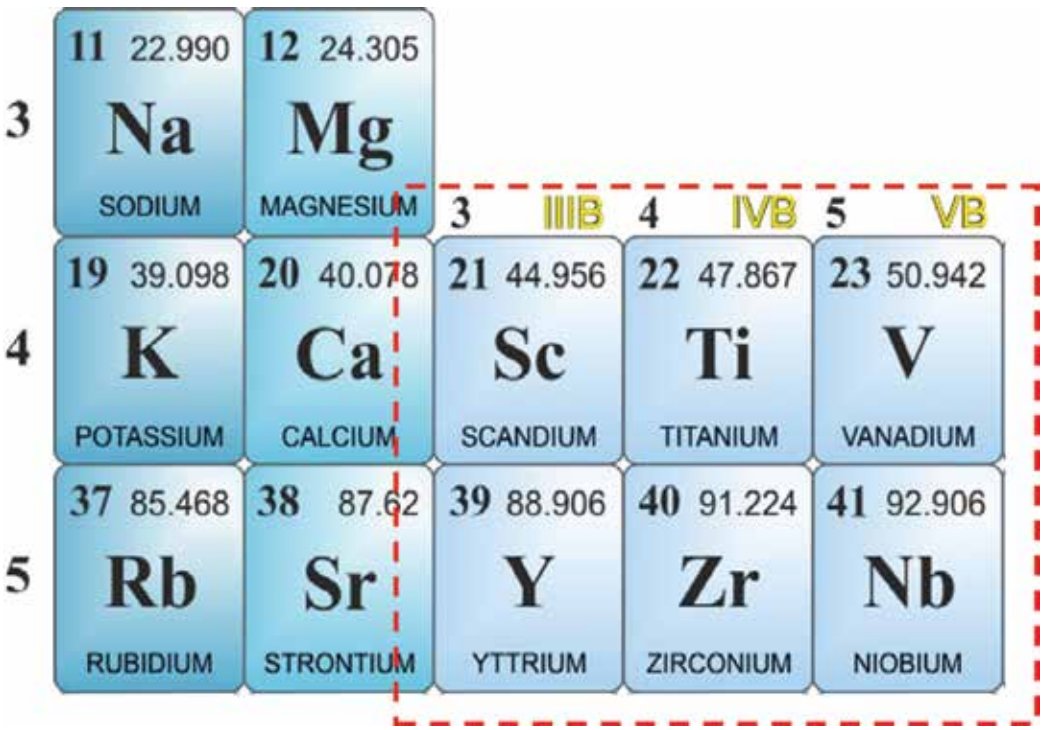

Figure 5. Region of the periodic table with low atomic number transition metals (dotted red outline) investigated using DFT calculations of electronic bands and phonon dispersions.

analysis, we evaluate similarities and differences to MgB_2, in order to identify parameters that control the unique features of superconductivity in MgB_2.

3.1. Row 4 diborides

Figures 6 and **7** display the DFT calculated EBS and PD for the transition metal elements (Z = 21–23; Z = 39–41) identified in **Figure 5**. Of the transition metal diborides shown in **Figures 6** and **7**, ScB_2 shows the most prospective resemblance to MgB_2 albeit with substantially reduced features. Both PDs display depressions or anomalies in their E_{2g} branches near **Γ** from which temperatures can be extracted and correlated with a corresponding T_c [29, 30, 34]. The anomalies derive from co-existing heavy and light effective masses for approximate inverted parabolas in key sections of their EBS. These inverted parabolas are centred above the Fermi level at **Γ** for MgB_2. However, for ScB_2 the inverted parabolas at **Γ** are below the Fermi level yet degenerate bands of an inverted parabola format are also centred at **A**. In addition, the order of optical modes in the PD is different in ScB_2 compared to MgB_2 with the E_{2g} modes at the highest frequency.

This apparent discrepancy in behaviour compared with MgB_2 can be reconciled by considering the signs of the relevant orbitals and their likely contribution to hybrid bonding between boron and the metal atoms along the *c*-direction. Metals in a higher row, including Sc, Ti and V, provide valence electrons from d orbitals while in MgB_2, p orbitals are predominant. While the lobes of p orbitals have opposite signs, those of d orbitals have the same sign. Thus, while hybridization of pure p orbitals in MgB_2 produces a periodic pattern of orbitals in a single unit cell, hybridization of mixed p and d orbitals in ScB_2 requires a double supercell to establish an appropriate periodic orbital pattern.

3.2. Row 5 diborides

As shown in **Figure 7**, the EBS for YB_2 is similar to that shown in **Figure 6** for ScB_2; in particular, the configuration of heavy and light effective masses above the Fermi level at the boundary point **A**. Note also, that as with ScB_2, bands at **Γ** in the EBS are below the Fermi level. A similar evaluation of the respective d orbital contribution to hybrid bonds as noted for ScB_2 may also apply to YB_2. However, the PD in **Figure 7b** does not clearly show an anomaly, but rather displays overlap between two E_{2g} branches; one of which is concave and the other convex in the **Γ–M** and **Γ–K** directions. The reason for this difference in PD between YB_2 and ScB_2 is unclear but may be due to insufficient Δk grid resolution [13]. In addition, the calculation for YB_2 determines a Fermi energy of −1.62 eV, which is often referred to an average zero-point in the interstitial space and may indicate large vacuum regions in the unit cell [48]. Nevertheless, these DFT calculations for YB_2 suggest potential for constructive moderation of conduction properties by conventional materials methods including metal substitution or application of pressure.

Other metal diborides, such as VB_2, TiB_2, ZrB_2 and NbB_2, do not display co-existing light and heavy effective mass σ bands that intersect the Fermi level in their EBS. Therefore, approximately parallel Fermi surfaces and important deformation potentials, which are strongly linked to the superconductivity in MgB_2 and in other compounds, cannot be defined in these

http://dx.doi.org/10.5772/intechopen.79216

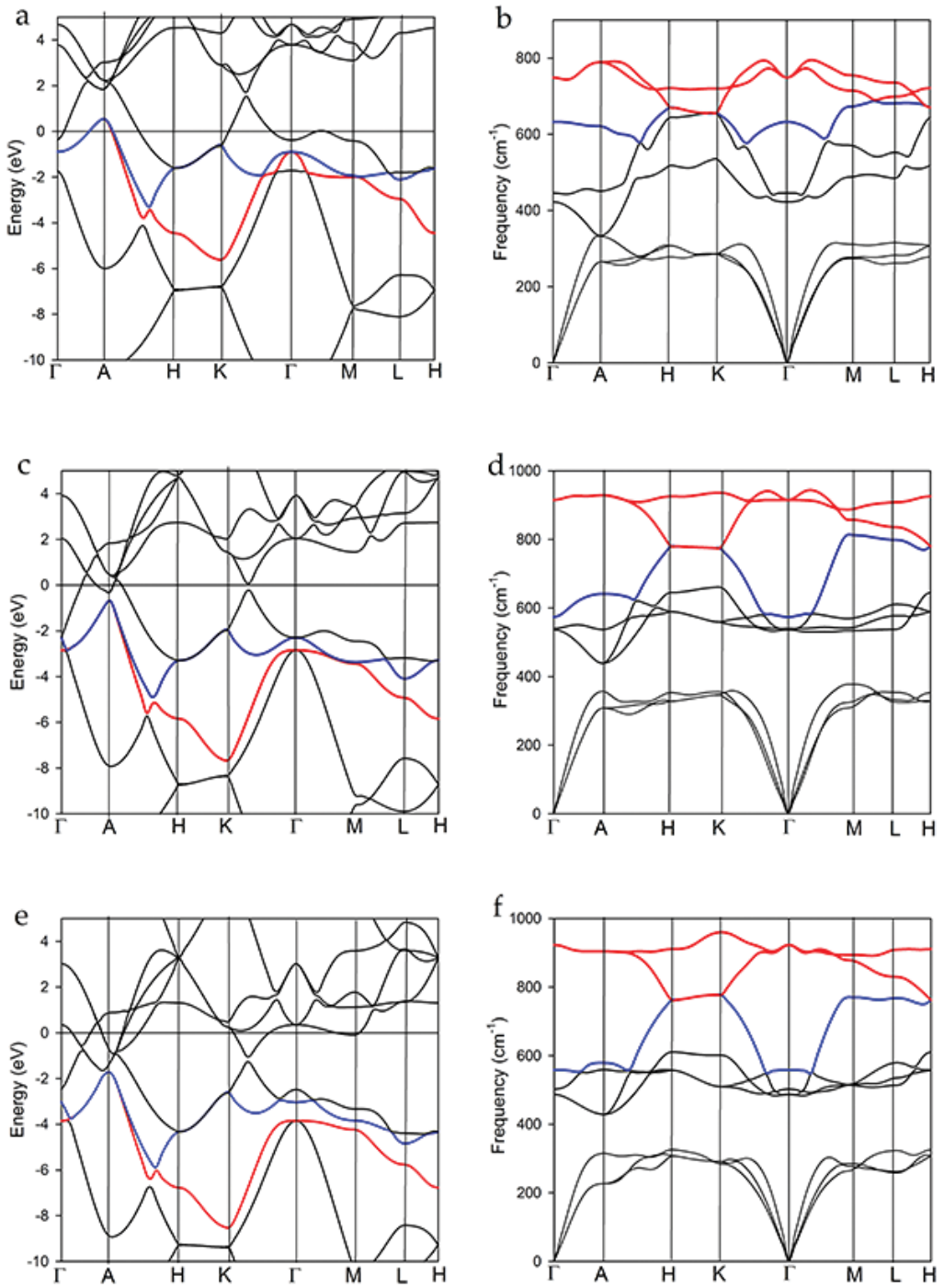

Figure 6. DFT calculated electronic bands and phonon dispersions for the first 3d transition metal diborides. **(a)**, **(c)** and **(e)** shows EBS for ScB_2, TiB_2 and VB_2, respectively, in which the two parabolic bands similar to the σ bands of MgB_2 are identified as red and blue lines; **(b)**, **(d)** and **(f)** shows PDs for ScB_2, TiB_2 and VB_2 respectively, in which E_{2g} (red) and B_{2g} (blue) phonon modes are identified.

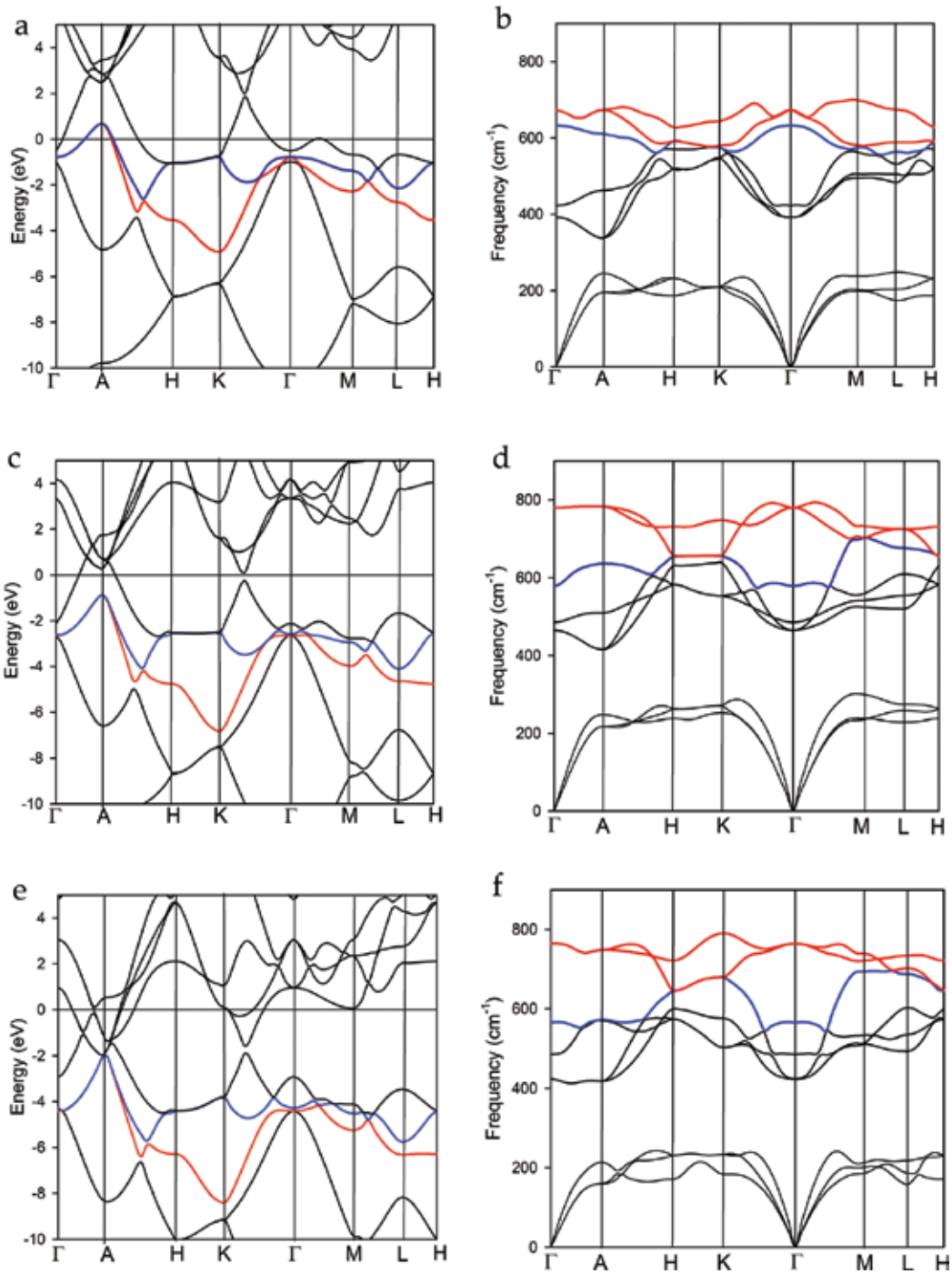

Figure 7. DFT calculated electronic bands and phonon dispersions for the first 4d transition metal diborides. **(a)**, **(c)** and **(e)** shows EBS for YB_2, ZrB_2 and NbB_2, respectively, in which the two parabolic bands similar to the σ bands of MgB_2 are identified as red and blue lines; **(b)**, **(d)** and **(f)** shows PDs for YB_2, ZrB_2 and NbB_2 respectively, in which E_{2g} (red) and B_{2g} (blue) phonon modes are identified.

cases. Therefore, these compounds are unlikely to be superconducting without some modification (e.g. element doping or substitution) and do not display anomalies in their phonon dispersions. Such modification to the structure type, for example, adding boron to form $NbB_{2.5}$ [49], or substituting other elements, such as in $Zr_{1-x}V_xB_2$ [50–52] or $Zr_{1-x}Nb_xB_2$ [53] leads to superconductivity; as also suggested by Pickett et al. [54] based on DFT calculations of AlB_2-type structures. These minor modifications to the stoichiometry of an MB_2 structure are excellent examples of "fine-tuning" that achieves a dramatic change in material property. We surmise that this fine-tuning would be manifest in the EBS as coexisting σ bands shifting to above the Fermi level and the appearance of a Kohn anomaly in a PD centred around **Γ**.

3.3. Diboride fine tuning

Strategic utilisation of DFT models allows snapshots of dynamic electron interactions in solids. An and Pickett [55] used DFT to determine deformation potential—or the energy required to break the degeneracy of σ electronic bands per unit length of inter-bond distances—in superconductors. This work also showed that for MgB_2, the E_{2g} phonon modes are of greater significance for superconductivity than other optical phonon modes in this structure; confirming many other experimental studies at the time. To utilise this approach, the electron density (ED) distributions of relevant bonds are determined at discrete steps of atom displacements along a bond direction. The computational technique requires calculation of the EBS for a particular frozen atom configuration with due consideration of symmetry conditions invoked by the displaced atom positions [35]. For MgB_2, the structure affords an uncommon opportunity to evaluate deformation potentials along the direction(s) of the E_{2g} mode which parallel the B–B bonds in the *a*-*b* plane.

As boron atoms are displaced from their equilibrium positions, a degeneracy at the vertex of the inverted σ band parabolas is broken and a deformation potential is created [55]. A critical displacement is identified where the lower effective mass σ band becomes tangential to the Fermi level. At this point, the σ band becomes filled and can no longer take part in electron transitions between the heavy and light σ bands. Thus, coherency is lost and superconductivity is destroyed [35]. An example of this condition is shown in **Figure 8a** in which the EBS for atom displacement, $D_x = 0.006$ (or a change of ~3.5% of the bond length after converting from fractional values of the *a*-lattice parameter) along the E_{2g} mode is shown compared with the equilibrium positions (blue lines) for boron atoms in MgB_2 [35]. **Figure 8b** shows the region around **Γ** in greater detail depicting the relative shift of each band and the loss of degeneracy with atom displacement.

The PDs for models of deformation potential for diboride structures show corresponding shifts in the phonon anomaly with displacement of atoms along the E_{2g} mode directions [35]. **Figure 8c** and **d** shows a partial PD for the **Γ–K** and **Γ–M** orientations of MgB_2 at equilibrium and at $D_x = 0.006$ relative displacement of boron atoms from equilibrium. At the critical displacement (**Figure 8d**), the E_{2g} mode is similar in energy to the B_{2g} mode, as if the total (temperature or kinetic) energy associated with the anomaly has been stored into deformation potential energy. In addition, the E_{2g} modes are clearly non-degenerate in these orientations, including **Γ**, for atom displacement $D_x = 0.006$ (**Figure 8d**). The difference in Fermi energies between the critical displaced position and the equilibrium position also shows a strong correlation with the superconducting energy gap [35].

The bond charges, which are highly localised along the covalent bond positions, display modulations which can be interpreted as superlattices of dynamic charge distribution [35]. Because the charge that is transferred between bonds is a fraction of the total bond charge, the superlattice modulation is subtle and may not be resolved by conventional diffraction techniques that typically reflect average models of atomic structures. Higher intensity and/or resolution probes, such as synchrotron radiation and time resolved experiments, may be required to detect these subtle modulations of charge distribution.

ScB_2 shows features in the PD that suggest superconductivity occurs at low temperature (**Figure 6b**) and experiment shows that the T_c for ScB_2 is 1.5 K (as reported by Sichkar and Antonov [56]). However, as shown in **Figure 6a**, the inverted parabolas around **Γ** in the EBS are degenerate but ~1 eV below the Fermi level. A comparison of the full ScB_2 EBS with MgB_2 (blue lines) and a more detailed view of the region around **Γ** is shown in **Figure 9a** and **b**, respectively. The potential to invoke band tuning, whereby substitution of another element

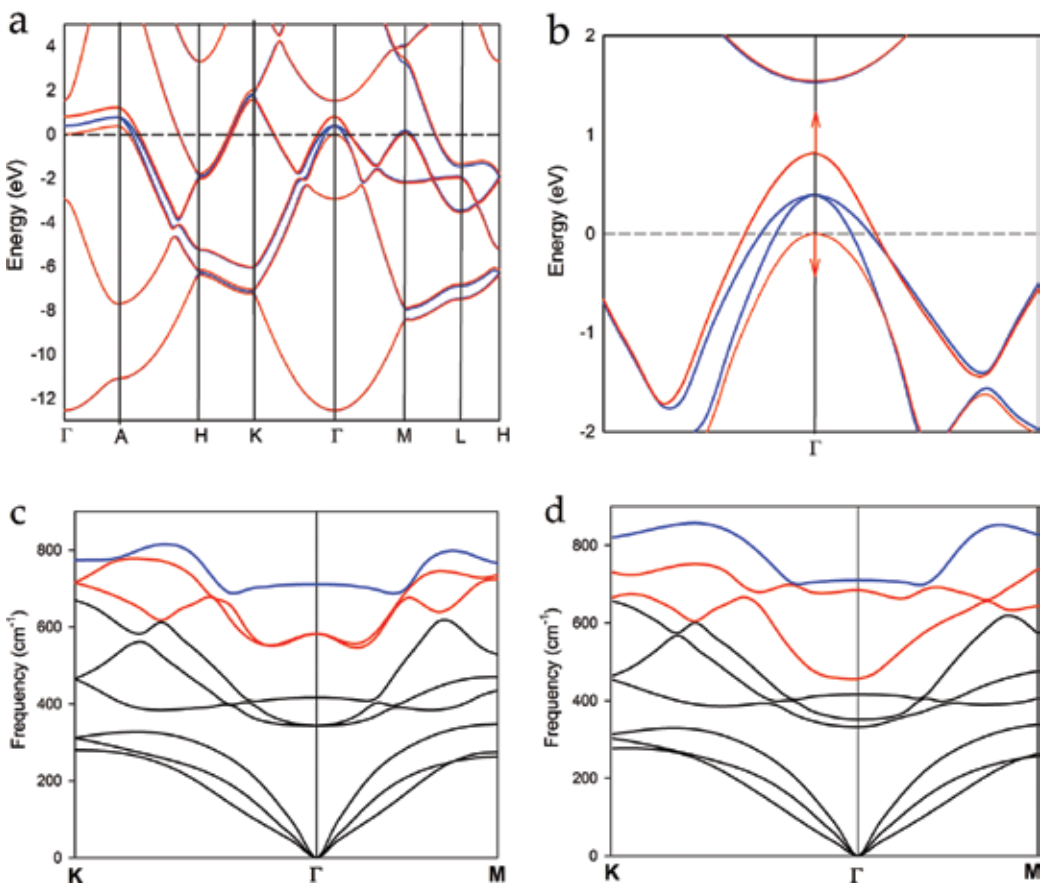

Figure 8. EBS using the LDA functional with $\Delta k = 0.02$ A^{-1} for (a) for MgB_2 at equilibrium (blue) and with relative atom displacement $D_x = 0.006$ (red) along the E_{2g} mode direction (i.e. the B–B bond); (b) enlarged view around **Γ** showing the shift of σ bands causing loss of degeneracy. Partial PD for MgB_2 calculated using the LDA functional for $k = 0.01$ A^{-1} in the **Γ–K** and **Γ–M** orientations showing changes in the E_{2g} (red) and B_{2g} (blue) modes under conditions of (c) equilibrium for $D_x = 0.0$ and (d) with atom displacement $D_x = 0.006$.

http://dx.doi.org/10.5772/intechopen.79216

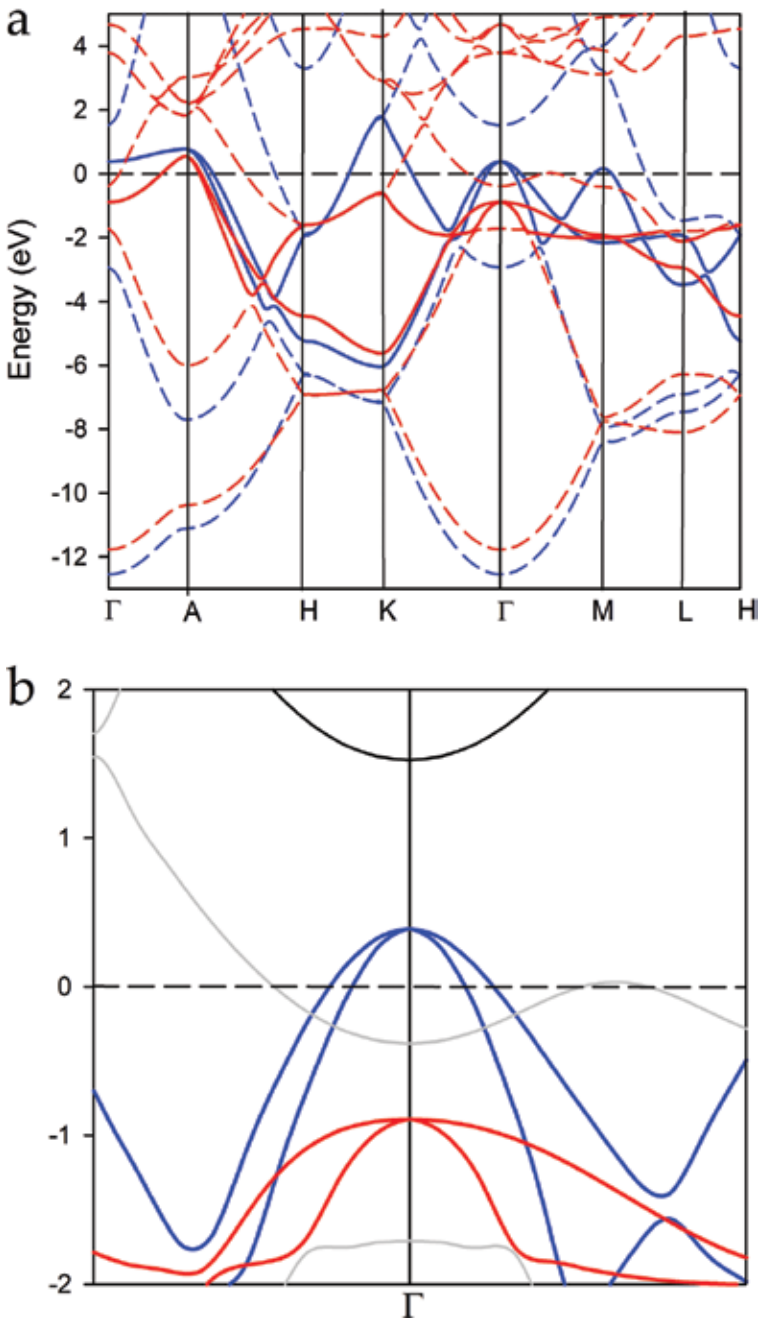

Figure 9. (a) EBS using the LDA functional with $\Delta k = 0.02$ A^{-1} for MgB_2 (blue) compared with ScB_2 (red) showing degenerate parabolas at **Γ** above and below the Fermi level, respectively; note the degenerate parabola for ScB_2 centred around **A**; (b) enlarged view for MgB_2 (blue) and ScB_2 (red) around **Γ**.

for Sc shifts the degenerate parabolas above the Fermi level, may be a viable strategy to achieve a higher T_c for $Sc_{1-x}M_xB_2$. Experiment shows that Sc substitutes for Mg in $Mg_{1-x}Sc_xB_2$ [32] and, in general, is superconducting for $x < 0.3$ [33]. Calculations on the variation of phonon anomaly

with substitution of Sc in MgB_2 show a similar correlation between T_δ and experimentally determined T_c [30].

Figure 8 and similar comparisons in other work [30, 55] show that, in general, PDs are more sensitive indicators of change in electron–phonon coupling, or electron distribution [35], than EBS. This sensitivity to change—either via complete or partial substitution of the metal ion into the structure—is also evident in the comparative energy shifts in phonon modes and the order of modes with change of composition. For example, the type structure for this suite of materials is AlB_2 for which the E_{2g} mode is at the highest frequency (~950 cm^{-1} at **Γ**) and the B_{2g} mode is significantly lower in energy (~500 cm^{-1} at **Γ**) [30]. In addition, the PD for AlB_2 does not show an anomalous form for any optical mode while the EBS shows σ band parabolas at **Γ** and degenerate bands along **Γ–A** below the Fermi level. In comparison, substitution of Mg into the type structure clearly shifts both the phonon modes—reversing the order and frequencies of E_{2g} and B_{2g} (~580 and ~710 cm^{-1} at **Γ**)—and the σ bands albeit the change with the latter is less obvious to the casual observer. For ScB_2, a similar behaviour is evident: an anomaly with degenerate E_{2g} modes at **Γ** and along **Γ–A** in the PD and symmetric, degenerate σ band parabolas around **A** and **Γ** (above and below the Fermi level, respectively; **Figure 6a** and **b**). Again, the change in behaviour for ScB_2 from the type structure, AlB_2, is more evident via the PD.

4. MgB_2: low-frequency Raman peaks

Experimental syntheses of MgB_2 by vapour [57] or solid state [31, 58] methods are well documented in the literature and, in comparison to syntheses of many other superconductors, are uncomplicated. Commercial production of MgB_2 wires [59, 60] was achieved soon after the publication by Nagamatsu et al. [21]. Nevertheless, there are cautionary notes about synthesis of high quality MgB_2 [31, 61, 62]; a particularly relevant matter for Raman spectroscopy because different microstructures can be formed due to small changes in processing conditions (see Figure 2 in Ref. [34]).

In a comparative study of morphologies produced under similar conditions [34], large, micron-sized aggregates containing interpenetrating, euhedral grains of MgB_2 displayed more peaks than those reported in prior Raman characterizations of MgB_2 [34]. Importantly, the signal/noise ratio for these aggregates under identical conditions was significantly higher than the plate morphology aggregates which recorded a lower T_c value of 38.0 K [63]. The quality of Raman signal from the aggregates of euhedral MgB_2 grains with T_c = 38.5 K [63], enabled detection of Raman peaks at low frequencies. Unlike Raman spectra of MgB_2 single crystals targeting specific polarizations oriented along particular crystallographic axes [64, 65], a non-specific geometry with quality, randomly oriented grains presents a modified, atypical response compared to conventional Raman spectra.

By inspection, the most obvious interpretation of atypical Raman spectra is the activation of extra peaks, including those at lower frequencies [34]. These extra peaks suggest that the well-known P6/mmm symmetry determined by bulk techniques may be incorrect or perhaps may indicate a lower symmetry condition. As is known, highly symmetric structures are expected

to have a high number of degeneracies compared with a monoclinic or triclinic structure. As the symmetry of a particular structure is lowered, some degeneracies can be broken and, for example, additional peaks may appear in Raman spectra. In addition, the bulk powder XRD patterns for these MgB_2 samples are consistent with the accepted P6/mmm symmetry. Thus, if symmetry reduction is a viable interpretation of Raman spectra, the effect would likely be subtle and related to a sub-group of the P6/mmm space group. Of note, careful and sophisticated XRD techniques have been used to show that superlattices do occur in MgB_2 [66].

DFT interpretation of the Raman spectra shows that all the observed frequencies, except the low frequency values (i.e. less than ~300 cm^{-1}) are, in fact, part of the list of possible frequencies for MgB_2 [34] with P6/mmm symmetry or related symmetry sub-groups. Raman activity changes between modes depending on the particular sub-group of P6/mmm. Further reduction of the symmetry required a double supercell in the *c*-axis direction to represent all elements of symmetry. When calculations include a superlattice structure for MgB_2, all relevant frequencies are reproduced and additional frequencies, including the low frequencies, match experimental values measured using Raman and IR [34].

In essence, modes that are part of the zone boundary at **A** in the reciprocal lattice representation of the PD (i.e. parallel to the *c*-axis direction) are folded at the mid-point to that boundary for the lower symmetries, and therefore, become part of the **Γ**-point modes of a 2*c*-superlattice. This interpretation of symmetry breaking for MgB_2 is instructive, not only because of the consistent explanation provided to experimentally determined Raman and IR spectra, but also because it allows for additional refinements in understanding. For example, the mode frequencies for MgB_2 can be grouped, to a first approximation, as multiples of a harmonic frequency that shows a clear relationship to the superconducting energy gap [25, 34]. This basic frequency is equal to the pitch or slope of the linear proportionality of harmonic modes and is demonstrated for the obvious case of boron isotopes in MgB_2 [25].

5. Extrinsic influences on MgB_2

There are many external factors that influence superconductivity in MgB_2; the most obvious of which is temperature. The maximum value of a computational modelling program is, *a priori*, to predict behaviour of a material under specific conditions. The capacity to predict the temperature at which a solid transitions to a superconducting state is not an unreasonable demand on DFT when used carefully. Two other extrinsic influences on superconductivity well founded on experimental data are elemental substitution and pressure. For example, the influence of substituent elements, including metals, on the value of T_c for many superconducting families including the cuprates and chalcogenides is well known [67–69]. In addition, pressure applied to single atom metals was first demonstrated in the 1920s and subsequently, led to discovery of 22 elemental solid superconductors [70]. We now briefly describe how attention to PDs and EBSs using DFT modelling provides excellent correlation with experimentally determined superconducting properties for metal substituted MgB_2 and for MgB_2 under pressure.

5.1. Metal substitution

The solubility of other metal atoms in MgB_2, that is, the substitution of Mg within the structure by some other metal, is limited yet well-studied [31, 71, 72] in the wake of Nagamatsu et al. work [21]. Substitution by Al extends to more than 0.5 formula units (e.g. $(Mg_{0.5}Al_{0.5})B_2$) while significant proportions of Sc [32, 33] and Ti [73] are known to substitute into MgB_2. Other elements such as Li, Mn and Fe will substitute for Mg but at much lower amounts as stable phases (e.g. Li < 0.11 formula units) [31]. In nearly all cases, substitution of a metal for Mg in the structure results in a lower T_c compared with the T_c for MgB_2 [30]. Exceptions may be the Ba, Rb and Cs substitutions reported to increase T_c above 40 K by Palnichenko et al. [74], determined using ac susceptibility.

A DFT evaluation of Al substitution in MgB_2 [29] requires the use of superlattices to build a range of $Mg_{1-x}Al_xB_2$ compositions as described in Section 2. PDs for a series of Al-substituted compositions show that the Kohn anomaly changes as Al content is increased. The value of δ decreases with increased Al content. As shown in **Figure 10**, the EBS for $Mg_{0.5}Al_{0.5}B_2$ shows similar format to the MgB_2 parabolic bands that are degenerate at **Γ** and also along **Γ–A**. However, these bands are shifted to lower energy, and ultimately to below or at the Fermi level, with increased substitution of Al for Mg in the structure. For $Mg_{0.5}Al_{0.5}B_2$, the degenerate bands at **Γ** are parallel with the Fermi level which suggests that superconductivity for this composition is minimal or that the T_c is very low. The PD for $Mg_{0.5}Al_{0.5}B_2$ shows a small but measureable anomaly, δ, that provides a T_δ ~ 4.5 K [29] and reiterates the intrinsic value of evaluating both the EBS and PD of superconducting materials.

Using the same methodology noted earlier, the calculated value for thermal energy of the anomaly also reduces consistently with experimentally determined values of T_c, within estimated errors [29]. A plot of T_δ calculated from the change in depth of the phonon anomaly in Al substituted MgB_2 compared with the experimentally determined T_c for similar compositions is shown in **Figure 11** [29]. This example, and others with the AlB_2-type structure [29, 30] demonstrate that *ab initio* DFT modelling can provide consistent and predictable data on the presence/absence of superconductivity for BCS-type materials. In addition, parameters extracted from these models correlate well with experimental data on T_c without requirement to *post-facto* adjust well-known proximal equations.

A computational limitation of this approach is the number of integer superlattice constructs that can be reasonably accommodated within the constraints of multi-user high performance computing facilities to evaluate a wide range of substituted compositions. Nevertheless, with careful attention to experimental details, the same approach has been applied to estimate the T_δ for Sc and Ti substituted MgB_2 [30]. Again, as with Al-substituted MgB_2, the calculated T_δ obtained from measuring the depth of the phonon anomaly correlates very well—within systematic errors—with the experimental values of T_c determined for each composition [29, 30].

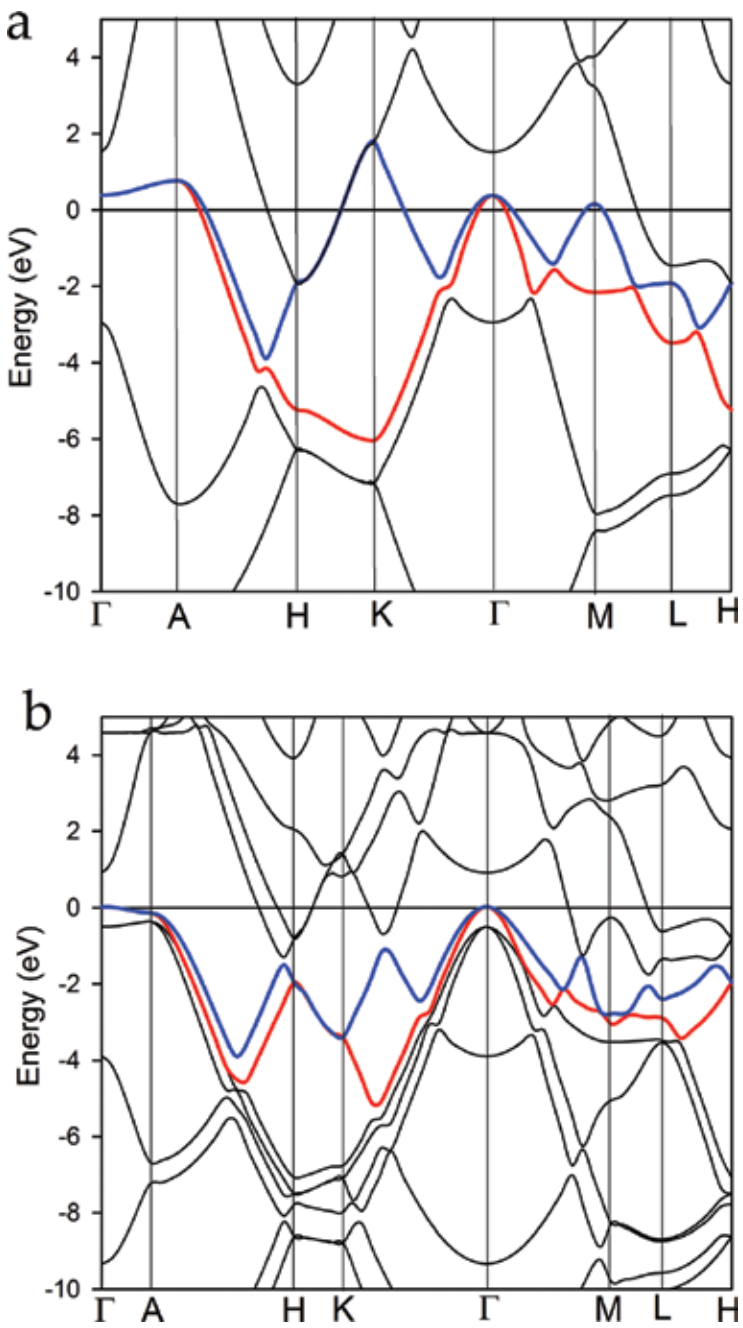

Figure 10. EBS calculated using the LDA functional with $\Delta k = 0.01$ A^{-1} highlighting the two key parabolic bands (blue and red lines) degenerate at **Γ** and along **Γ–A** for (a) MgB_2 and (b) $Mg_{0.5}Al_{0.5}B_2$. In comparison to MgB_2, the superlattice construct for $Mg_{0.5}Al_{0.5}B_2$ results in multiple bands and differences in the relative widths of reciprocal dimensions (e.g. **H–K** and **M–L**) that encompass *c*-axis directions. The degenerate bands at **Γ** for $Mg_{0.5}Al_{0.5}B_2$ are parallel with the Fermi level suggesting a lower value for T_c compared with MgB_2.

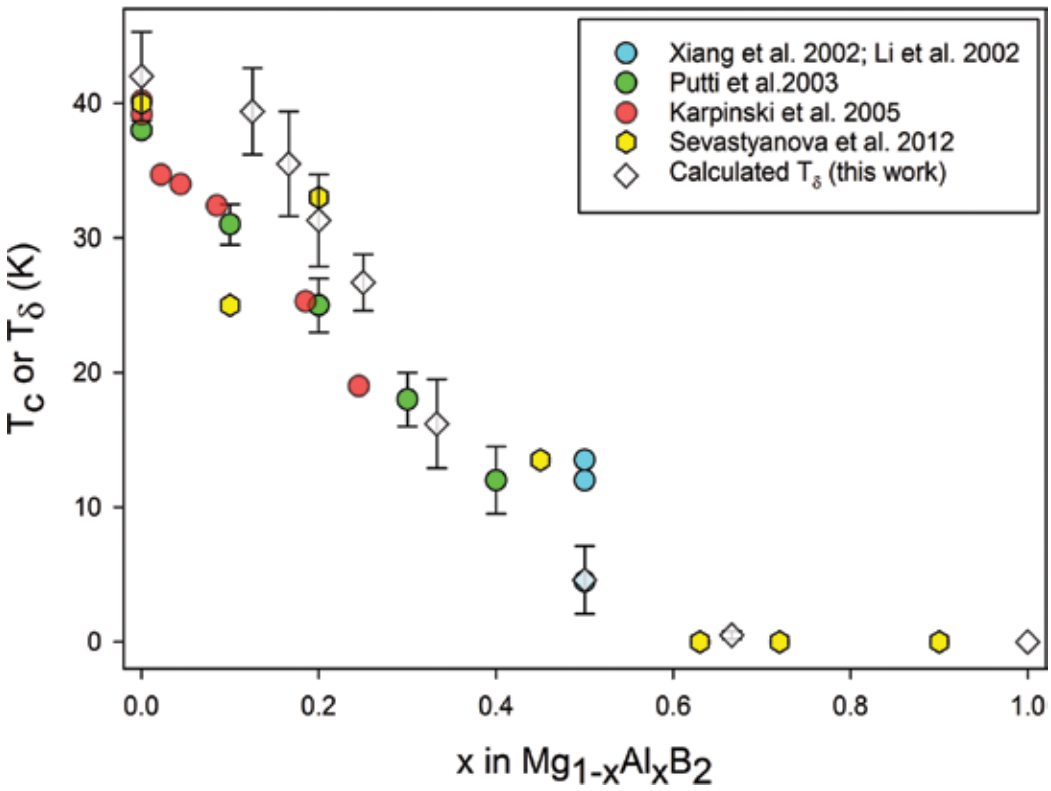

Figure 11. DFT calculated values for T_δ (unfilled diamonds) based on the depth of the phonon anomaly, δ, for Al-substituted MgB_2 compared with experimentally determined values (filled symbols) for T_c (reproduced from [29]).

5.2. Hydrostatic pressure

Application of hydrostatic pressure to many superconducting materials results in a change in the value of T_c [70]. For many materials, increased hydrostatic pressure results in a decreased T_c compared with ambient conditions although care is required with the experimental conditions to apply pressure [27]. For MgB_2, there is abundant experimental work ([11], and references therein) on the pressure dependence of T_c including Raman and lattice parameter variations up to ~57 GPa [75, 76]. Similar pressure effects can be determined using *ab initio* DFT and, more importantly, the effects of pressure changes on EBS and PDs are demonstrable [11], noting that hydrostatic pressure is one of the few external pressure conditions for which PDs can be calculated [44].

Figure 12 shows the EBS and PD for MgB_2 at 0 GPa and 20 GPa, respectively, and demonstrates a shift in the σ bands at the Fermi level although no loss of degeneracy around **Γ**. The shift of the σ bands to lower energy at 20 GPa is equivalent to ~0.05 eV. In comparison, the PD for MgB_2 under these conditions is more sensitive to pressure as indicated by the relative depth, δ, of the phonon anomaly centred around **Γ**. The change in value for δ is related to the thermal energy, T_δ, of the phonon anomaly [29] and shows a linear relationship with change in pressure up to 20 GPa as well as strong correlation with experimentally determined T_c [11]. In **Figure 12**, the value of δ_1 for MgB_2 at 0 GPa is ~128 cm^{-1} while δ_2 at 20 GPa is ~75 cm^{-1}. These values result in

http://dx.doi.org/10.5772/intechopen.79216

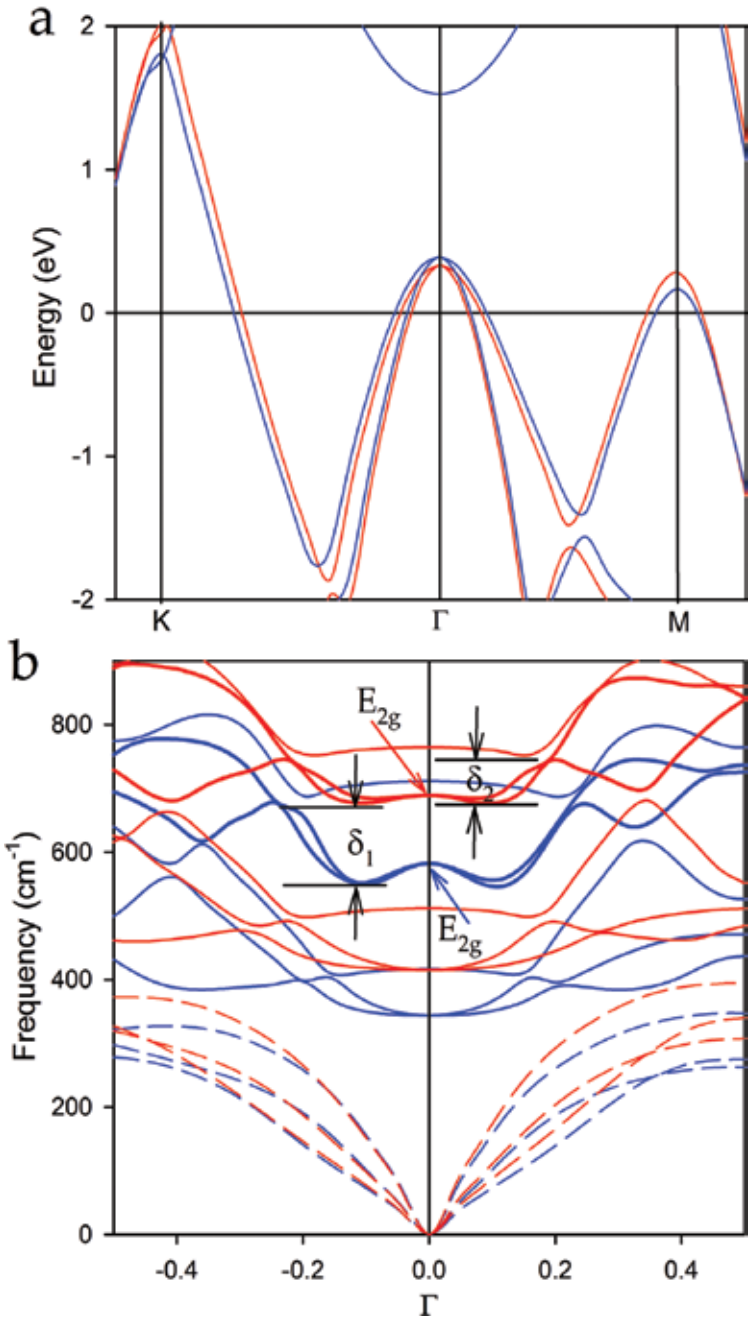

Figure 12. *Ab initio* DFT calculations for MgB_2 at 0 (blue lines) and 20 GPa (red lines) using the LDA functional with $\Delta k = 0.02$ A^{-1} for (a) electronic bands and (b) phonon dispersions centred around **Γ**. Note the substantial change in the depth of the phonon anomaly between 0 (δ_1) and 20 GPa (δ_2) and the higher frequencies for E_{2g} at 20 GPa.

a calculated T_δ ~40 and ~20 K, at 0 and 20 GPa, respectively, consistent with experimentally measured T_c values for MgB_2 [11, 27]. Another expected effect of increased hydrostatic pressure is an overall shift of phonon modes to higher frequency as shown in **Figure 12b**.

The shift of σ bands in the EBS for MgB_2 follows a consistent trend to that observed for other structural variations such as metal substitution and electron density as shown above. Goncharov and Struzhkin [75] suggested on the basis of approximations to the Eliashberg formulation, that degenerate electronic bands split above and below the Fermi level at 20 GPa at which point experimental data diverge slightly from a linear relationship between T_c and P. However, it is clear from these *ab initio* DFT calculations that MgB_2 retains the aforementioned superconductivity characteristics at 20 GPa and experimental data shows superconductivity [27]. With increased pressure, the separation of Fermi surfaces, or the inter-tubular distance as described above, also decreased [11]. While this decrease in inter-tubular distance is subtle, its relationship to the value of δ and appropriate choice of Δk grid resolution provides clarity of interpretation [11, 34] and shows that this region of reciprocal space is key to the determination of superconductivity for MgB_2 and derivative structures [19]. The link between electron and phonon behaviour in MgB_2, including the onset of superconductivity, is well modelled using *ab initio* DFT for a wide range of equivalent experimental conditions.

5.3. Prediction using DFT

The foregoing description of computational outcomes facilitated by a consistent *ab initio* DFT methodology using the same functionals to achieve convergent PDs across a wide range of conditions and compositions implies that the approach is suited to predicting electronic properties of other diborides, and perhaps, other structure types. Furthermore, the obvious but oft forgotten interdependence of the EBS and the PD of solids suggests that the strong electron–phonon interactions of BCS superconductors are calculable without modification and are predictable.

Implicit prediction of T_c for metal substituted MgB_2 occurred soon after the announcement by Nagamatsu et al. [21] and took the form of syntheses with hole doped additions that, in general, led to a decrease in T_c compared with the parent compound [31, 77]. However, other researchers used the Eliashberg formulation to show that Na and/or Ca substitution into MgB_2 would increase T_c [78] but there is little evidence to suggest that Na, for example, is soluble in MgB_2 [79] and, to date, a Na-substituted MgB_2 has not been synthesised. More recently, the depth of the phonon anomaly at **Γ** has been used to calculate the T_δ of "unknown" metal substituted MgB_2 as well as other compounds such as BaB_2 [29, 30]. For BaB_2, the PD does not converge until a hydrostatic pressure ~16 GPa is applied at which the estimated T_δ is between ~60 and ~80 K depending on the linear response method chosen [29]. Using a similar strategy, Ba-substituted MgB_2 shows a T_δ ranging between ~62 and ~64 K (± ~6 K) depending on the level of substitution [29]. To date, clear evidence for synthesis of these specific modelled compositions is not extant.

As noted above, Palnichenko et al. [74] report syntheses of MgB_2 in the presence of Rb, Cs and Ba which, on the basis of ^{11}B NMR data, suggests substitution of these elements into the MgB_2 structure in a proportion of the product. Measurement of T_c using ac susceptibility shows possible onsets of superconductivity at 52, 58 and 45 K, respectively in the products. Despite the difficulty in interpreting the NMR data in terms of specific crystal structure(s), the implication from this experimental work—among the few reported attempts at charge carrier donation—is

that Ba substitution into MgB_2 has increased T_c above that for MgB_2 [74]. The trend of this experimental work is consistent with the outcomes calculated for T_δ from the PDs of $Mg_{1-x}Ba_xB_2$ [29, 30] and suggests that *a priori* prediction of T_c for unknown, or "new," compounds is achievable.

6. Superlattices

Consideration of superlattices derived from a primary structural model provides an effective interpretation of fine-scale experimental data that reflect dynamic atom (or electron-ion core) interactions in the solid state. A superlattice may enable facile resolution of computational models that invoke atom substitution or show dynamic symmetry conditions manifest in subtle shifts of electron density within a structure and that are detectable using experimental techniques such as Raman spectroscopy. In principle, the textbook superlattice example is of the mass modulation of a linear chain of identical masses denoted by m [3, 10]. The original mass m, separated by equal distances *a*, displays only acoustic modes of vibration, which have a group velocity related to the sound velocity. When a modulation of the masses is introduced through masses m and M, the new real space periodicity becomes 2*a*, resulting in a folding of reciprocal space at half the reciprocal space Π/2*a*. This action introduces the so called optic modes that have flatter dispersions than the acoustic modes as demonstrated in the PDs above. Similar behaviour can also be attributed to a modulation of the forces between identical masses [80] and this is exemplified by the phonon response to bond deformation in MgB_2 as shown above.

Nevertheless, interpretation of these phenomena, particularly when dissecting the richness of current generation DFT models, requires careful attention to the following:

a. Multiplicity: When a superlattice is constructed, the number of atoms in the cell are multiplied by the integer order of the superlattice. Thus, the number of degrees of freedom 3 N for N atoms is multiplied accordingly. This multiplicity can result in very complex EBSs and PDs that are difficult to interpret in a practical manner and, of course, significantly increases the computational payload required for a calculation.

b. Folding of reciprocal space: Original values or modes at a boundary zone become folded and part of the spectrum of the superlattice **Γ** point. While folding will bring about beneficial information for modest sized superlattices (as shown above for MgB_2), interpretation of models for very large superlattices may also become complex, particularly for low symmetry structures.

c. Computational resolution: PD calculations are particularly sensitive to Δk grid resolution in that a phonon anomaly may not be evident or may have a very irregular appearance if the interval for **k** is too coarse [13, 34].

With attention to the above caveats, DFT is an excellent tool for real space interpretation of solid state phenomena that respond to variations in electron distributions induced by external factors.

7. Conclusions

Ab initio DFT models of electron and phonon behaviour in superconducting materials provide powerful tools for interpretation of existing, known compounds as well as for prediction of new compositions that may demonstrate novel, or desired, conduction properties. The full capacity of DFT, manifest in EBS and PD reciprocal space representations, when considered together for a particular compound provides unambiguous indication of potential for superconductivity as well as a credible estimate of T_c and an estimate of error for T_c. Either an EBS or PD alone may be sufficient to indicate superconductivity—for BCS-type materials—but both representations are necessary for minimal ambiguity. In particular, for AlB_2-type structures degenerate parabolic σ bands focused at a crystallographic boundary above the Fermi level and with split bands at the Fermi level are *a priori* indicators of superconductivity, or that superconductivity is a strong possibility with fine-tuning of the structure. In addition, a phonon anomaly of the optical E_{2g} modes degenerate at **Γ** is similarly an *a priori* indicator of superconductivity in AlB_2-type structures. We have applied these basic principles to other high symmetry compounds (e.g. cubic or tetragonal superconductors and/or insulators) with similar interpretative clarity particularly when transcribed to real space configurations. To experimentally validate these principles across all superconductor families, and to design new predictive targets for synthesis, requires real space descriptions of compounds for rapid evaluation of appropriate synthesis techniques. We encourage further systematic and critical comparisons of the known 32 families of superconductors [81] using these DFT tools.

Acknowledgements

This research did not receive any specific grant from funding agencies in the public, commercial or not-for-profit sectors. Access to, and ongoing assistance with, QUT's HPC facilities particularly from Ashley Wright, Abdul Sharif and Hamish Macintosh, is gratefully acknowledged. The authors are grateful to Associate Professor Alexey Kolmogorov for alerting them to the results in the article by Palnichenko et al. [74].

Author details

Jose A. Alarco and Ian D.R. Mackinnon*

*Address all correspondence to: ian.mackinnon@qut.edu.au

Institute for Future Environments and Science and Engineering Faculty, University of Technology (QUT), Brisbane, Queensland, Australia

References

[1] Urch DS. Orbitals and Symmetry. Harmondsworth, Middlesex, England: Penguin Books Ltd; 1970

[2] Brandt NB, Chudinov SM. Electronic Structure of Metals. Moscow: Mir Publishers; 1975

[3] Ziman JM. Electrons and Phonons: The Theory of Transport Phenomena in Solids. Oxford: Oxford University Press; 1960

[4] Born M, Huang K. Dynamical Theory of Crystal Lattices Oxford Classic Texts in the Physical Sciences. Oxford: Clarendon Press; 1988

[5] Ziman JM. Principles of the Theory of Solids. 2nd ed. Cambridge: Cambridge University Press; 1972

[6] Kohn W. Nobel lecture: Electronic structure of matter—Wave functions and density functionals. Reviews of Modern Physics. 1999;**71**(5):1253-1266

[7] Giustino F. Materials Modelling Using Density Functional Theory—Properties and Predictions. Oxford: Oxford University Press; 2014

[8] Born M, Oppenheimer R. Zur Quantentheorie der Molekeln. Annalen der Physik. 1927;**4**(84):457-484

[9] Altmann SL. Band Theory of Solids: An Introduction from the Point of View of Symmetry. Oxford: Clarendon Press; 2002

[10] Sherwood PMA. Vibrational Spectroscopy of Solids. Cambridge: Cambridge University Press; 1972

[11] Alarco JA, Talbot PC, Mackinnon IDR. Phonon dispersion models for MgB_2 with application of pressure. Physica C: Superconductivity and Its Applications. 2017;**536**:11-17

[12] Singh PP. From E_{2g} to other modes: Effects of pressure on electron-phonon interaction in MgB_2. Physical Review Letters. 2006;**97**(24):247002

[13] Heid R, Bohnen K-P, Renker B. Electron-phonon coupling and superconductivity in MgB_2 and related diborides. Advances in Solid State Physics. 2002;**42**:293-305

[14] Bardeen J, Cooper LN, Schrieffer JR. Theory of superconductivity. Physics Review. 1957;**108**:1175-1204

[15] Duan F, Guojun J. Introduction to Condensed Matter Physics. Vol. 1. Singapore: World Scientific; 2007

[16] Mourachkine A. Room-Temperature Superconductivity. Cambridge: Cambridge International Science Publishing; 2004

[17] Wilson EBJ, Decius JC, Cross PC. Molecular Vibrations—The Theory of Infrared and Raman Vibrational Spectra. New York: Dover Publication, Inc.; 1955

[18] Geballe TH, Hammond RH, Wu PM. What T-c tells. Physica C: Superconductivity and Its Applications. 2015;**514**:9-16

[19] Alarco JA, Talbot PC, Mackinnon IDR. A complete and accurate description of superconductivity of AlB2-type structures from phonon dispersion calculations. Journal of Superconductivity and Novel Magnetism. 2018;**31**:727-731

[20] Carbotte JP. Properties of boson exchange superconductors. Reviews of Modern Physics. 1990;**62**(4):1027-1157

[21] Nagamatsu J, Nakagawa N, Muranaka T, Zenitani Y, Akimitsu J. Superconductivity at 39 K in magnesium diboride. Nature. 2001;**410**:63-64

[22] Jorgensen JD, Hinks DG, Short S. Lattice properties of MgB_2 versus temperature and pressure. Physical Review B. 2001;**63**(224522):1-5

[23] Narlikar A. Superconducting magnesium diboride. In: Studies of High Temperature Superconductors. Vol. 38. New York: NOVA Science Publishers Inc.; 2002. 514pp

[24] Buzea C, Yamashita T. Topical review—Review of the superconducting properties of MgB_2. Superconductor Science and Technology. 2001;**14**:R115-R146

[25] Alarco JA, Talbot PC, Mackinnon IDR. Coherent phonon decay and the boron isotope effect for MgB_2. Physical Chemistry Chemical Physics. 2014;**16**(46):25386-25392

[26] Hinks DG, Claus H, Jorgensen JD. The complex nature of superconductivity in MgB_2 as revealed by the reduced total isotope effect. Nature. 2001;**411**(6836):457-460

[27] Deemyad S et al. Dependence of the superconducting transition temperature of single and polycrystalline MgB_2 on hydrostatic pressure. Physica C: Superconductivity. 2003;**385**(1):105-116

[28] Tang J et al. Lattice parameter and T_c dependence of sintered MgB_2 superconductor on hydrostatic pressure. Physical Review B. 2001;**64**(13):132509

[29] Alarco JA, Talbot PC, Mackinnon IDR. Phonon anomalies predict superconducting T_c for AlB_2-type structures. Physical Chemistry Chemical Physics. 2015;**17**(38):25090-25099

[30] Mackinnon IDR, Talbot PC, Alarco JA. Phonon dispersion anomalies and superconductivity in metal substituted MgB_2. Computational Materials Science. 2017;**130**:191-203

[31] Karpinski J, Zhigadlo ND, Katrych S, Puzniak R, Rogacki K, Gonnelli R. Single crystals of MgB_2: Synthesis, substitutions and properties. Physica C. 2007;**456**:3-13

[32] Agrestini S et al. Sc doping of MgB_2: The structural and electronic properties of $Mg_{1-x}Sc_xB_2$. Journal of Physics and Chemistry of Solids. 2004;**65**(8-9):1479-1484

[33] Agrestini S et al. Substitution of Sc for Mg in MgB_2: Effects on transition temperature and Kohn anomaly. Physical Review B. 2004;**70**(13):134514

[34] Alarco JA, Chou A, Talbot PC, Mackinnon IDR. Phonon modes of MgB_2: Super-lattice structures and spectral response. Physical Chemistry Chemical Physics. 2014;**16**:24443-24456

[35] Alarco JA, Talbot PC, Mackinnon IDR. Electron density response to phonon dynamics in MgB_2: An indicator of superconducting properties. Modelling and Numerical Simulation of Material Science. 2018;**8**:21-46

[36] Martin RM. Electronic Structure—Basic Theory and Practical Methods. Cambridge: Cambridge University Press; 2005

[37] Xi XX. Two-band superconductor magnesium diboride. Reports on Progress in Physics. 2008;**71**(116501):26

[38] Almutairi A, Zhang C, Du A, Lipton-Duffin J, Farrell T, Alarco JA. Approximate parabolic and tight binding equations for the electronic bands of MgB_2 under a range of external conditions. submitted 2018, under review. 2018;**31**:727-731

[39] Phillips JC. Bonds and Bands in Semiconductors. New York, London: Academic Press; 1973

[40] Sutton AP. Electronic Structure of Materials. Oxford: Clarendon Press - Oxford Science Publications; 2004

[41] Kohn W. Image of the Fermi surface in the vibration spectrum of a metal. Physical Review Letters. 1959;**2**(9):393-394

[42] Baron AQR et al. Kohn anomaly in MgB_2 by inelastic X-ray scattering. Physical Review Letters. 2004;**92**(19):19700

[43] Baron AQR et al. Review: Phonon spectra in pure and carbon doped MgB_2 by inelastic X-ray scattering. Physica C. 2007;**456**:83-91

[44] Accelrys. Materials Studio CASTEP Online Help: "Requesting Vibrational Properties". Available from: http://www.tcm.phy.cam.ac.uk/castep/documentation/WebHelp/html/tskcastepreqvibprops.htm

[45] Xiang JY et al. Superconducting properties and c-axis superstructure of $Mg_{1-x}Al_xB_2$. Physical Review B. 2002;**65**:214536

[46] Zandbergen HW, Wu MY, Jiang H, Hayward MA, Haas MK, Cava RJ. The complex superstructure in $Mg_{1-x}Al_xB_2$ at x~0.5. Physica C. 2002;**366**:221-228

[47] Li JQ, Li L, Liu FM, Dong C, Xiang JY, Zhao ZX. Superconductivity, superstructure, and structure anomalies in $Mg_{1-x}Al_x$B2. Physical Review B. 2002;**65**:132505

[48] Blaha P, Schwarz K, Luitz J. WIEN2k-FAQ: Positive Fermi Energy: What Does it Mean? 2001. Available from: http://susi.theochem.tuwien.ac.at/reg_user/faq/neg_fermi_energy.html

[49] Escamilla R et al. Crystalline structure and the superconducting properties of NbB_{2+x}. Journal of Physics: Condensed Matter. 2004;**16**:5979-5990

[50] Machado AJS, Renosto ST, dos Santos CAM, Alves LMS, Fisk Z. Defect structure versus superconductivity in MeB_2 compounds (Me = refractory metals) and one-dimensional superconductors. In: Gabovich A, editor. Superconductors—Materials, Properties and Applications. London: InTechOpen; 2012. pp. 45-60

[51] Renosto ST et al. Evidence of multiband behavior in the superconducting alloy $Zr_{0.96}V_{0.04}B_2$. Physical Review B. 2013;**87**(174502):1-6

[52] Jung S-G et al. Critical current density and flux pinning in $Zr_{0.96}V_{0.04}B_2$ superconductor with AlB_2 structure. Journal of Applied Physics. 2013;**114**(133905):1-4

[53] Marques MDR et al. Study of the superconducting properties of the new intermetallic compound $Zr_{1-x}Nb_xB_2$. Superconductor Science and Technology. 2016;**95007**:1-6

[54] Pickett WE, An JM, Rosner H, Savrasov SY. Role of two dimensionality in MgB_2. Physica C. 2003;**387**:117-121

[55] An JM, Pickett WE. Superconductivity of MgB_2: Covalent bonds driven metallic. Physical Review Letters. 2001;**86**(19):4366-4369

[56] Sichkar SM, Antonov VM. Electronic structure, phonon spectra and electron–phonon interaction in ScB_2. Low Temperature Physics. 2013;**39**(7):595-601

[57] Chen K et al. Properties of MgB_2 films grown at various temperatures by hybrid physical–chemical vapour deposition. Superconductor Science and Technology. 2008;**21**(9):095015

[58] Kim Y-S, Shin H-S. Preparation and characterization of magnesium diboride superconductor by melting process. Korean Journal of Chemical Engineering. 2003;**20**(6):1183-1187

[59] Grasso G et al. Transport properties of powder-in-tube processed MgB_2 tapes. Physica C. 2002;**378-381**:899-902

[60] Malagoli A, Braccini V, Scati N, Roncallo S, Siri AS, Grasso G. Fabrication and superconducting properties of powder-in-tube processed MgB_2 tapes. Physica C. 2002;**372-376**: 1245-1247

[61] Cava RJ, Zandbergen HW, Inumaru K. The substitutional chemistry of MgB_2. Physica C. 2003;**385**:8-15

[62] Bud'ko SL, Canfield PC. Superconductivity of magnesium diboride. Physica C: Superconductivity and Its Applications. 2015;**514**:142-151

[63] Mackinnon IDR, Winnett A, Alarco JA, Talbot PC. Synthesis of MgB_2 at low temperature and autogenous pressure. Materials. 2014;**7**(5):3901-3918

[64] Hlinka J et al. Phonons in MgB_2 by polarized Raman scattering on single crystals. Physical Review B. 2001;**64**:140503

[65] Quilty JW, Lee S, Yamamoto A, Tajima S, Yamanaka A. A Raman scattering study of superconductivity in MgB_2. Physica C. 2003;**388-389**:131-132

[66] Campi G et al. Study of temperature dependent atomic correlations in MgB_2. European Physical Journal B. 2006;**52**(1):15-21

[67] Pena O. Chevrel phases: Past, present and future. Physica C: Superconductivity and Its Applications. 2015;**514**:95-112

[68] Fournier P. T′ and infinite-layer electron-doped cuprates. Physica C: Superconductivity and Its Applications, Review. 2015;**514**:314-338

[69] Chu CW, Deng LZ, Lv B. Hole-doped cuprate high temperature superconductors. Physica C: Superconductivity and Its Applications. 2015;**514**:290-313

[70] Schilling JS. What high pressure studies have taught us about high-temperature superconductivity. In: Frontiers of High Pressure Research II: Application of High Pressure to Low-Dimensional Novel Electronic Materials. Springer Netherlands, Dordrecht: Springer; 2001. pp. 345-360

[71] Hinks DG, Jorgensen JD, Zheng H, Short S. Synthesis and stoichiometry of MgB_2. Physica C. 2002;**382**:166-176

[72] Karpinski J et al. Al substitution in MgB_2 crystals: Influence on superconducting and structural properties. Physical Review B. 2005;**71**(17):174506

[73] Lee BW, Choia I, Junga CU, Leeb SI. Doping in MgB_2 superconductors using a high-pressure furnace. Journal of Magnetism and Magnetic Materials. 2008;**320**:e484-e486

[74] Palnichenko AV, Vyaselev OM, Sidorov NS. Influence of Rb, Cs, and Ba on the superconductivity of magnesium diboride. JETP Letters. 2007;**86**(4):272-274

[75] Goncharov AF, Struzhkin VV. Pressure dependence of the Raman spectrum, lattice parameters and superconducting critical temperature of MgB_2: Evidence for pressure-driven phonon-assisted electronic topological transition. Physica C: Superconductivity. 2003;**385**(1-2):117-130

[76] Goncharov AF et al. Raman spectrum and lattice parameters of MgB_2 as a function of pressure. Physical Review B. 2001;**64**(10):100509

[77] Karpinski J et al. MgB_2 single crystals substituted with Li and with Li-C: Structural and superconducting properties. Physical Review B. 2008;**77**(21):214507

[78] Neaton JB, Perali A. On the Possibility of Superconductivity at Higher Temperatures in sp-Valent Diborides. arXiv:Cond-Mat/0104098 [Cond-Mat.Supr-Con]; 2001. pp. 1-27

[79] Mackinnon IDR, Shahbazi M, Alarco JA, Talbot PC. Low temperature decomposition of metal borohydride drives autogenous synthesis of MgB_2. Superconductor Science and Technology. 2017;**30**:055004

[80] Janot C. Quasicrystals—A Primer. Oxford: Clarendon Press - Oxford Science Publications; 1997

[81] Hirsch JE, Maple MB, Marsiglio F. Superconducting materials classes: Introduction and overview. Physica C: Superconductivity and Its Applications. 2015;**514**:1-8

Chapter 6

Phononic Crystal Resonators

Bao Jing-Fu, Muhammad Ammar Khan and
Bao Fei-Hong

Additional information is available at the end of the chapter

http://dx.doi.org/10.5772/intechopen.78584

Abstract

In this chapter we present the theory of phononic crystal, classification of PnC according to its physical nature, and phononic crystal (PnC) phenomena in locally resonant materials with 2D, and 3D crystals structure. In this chapter, phononic crystal (PnC) micro-electro mechanical system (MEMS) resonators with different transduction schemes such as electrostatically, piezoresistively, piezoelectrically transduced MEMS resonators are explained. In this chapter, we employed phononic crystal strip in MEMS resonators is explained to reduce anchor loss, and analysis of eigen frequency mode of the resonators. The phononic crystal strip with supporting tethers is designed to see the formation of band gap by introducing square holes, and improvement of quality factor and harmonic response. We show that holes can help to reduce the static mass of PnC strip tether without affecting on band gaps.

Keywords: MEMS resonator, phononic crystal, piezoelectric, band gap, anchor loss

1. Introduction

Because of merits of easy fabrications and less power consumption and the better performance with high accuracy phononic crystals MEMS resonator has become hot topic in the family of flexible electronics. The concept of phononic crystal followed by a few years the analogous concept of photonic crystals [1, 2] for the propagation of electromagnetic waves.

Phononic crystals are actually the acoustic waves with periodic structures which is same as electrons crystalline structure, sometimes the acoustic waves are also refer to elastic waves. Simply we can say phononic crystals are the artificial materials are arranged in a highly ordered microscopic structure of array of particles. Phononic crystals (PnCs) have paid attention by researchers over the past two decades [3]. Phononic crystals have many potential applications,

especially in the field of information and communication technologies. Propagation of waves can be control by phononic crystals. The field of phononics is progressing very quickly.

Nowadays there are many advances in the field of phononic crystals. Scientist and engineers are paying deep attention in phononic crystals (PnCs) MEMS resonator. The PnCs have significance role in the advancement of micro- and nanofields. PnCs supported tether configurations to isolate the energy leakage from resonator body into substrate [4]. A perfect PnC allows for the design of devices like waveguides and cavities to control the propagation of acoustic waves inside the band [5, 6, 34]. The PnCs can operate as coupling elements between resonators [6, 7]. Moreover the combination of PnCs and n-type doped silicon in nanostructures is a potential/promising candidate for thermoelectric applications [7].

In fact, the concept of phononic crystals is extended from one of photonic crystals for the propagation of electromagnetic waves [1–9]. The nature of phononic crystals is controlling and manipulating the propagation of elastic/acoustic waves. For example, the PnCs can prohibit the propagation of acoustic (elastic waves) inside their structures through existence of band gaps (PBG). Band gap is a frequency range in which there are no resonant guided modes or wave propagation within the structure.

2. Theory of phononic crystal

As mention above that phononics crystal is an artificial material composed by a periodic repetition of incorporation in a matrix. This periodic structure is formed by scattering inclusions located in consistent material as a lattice structure resemble with crystal lattice existed in the crystalline solid [10–12].

2.1. Lattice structure

The phononic band structure may be tailored with appropriate choices of materials, and crystal lattices. An ideal crystalline solid composed of the atoms or basis (group of atoms) are arranged by attachment of every lattice point. Let any lattice point r' can be formed from any other lattice point r in the space using translational operation [10]

$$r' = r + T \tag{1}$$

In above equation, T is the translation vector can be written as

$$T = u_1 a_1 + u_2 a_2 + u_3 a_3 \tag{2}$$

where $\boldsymbol{a_1}$, $\boldsymbol{a_2}$ and $\boldsymbol{a_3}$ three fundamental translation vectors (primitive vectors/axis) can be lie in arbitrary directions and u_1, u_2 and u_3 are three arbitrary integers.

Lattice is formed by the repetition of smallest unit cell called a primitive cell. A primitive cell (volume of space having one lattice point) is the parallelepiped defined by primitive axes $\boldsymbol{a_1}$, $\boldsymbol{a_2}$ and $\boldsymbol{a_3}$. For primitive crystal Systems with higher symmetry we use reciprocal lattice (the sum

http://dx.doi.org/10.5772/intechopen.78584

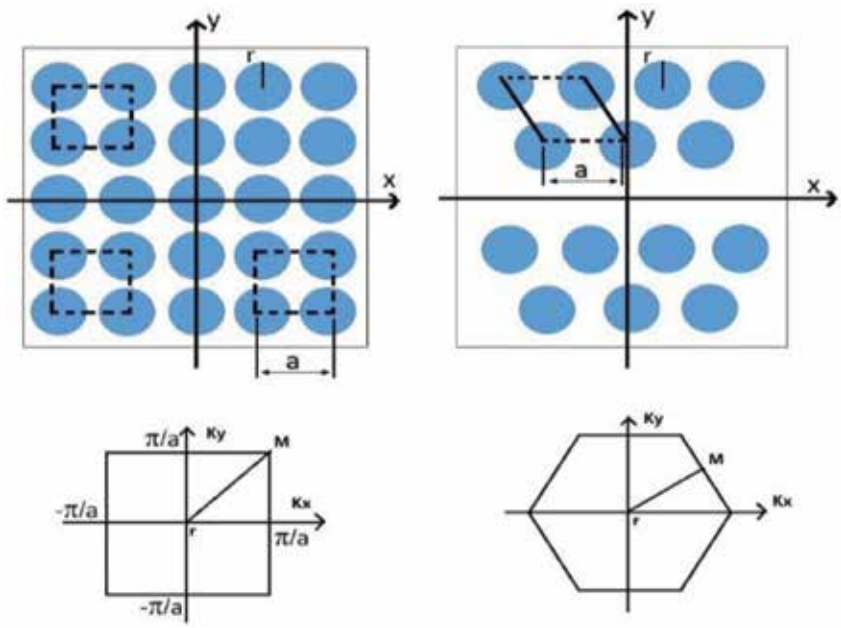

Figure 1. Brillouin zones of two-dimensional cross sections of square and hexagonal lattices with elementary unit cell of lattice parameter "a," and the radius of the inclusions "r."

of the components in the *k*-space). Therefore, the axis vectors of the reciprocal lattice can be constructed from three fundamental translation vectors $\boldsymbol{a_1}$, $\boldsymbol{a_2}$ and $\boldsymbol{a_3}$ [10] (**Figure 1**).

$$b_1 = \frac{2\pi(a_2 \times a_3)}{a_1.a_2 \times a_3}, b_2 = \frac{2\pi(a_3 \times a_1)}{a_1.a_2 \times a_3}, b_3 = \frac{2\pi(a_1 \times a_2)}{a_1.a_2 \times a_3} \tag{3}$$

Any periodic structure, the propagation of acoustic waves in a phononic crystal is determined by the Bloch [12] from which the band structure can be derive in the Brillouin zone. The Brillouin zone is a unit cell in the reciprocal lattice. It should be noted that Brillouin zone can be in one (1D), two (2D), or three dimensions (3D). For desiring the possibility of absolute band gaps phononic crystals has been studied in One Dimension (1D) phononic crystals [13] on the basis of literature, Two Dimension (2D) [14, 15], and Three Dimension 3D [14, 15].

2.2. Band gap

Band gaps are used to explain electronic band structures of materials. Bloch theorem tells us that waves of a certain frequency can propagate without scattering through periodic media. But the propagation of waves is stopped at other frequencies. The frequencies range where the propagation is allowed is called bands and where the propagation is stopped is called band gaps. Phononic band gap in the periodic structure can cause the reflection of mechanical wave when incident on phononic crystals. So the propagation is stopped by generating the mechanical wave inside the phononic crystal. The propagation of mechanical wave with audible frequency range is not permitted in phononic crystals of periodicities ranging from meters to centimeters.

To find the band gap in a phononic crystals, we need to understand the energy band structure of a solid for electrons in a crystalline solid by using following Schrödinger equation [16]:

$$E\psi(r) = -\left[\frac{\hbar^2}{2m}\nabla^2 + V(r)\right]\psi(r) \tag{4}$$

where E is the total energy, Ψ is the wave function, $\hbar$ is the Planck's constant, m is the effective mass and V is the potential, r is the position vector, and ∇^2 is the differential operator.

The above single nonrelativistic particle Eq. (4) shows the total energy is the sum of kinetic energy, and potential energy. Bloch proved the solutions of the wave function in the Schrödinger equation for a periodic potential with periodic function u analogous with crystal as

$$\psi_k(r) = u_k(r)e^{ikr} \tag{5}$$

where ψ is the Bloch wave, k is the crystal wave vector, r is the position, e is Euler's number with imaginary unit i. Actually it consist of product of a plane wave, and a periodic function u_k. The band structure is usually in the form of a dispersion relation between the angular frequency ω and the wave vector k. And k should be in the primitive cell of the primitive lattice vectors of the reciprocal lattice (the first Brillouin zone). Let "a" is the periodicity of one dimensional system, then primitive reciprocal lattice vector is $P = (2\pi/a)$. So the region $[(-\pi/a), (\pi/a)]$ is the first Brillouin zone (**Figure 2**) [10].

Note that gaps width depends upon the difference of wave velocities in the two materials. It means that more difference in periodic medium gives wider band gap. Now comes to phononic band gap. As we are much familiar that in a solid medium (material) atoms cannot move independently since they are connected by chemical bonds and also they move around their equilibrium positions and exert a force on their neighboring atoms to displace, and this displacement cause the phonons creation. The phononic crystals' band structure depend upon the propagation of the elastic/ acoustic waves with suitable materials, shape, crystal lattices, and inclusions with background material [17–19] based on Bragg scattering [17] or by local

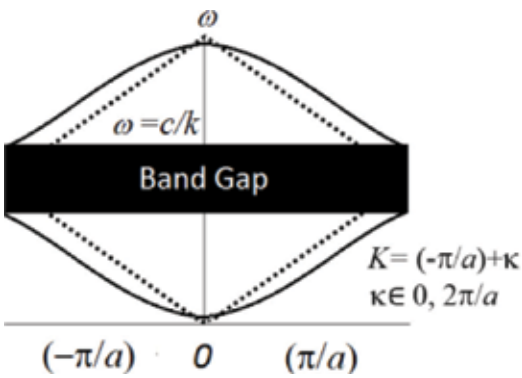

Figure 2. Frequency vs. wave vector for one dimensional linear homogeneous medium (dotted lines), and two dimensional periodic medium (solid lines).

resonance (LR) mechanism [17, 20] in which band gap formed by the internal resonances of the individual inclusions.

As we are familiar with propagation of wave with the motion of atom (say n) with wave number k and angular frequency ω which satisfy the following equation

$$\psi_n = Ae^{ikna}e^{i\omega t} \tag{6}$$

With dispersion relation ω, and upper bound limit of angular frequency ω_0

$$\omega = \omega_0 \left| \sin k\frac{a}{2} \right| \tag{7}$$

So the dispersion relation is in symmetric interval wave vector k $\in(-\pi/2, \pi/2)$.

2.3. Dispersions in phononic crystal

The dispersion relations are expressed in terms of the angular frequency $\omega(k)$ and wavenumber (wave vector) k. Dispersion represent the band structure.

$$\omega(k) = V(k)k \tag{8}$$

where $V(k)$ is the wave speed (V is the function of k), and k is the wave vector can be written as $k = 2\pi/\lambda$. In term of phase velocity k should be $V_p=\omega/k$. So the rate of change of angular frequency with respect to time is

$$V_g = \frac{\partial\omega}{\partial k} \tag{9}$$

Eq. (8) shows that dispersion curves are dependent of materials characteristics like elastic constant, and phononic crystal structure. The band gap can be calculated as frequency range between two continuous dispersion curves associated with wave vector k. The propagation of acoustic wave in phononic crystal can be more due to large gap. **Figure 14** describes the band structure with dispersion curves in phononic crystal.

3. Physical nature of phononic crystal

Nature of materials (solid or fluid), and physical characteristics (density and elastic constants) of the inclusions plays an important role in the gaps bandwidth. So, PnC can be define into three classification according to its physical nature.

3.1. Solid–solid phononic crystals

The band gap in these structures is formed by the low and high contrast [20] between different materials. This type of PnC can be square, triangle, and honeycomb [21] which shows its band

gap impact. Moreover for two dimensional solid-solid PnC the elastic displacement is perpendicular to the cylindrical axis in-plane propagation, and parallel to the cylindrical axis out-of-plane propagation [22].

3.2. Fluid–fluid phononic crystals

Only longitudinal modes can exist in these PnCs. These PnCs made up of two different fluids. Large band gap for this PnC can be found by arrangement of Soft polymer hollow cylinders in a water background at low frequencies [23].

3.3. Solid–fluid (mixed composite) phononic crystals

These PnCs can be constructed by solid inclusions in a fluid (condensed liquid [24, 25, 33] or a gas [26, 27]) matrix and vice versa. Only complex modes of vibration occur from longitudinal in the fluid to longitudinal and transverse in the solid region. So that is why the mixed composite PnCs' acoustic band structures cannot be predicted accurately by using plane wave expansion (PWE) method [23].

Moreover shape of the inclusions play an important role in the formation of band gap. According to geometry PnCs can be in one (1D), two (2D), or three dimensions (3D). Absolute phononic gap should be appear at frequency below the Bragg limit, so this phenomena can happen in locally Resonant materials [28] and can obtained in 2D, and 3D phononic crystals.

4. Phononic crystal composition

Phononic crystals consist of different dimensional periodicity structure having their own characteristics.

4.1. One dimensional phononic crystal

One dimensional phononic crystals (PnCs strip) [4, 18, 20, 29] are composed of two or many layers repetition of geometrical space in a certain direction. The one -dimensional PnCs are also called super lattices (SLs) [30]. The combination of solid–solid or solid–fluid-layered formed each cell of super lattices. The only one direction is responsible for the propagation of an elastic (acoustic) waves in these models.

The periodic band gap structures of SLs consist of crystalline, amorphous semi-conductors. One-dimensional PnC is made up of N cells which show two types of confined states [12]:

i. N–1 states in the allowed bands

ii. One and only one state corresponding to each band gap and do not depend on the width of the crystal N [31].

http://dx.doi.org/10.5772/intechopen.78584

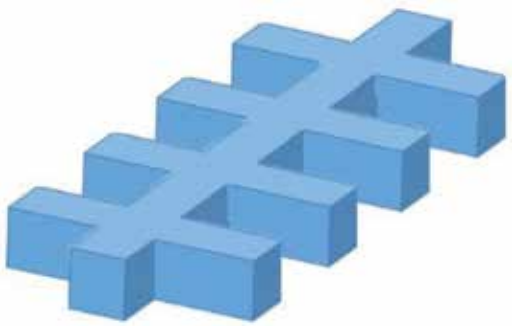

Figure 3. 1D phononic crystal structure.

From 1D systems we conclude that their design is more suitable and based on very simple analytical and numerical calculations to understand different physical properties relevant with band gaps. One dimensional PnCs mainly focus on exploiting the properties of stubs like the shape of the stubs, locations of stubs on the background material, types of waves and creation of defect of background to widen or lower band gaps [18]. In the range of low-frequency there is a wave speed for propagation perpendicular/parallel to layering [31, 32], the one-wave speed for propagation perpendicular to the layering, and two-wave speeds for propagation parallel to the layering (**Figure 3**).

4.2. Two dimensional phononic crystal

As compare to one dimension (1D) PnC the two dimension (2D) PnC has better ability to trap the elastic energy. Repetition of the periodicity in two directions of the space formed a 2D PnCs structure. Its structural arrangement is like the pattern of air holes on silicon or piezoelectric materials [5, 6]. This type of PnC slab can be constructed in square, triangle, hexagonal lattices, or folded structure [34] stepped pillars and holes [3], honeycomb lattice [33], square pillar [19], chessboard-patterned bi-component array, square lattice with cylinder pillars [35], and polygonal graphene like lattice [36]. Following is the schematic of square pillars PnC plate (**Figure 4**) [18].

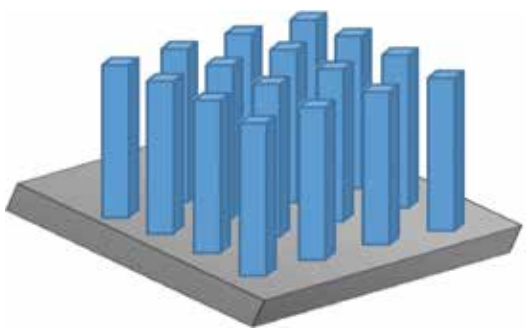

Figure 4. 2D phononic crystal structure.

A triangular Bravais lattice crystal [37] having cylinders shaped assembled structure with vertices of the equilateral triangles with vectors $\boldsymbol{a_1}$, $\boldsymbol{a_2}$ considered as direct lattice, and b_1, b_2 correspond to reciprocal lattice as shown in structure below.

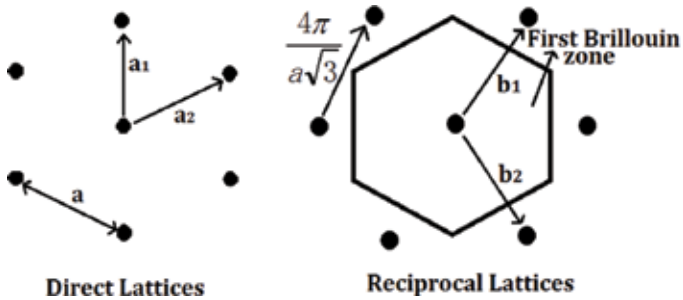

$\vec{a_i} . \vec{b_j} = 2\pi\delta_{ij}$, and $\left|\vec{b_1}\right| = \left|\vec{b_2}\right| = \frac{4\pi}{a\sqrt{3}}$, δij is known as Kronecker delta.

4.3. Three dimensional phononic crystal

Crystals with scattering units (rod, sphere) [25] that are simply air void cylinder which gives rise to Bragg reflections of the acoustic (elastic) waves. So constructive or destructive interference creates in crystal and these constructive and destructive interference creates frequency range at which wave propagate or block. The propagation, and blocking of waves refer to pass bands, and stop bands respectively. Structure of crystal plays an important role in the creation of band gap. It means that contrast between the materials can be produced with the large band gaps. Like changing from water to epoxy (liquid matrix to the solid) gives larger band gaps [38]. The fabrication process of the 3D phononic crystals requires high accuracy of structural patterns (**Figure 5**) [38, 51].

Structure of 3D phononic crystal is made up of a face-centered cubic (FCC) crystal having spheres shaped assembled structure obtained from one sphere which is added to the center of each face of the simple cubic unit cell.

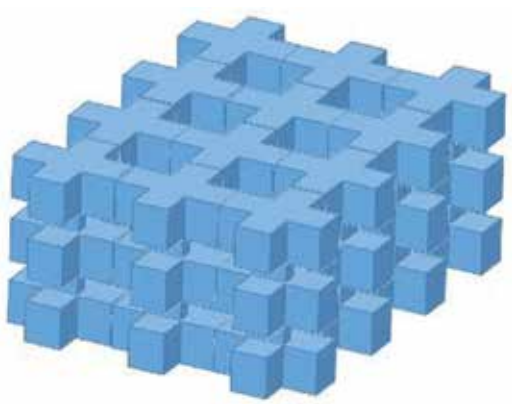

Figure 5. 3D phononic crystal structure.

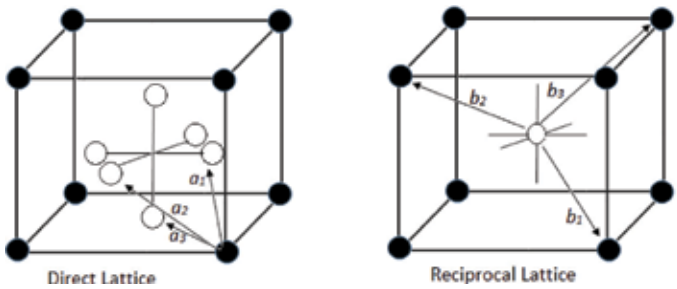

where $\vec{a_1}$, $\vec{a_2}$, $\vec{a_3}$, $\vec{b_1}$, $\vec{b_2}$, $\vec{b_3}$ are the primitive vectors, and a is the cube edge length.

$\left|\vec{a_1}\right| = |a_2| = |a_3| = \frac{a}{\sqrt{2}}$, and $\left|\vec{b_1}\right| = \left|\vec{b_2}\right| = \left|\vec{b_3}\right| = \frac{2\sqrt{3}\pi}{a}$.

So artificially complex structure of 3D phononic crystal fascinating the researcher to develop new kind of phononic crystal with more precise attenuation band in the range of acoustic frequency with better performance used in an engineering field.

5. Phononic crystal based MEMS resonator

Now a days MEMS technologies and the applications of MEMS resonators in communication systems are widely used. MEMS technologies covers many of devices like micro-sensors, actuators, accelerometers, variable capacitors, switching filters, oscillators, couplers, and the main is resonators, and other sensing devices. These operation of PnC MEMS devices is based on the energy conversion between the mechanical and electrical domains [9]. There are many MEMS component which are used in electronic application systems, Telematics, Medical Electronics, etc., but PnC MEMS resonator play an important role in such kind of application systems and improve the performance of devices by resonant frequency stability, quality factor, motional resistance, nonlinearity, and power handling. Insertion loss in the filters, and phase noise in the oscillators can be reduce by PnC MEMS resonators. It can also help to avoid signal distortion and stabilize the operating frequency. Air scattering inclusion on solid background and two-dimensional structures are common employing in PnCs MEMS resonators. The micro-mechanical structures of MEMS resonators operate on an electromechanical transduction mechanism. This mechanism is the conversion of reversible process between electrical and mechanical energy [39]. Electrostatic, piezoresistive, and piezoelectric are the three main

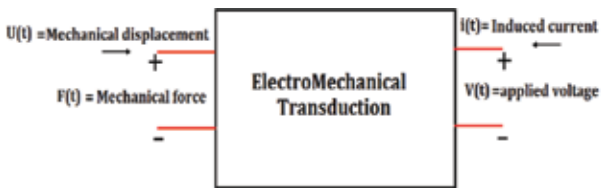

Figure 6. Transduction mechanism.

Transduction methods which are used in MEMS resonators. Following diagram shows the basis transduction mechanism in MEMS resonators (**Figure 6**).

5.1. Electrostatically-transduced MEMS resonators

Electrostatically-transduced MEMS Resonators are also known as capacitive MEMS resonators. The basic principle of this kind of resonator is variation between electrodes and resonating body when the resonant structure vibrates in its mode shape so that the capacitance change. The current is change at output due to change in capacitance by following relation [11].

$$i_m(\omega) = \frac{\partial C_d}{\partial x} V_{DC} \dot{x}(\omega) \tag{10}$$

where $i_m(\omega)$ is the motional current, ω is the angular frequency, C_d is the capacitance between the gap and resonant body with bias voltage V_{DC}, and $\dot{x}(\omega)$ is the vibration amplitude of the resonator. A direct current (DC) (which is bias voltage) is applied to the resonator body, and an alternating current (AC) signal to input electrodes. So the capacitance takes place between the output electrode and resonant body. Due to this phenomena an electrostatic force between the input/drive electrodes and resonant body generates from the combination of the AC and DC voltages. So the structure is set into its resonant mode (frequency of the drive signal is same as the resonant frequency of the resonator) (**Figure 7**).

The above structural mechanism is quite very simple it consist of two parallel-plates called electrodes one is input (excite) and other is output (sense) electrode placed at two sides of the resonator. Applied the DC voltage to the resonant body through anchor/support tether. The output signal is taken from the sense electrode by giving AC signal to excite electrode. Although a very high Q is the great advantage of electrostatic transduction through capacitive MEMS resonators. But the main drawback of such resonator are high impedance and low transduction efficiency at the high frequency [40].

5.2. Piezoresistively-Transduced MEMS resonators

In 1856 L. Kelvin discovered the piezoresistive effect, and later this effect is applied on MEMS resonators as a transduction which is studied by some researchers. [41–44]. These kind of

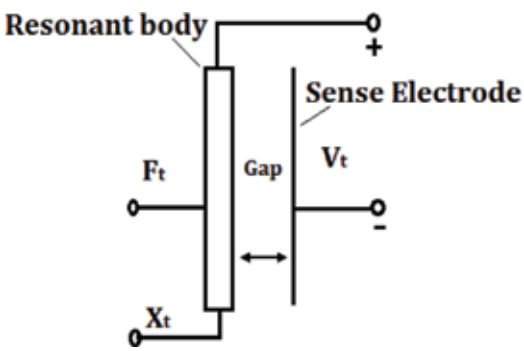

Figure 7. Electrostatic transduction scheme.

MEMS resonators operate based on the change of electrical resistance of material caused by applied mechanical stress or material deformation by using transduction scheme with silicon piezoresistive. Such phenomena can be seen in some crystalline (non-amorphous) materials. Piezoresistive MEMS resonator show low effective impedance. Moreover piezoresistivity depend upon electrical resistivity by following Eq. (11)

$$\frac{\Delta\rho}{\rho} = (GF)\varepsilon \tag{11}$$

where $\Delta\rho/\rho$ is the relative change in specific resistivity with piezoresistor strain ε, and GF is the strain factor (Gauge factor). Some times GF can be expressed as πE. Here E is the Young's modulus and π is the piezoresistivity matrix expressed below.

$$\pi = \begin{bmatrix} \pi_{11} & \pi_{12} & \pi_{12} & 0 & 0 & 0 \\ \pi_{12} & \pi_{11} & \pi_{12} & 0 & 0 & 0 \\ \pi_{12} & \pi_{12} & \pi_{11} & 0 & 0 & 0 \\ 0 & 0 & 0 & \pi_{44} & 0 & 0 \\ 0 & 0 & 0 & 0 & \pi_{44} & 0 \\ 0 & 0 & 0 & 0 & 0 & \pi_{44} \end{bmatrix}$$

The principle of piezoresistively-transduced MEMS resonator is not so complicated. The electrodes of resonator is applied by both voltage sources AC and DC then vibration is generated by the electrostatic force and the resistance of resonator changes due to this effect, also an AC current is induce by this vibration [44, 45] (**Figure 8**).

V_{DC} is connected through the resistors while V_{AC} is applied through the capacitor, and from the supporting tether the output current has been taken.

5.3. Piezoelectrically-transduced MEMS resonators

In 1880 French physicist P. Curie was first found the piezoelectric phenomena [46] on crystals of quartz, tourmaline, cane sugar, topaz. Piezoelectrically transduced MEMS resonators have been developed in recent years based upon piezoelectric effects and early studies on quartz

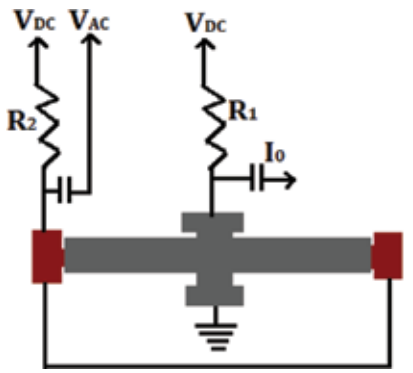

Figure 8. Schematic of piezoresistive resonator.

piezoelectric resonators. The basic principle of the piezoelectric MEMS resonators is that piezoelectric effect happening in piezoelectric materials to induce electric charges on surface of output electrodes. DC voltage must applied to resonator for operation. The impedance of the resonators can be reduced by increasing the DC voltage, so it can improve the performance of resonator. Electromechanical coupling of the resonators is effected by the gap between electrodes and resonant body. Coupling can be high if the gap is narrow. In Electrostatically-Transduced, and piezoresistively-Transduced MEMS Resonators there is a problem of high motional impedance, so this sort of problem can be reduce by piezoelectrically-Transduced scheme because piezoelectric operates on vibration mode then induces charges on the surface of output electrodes when AC is applied to electrodes.

Moreover the performance of resonator depends upon quality factor, resonant frequency, motional resistance, power handling, nonlinearity and frequency stability. Quality factor and operating frequency are the two main parameters that can improve the performance of MEMS devices such as electrostatically-transduced MEMS devices and piezoresistively-transduced MEMS devices which is known as silicon-on-insulator (SOI) technology [42, 49]. But the electrostatically transduced based designs is almost limited at high frequencies due to their inherently small coupling coefficients.

5.4. Quality factor and band width

Quality factor is the ability of energy storage under damping mechanisms at their resonant frequency. When the quality factor is higher, the better the performance of resonator will be better. An ideal resonator can have an infinite quality factor value. Attenuation of quality factor may cause the damping sources. Damping can be generated by temperature, and the nature of materials. If Q factor is higher, then energy loss is low.

Figure 9 above shows the resonance width (band width) Δf, and f (refer to f_r) is the resonant frequency. So $Q = f/\Delta f = 2\pi\ E_{stored}/E_{dissipate\ per\ cycle}$, where E refers to energy.

Figure indicates the high, low, and intermediate Q factors are said to be an underdamped ($Q > 1/2$), over damped ($Q < 1/2$), and critically damped ($Q = 1/2$) respectively. The parameters like bandwidth, spurious signals, ringing also dependent on Q. When the value of Q factor increase

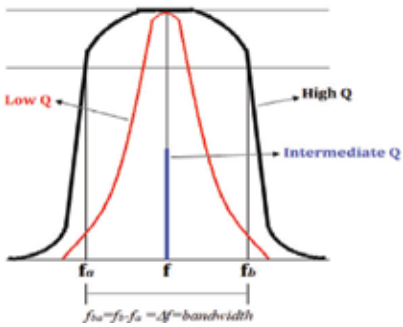

Figure 9. Different frequency responses in MEMS resonators.

the band width of circuit must decrease, so energy storage is better and response of circuit can increase. Moreover when the value of Q increase the spurious signals can be removed by the circuit (losses decrease) and circuit will be able to ring more.

5.5. Motional resistance

Motional resistance is an impedance of resonator can be expressed by the following formula having angular frequency ω, resonator's equivalent mass m_{eq}, and quality factor Q.

$$R_m = \frac{\omega m_{eq}}{\eta_1 \eta_2 Q} \tag{12}$$

where

$$m_{eq} = {}^{eq} \frac{\rho T}{U_m(x_m, y_m)^2} \int\int U(x,y)^2 dxdy \tag{13}$$

In above equation η is the mechanical coupling coefficient which depends upon piezoelectric transduction mechanism (ratio of the current passing through the resonator to the maximum velocity) can be expressed as

$$\eta = \frac{i}{v_{\max}} = \frac{Q_T}{U_{\max}} \tag{14}$$

where Q_T is the induced electric charge can be expressed as

$$Q_T = \int\int D_i dxdy \tag{15}$$

The motional resistance and quality factor of MEMS resonators are inversely proportional to each other.

6. Phononic crystal strips in MEMS resonator

The phononic crystals are presented as main theories for designing the support tethers in thin film aluminum nitride on diamond contour mode MEMS resonators.

6.1. Support tether configuration

Here we introduce our work [47] on MEMS Resonators with supporting tether configurations which is based on reflector and phononic crystal strip by using thin films piezoelectric material (Aluminum Nitride) on diamond. Diamond is used as a substrate material. **Figure 10** shows the PnC strips support tethers of MEMS resonators.

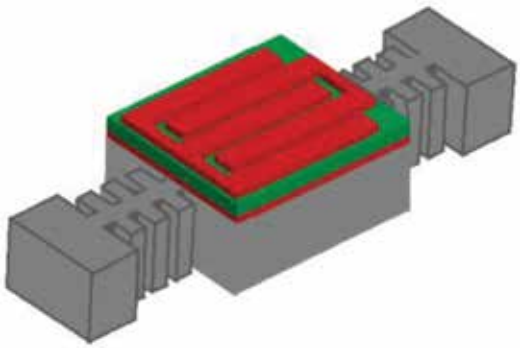

Figure 10. PnC MEMS resonator with supporting tethers.

In this work the quality factor has been improved. Because the tether structures improve the quality factor of MEMS resonators. PnCs also support elimination of anchor loss in the resonators. PnCs can also be designed for sensor applications.

From **Figure 11** we see that each resonator consists of a thin-film aluminum nitride piezoelectric layer sandwiched between two gold (Au) metallic electrode layers which is located on thick diamond substrate layer and operate at 115 and 156 MHz, respectively. Gold has a very high electrical conductivity and very low resistivity [47] so it can reduce the energy dissipation. When thin film aluminum nitride is applied by an electric field from gold electrodes then strain field is created in the thin film and mechanical vibration of resonators increase. Following Eq. (16), and Eq. (17) represent the resonant frequency of WG and WS resonator with effective mass density ρ_{eff} respectively.

$$f_{WG} = \frac{1}{2L}\sqrt{\frac{E_{eff}}{(1+V_{eff})\rho_{eff}}} \tag{16}$$

$$f_{WS} = \frac{1}{2W}\sqrt{\frac{E_{eff}}{\rho_{eff}}} \tag{17}$$

where L is the side length, and W is the side width of WG resonator, and WS resonator respectively, E_{eff}, and v_{eff} is the effective Young's modulus, and the effective Poisson's ratio respectively. We can calculate the values of E_{eff}, v_{eff}, and ρ_{eff} by using following formula

$$P_{eff} = \frac{t_{AIN}p_{AIN} + 2t_{AU}p_{AU} + t_{Di}p_{Di}}{t_{AIN} + 2t_{AU} + t_{Di}} \tag{18}$$

where t_{AlN}, t_{Au} and t_{Di} are the thickness of aluminum nitride.

Clamping of tether with MEMS resonators at corners is obtained by COMSOL through FE simulation as shown in **Figure 11** above. Now come to the PnC strip with supporting tether [47], as we discussed above that PnC is a highly periodic structure of unit cell which is the basic block. In this work we take the PnC strip of five unit cells as shown below (**Figure 12**).

http://dx.doi.org/10.5772/intechopen.78584

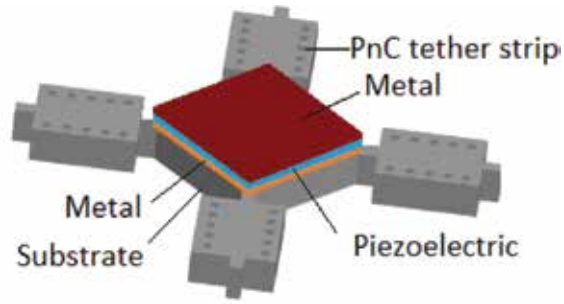

Figure 11. Resonators with Eigen mode shapes.

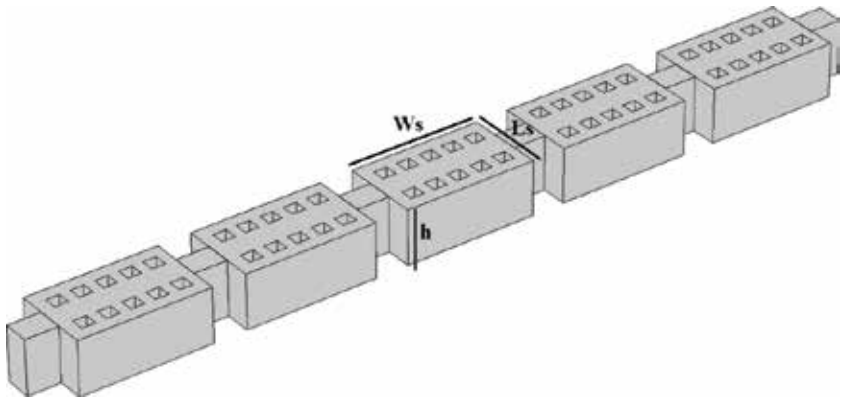

Figure 12. Phononic crystal strip.

Moreover this work only investigates the band gap variation with W_s (stub width), L_s (stub length), and W_h (side hole) of unit cells of the PnC strip.

The parameters of the WG and WS mode resonators and a unit cell of the PnC strip are given in **Table 1**. Following **Figure 13** shows the analysis of eigen frequency mode of the resonators for positioning of anchor tether placement location.

As we discussed above that band gaps is used to explain electronic band structures of materials and can cause the reflection of mechanical wave in the periodic structure when incident on phononic crystals. So here is the band structure with simulated dispersion curve represented as blue dotted lines, and band gaps represented in yellow area having stub width: Ws = 28 μm, stub length: Ls = 30 μm, and hole width: Wh = 2.5 μm (**Figure 14**).

From these results we arrived at this point that.

The role of Stub is important in the formation of band gaps, particularly in its length. If L_s is large the band gap is wide.

i. Holes can help to reduce the static mass of the PnC strip tether without effecting on band gaps.

	WG				WS					
	Resonator	**Electrode**	**Substrate**	**Piezoelectric**	**Resonator**	**Electrode**	**Substrate**	**Piezoelectric**	**Unit cell**	**Stub**
Thickness (μm)		0.1	3	0.4		0.1	3	0.2	3	
Width (μm)	60	60			48	23			6	28
Length (μm)	60				80					30

Table 1. Parameters of PnC strip WG and WS mode resonators.

http://dx.doi.org/10.5772/intechopen.78584

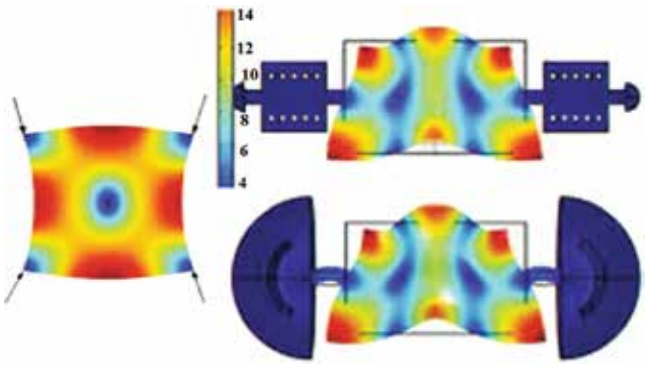

Figure 13. Resonators with Eigen mode shapes.

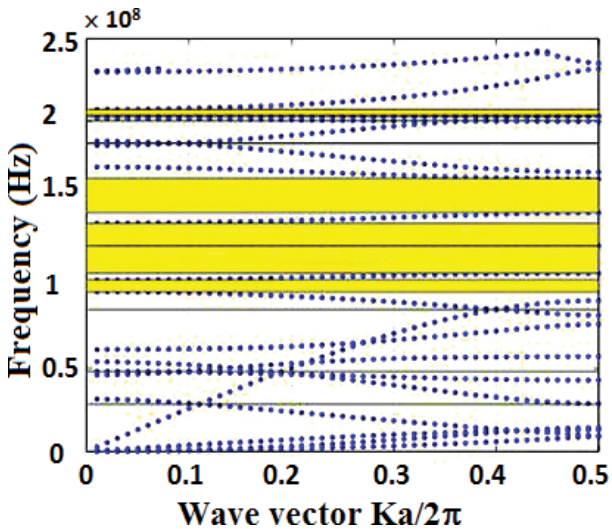

Figure 14. Band structure with dispersion curves in PnC.

6.2. Quality factor and harmonic response

Several MEMS resonators has been fabricated [48] with high quality factor, temperature stability with high frequency. Several techniques have been used to minimize the anchor loss, and improve quality factor in resonator such as impedance mismatching between resonator body and support tethers, quarter-wavelength tethers, narrowed-width tethers, geometrical shape-based tethers, acoustic wave reflection based tethers. And one of the sound technique is phononic crystal (PnC) based tethers [47] which is highly effective in reduction of anchor loss, and improve the quality factor in resonator. High quality factor reduces motional resistance. Phononic crystals boosting the anchor quality factor and present the ability of acoustic/elastic wave propagation isolation as well as reflection. **Figure 15** shows the Q factor, and anchor Q factor for PnC strip tethers.

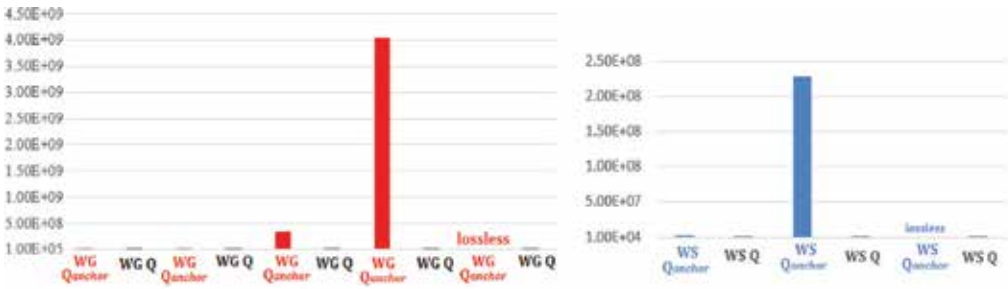

Figure 15. WG and WS modes for PnC strip supporting tethers.

The maximum value of Q obtained from WG mode resonator with five-unit cell PnC strip tethers is 398.5% and from WS mode resonator with three-unit cell PnC strip tethers is 591.1%. The values of Q and Qanchor for WS WG mode resonator, and WS mode resonator for their corresponding unit cells are shown in **Table 2**.

To see the harmonic response of resonators voltage is applied by two sources 1 V and -1 V. **Figure 15** depicted the curve between frequency and displacement. Narrow curve indicate that the quality factor is much higher, but this is fact that the quality factor is always limited by energy losses. In MEMS resonator the harmonic response is represented by electric charge and admittance (**Figure 16**).

6.3. Anchor loss

Anchor is basically the attachment of supporting frame mechanical connection between the resonators In all micromechanical resonator there must be the energy loss called an anchor damping or anchor loss due to radiation of acoustic wave energy from the resonant structure via supporting tether [10, 48, 50, 51], so the energy entered in the substrate when resonator vibrate.

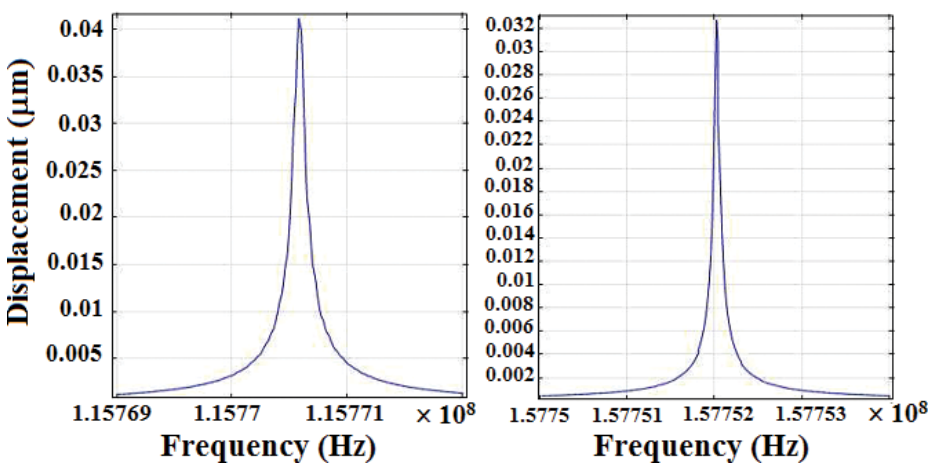

Figure 16. Harmonic response: WG and WS mode PnC strip resonators with supporting tethers.

Unit Cell	WG mode		WS mode	
	Q_{anchor}	Q	Q_{anchor}	Q
1	1.2954E6	4.5638E5	3.0251E6	3.1128E5
2	2.7839E7	6.9205E5	2.2752E8	3.8383E5
3	3.3660E8	7.1349E5	lossless	4.1347E5
4	4.0541E9	7.2244E5	—	
5	lossless	7.2406E5	—	

Table 2. Q, and Q_{anchor} of PnC strip tether resonators.

In other words we can say that in the resonator, elastic waves are trapped at resonance. This phenomena may cause the loss of energy. The anchor size is responsible for the loss of energy (anchor loss). One way of reduce the anchor loss is to increase the number of tethers and slightly reduce the size of tethers [52].

7. Summary

This chapter has employed the theory of phononic crystal, classification of PnC according to its physical nature, and PnC phenomena in locally resonant materials with 2D, and 3D crystals structure. In this chapter PnC MEMS resonators with different transduction schemes such as electrostatically, piezoresistively, piezoelectrically-transduced MEMS resonators are explained. In this chapter phononic crystal strip in MEMS resonators is explained to reduce anchor loss, so phononic crystal strip with supporting tethers is designed to see the formation of band gap by introducing square holes, and improvement of quality factor. Moreover few simulation tools like COMSOL Multi-physics for designing, MATLAB for extracting parameters and EXCEL for representation of graphs are used.

Author details

Bao Jing-Fu*, Muhammad Ammar Khan* and Bao Fei-Hong

*Address all correspondence to: baojingfu@uestc.edu.cn and ammar@uestc.edu.cn

School of Electronic Science and Engineering, University of Electronic Science and Technology of China, P.R. China

References

[1] Yablonovitch E. Inhibited spontaneous emission in solid-state physics and electronics. Physical Review Letters. 1987;**58**:2059-2062

[2] Joannopoulos JD, Meade RD, Winn JN. Molding the Flow of Light. Princeton: Princeton University Press; 1995

[3] Assouar MB, Sun J, Lin F, Hsu J. Hybrid phononic crystal plates for lowering and widening acoustic band gaps. Ultrasonics. 2014;**54**(8):2159-2164

[4] Sause MGR, Hamstad MA. Numerical modeling of existing acoustic emission sensor. Sensors & Actuators A: Physical. 2018;**269**:294-307

[5] Nassar H, Chen H, Norris AN, Huang GL. Quantization of band tilting in modulated phononic crystals. Physical Review B. 2018;**97**:014305

[6] Rottenberg X, Jansen R, Tilmans HAC. Phononic bandgap coupled bulk acoustic wave resonators. IEEE 25th International Conference on Micro Electro Mechanical Systems (MEMS). 2012:725-728

[7] Nomura M, Kage Y, Müller D, et al. Electrical and thermal properties of polycrystalline Si thin films with phononic crystal nanopatterning for thermoelectric applications. Applied Physics Letters. 2015;**106**(22):12727

[8] Joannopoulos JD, Johnson SG, Winn JN, Meade RD. Photonic Crystal Molding the Flow of Light. 2nd ed. Princeton, NJ, USA: Princeton University Press; 2008

[9] Ha TD, Bao J-F. A phononic crystal strip based on silicon for support tether applications in siliconbased MEMS resonators and effects of temperature and dopant on its band gap characteristics. AIP Advances. 2016;**6**:045211

[10] Kittel C. Introduction to Solid State Physics. New York: Wiley; 1996

[11] Wang QP, Bao JF, Ling Y, Li XY. Design of a novel RF MEMS square resonator. Microsystem Technologies. 2015;**21**(8):1805-1810

[12] Ren S-Y. Complete quantum confinement of one-dimensional Bloch waves. Physical Review B. 2001;**64**(3):314-319

[13] El Boudouti EH, Djafari Rouhani B, Akjouj A, Dobrzynski L. Acoustic waves in solids and fluid layered materials. Surface Science Reports. 2009;**64**:471

[14] Meng L, Shi Z, Cheng Z. A new perspective for analyzing complex band structures of phononic crystals. Journal of Applied Physics. 2018;**123**(10):095102

[15] Zhang WQ, Zhang X, Wu FG, et al. Angular control of acoustic waves oblique incidence by phononic crystals based on Dirac cones at the Brillouin zone boundary. Physics Letters A. 2018;**382**(6):423-427

[16] Momox E, Zakhleniuk N, Balkan N. Solution of the 1D Schrödinger equation in semiconductor heterostructures using the immersed interface method. Journal of Computational Physics. 2012;**231**(18):6173-6180

[17] Ma C, Guo J, Liu Y. Extending and lowing band gaps in one-dimensional phononic crystal strip with pillars and holes. Journal of Physics and Chemistry of Solids. 2015;**87**:95-103

[18] Zou K, Ma T, Wang Y. Investigation of complete bandgaps in a piezoelectric slab covered with periodically structured coatings. Ultrasonics. 2016;**65**:268-276

[19] Babaee S, Wang P, Bertoldi K. Three-dimensional adaptive soft phononic crystals. Journal of Applied Physics. 2015;**117**(24):962-318

[20] Charles C, Bonello B, Ganot F. Propagation of guided elastic waves in 2D phononic crystals. Ultrasonics. 2006;**44**(4):1209-1213

[21] Hassouani YE, Li C, Pennec Y, et al. Dual phononic and photonic band gaps in a periodic array of pillars deposited on a thin plate Phys. Rev. B. 2010;**82**:155405

[22] Khelif A, Adibi A. Phononic Crystals Fundamentals and Applications. New York: Springer-Verlag; 2016

[23] Lambin P, Khelif A, Vasseur JO, Dobrzynski L, Djafari-Rouhani B. Stopping of acoustic waves by sonic polymer-fluid composites. Physical Review E. 2001;**63**:066605

[24] Vasseur JO, Deymier PA, Chenni B, Djafari-Rouhani B, Dobrzynski L, Prevost D. Experimental and theoretical evidence for the existence of absolute acoustic band gaps in two dimensional solid phononic crystals. Physical Review Letters. 2001;**86**(14):3012

[25] Liu Z, Chan CT, Sheng P, Goertzen AL, Page JH. Elastic wave scattering by periodic structures of spherical objects: Theory and experiment. Physical Review B. 2000;**62**:2446

[26] Soukoulis CM. Photonic Crystals and Light Localization in the 21st Century. 2001. Vol. 34 (12):1997. Kluwer Academic Publisher

[27] Caballero D, Sanchez-Dehesa J, Rubio C, Martinez-Sala R, Sanchez-Perez JV, Meseguer F, Llinares J. Large two-dimensional sonic band gaps. Physical Review E. 1999;**60**(6316)

[28] Liu Z, Zhang X, Mao Y, Zhu YY, Yang Z, Chan CT, Sheng P. Locally resonant sonic materials. Science. 2000;**289**(5485):1734-1736

[29] Feng D, Xu D, Wu G, et al. Phononic crystal strip based anchors for reducing anchor loss of micromechanical resonators. Journal of Applied Physics. 2014;**115**(2):251-701

[30] Esaki L, Tsu R. Superlattice and negative differential conductivity in semiconductors. IBM Journal of Research & Development. 1970;**14**(61):61-65

[31] Ren SY. Two types of electronic states in one-dimensional crystals of finite length. Annals of Physics. 2002;**301**(1):22-30

[32] Schouenberg M. Wave propagation in alternating solid and fluid layers. Wave Motion. 1984;**6**(3):303-320

[33] Gao Z, Fang J, Zhang Y, Jiang L. Band structure research of a 2D honeycomb lattice Phononic crystal. International Journal of Electrochemical Science. 2013;**8**(6):7905-7917

[34] Wang S, Popa LC, Weinstein D. GaN MEMS resonator using a folded phononic crystal structure. In: Solid-State Sensors, Actuators, and Microsystems Workshop. 2014. pp. 72-75

[35] Pourabolghasem R, Mohammadi S, Eftekhar AA, et al. Experimental evidence of high-frequency complete elastic bandgap in pillar-based phononic slabs. Applied Physics Letters. 2014;**105**(23):111902

[36] Huang Z, Su C. Band gap effects in a two-dimensional regular polygonal Graphene-like structure. Crystal Structure Theory and Applications. 2014;**3**(1):10-21

[37] Deymier PA. Springer Series in Solid-State Sciences: Acoustic Metamaterials and Phononic Crystals. USA; 2013

[38] Page JH, Yang S, Cowan ML, Liu Z, Chan CT, Sheng P. 3D phononic crystals. In: Wave Scattering in Complex Media: From Theory to Applications. Amsterdam: Kluwer Academic Publishers: NATO Science Series; 2003. pp. 283-307

[39] Tilmans HAC. Equivalent circuit representation of electromechanical transducers: I. Lumped-parameter systems. Journal of Micromechanics and Micro engineering. 1996; **6**(1):157-176

[40] Wang J, Butler JE, Feygelson T, Nguyen CT-C. 1.51-GHz polydiamond micromechanical disk resonator with impedance-mismatched isolating support. IEEE International Conference on Micro Electro Mechanical Systems. 2004:641-644

[41] Bao F-H, Bao L-L, Zhang X-S, et al. Frame structure for thin-film piezoelectric-on-silicon resonator to broader enhance quality factor and suppress spurious modes. Sensors and Actuators A: Physical. 2018;**274**:101-108

[42] Tu C, Zhu H, Xua Y, et al. Differential capacitive input and differential piezoresistive output enhanced transduction of a silicon bulk-mode microelectromechanical resonator. Sensors and Actuators A: Physical. 2014;**210**(1):41-50

[43] Xu Y, Zhu H, Lee JEY. Piezoresistive sensing in a strongly coupled high Q Lamé mode silicon MEMS resonator pair. IEEE International Conference on Frequency Control Symposium (FCS). 2014:1-5

[44] Vamshi V, Nair DR, DasGupta A. Design a piezoresistive MEMS resonator operating beyond 1 GHz. Physics of Semiconductor Devices. 2014:461-464

[45] Tu C, Lee JEY. Observations on stability in a carrier injected SOI Piezoresistive resonator. Procedia Engineering. 2012;**47**(7):969-972

[46] Manbachi A, Cobbold RSC. Development and application of piezoelectric materials for ultrasound generation and detection. Geophysics. 2011;**80**(2):187-196

[47] Ha TD, Bao. Reducing anchor loss in thin-film aluminum nitride on diamond contour mode MEMS resonators with support tethers based on phononic crystal strip and reflector. Microsystem Technologies. 2016;**22**(4):791-800

[48] Nguyen CTC. MEMS Technology for Timing and Frequency Control. IEEE Transactions on Ultrasonics, Ferroelectrics, and Frequency Control. 2007;**54**(2):251-270

[49] Fu JL, Tabrizian R, Ayazi F. Dual-mode AlN-on-silicon micromechanical resonators for temperature sensing. IEEE Transactions on Electron Devices. 2014;**61**(2):591-597

[50] Ho GK, Abdolvand R, Sivapurapu A, et al. Piezoelectric-on-silicon lateral bulk acoustic wave micromechanical resonators. Journal of Microelectromechanical Systems. 2008;**17**(2): 512-520

[51] Delpero T, Schoenwald S, Zemp A, Bergamini A. Structural engineering of three-dimensional phononic crystals. Journal of Sound and Vibration. 2016;**363**(2):156-165

[52] Multi-stage phononic crystal structure for anchorloss reduction of thin-film piezoelectric-on-silicon microelectromechanical-system resonator. Applied Physics Express. 2018;**11**:067201

Chapter 7

Absorption of Acoustic Phonons in Fluorinated Carbon Nanotubes with Non-Parabolic, Double Periodic Band

Daniel Sakyi-Arthur, S. Y. Mensah, N. G. Mensah,
Kwadwo A. Dompreh and R. Edziah

Additional information is available at the end of the chapter

http://dx.doi.org/10.5772/intechopen.78231

Abstract

We studied theoretically the absorption of acoustic phonons in the hypersound regime in Fluorine modified carbon nanotube (F-CNT) Γ_q^{F-CNT} and compared it to that of undoped single walled carbon nanotube (SWCNT) Γ_q^{SWCNT}. Per the numerical analysis, the F-CNT showed less absorption to that of SWCNT, thus $|\Gamma_q^{F-CNT}| < |\Gamma_q^{SWCNT}|$. This is due to the fact that Fluorine is highly electronegative and weakens the walls of the SWCNT. Thus, the π-electrons associated with the Fluorine causes less free charge carriers to interact with the phonons and hence changing the metallic properties of the SWCNT to semiconductor by the doping process. From the graphs obtained, the ratio of hypersound absorption in SWCNT to F-CNT at $T = 45K$ is $\frac{\Gamma_{(SWCNT)}}{\Gamma_{(F-CNT)}} \approx 29$ while at $T = 55K$, is $\frac{\Gamma_{(SWCNT)}}{\Gamma_{(F-CNT)}} \approx 9$ and at $T = 65K$, is $\frac{\Gamma_{(SWCNT)}}{\Gamma_{(F-CNT)}} \approx 2$. Clearly, the ratio decreases as the temperature increases.

Keywords: carbon nanotube, fluorinated, acoustic effects, hypersound

1. Introduction

Acoustic effects in bulk and low dimensional materials have attracted lots of attention recently. This is due to the need of finding coherent acoustic phonons for scientific applications as against the use of conventional direct current [1]. Materials such as homogenous semiconductors, superlattices (SL), graphene and carbon nanotubes (CNT) are good candidates for such studies due to their novel properties such as the high scattering mechanism, the high-bias mean-free path (l) and their sizes which enable strong electron-phonon interaction to occur in them resulting in acoustic phonon scattering. Acoustic waves through these materials are

characterized by a set of elementary resonance excitations and dynamic nonlinearity which normally leads to an absorption (or amplification), acoustoelectric effect (AE) [2], and acousto-magnetoelectric effect (AME) [3, 4]. The concept of acoustic wave amplification was first predicted in bulk materials [5], and later in n-Ge [6]. In SLs, Mensah et al. [7] studied hypersound absorption (amplification) and established its use as a phonon filter, and in [8], predicted the use of the SL as a hypersound generator which was confirmed in [1]. In Graphene, Nunes et al. [9] treated theoretically hypersound amplification, but Dompreh et al. [10] further proved that absorption also occurs in the material. Experimentally, Miseikis et al. [11] and Bandhu and Nash [12] have studied acoustoelectric effect in Graphene.

Carbon nanotubes (CNTs), on the other hand, are cylindrical hollow rod of graphene sheets whose electronic structures are determined by the localized π-electrons in the sp^2- hybridized bonds. Absorption (Amplification) of hypersound in undoped CNT has been carried out theoretically by Dompreh et al. [13, 14] and experimentally by [15, 16]. Other forms of research such as hot-electron effect [17], thermopower in CNT [18] have been carried out. Flourine-modified CNT (F-CNT) is off-late attracting a lot of scientific interest. This is attained by doping the CNT with Fluorine thus forming double periodic band CNT changing from metallic to semiconductor. As per the studies conducted by Jeon et al. [19], absorption in F-CNT is less than that of SWCNT but no studies have been done on the absorption of F-CNT in the hypersound regime. In this paper, the study of absorption of acoustic phonons in metallic SWCNT and F-CNT are theoretically studied. Here, the acoustic wave considered has wavelength $\lambda = 2\pi/q$, smaller than the mean-free path of the CNT and then treated as a packet of coherent phonons (monochromatic phonons) having a δ-function distribution as

$$N(k) = \frac{(2\pi)^3}{\hbar\omega_q v_s}\Phi\delta(k-q) \tag{1}$$

where k is the phonon wavevector, $\hbar$ is the Planck's constant divided by 2π, and Φ is the sound flux density, and ω_q and v_s are respectively the frequency and the group velocity of sound wave with wavevector q. It is assumed that the sound wave is propagated along the z-axis of the CNT.

This paper is organized as follows: In Section 2, the absorption coefficient for F-CNT and SWCNT are calculated. In Section 3, the final equations are analyzed numerically and presented graphically. Section 4 presents the conclusion of the study.

2. Theory

Fluorination plays a significant role in the doping process, as it provides a high surface concentration of functional groups, up to C_2F without destruction of the tube's physical structure. Doping is an easy, fast, exothermic reaction and the repulsive interactions of the Fluorine atoms on the surface debundles the nanotube, thus enhancing their electron dispersion [20]. **Figure 1** shows a one dimensional SWCNT doped with Fluorine atoms [21]. Consider a Fluorine modified

CNT (n, n) with the Fluorine atoms forming a one-dimensional chain. A nanotube of this nature is equivalent to a band with unit cell as shown in **Figure 2**, where b is the bond length (C-C) [22].

The width for the F-(n, n) tube equals n periods (with a periodic length of $3b$), and this unit cell contains $N = 4n - 2$ carbon atoms which is shown in **Figure 3** [22]. **Figure 3** shows the atomic numbering in the unit cell of the F-(n, n) nanotube. For a conjugated $\pi-$ system, in which there is alternation of single and double bonds along a linear chain, the Hückel matrix approximation is

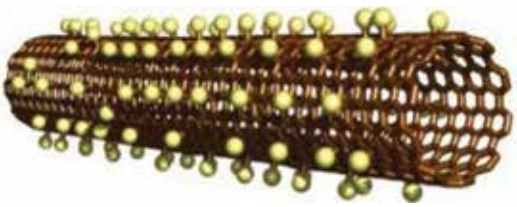

Figure 1. Fluorine modified SWCNT with the Fluorine atoms showing as yellow balls.

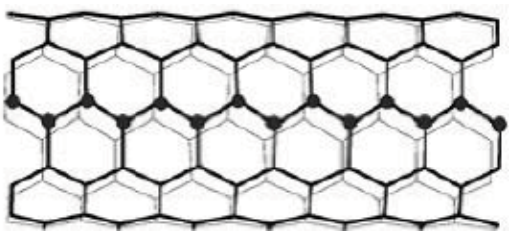

Figure 2. Fluorinated nanotube $F-(n,n)$ (dots denotes the positions of Fluorine atoms of Fluorine atoms that are covalently bonded to C atoms).

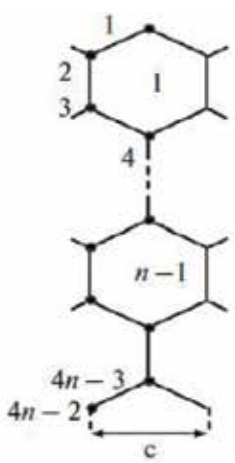

Figure 3. Atom numbering in the unit cells of nanotubes $F-(n,n)$.

employed to determine the electronic energy band. Proceeding as in [8, 23], we employ the Hamiltonian of the electron-phonon system in the FCNT in the second quantization formalism as

$$H = \sum_{p,\nu} \varepsilon^{(\nu)}(p)\left(p - \frac{e}{c}A(t)\right)a_p^{(\nu+)}a_\nu^{(\nu)} + \sum_k \omega_k b_k^+ b_k \ldots + \frac{1}{\sqrt{N}}\sum_{p,k}\sum_{\nu\nu' n} c_k m_{\nu\nu'}(k_z)a_p^{(\nu+)}a_{p-k+ng}^{\nu'}\left(b_k^+ + b_{-k}\right) \tag{2}$$

where $\nu = 1, 2\ldots$ and for a chemically modified F-CNT, where the Fluorine atoms form a one-dimensional chain, the energy dispersion can be deduced by using the Huckel matrix method where translational symmetry is accounted for in [22] as

$$\varepsilon\left(p_z\right) = \varepsilon_o + \Xi_n\gamma_0\cos^{2N-1}\left(ap_z\right) \tag{3}$$

where $a = \sqrt{3}b/(2\hbar)$, Ξ is a constant, N is an integer, and ε_o is the minimum energy of the $\pi-$ electrons within the first Brillouin zone. For $N = 2$, the energy dispersion for F-CNT at the Fermi surface at the edge of the Brillouin zone is

$$\varepsilon\left(p_z\right) = \alpha_\pi + 8\gamma_o\cos^3\left(ap_z\right) \tag{4}$$

Eq. (4) can be expanded as

$$\varepsilon\left(p_z\right) = \varepsilon_o + \Delta_1\cos\left(3ap_z\right) + \Delta_2\cos\left(ap_z\right) \tag{5}$$

where ε_o is the electron energy in the first Brillouin zone with momentum p_o, i.e., $-\pi/a \leq p_o \leq \pi/a$, $\Delta_1 = \Delta/k_BT$, $\Delta_2 = 3\Delta/k_BT$ and $\Delta = 2\gamma_o$. By employing the coulombs gauge, the electromagnetic wave $E(t) = E_o\sin\omega t$ is related to the vector potential $A(t)$ is the vector potential related to the external electric field of the electromagnetic wave $E(t) = E_o\sin\omega t$ by the relation $E = -(1/c)(\partial A/\partial t)$ and is directed along the F-CNT tubular axis. $a_p^{(+)}$ and a_p are the creation and annihilation operators of an electron with quasi-momentum p in the νth miniband respectively, and b_k^+ and b_k are the phonon creation and annihilation operators respectively. N is the number of FCNT periods, $g = (0, 0, 2\pi/d)$ is the FCNT reciprocal vector, and $m_{\nu\nu'}$ is given by

$$m_{\nu\nu'}(k_z) = \int \varphi_{\nu'}^*(z)\varphi_\nu(z)e^{ik_z}dz \tag{6}$$

where $\varphi_\nu(z)$ is the wavefunction of the νth state in one of the one-dimensional potential wells from which the FCNT potential is formed. The electromagnetic wave frequency is assumed to be large compared with the inverse of the electron mean free time $1/\tau$ and the wavelength is taken to be large compared with the FCNT period, electron mean free path and the de Broglie wavelength. This opens the way for us to use the dipole approximation as in [8]. Moreover, the plane electromagnetic wave of frequency ω satisfies $\omega/\omega_p > 1$, where ω_p is the plasma frequency. In the case of the phonons, we confine our considerations to those for which the wavevector $\mathbf{q}$, satisfies the conditions $ql \gg 1$ where l is the electron mean free path in FCNT. Such phonons constitute a well-defined elementary excitations of the system.

For $\omega\tau \gg 1$ and $\omega > \omega_p$, ensures that the electromagnetic wave penetrate the sample and the condition $ql \gg 1$ means that the hypersound wavelength is far smaller than the electron mean free path. The phonon dispersion relation then reads as

$$i\frac{\partial}{\partial t}\langle b_q\rangle_t = \langle [b_q, H]\rangle_t = \omega_q\langle b_q\rangle_t + \frac{1}{\sqrt{N}}C_{-q}\sum_p m_{ss'}(-q_z)\left\langle a_p^{(s+)}a_{p+qng}^{(s)}\right\rangle_t \tag{7}$$

After much simplification, the phonon transition rate in the presence of the electromagnetic reduces to

$$\Gamma(q) = -Im\,\Omega = \frac{2\pi\Phi}{\omega_q V_s}\sum_{p_z,\,n'}\sum_{\ell=-\infty}^{\infty} J_\ell^2(\xi)$$
$$\times\left[f\left(\varepsilon_{n'}(p_z)\right) - f\left(\varepsilon_{n'}(p_z+\hbar q)\right)\right]\delta\left(\varepsilon_{n'}(p_z+\hbar q) - \varepsilon_{n'}(p_z) - \hbar\omega_q - \ell\Omega\right) \tag{8}$$

that is, the imaginary part of the polarization vector. In Eq. (8) $J_\ell(x)$ is the Bessel function of order ℓ and argument x. It follows from Eq. (8) that if $\Gamma(q) > 0$ we have hypersound attenuation, whereas if $\Gamma(q) < 0$ we have hypersound amplification due to absorption $\Gamma(q) > 0$ and emission $\Gamma(q) < 0$ of $|\ell|$ photons from the intensified laser field.

In the region of an intense laser field, i.e., $\xi \gg \omega$, only the electron-phonon collisions with the absorption or emission of $\ell \gg 1$ photons are significant. Accordingly, in the case of $\xi \gg \omega$ the argument of the Bessel function $J_\ell(\xi)$ is large. For large values, the Bessel function $J_\ell(\xi)$ is small except when the order is equal to the argument.

$$\xi = \frac{eE_o a^2\Delta q}{\Omega^2} \tag{9}$$

Taking the sum over $|\ell|$ using the approximation in Eq. (10)

$$\sum_{\ell=-\infty} J_\ell^2(\xi)\delta(E-\ell\Omega) \approx \frac{1}{2}[\delta(E-\xi) + \delta(E+\xi)] \tag{10}$$

where $E = \varepsilon(p_z+\hbar q) - \varepsilon(p_z) - \hbar\omega_q$. Using the Fermi Golden Rule, the phonon transition rate reduces $\Gamma(q) = U_{n,n'}^{ac}$ where

$$U_{n,n'}^{ac} = \frac{2\pi\Phi}{\omega_q V_s}\sum_{p_z,\,p_z'}\sum_{n,\,n'}\Big\{\left|G_{p_z-\hbar q,p_z}\right|^2\left[f\left(\varepsilon_n(p_z-\hbar q)\right) - f\left(\varepsilon_n(p_z)\right)\right]\delta\left(\varepsilon_n(p_z-\hbar q) - \varepsilon_n(p_z) + \hbar\omega_q - \xi\right)$$
$$+\left|G_{p_z+\hbar q,p_z}\right|^2\left[f\left(\varepsilon_{n'}(p_z+\hbar q)\right) - f\left(\varepsilon_{n'}(p_z)\right)\right]\delta\left(\varepsilon_{n'}(p_z+\hbar q) - \varepsilon_{n'}(p_z) - \hbar\omega_q + \xi\right)\Big\} \tag{11}$$

$f(p_z) = f\left(\varepsilon_{n,n'}(p_z)\right)$ is the unperturbed distribution function, $\varepsilon_{n,n'}(p_z)$ is the energy band, n and n' denotes the quantization of the energy band, and $G(p_z \pm \hbar q, p_z)$ is the matrix element of the electron-phonon interaction. Letting $p_z' = p_z \pm \hbar q$ and employing the principle of detailed balance, we assume that scattering into a state p_z' and out of the state p_z is the same, and hence

$$\left|G_{p',p}\right|^2 = \left|G_{p,p'}\right|^2 \tag{12}$$

Substituting Eq. (12) into Eq. (11) and also converting the summation over $p_z^{'}$ into an integral, we obtain

$$\Gamma(q) = \frac{2\pi\Phi}{\omega_q v_s} \cdot \sum_{n,\,n'} \left|G_{p',p}\right|^2 \int \left[f\left(\varepsilon\left(p_z\right)\right) - f\left(\varepsilon\left(p_z + \hbar q\right)\right)\right] \delta\left(\varepsilon_{p_z+q} - \varepsilon_{p_z} - \hbar\omega_q + \xi\right) dp_z \tag{13}$$

The matrix element of the electron-phonon interaction is given as

$$\left|G_{p',p}\right| = \frac{\Lambda q}{\sqrt{2\sigma\omega_q}} \tag{14}$$

where Λ is the deformation potential constant, and σ is the density of F-CNT. Substituting Eq. (14) into Eq. (13), we obtain

$$\begin{aligned}\Gamma(q) = \frac{2\pi\Phi}{\omega_q v_s}\left(\frac{\Lambda q}{\sqrt{2\sigma\omega_q}}\right)^2 \sum_{n,\,n'} \left[f\left(\varepsilon_{n'}\left(p_z\right)\right) - f\left(\varepsilon_{n'}\left(p_z + \hbar q\right)\right)\right] \\ \times\, \delta\left(\varepsilon_{n'}\left(p_z + \hbar q\right) - \varepsilon_{n'}\left(p_z\right) - \hbar\omega_q + \xi\right) dp_z\end{aligned} \tag{15}$$

The electron distribution function is obtained by obtained by solving the Boltzmann transport equation in the presence of external electric field

$$\frac{\partial f(r,p,t)}{\partial t} + v(p).\nabla_r f(r,p,t) + eE\nabla_p f(r,p,t) = -\frac{f(r,p,t) - f_o(p)}{\tau} \tag{16}$$

and has a solution of

$$f\left(p_z\right) = \int_0^\infty \frac{dt'}{\tau} \exp\left(-t/\tau\right) f_o\left(p_z - ea\mathbf{E}t'\right) \tag{17}$$

and $f_o\left(p_z\right)$ is the Fermi-Dirac distribution given as

$$f_o\left(p_z\right) = \frac{1}{\left[\exp\left(-\left(\varepsilon\left(p_z\right) - \mu\right)/k_B T\right) + 1\right]} \tag{18}$$

where μ is the chemical potential which ensures the conservation of electrons, k_B is the Boltzmann's constant, T is the absolute temperature in energy units. Substituting Eqs. (17) and (18) into Eq. (15), we obtain an equation for $\Gamma(q)$ which contains Fermi-Dirac integral of the order $1/2$ as

$$F_{1/2}\left(\eta_f\right) = \frac{1}{\Gamma(1/2)} \int_0^\infty \frac{\eta_f^{1/2} d\eta}{1 + \exp\left(\eta - \eta_f\right)} \tag{19}$$

where $(E_F - E_c)/k_BT \equiv \eta_f$. For nondegenerate electron gas, where the Fermi level is several k_BT below the energy of the conduction band E_c (i.e., $k_BT \ll E_c$), the integral in Eq. (19) approaches $2/\sqrt{\pi}\exp\left(\eta_f\right)$. Eqs. (18) and (19) then simplifies to

$$f_o(p_z) = C\exp\left(-\left[\varepsilon(p_z) - eaE\tau\right]/k_BT\right) \tag{20}$$

where C is the normalization constant to be determined from the normalization condition $\int f(p)dp = n_o$ as

$$C = \frac{3n_oa^2}{2I_o(\Delta_1)I_o(\Delta_2)}\exp\left(\frac{\varepsilon_o - E_F}{k_BT}\right) \tag{21}$$

where n_o is the electron density concentration, T is the absolute temperature in energy units and $I_o(x)$ is the modified Bessel function of zero order.

From the conservation laws, the momentum (p_z) can be deduced from the delta function part of Eq. (15) as

$$p_z = -\frac{\hbar q}{2} + \frac{1}{4a}\arcsin\left(\frac{\omega_q}{12\gamma_o aq}\right) \tag{22}$$

By substituting p_z into the distribution function in Eq. (15), and after some cumbersome calculations yields

$$\begin{aligned}\Gamma_q^{FCNT} = \Gamma_o\Bigg\{&\sinh\left[\Delta_1\cos(3p'a)\sin A\sin\left(\frac{3}{2}a\hbar q\right) + \Delta_2\cos(p'a)\sin B\sin\left(\frac{a}{2}\hbar q\right)\right]\\ &\times\cosh\left[\Delta_1\cos(3p'a)\cos A\cos\left(\frac{3}{2}a\hbar q\right) + \Delta_2\cos(p'a)\cos B\cos\left(\frac{a}{2}\hbar q\right)\right]\\ &-4\Bigg(\Delta_2\sin(p'a)\cos B\sin\left(\frac{a}{2}\hbar q\right) + \Delta_1\cos A\sin(3p'a)\sin\left(\frac{3}{2}a\hbar q\right)\\ &+\Delta_1\Delta_2\sin(p'a)\sin(3p'a)\cos A\cos B\sin\left(\frac{a}{2}\hbar q\right)\sin\left(\frac{3}{2}a\hbar q\right)\Bigg)\\ &\times\sinh\left[\Delta_1\cos(3p'a)\cos A\cos\left(\frac{3}{2}a\hbar q\right) + \Delta_2\cos(p'a)\cos B\cos\left(\frac{a}{2}\hbar q\right)\right]\\ &\times\cosh\left[\Delta_1\cos(3p'a)\sin A\sin\left(\frac{3}{2}a\hbar q\right) + \Delta_2\cos(p'a)\sin B\sin\left(\frac{a}{2}\hbar q\right)\right]\Bigg\}\end{aligned} \tag{23}$$

where $\chi = \hbar\omega_q a/v_s$, Θ is defined to be the Heaviside step function, $\alpha = \omega_q/12\gamma_o aq = \omega_q/6\Delta_1 aq$. In the absence of an external electric field

$$\Gamma_q^{FCNT} = \Gamma_o \left[\sinh \left\{ \Delta_1 \sin \left(\frac{3}{2} a\hbar q \right) \sin A + \Delta_2 \sin \left(\frac{a}{2} \hbar q \right) \sin B \right\} \times \cosh \left\{ \Delta_1 \cos \left(\frac{3}{2} a\hbar q \right) \cos A + \Delta_2 \cos \left(\frac{a}{2} \hbar q \right) \cos B \right\} \right] \tag{24}$$

and

$$\Gamma_o = \frac{n_o a^2 \Phi \Lambda^2 q \Theta \left(1 - \alpha^2\right)}{48\pi I_o \left(2\gamma_o \beta\right) I_o \left(6\gamma_o \beta\right) \omega_q^2 \sigma v_s \gamma_o \hbar \sqrt{1 - \alpha^2}}$$
$$A = \frac{3}{4} \arcsin\left(\frac{\omega_q}{12\gamma_o aq} \right) \quad B = \frac{1}{4} \arcsin\left(\frac{\omega_q}{12\gamma_o aq} \right) \alpha = \frac{\omega_q}{12\gamma_o aq} \tag{25}$$

To compare the result with an undoped SWCNT, we follow the same procedure as that of F-CNT. Using the tight-binding energy dispersion of the p_z orbital which is given as:

$$\varepsilon\left(p_z\right) = \pm\gamma_o \sqrt{1 + 4\cos\left(\frac{\nu\pi}{n}\right)\cos\left(\frac{p_z\sqrt{3}b}{2\hbar}\right) + 4\cos^2\left(\frac{p_z\sqrt{3}b}{2\hbar}\right)} \tag{26}$$

where $\gamma_o = 2.6\,\text{eV}$ is the hopping integral parameter, $b = 0.142\,\text{nm}$ is the C-C bonding distance, and (+) and (−) signs are respectively the conduction and valence band. When $\nu = 0$, the conduction and valence bands cross each other near the Fermi points, $p_F = \pm 2\pi\hbar/3\sqrt{3}b$ giving the metallic nature to the armchair tube. Putting $\nu = 0$, and making the substitution, $p_z = p_z + 3p_o/2\hbar$ in Eq. (26) gives

$$\varepsilon\left(p_z\right) = \pm\gamma_o \left(1 - 2\cos\left(\frac{p_z\sqrt{3}b}{2\hbar}\right)\right) \tag{27}$$

where $p_o = 2p_F = 4\hbar\pi/3\sqrt{3}b \approx 1.7 \times 10^{10}\text{m}^{-1}$ see [24]. Eq. (27) is equivalent to the energy dispersion in Eq. (5) when $n = 1$, which is

$$\varepsilon\left(p_z\right) = \varepsilon_o + \Xi\gamma_o \cos\left(ap_z\right) \tag{28}$$

Using Eq. (15), the absorption in SWCNT is calculated as

$$\Gamma_q^{SWCNT} = \frac{\pi^2 \Lambda^2 q^2 \Phi n_o \Theta\left(1 - \alpha^2\right)}{4\gamma_o^2 \omega_q^2 v_s \sigma \sin\left(a\hbar q/2\right) I_o\left(2\gamma_o \beta\right)\sqrt{1 - \alpha^2}} \times \sinh\left\{\beta\hbar\omega_q\right\} \cosh\left\{4\gamma_o \beta\sqrt{1 - \alpha^2}\cos\left(\frac{a\hbar q}{2}\right)\right\} \tag{29}$$

where

$$\alpha = \frac{\hbar\omega_q}{4\gamma_o \sin(a\hbar q/2)} \tag{30}$$

3. Results and discussions

In this formulation, we consider a novel concept of monochromatic acoustic phonon amplification at the THz frequencies regime. Impulsive phonon excitation by a femtosecond optical pulse generates coherent FCNT and SWCNT phonons propagating in the forward and backward direction along the FCNT and SWCNT axis, that is setting up an stationary acoustic wave. Interaction of the propagating acoustic wave with an electrically driven intraminiband transition electron current allows for phonon absorption, connected with electron transitions between states within an electronic miniband. The intravalley or intraminiband character of the electron transport allows for much higher currents than interminiband electron or electron tunneling and thus, a much stronger phonon absorption.

The general expressions for the hypersound absorption in F-CNT (Γ_q^{F-CNT}) and in SWCNT (Γ_q^{SWCNT}) are presented in Eqs. (24) and (29) respectively. In both equations, the absorptions are dependent on the frequency (ω_q), the acoustic wavenumber (q), and temperature (T) as well as other parameters such as the inter-atomic distances, the velocity of sound (v_s) and the deformation potential (Λ). In both expressions (see Eqs. (24) and (29)) a transparency window is observed: for F-CNT is $\omega_q \gg 12\gamma_o aq$; and for SWCNT is $\omega_q \gg \gamma_o \sin\left(\frac{1}{2}a\hbar q\right)/\hbar$. These are the consequence of conservation laws. The Eqs. (24) and (29), are analyzed numerically with the following parameters used: $\Lambda = 9\,\text{eV}$, $q = 10^5\,\text{cm}^{-1}$, $\omega_q = 10^{12}\,\text{s}^{-1}$, $v_s = 5 \times 10^3\,\text{m/s}$, $\Phi = 10^4\,\text{Wb/m}^2$, and $T = 45\,\text{K}$. The results are graphically plotted (see **Figures 4–7**). **Figure 4** shows the dependence of the sound absorption coefficient on the frequency (ω_q) for varying q. In both graphs, the absorption is initially high but falls off sharply and then changes slowly at high values of ω_q. Increasing the values of q correspondingly increases the obtained graph in both doped F-CNT and undoped SWCNT though the magnitude of absorption obtained in SWCNT exceeds that of F-CNT, that is, $|\Gamma_q^{SWCNT}| > |\Gamma_q^{F-CNT}|$. This is in accordance with the work of Jeon et al. [19]. In **Figure 2**, the graph increases to a maximum point then drops off. It then changes again slowly at high q for both undoped SWCNT and doped F-CNT. By increasing the temperature, the amplitude of the graphs reduces. For $T = 45\,K$, the maximum absorption in $\Gamma_q^{SWCNT} = 8.2 \times 10^4$ whilst that of $\Gamma_q^{F-CNT} = 2867$ which gives the ratio of the absorption $\frac{\Gamma_{(SWNT)}}{\Gamma_{(F-CNT)}} \approx 29$, whilst at $T = 55\,K$, $\frac{\Gamma_{(SWNT)}}{\Gamma_{(F-CNT)}} \approx 9$ and at $T = 65\,K$, we had $\frac{\Gamma_{(SWNT)}}{\Gamma_{(F-CNT)}} \approx 2$. Clearly, we noticed that the ratio decreases with an increase in temperature. The nonlinear behavior in **Figure 5** is as a result of the fact that, increasing temperature increases the scattering process in the material. The majority of electrons in this case acquire a higher velocity, shorter collision time, and higher energy. This energetic electrons, which are the majority undergo inter-mini-band transition (tunneling) allowing only a handful to undergo intra-mini-band transition. This allows only the few intra-mini-band electrons to interact with the copropagating phonons

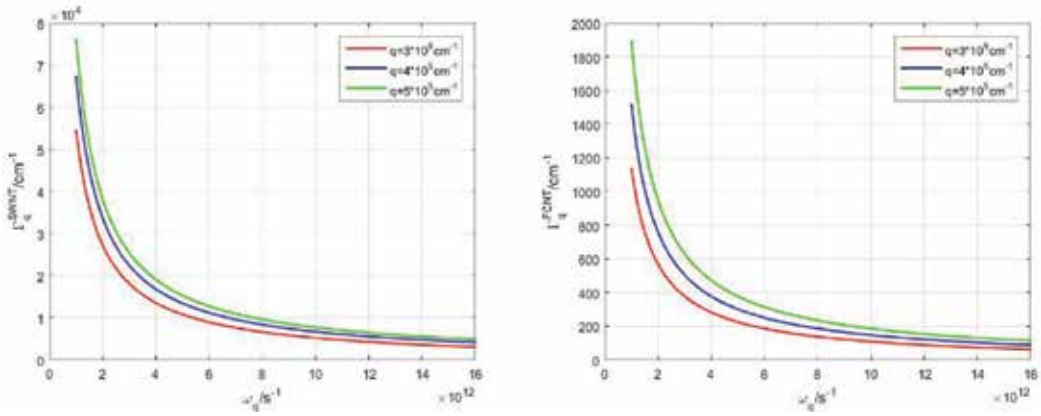

Figure 4. Dependence of Γ_q on ω_q (left) for an undoped SWCNT, and (right) for a F-CNT by varying q at $T = 45$ K.

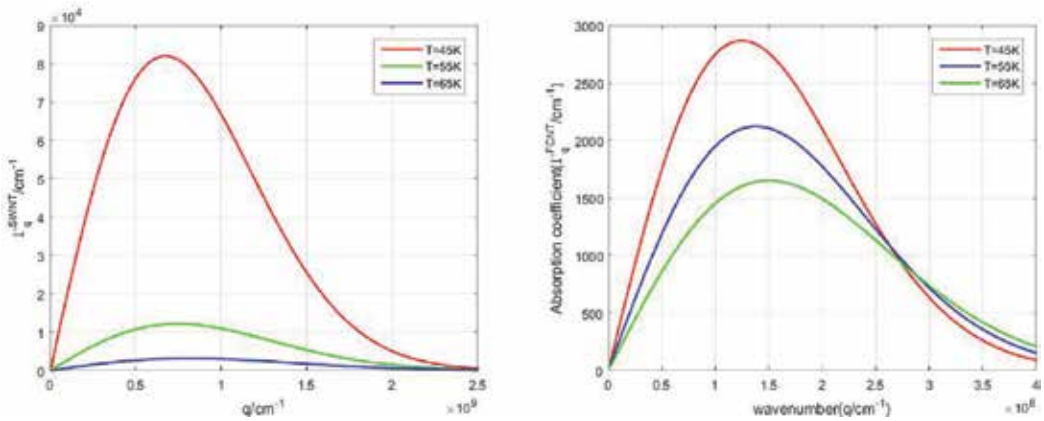

Figure 5. Dependence of Γ_q on q (left) for undoped SWCNT and (right) for doped F-CNT at $T = 45, 55, 65$ K.

leading to a decrease in absorption of the acoustic phonons. To aid a better understanding of the comparison between the absorption obtained in both SWCNT and F-CNT, a semilog plot is presented in **Figure 6**, which clearly shows that the undoped SWCNT absorbs more than the doped F-CNT. This can be attributed to the fact that the presence of F-CNT atoms leads to chemical activation of a passive surface CNT by adding additional electronic band structure and altering the carbon π-bonds around the Fermi level in a non-linear manner thus forming a band structure of width two periods [22]. As Flourine is highly electronegative it thus weakens the walls of the CNT as it approaches it. The π-electrons attached to the Flourine which causes less free charge carriers to interact with the phonons. Current researches have predicted sp^2 bonding charge change to sp^3 by F-functionlization [25–27]. This bonding charge change would reduce the density of free carriers, consequently leading to the magnitude reduction of the absorption [22] (**Figures 4–6**).

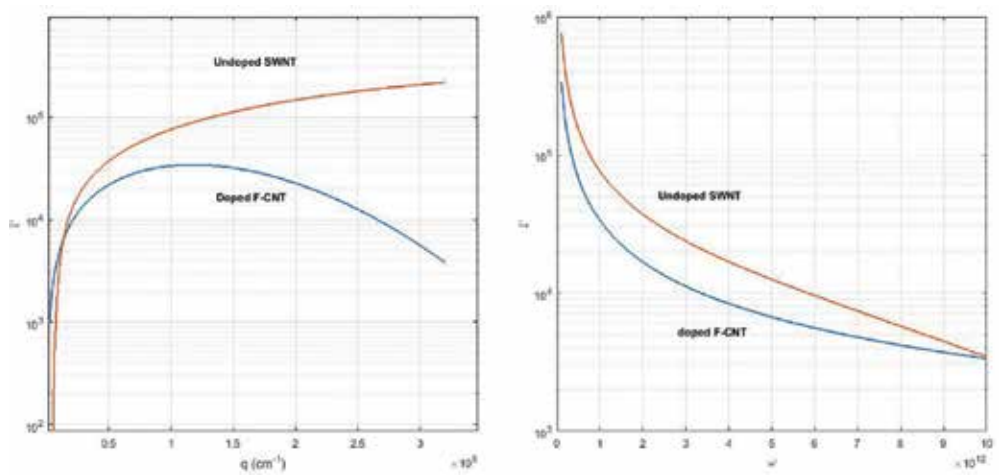

Figure 6. Semilog plot of Γ_q dependence on q and ω_q for doped F-CNT and undoped SWCNT.

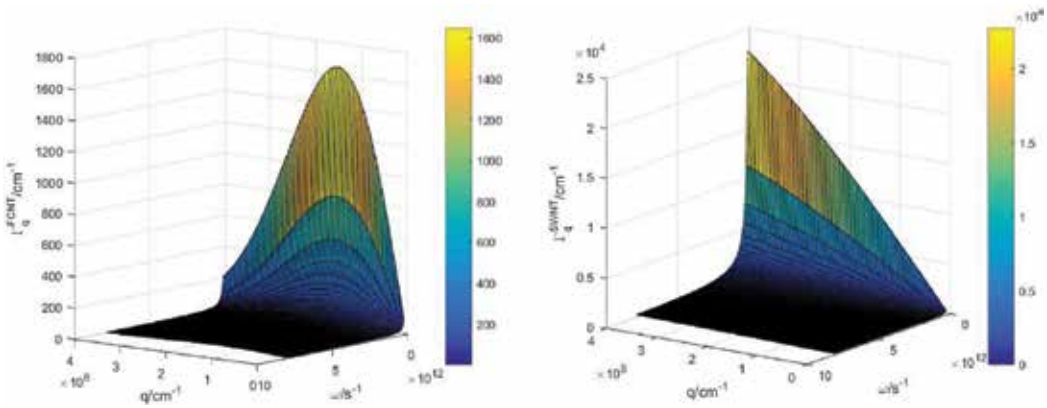

Figure 7. A three dimensional plot of Γ_q dependence on q and ω_q for doped and undoped SWCNT.

In order to put our observations in perspective, we display **Figures 4** and **5** in a three-dimensional behavior of the sound coefficient as a function of the frequency (ω_q) and the wavevector q (**Figure 7**).

4. Conclusion

Theoretical investigation of strong absorption of coherent acoustic phonons in an FCNT and SWCNT at low temperature utilizing the Boltzmann's transport equation is carried out in the regime $ql \gg 1$. The absorption coefficient obtained is highly nonlinear and depends on the

stimulated absorption of acoustic phonons by electrically determined electrons experiencing intraminiband transport. The study is appropriate and furthermore considers a strong absorption of energized FCNT and SWCNT phonons. The Flourine doping affects the absorption properties of F-CNT, whereas SWCNT absorbs better than the F-CNT as was observed by Jeon et al. [19]. The phonons absorbed in this study have THz frequencies with wavelengths in the nanometer run, and takes into account examinations with high spatial determination, e.g., in phonon filters, spectroscopy (phonon spectrometer), microbiology, micro-nanoelectronic gadgets, tetrahertz adjustment of light, nondestructive testing of microstructures, and acoustic examination.

Author details

Daniel Sakyi-Arthur[1]*, S. Y. Mensah[1], N. G. Mensah[2], Kwadwo A. Dompreh[1] and R. Edziah[1]

*Address all correspondence to: daniel.sekyi-arthur@stu.ucc.edu.gh

1 Department of Physics, College of Agriculture and Natural Sciences, University of Cape Coast, Ghana

2 Department of Mathematics, College of Agriculture and Natural Sciences, University of Cape Coast, Ghana

References

[1] Shinokita K, Reimann K, Woerner M, Elsaesser T, Hey R, Flytzanis C. Strong amplification of coherent acoustic phonons by Intraminiband currents in a semiconductor Superlattice. Physical Review Letters. 2016;**116**(7):075504

[2] Gokhale VJ, Shim Y, Rais-Zadeh M. Observation of the acoustoelectric effect in gallium nitride micromechanical bulk acoustic filters. In: Frequency Control Symposium (FCS), 2010 IEEE International. IEEE; 2010. pp. 524-529

[3] Mensah SY, Allotey FKA, Adjepong SK. Acoustomagnetoelectric effect in a superlattice. Journal of Physics: Condensed Matter. 1996;**8**(9):1235

[4] Dompreh KA, Mensah SY, Abukari SS, Edziah R, Mensah NG, Quaye HA. Acoustomagnetoelectric effect in Graphene Nanoribbon in the presence of external electric and magnetic fields. Nanoscale Systems: Mathematical Modeling, Theory and Applications. 2014;**4**(1)

[5] Sharma GS, Skvortsov A, MacGillivray I, Nicole K. Acoustic performance of gratings of cylindrical voids in a soft elastic medium with a steel backing. The Journal of the Acoustical Society of America. 2017;**141**(6):4694-4704

[6] Ge H, Yang M, Ma C, Ming-Hui L, Chen Y-F, Fang N, Ping S. Breaking the barriers: Advances in acoustic functional materials. National Science Review. 2017

[7] Mensah SY, Allotey FKA, Adjepong SK. The effect of a high-frequency electric field on hypersound amplification in a superlattice. Journal of Physics: Condensed Matter. 1994; **6**(19):3479

[8] Mensah SY, Allotey FKA, Mensah NG, Elloh VW. Amplification of acoustic phonons in a degenerate semiconductor superlattice. Physica E: Low-dimensional Systems and Nanostructures. 2003;**19**(3):257-262

[9] Nunes OAC, Fonseca ALA. Amplification of hippersound in graphene under external direct current electric field. Journal of Applied Physics. 2012;**112**:043707

[10] Dompreh KA, Mensah NG, Mensah SY. Amplification of hypersound in graphene with degenerate energy dispersion. arXiv preprint arXiv. 2015;**1503**:07360

[11] Miseikis V, Cunningham JE, Saeed K, ORorke R, Davies AG. Acoustically induced current flow in graphene. Applied Physics Letters. 2012;**100**(13):133105

[12] Bandhu L, Nash GR. Temperature dependence of the acoustoelectric current in graphene. Applied Physics Letters. 2014;**105**(26):263106

[13] Dompreh KA, Mensah NG, Mensah SY, Abukari SS, Sam F, Edziah R. Hypersound absorption of acoustic phonons in a degenerate carbon nanotube. arXiv preprint arXiv. 2015;**1502**:07636

[14] Dompreh KA, Mensah NG, Mensah SY, Sam F, Twum AK. Acoustoelectric effect in degenerate carbon nanotube. arXiv preprint arXiv. 2015;**1504**:05484

[15] Reulet B, Kasumov AY, Kociak M, Deblock R, Khodos II, Gorbatov YB, Volkov VT, Journet C, Bouchiat H. Acoustoelectric effects in carbon nanotubes. Physical Review Letters. 2000;**85**(13):2829

[16] Ebbecke J, Strobl CJ, Wixforth A. Acoustoelectric current transport through single-walled carbon nanotubes. Physical Review B. 2004;**70**(23):233401

[17] Amekpewu M, Abukari SS, Adu KW, Mensah SY, Mensah NG. Effect of hot electrons on the electrical conductivity of carbon nanotubes under the influence of applied dc field. The European Physical Journal B. 2015;**88**(2):1-6

[18] Mensah SY, Allotey FKA, Mensah NG, Nkrumah G. Differential thermopower of a CNT chiral carbon nanotube. Journal of Physics: Condensed Matter. 2001;**13**(24):5653

[19] Jeon T-I, Son J-H, An KH, Lee YH, Lee YS. Terahertz absorption and dispersion of fluorine-doped single-walled carbon nanotube. Journal of Applied Physics. 2005;**98**(3):34316

[20] Hattori Y, Touhara H. Fluorination-defluorination and fluorine storage properties of single-wall carbon nanotubes and carbon nanohorns. New Fluorinated Carbons: Fundamentals and Applications. 2017:113-133

[21] Zhang KS, Pham D, Lawal O, Ghosh S, Gangoli VS, Smalley P, Kennedy K, et al. Overcoming catalyst residue inhibition of the functionalization of single-walled carbon nanotubes via the Billups-birch reduction. ACS Applied Materials & Interfaces. 2017;**9**(43):37972-37980

[22] Sadykov NR, Kocherga EY, Dyachkov PN. Nonlinear current in modified nanotubes with exposure to alternating and constant electric fields. Russian Journal of Inorganic Chemistry. 2013;**58**(8):951-955

[23] Mensah SY, Allotey FKA, Mensah NG. Nonlinear acoustoelectric effect in a semiconductor superlattice. Journal of Physics: Condensed Matter. 2000;**12**(24):5225

[24] Hasan S. Electron phonon interaction in carbon nanotube devices [PhD dissertation]. West Lafayette: Purdue University; 2007

[25] Chen J, Yan L. Recent advances in carbon nanotube-polymer composites. Advances in Materials. 2017;**6**(6):129

[26] Bauschlicher CW, So CR. High coverages of hydrogen on (10, 0), (9, 0) and (5, 5) carbon nanotubes. Nano Letters. 2002;**2**(4):337-341

[27] Sharma B, Kar R, Pal AR, Shilpa RK, Dusane RO, Patil DS, Suryawanshi SR, More MA, Sinha S. Role of hydrogen diffusion in temperature-induced transformation of carbon nanostructures deposited on metallic substrates by using a specially designed fused hollow cathode cold atmospheric pressure plasma source. Journal of Physics D: Applied Physics. 2017;**50**(15):155207

Chapter 8

Mesoscopic Physics of Phonon Transport in Carbon Materials

Kenji Sasaoka and Takahiro Yamamoto

Additional information is available at the end of the chapter

http://dx.doi.org/10.5772/intechopen.81292

Abstract

We give a theoretical review of recent development of the mesoscopic physics of phonon transport in carbon nanotubes, including the quantization of phonon thermal conductance, phonon Anderson localization, and so on. A single-walled carbon nanotube (SWCNT) can be regarded as a typical one-dimensional phonon conductor and exhibits various interesting phenomena originating from its one dimensionality. For example, a pristine SWCNT without any defects shows the quantization of phonon thermal conductance at low temperature. On the other hand, a defective SWCNT with randomly distributed carbon isotopes shows the phonon Anderson localization originating from the interference between phonons scattered by isotope impurities.

Keywords: carbon nanotube, ballistic phonon, quantized thermal conductance, phonon Anderson localization, phonon waveguide

1. Introduction

Heating of electronic devices is an unavoidable serious problem toward the realization of next-generation nanoscale devices. Carbon nanotube (CNT) is expected to be a potential material for removing the heat from heated devices because of its high thermal conductivity. However, concern has been raised that intrinsic high thermal conductivity of pure CNTs is lost because of the presence of defects in synthesized CNTs.

In this chapter, we give a review of recent progress of theoretical works on phonon transport in CNTs focusing on the quantization of phonon thermal conductance, phonon Anderson localization, and so on. The phonon transport in CNTs shows fully quantum behaviors at low

temperatures and exhibits strong nonlinear behaviors due to phonon-phonon interaction at high temperatures. Therefore, traditional transport theories for bulk objects are not applicable to the thermal transport in CNTs. In the chapter, we will introduce a novel theory for mesoscopic phonon transport we developed and will describe various results and their physical interpretations.

2. Coherent phonon thermal transport in carbon nanotubes

2.1. Quantized thermal conductance of carbon nanotubes

In the one-dimensional (1D) phonon system formed between heat and cold baths, the thermal current density is described as the Landauer energy flux [1–3], which is given by

$$\dot{Q}_{\mathrm{ph}} = \sum_m \int_0^\infty \frac{dk}{2\pi} \hbar\omega_m(k) v_m(k) [\eta(\omega_m, T_{\mathrm{hot}}) - \eta(\omega_m, T_{\mathrm{cold}})] \zeta_m(k) \tag{1}$$

where $\hbar\omega_m(k)$ a phonon energy dispersion of wave number k and a phonon mode index m, $v_m(k) = d\omega_m(k)/dk$ a group velocity, $\eta(\omega_m, T_\alpha) = \left[\exp\left(\hbar\omega_m(k)/k_B T_\alpha\right) - 1\right]^{-1}$ the Bose-Einstein distribution function in heat baths, and $\zeta_m(k)$ is the transmission probability between the system and heat baths [1].

Analytically, performing the integration in Eq. (1) is, generally, very difficult, and it requires a knowledge of $\omega_m(k)$ and $\zeta_m(k)$ as a function of m and k. However, transformation of the integration variable in Eq. (1) from k to $\omega_m(k)$ leads to a cancelation between $v_m(k)$ and the density of state, $dk/d\omega_m$, so that Eq. (1) is rewritten as

$$\dot{Q}_{\mathrm{ph}} = \sum_m \int_{\omega_m^{\min}}^{\omega_m^{\max}} \frac{d\omega_m}{2\pi} \hbar\omega_m [\eta(\omega_m, T_{\mathrm{hot}}) - \eta(\omega_m, T_{\mathrm{cold}})] \zeta_m(\omega_m) \tag{2}$$

Here $\omega_m^{\min}$ and $\omega_m^{\max}$ are the minimum and maximum angular frequencies of the mth phonon dispersion, respectively. It is noted that Eq. (2) depends on only $\omega_m^{\min}$ and $\omega_m^{\max}$ regardless of the energy dispersion. Furthermore, within the linear response limit, $\Delta T \equiv T_{\mathrm{hot}} - \mathrm{T}_{\mathrm{cold}} \ll T \equiv (T_{\mathrm{hot}} + T_{\mathrm{cold}})/2$, and the limit of adiabatic contact between the system and heat baths, $\zeta_m(\omega_m) = 1$, the thermal conductance, $\kappa_{\mathrm{ph}} = \dot{Q}_{\mathrm{ph}}/\Delta T$, is simplified as

$$\kappa_{\mathrm{ph}} = \frac{k_{\mathrm{B}}^2 T}{2\pi\hbar} \sum_m \int_{x_m^{\min}}^{x_m^{\max}} dx \frac{x^2 e^x}{(e^x - 1)^2} \tag{3}$$

Carrying out the integration in Eq. (3), we can derive an analytical expression of the thermal conductance, which can easily apply to various 1D ballistic phonon systems, $\kappa_{\mathrm{ph}} = \kappa_{\mathrm{ph}}^{\min} - \kappa_{\mathrm{ph}}^{\max}$:

$$\kappa_{\mathrm{ph}}^{\alpha} = \frac{2k_{\mathrm{B}}^2 T}{h} \sum_m \left[\phi\left(2, e^{-x_m^{\alpha}}\right) + x_m^{\alpha} \phi\left(1, e^{-x_m^{\alpha}}\right) + \frac{\left(x_m^{\alpha}\right)^2}{2} \eta\left(x_m^{\alpha}\right) \right] \tag{4}$$

Here, α denotes "min" or "max," $\phi(z,s) = \sum_{n=1}^{\infty} (s^n/n^z)$ is the Appel function, and $x_m^{\alpha} = \hbar\omega_m^{\alpha}/k_{\mathrm{B}}T$. In particular, an acoustic mode ($\omega_m^{\min} = 0$) contributes a universal quantum of $\kappa_0 = \pi^2 k_{\mathrm{B}}^2 T/3h$ to the thermal conductance.

The thermal conductance in single-walled carbon nanotubes (SWCNTs) can be obtained by knowing the values of $\omega_m^{\min}$ and $\omega_m^{\max}$ for all m. These values can be obtained from the diagonalization of the dynamical matrix, constructed with the scaled force-constant parameters [4, 5]. **Figure 1** shows energy dispersion curves for the region near $k = 0$ for a CNT with chiral vector $\boldsymbol{C}_{\mathrm{h}} = (10, 10)$, where $|\boldsymbol{T}|$ is the magnitude of the unit vector along the tube axis. Here, the chiral vector(n, m) uniquely determines the geometrical structure of CNTs [5, 7]. **Figure 1** shows four acoustic modes with linear dispersion: a longitudinal acoustic one, doubly degenerate transverse acoustic ones, and a twisting one. The lowest doubly degenerate optical (E_{2g} Raman active) modes have an energy gap of $\hbar\omega_{\mathrm{op}} = 2.1$ meV at $k = 0$. As shown in the inset of **Figure 1**, $\hbar\omega_{\mathrm{op}}$ depends only on the tube radius R and decreases approximately according to $\sim 1/R^2$ [5, 7]. These modes always lie in low-energy dispersion relations, independent of the geometry of SWCNTs.

Figure 2(a) shows the thermal conductances normalized to a universal value of $4\kappa_0$ (as explained later) as a function of temperature. The calculated values approach unity in the

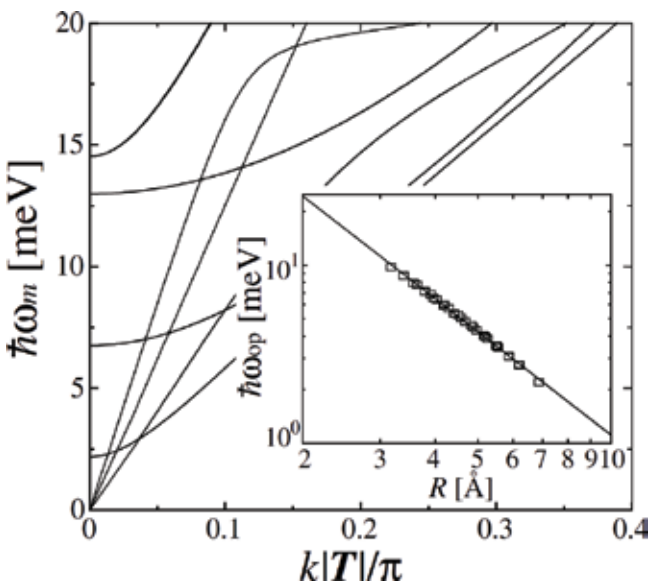

Figure 1. Low-energy phonon dispersion curves for a (10,10) SWCNT [6]. The inset shows the energy gap of the lowest optical modes. Copyright 2004 American Physical Society.

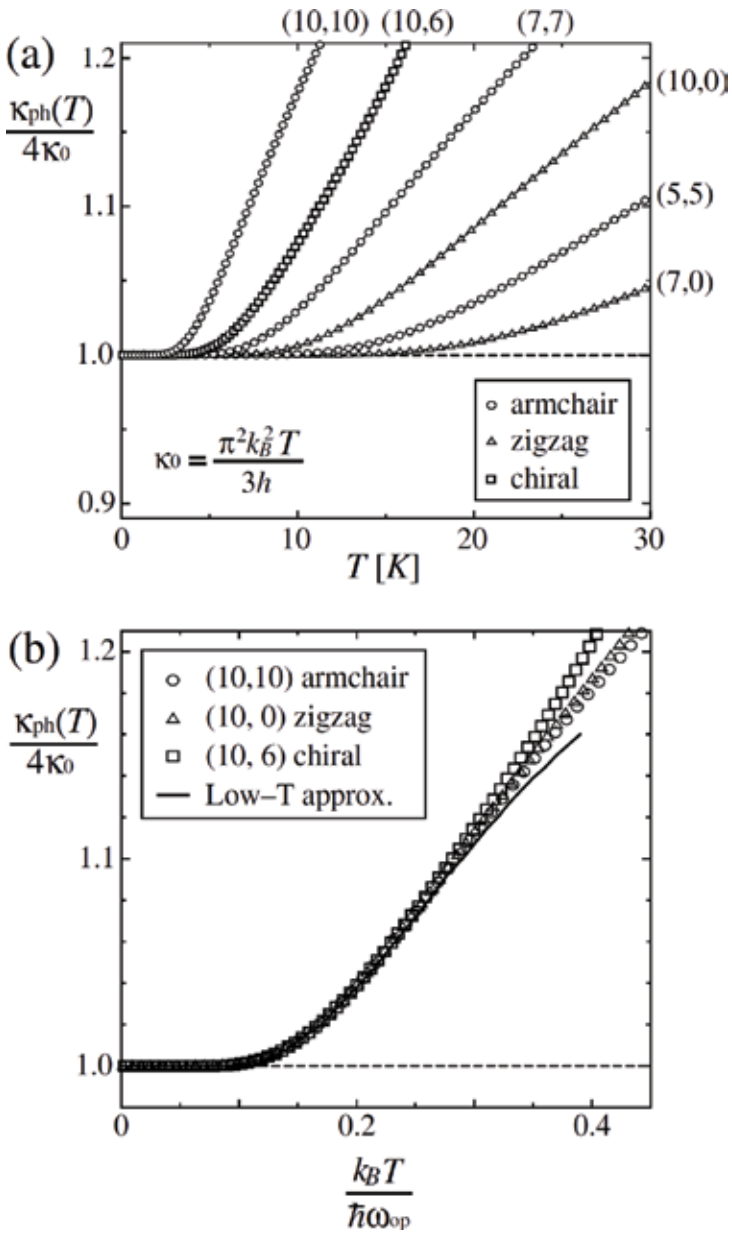

Figure 2. Thermal conductance as a function of temperature (a) in units of Kelvin and (b) scaled by the energy gap of the lowest optical mode [6]. Copyright 2004 American Physical Society.

low-temperature limit, meaning that the phonon thermal conductance of SWCNTs is quantized in unit of a universal value of $4\kappa_0$, independent of the chirality of SWCNTs. The origin of the quantization of thermal conductance is low-energy excitations of long wavelength acoustic phonons (four branches in **Figure 1**) at temperatures sufficiently low that the two lowest optical modes with $\hbar\omega_{op}$ are not excited (lowest gapped branch in **Figure 2**). The quantization

can also be derived analytically from Eq. (4). Only the first term contributes to the conductance at the low-T limit, leading to $4\left(\pi^2 k_B^2 T/3h\right) = 4\kappa_0$. Here, 4 is the number of acoustic branches.

As another important finding, the different curves of $\kappa_{ph}(T)$ for various SWCNTs seen in **Figure 2(a)** exhibit a universal feature when a scaled temperature is introduced, $\tau_{op} = k_B T/\hbar\omega_{op}$. Taking account of the four acoustic and two lowest optical modes and substituting the values of ω_m^{min} for these branches at the $k = 0$ into Eq. (2), the thermal conductance can be given as

$$\frac{\kappa_{ph}}{4\kappa_0} \approx 1 + \frac{3}{\pi^2} e^{-1/\tau_{op}} \left(1 + \frac{1}{\tau_{op}} + \frac{1}{2\tau_{op}^2}\right) \tag{5}$$

The curves in **Figure 2(a)** are replotted against the curve of Eq. (5) with τ_{op} in **Figure 2(b)**. It is evident that all curves (only three curves are shown for clarity) fall on a single curve coinciding with the curve of Eq. (5) in the low-T limit. The curves turn upward at around $\tau_{op} \approx 0.14$ from a linear region in this plot (quantization plateau), with the plateau width determined by the relation $\sim 1/R^2$ (see result in the inset of **Figure 1**). This universal feature of $\kappa_{ph}(T)$ of SWCNTs indicates that the optical phonon energy gap, which is decided only by R, characterizes low-temperature phonon transport, as shown in the inset of **Figure 1**. This theoretical result supports both the experimental observations and the inferred tube-radius dependence of the width of the thermal conductance plateau, although the unknown extrinsic factors in the experiment makes it impossible to compare the absolute values between the experiment and theory directly [8, 9].

The contribution of electrons to thermal conductance can be determined in a simple manner by replacing $\eta(\omega_m, T)$ in Eq. (1) with $f(\epsilon_m, T) = 1/\left[e^{(\epsilon_m - \mu)/k_B T} + 1\right]$ and then substituting the electron energy bands, ϵ_m, into the formula. According to this formulation, all conduction bands crossing the Fermi energy level yield κ_0, as that of phonons, even though electrons obey different statistics. Generally, the quantum of thermal conductance should be universal out of relation to particle statistics [1, 10].

The low-T behavior of the electronic thermal conductance in SWCNTs is dependent on whether the SWCNT is metallic or semiconducting, which is sensitive to radius and chirality [11, 12]. For semiconducting SWCNTs, the electronic thermal conductance, κ_{el}, should vanish roughly exponentially in the limit of $T \to 0$, having an energy gap of the order of 0.1 eV [13–15]. For metallic SWCNTs, two linear energy bands crossing the Fermi level at $k > 0$ [5] contribute toκ_{el} at low temperatures, resulting in a universal value of $\kappa_{el} = 4\kappa_0$, where 4 is the number of two spin-degenerate channels crossing the Fermi level. This result also satisfies the Wiedemann-Franz relation between electrical conductance and electronic thermal one [16–18]. The total thermal conductance of metallic SWCNTs is given by $\kappa = \kappa_{el} + \kappa_{ph} = 8\pi^2 k_B^2 T/3h$ at low temperatures.

Finally, in this subsection, a significant difference was recognized between the widths of the quantization plateau for phonons and those for electrons in metallic SWCNTs. The characteristic

energy for phonon transport at low temperature is $\hbar\omega_{op}$, typically a few meV, as described in **Figure 2(b)**, while that for electron transport is of the order of 0.1 eV, which corresponds to the energy at a Van Hove singularity measured from the Fermi level [19]. As a result, it is predicted that the quantized nature of electron thermal conductance survives up to room temperature, at which phonons already cease to exhibit thermal quantization, giving rise to high thermal conductance. In other words, the contribution from electrons to thermal conductance is negligible compared to that from phonons at moderate temperatures. In **Figure 3**, the temperature dependence of the ratio of thermal conductance κ_{el}/κ_{ph} for electrons and phonons is illustrated. The experimentally observed ratio [20] is 1 order of magnitude lower than the present value. The discrepancy is attributed to the theoretical treatment of SWCNTs as purely metallic, whereas only a certain fraction $(\sim 1/3)$ [5, 11] of the crystalline ropes of SWCNTs in the experiment will be metallic and contribute to κ_{el}.

2.2. Carbon nanotube as phonon waveguide

In this subsection, nonequilibrium molecular dynamics (NEMD) simulations are carried out with the Brenner bond-order potential for carbon-carbon covalent bonds [21] and the Lennard-Jones one for van der Waals interaction between the tube walls [22]. In our NEMD simulations, different temperatures, T_C (= 290 K) and T_H (= 310 K), are assigned to several layers of the left- and right-hand sides of a SWCNT. This leads to a thermal current from the right to left through the SWCNT, as shown in **Figure 4**. The Nosé-Hoover thermostat is utilized to control the temperature of the left and right-hand side several layers [24, 25], and we impose the fixed boundary condition, so that the edge atoms of SWCNTs are fixed rigidly. The length of the

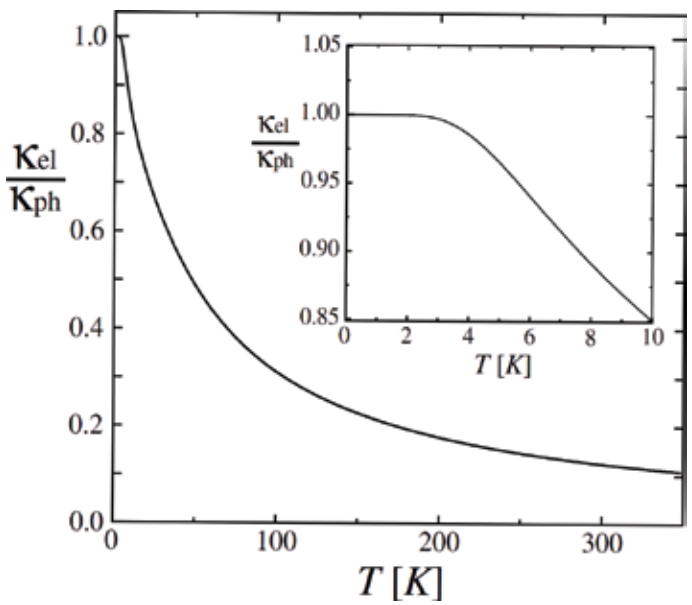

Figure 3. Ratio of thermal conductance by electrons, to that by phonons for a (10,10) SWCNT [6]. The inset gives results at low temperatures on an expanded scale. Copyright 2004 American Physical Society.

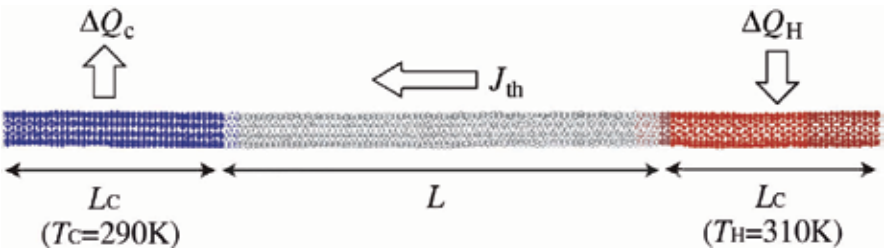

Figure 4. Schematic of the SWCNT in which different temperatures are assigned to the left- and right-end several layers [23]. Copyright 2009 the Japan Society of Applied Physics.

temperature-controlled layers is taken to be $L_C = L/2$, where L is the length of the phonon-conduction region. The tunable parameters in the Nosé-Hoover thermostat method were optimized so as to minimize contact thermal resistance [26]. In our simulations, we solve Hamilton's classical equations of motion using second-order operator splitting integrators [27] with the molecular-dynamics (MD) time step of 0.5 fs.

In this subsection, the thermal conductance κ is treated as

$$\kappa = \frac{J_{\text{th}}}{T_{\text{H}} - T_{\text{C}}} \tag{6}$$

Here, the steady-state thermal current, J_{th}, is calculated as follows:

$$J_{\text{th}} = \frac{\sum_{j=1}^{n} [\Delta Q_{\text{H}}(j) - \Delta Q_{\text{C}}(j)]}{2n\Delta t} \tag{7}$$

where n represents the number of MD steps and $-\Delta Q_{\text{H(C)}}(j)$ is the amount of heat added to the right temperature-controlled layers (removed from the left ones) per unit time (see **Figure 4**).

First, the influence of bending deformation on the thermal conductance of SWCNTs is discussed. In our simulations, shortening the distance between the two ends of a SWCNT realizes bending. The right panels (a)-(c) in **Figure 5** illustrate the bent $(5,5)$ SWCNT for compression lengths $l_{\text{comp}} = 0, 60,$ and 120 nm, respectively. It can be seen that the CNT is severely bent as the edge-layer distance decreases. In the simulations, the bending deformation arises from stretching of carbon-carbon bond lengths, and the hexagonal network of carbon atoms in the SWCNT is not broken. The left panel in **Figure 5** shows the thermal conductance of the $(5,5)$ SWCNT with $L = 100$ nm as a function of the compression length. Our simulations exhibits that the bending does not affect the thermal conductance. Although the value of thermal conductance depends on L, the L-dependence is not discussed here because the conclusion of the study does not change qualitatively within the range from $L = 100$ to 250 nm as calculated. For the L-dependence, we refer the reader to other published papers [26, 28–31].

The bending robustness of κ can be understood through a perspective of the phonon dispersion relations as shown in **Figure 6**, given by the power spectra of velocity fluctuations calculated by MD simulations [26, 28]. **Figure 6(a)-(c)** show the dispersion relations of the bent

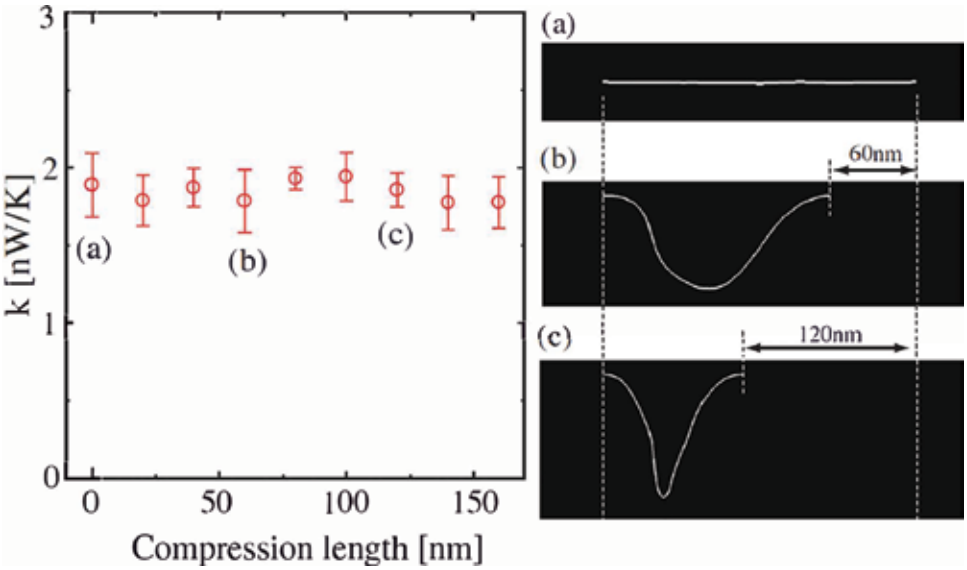

Figure 5. The thermal conductance of the (5,5) SWCNT with 200 nm length as a function of the compression length [23]. The right panels (a)–(c) represent the MD snapshots of a bended CNT. Copyright 2009 the Japan Society of Applied Physics.

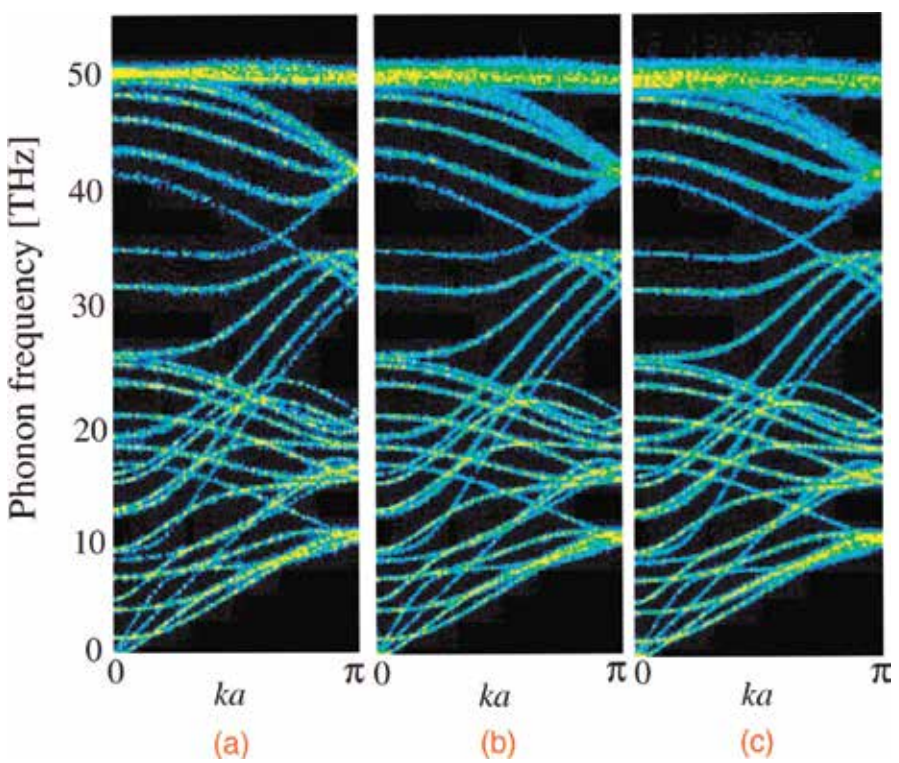

Figure 6. The phonon dispersion relations of the (5,5) SWCNT with the compression length (a) 0, (b) 60, and (c) 120 nm [23]. Copyright 2009 the Japan Society of Applied Physics.

(5, 5) SWCNT for $l_{\text{comp}} = 0, 60,$ and 120 nm, respectively. Since the bending deformation does not break the hexagonal network of the SWCNT is not broken by the bending deformation, a change of the dispersion structure due to the bending is very small. More specifically, the dispersion structure in the low-energy region remains unchanged after the bending, whereas that in the high-frequency region is slightly changed as shown in **Figure 6**. Consequently, κ at the room-temperature is unaffected by the local bond-length deformation due to the bending. The bending robustness obtained by our simulations supports the experimental results of Chang et al. [32].

2.3. Phonon Anderson localization in isotope-disordered carbon nanotube

This subsection is focused on the interference effects of coherent phonons in SWCNTs. Here, we performed calculations for two typical examples: a (5,5) metallic SWCNT with 15.0% ^{13}C and a (8,0) semiconducting SWCNT with 9.4% ^{14}C. Our simulation is based on the Landauer theory of phonon transport combined with the nonequilibrium Green's function (NEGF) technique [33–35]. We used the Brenner bond-order potential for the interaction between carbon atoms [21], as used in the previous subsection. It is assumed that isotope disorder exists only in a central region with a length L. This region is connected to semi-infinite pristine SWCNT leads, not including any defects or impurities (**Figure 7**). In accordance with the Landauer theory within the linear response with the temperature difference between hot and cold baths [1], the phonon derived thermal conductance can be expressed as $\kappa(T) = \int_0^\infty \frac{d\omega}{2\pi}\hbar\omega\frac{\partial f_B(\omega,T)}{\partial T}\langle\zeta(\omega)\rangle$, where s $\hbar$ is Planck's constant, T is the average temperature of the hot and cold baths, $f_B(\omega, T)$ is the Bose-Einstein distribution function for a phonon with a frequency ω in the baths, and $\langle\zeta(\omega)\rangle$ is the phonon-transmission function averaged over an ensemble of samples with different isotope configurations. We adopted over 200 realizations for each L at each ω.

In the NEGF technique, the phonon-transmission function $\zeta(\omega)$ is given by $\zeta(\omega) = \mathrm{Tr}[\boldsymbol{\Gamma}_L(\omega)\boldsymbol{G}(\omega)\boldsymbol{\Gamma}_R(\omega)\boldsymbol{G}^\dagger(\omega)]$, where $\boldsymbol{G}(\omega) = \left[\omega^2\boldsymbol{M} - \boldsymbol{D} - \boldsymbol{\Sigma}_L(\omega) - \boldsymbol{\Sigma}_R(\omega)\right]^{-1}$ is the retarded Green's function in the central region and $\boldsymbol{\Gamma}_{L(R)}(\omega) = i\left(\boldsymbol{\Sigma}_{L(R)}(\omega) - \boldsymbol{\Sigma}^\dagger_{L(R)}(\omega)\right)$ is the level broadening function due to the left (right) lead [33–35]. Here, $\boldsymbol{D}$ is a dynamical matrix in the central region, $\boldsymbol{M}$ a diagonal matrix with elements corresponding to the masses of the constituent atoms, and $\boldsymbol{\Sigma}_{L(R)}(\omega)$ a self-energy due to the left (right) lead. A merit of NEGF technique is that the phonon transport in micrometer-length nanotubes can be efficiently computed. We can easily calculate the statistical average of the phonon transmission for nanotubes within the wide range of tube

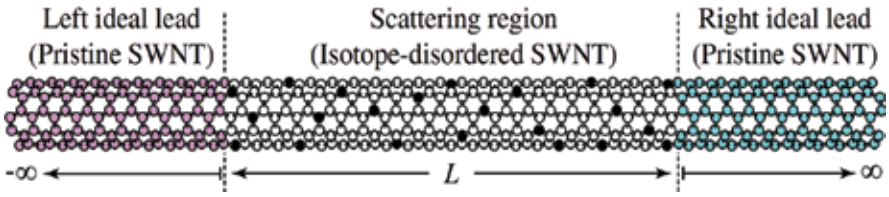

Figure 7. Schematic of an isotope-disordered SWCNT [36]. Copyright 2011 American Physical Society.

length with respect to huge number of isotope configurations. On the other hand, consideration of many-body interactions such as phonon-phonon scattering requires much computation time in the NEGF technique.

To perform the NEGF simulations, we first optimized the structures of a pristine (5,5) metallic and (8,0) semiconducting SWCNTs, and then calculated $\boldsymbol{D}$ from the second derivative of the total energy of the optimized structures with respect to the atom coordinate. By using $\boldsymbol{D}$ and the recursion method, we can easily compute $\boldsymbol{\Sigma}_{L(R)}(\omega)$. Moreover, we assume that the isotopes are taken into account only in $\boldsymbol{M}$.

Coherent-phonon transport is classified into three regions based on a relation among the length L of the central region: the ballistic regime for $L \ll l_{\mathrm{MFP}}(\omega)$, the diffusive one for $l_{\mathrm{MFP}}(\omega) \ll L \ll \xi(\omega)$, and the localization one for $L \gg \xi(\omega)$. Here, $l_{\mathrm{MFP}}(\omega)$ is the mean free path and $\xi(\omega)$ the localization length. Before discussing the phonon-transmission histogram, we first determine $l_{\mathrm{MFP}}(\omega)$ and $\xi(\omega)$ for isotope-disordered SWCNTs. We adopt the procedure used in Ref. [37] to estimate these lengths. **Figure 8(a)** shows the average phonon transmission $\langle\zeta(\omega)\rangle$ of the (5,5) SWCNT with 15% ^{13}C for various L up to 5 m. In the very low-frequency region, $\langle\zeta(\omega)\rangle$ does not decrease and is almost four, even in the presence of isotope impurities. Perfect transmission (i.e., ballistic transport) is realized because the wavelength of acoustic phonons in the low-ω region is much longer than L. The Landauer expression of thermal conductance eventually exhibits universal quantization of $4\kappa_0$ at low temperatures irrespective of the presence and absence of isotope impurities (the factor 4 reflects the number of acoustic phonon modes).

In contrast, $\langle\zeta(\omega)\rangle$ decreases rapidly in the higher frequency region with increasing L, as shown in **Figure 8(a)**. There are two possible mechanisms for the reduction of $\langle\zeta(\omega)\rangle$: diffusive scattering and phonon localization. For the former, $\langle\zeta(\omega)\rangle$ decreases with L according to $\langle\zeta(\omega)\rangle = M(\omega)/(1 + L/l_{\mathrm{MFP}}(\omega))$, where $M(\omega)$ means the number of phonon modes. On the other hand, for the latter mechanism, the phonon-transmission function decays exponentially with L according to the scaling law $\langle\ln\zeta(\omega)\rangle = -L/\xi(\omega)$. In other words, $\xi(\omega)$ is defined by the scaling law. To clarify these mechanisms for the phonon-transmission reduction, the L-dependences of $\langle\zeta(\omega)\rangle$ and $\langle\ln\zeta(\omega)\rangle$ are plotted in **Figure 8(b)** and **(c)** for the two mechanisms, respectively. As **Figure 8(b)** shows that the numerical data of $\langle\zeta(\omega)\rangle$ at $\omega = 34\ \mathrm{cm}^{-1}$ and $391\ \mathrm{cm}^{-1}$ are well fitted by the dashed lines. In particular, the slope of the dashed line for $\omega = 34\ \mathrm{cm}^{-1}$ is almost zero, implying that l_{MFP} is very long and the phonon transport is ballistic at this frequency, as has been discussed above. For $\omega = 391\ \mathrm{cm}^{-1}$, the slope is finite, which indicates that phonon transport at this frequency is in the diffusive regime. In contrast to the low frequencies, at higher frequencies ($\omega = 1071$,1207, and $1513\ \mathrm{cm}^{-1}$), the calculated values deviate from the dashed lines with increasing L, although they are well fitted in the short-L region. This deviation means that the phonon-transmission reduction for high-ω phonons of a long-L SWCNT cannot be explained by the diffusive scattering mechanism. As shown in **Figure 8(c)**, the data for $\omega = 1071$,1207, and $1513\ \mathrm{cm}^{-1}$ are well fitted by the dashed lines in the $\langle\ln\zeta\rangle$ plot. Thus, it can be concluded that phonon localization causes the phonon-transmission reduction for high-ω phonons in a long-L SWCNT.

http://dx.doi.org/10.5772/intechopen.81292

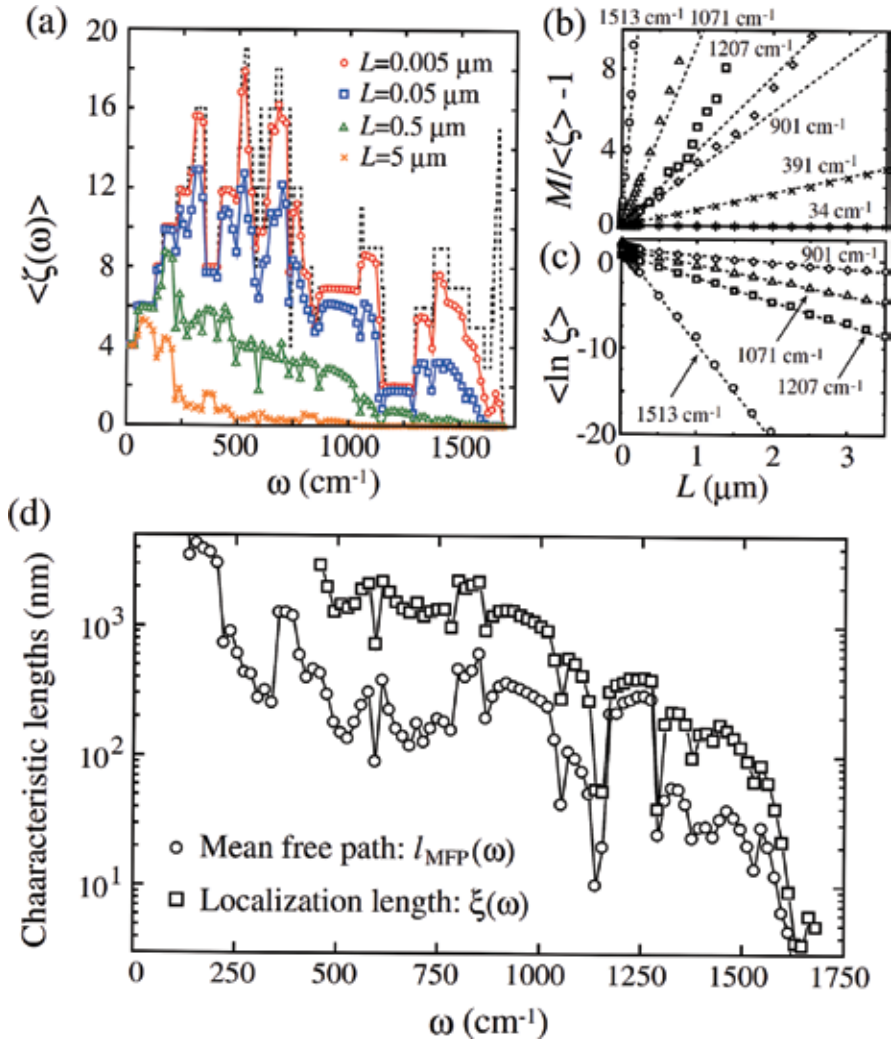

Figure 8. (a) The average phonon transmission of the (5,5) SWCNT with 15% ^{13}C [36]. (b) The length dependence of the transmission for estimating the mean free path and (c) for the localization length. (d) The mean free path and the localization length as functions of frequency. Copyright 2011 American Physical Society.

l_{MFP} and $\xi(\omega)$ can be estimated from the slope of dashed lines in **Figure 8(b)** and **(c)**, respectively. The estimated l_{MFP} and $\xi(\omega)$ for the (5,5) SWCNT with 15% ^{13}C are presented in **Figure 8(d)**. This result is in excellent agreement with the phenomenological Thouless relation, $\xi(\omega) = (M(\omega)+1)l_{\mathrm{MFP}}(\omega)/2$, similar to electron systems with time-reversal symmetry [38]. Thus, the three distinct regimes (ballistic, diffusive, and localization) could be clarified.

Figure 9 shows the ^{13}C-concentration dependence of $\kappa(T)$ in the (8,0) semiconducting SWCNT with 2 μm length at 300 K. As seen in **Figure 9**, thermal conductance decreases rapidly as the concentration increases. When the concentration overs about 20%, $\kappa(T)$ decreases by 80% in comparison with the pristine (8,0) SWCNT.

We now discuss the phonon-transmission fluctuation, defined by a standard deviation $\Delta\zeta(\omega) \equiv \sqrt{\left\langle \zeta(\omega)^2 \right\rangle - \langle \zeta(\omega) \rangle^2}$. **Figure 10** shows $\Delta\zeta(\omega)$ for (a) 625 nm-long (5,5) SWCNT with 15% ^{13}C and (b) 210 nm-long (8,0) SWCNT with 9.4% ^{14}C. The fluctuation of a physical quantity generally decreases as its average value increases. However, the fluctuation of phonon transmission is constant within the frequency region in the diffusive regime although $\langle \zeta(\omega) \rangle$ varies depending on ω [see also **Figure 8(a)**]. The constant value is estimated to be $\Delta\zeta(\omega) = 0.35 \pm 0.02$ and indicated by the dashed lines in **Figure 10(a)** and **(b)**. Thus, $\Delta\zeta(\omega)$ in the diffusive regime is universal and is independent of the background phonon transmission, the tube chirality and length, the isotope concentration, and the type of isotopes. This universal fluctuation is realized only in the diffusive regime and not in the ballistic and localization regimes. Interestingly, the value of $\Delta\zeta(\omega) = 0.35 \pm 0.02$ is the same as the value of the universal conductance fluctuation (UCF) for coherent electron transport in disordered quasi-1D systems,

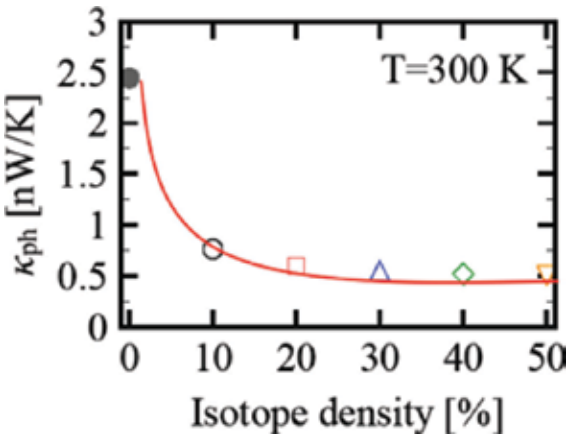

Figure 9. ^{13}C-concentration dependence of thermal conductance of the (8,0) SWCNT with 2 μm length at 300 K.

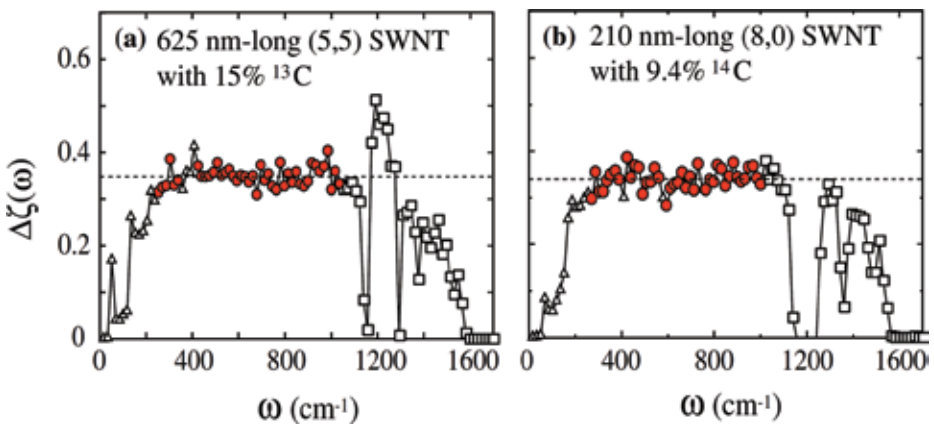

Figure 10. The root-mean-square phonon transmission for (a) the (5,5) SWCNT and (b) the (8,0) SWCNT [36]. Copyright 2011 American Physical Society.

$\Delta G/G_0 = 0.365$, within the statistical error. Here, G_0 and ΔG are respectively the electrical conductance quantum and the electrical conductance fluctuation. This means that the universal phonon-transmission fluctuation is closely related to the UCF even though electrons and phonons obey different quantum statistics. Similar to the UCF, the reason for the macroscopically observable phonon-transmission fluctuation can be qualitatively understood as follows: the fluctuations of phonon-transmission channels cannot cancel each other because there are very few effective transmission channels due to isotope scattering. To obtain a quantitative and complete understanding of the universal phonon-transmission fluctuation, some sophisticated microscopic theories are required.

In the final of this subsection, we discuss the phonon-transmission histogram $P(\zeta)$ that contains information for every moment of $\zeta(\omega)$. In **Figure 11(a)** and **(b)**, $P(\zeta)$ for several typical frequencies in the diffusive regime of (a) 625 nm-long (5,5) SWCNT with 15% ^{13}C and (b) 210 nm-long (8,0) SWCNT with 9.4% ^{14}C are shown. All the histograms in these figures are well described by a Gaussian distribution function with the universal fluctuation

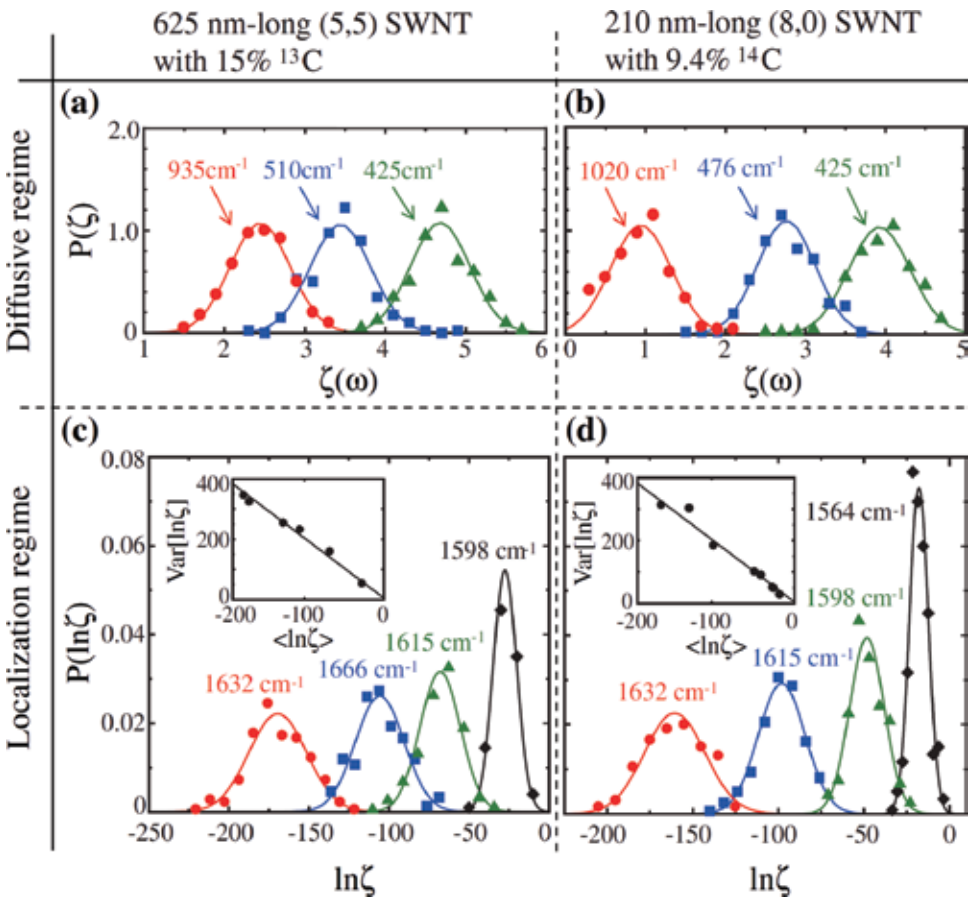

Figure 11. Phonon-transmission histograms for several frequencies in the diffusive regime for (a) the (5,5) SWCNT and (b) the (8,0) SWCNT, and in the localization regime for (c) the (5,5) SWNT and (d) the (8,0) SWCNT [36]. The insets show the variance. Copyright 2011 American Physical Society.

Phonon transport regime	Phonon-transmission histogram	Average	Standard deviation
Ballistic regime ($L \ll l_{MFP}$)	Nearly delta function	$\sim M(\omega)$	~0
Diffusive regime ($l_{MFP} \ll L \ll \xi$)	Gaussian distribution	Power-law decay with L	Universal ($\sim 0.35 \pm 0.02$)
Localization regime ($L \gg \xi$)	Lognormal distribution	Exponential decay with L	Decreases as $\langle \ln\zeta \rangle$

Table 1. Phonon-transmission histogram in ballistic, diffusive, and localization regimes [36]. Copyright 2011 American Physical Society.

$\Delta\zeta(\omega) = 0.35 \pm 0.02$. This is similar to the fact that the electrical conductance histogram in the diffusive region is expressed by a Gaussian distribution function with the UCF [38].

In $L \gg \xi(\omega)$ regime, $P(\zeta)$ becomes no longer a symmetric Gaussian distribution. By analogy with the electrical conductance histogram in the localization regime [39], one can easily expect that the asymmetric histogram is a lognormal function of ζ. In fact, $P(\ln\zeta)$ can be well described by a Gaussian distribution as shown in **Figure 11(c)** and **(d)**. Unlike the other regimes, the variance $\mathrm{Var}[\ln\zeta] \equiv (\Delta \ln\zeta)^2$ of $P(\ln\zeta)$ decreases with increasing $\langle \ln\zeta \rangle$ according to $\mathrm{Var}[\ln\zeta] \sim -2\langle \ln\zeta \rangle$ as shown in the insets of these figures, similar to the situation for electrons [38]. The transmission fluctuation in the localization regime is material independent in the sense that the slope of $\mathrm{Var}[\ln\zeta]$ does not depend on the tube geometry, isotope concentration, or the type of isotopes. The above-mentioned results for the ballistic, diffusive, and localization regimes are summarized in **Table 1**.

3. Crossover from ballistic to diffusive phonon transport

This section discusses the crossover from ballistic to diffusive phonon transport in SWCNT using some basic arithmetic which follows from the fictitious-probe idea. In this idea, the thermal conductance was found to formally have the same expression as the Landauer formula for coherent phonon transport [1, 6]:

$$\kappa = \sum_{\nu} \int_{\omega_\nu^{\min}}^{\omega_\nu^{\max}} \frac{d\omega}{2\pi} \hbar\omega \left[\frac{\partial f(\omega, T)}{\partial T}\right] T_\nu(\omega) \tag{8}$$

even when phonon-phonon scattering exists. Here, T is an averaged temperature as descried in the previous section, and $T_\nu(\omega)$ is a phonon transmission function, effectively including the phonon-phonon scattering given as

$$T_\nu(\omega) = \zeta_\nu^{LR}(\omega) + \frac{\zeta_\nu^{FL}(\omega)\zeta_\nu^{FR}(\omega)}{\zeta_\nu^{LF}(\omega) + \zeta_\nu^{FR}(\omega)} \tag{9}$$

where $\zeta_\nu^{\alpha\beta}(\omega)$ is the transmission function of a coherent phonon with a phonon mode ν and frequency ω flowing from α to β leads. Note that the inelastic component of thermal conductance in Eq. (8) is neglected, because it negligibly contributes to κ of CNTs in the quasiballistic regime.

Thus far, we have discussed the role of a single probe with temperature T_F . Generally, a spatial distribution of temperature exists inside the conductor. In order to incorporate this distribution, a conductor attaching N probes in series, with respective temperatures $T_i (i = 1, 2 \cdots, N)$ is introduced. For N probes, the transmission function $T_\nu^{\text{tot}}(\omega)$ propagating in a conductor of length L can be written as

$$T_\nu^{\text{tot}}(\omega) = \frac{L_\nu(\omega)}{L + L_\nu(\omega)} \sim \frac{\Lambda_\nu(\omega)}{L + \Lambda_\nu(\omega)} \tag{10}$$

where the characteristic length $L_\nu(\omega) \equiv T_\nu/\rho(1 - T_\nu)$ is expressed by the density of scatters in the conductor, $\rho = N/L$ and T_ν. The derivation process of Eq. (10) is analogous to that of effective transmission for inelastic electronic transport in mesoscopic conductors [40]. Here, it is explained that we can regard $L_\nu(\omega)$ in Eq. (10) as the mean free path $\Lambda_\nu(\omega) = \tau_\nu(\omega)|v_\nu(\omega)|$, where $\tau_\nu(\omega)$ and $v_\nu(\omega)$ are the backscattering time and group velocity of a phonon with $\{\nu, \omega\}$, respectively. For phonon propagation over the distance between neighboring probes $dL \equiv L/N = 1/\rho$, the reflection probability $R_\nu(\omega)$ is given by $R_\nu(\omega) = (dL/|v_\nu(\omega)|)/\tau_\nu(\omega)$ $= 1/\rho\Lambda_\nu(\omega)$. Thus, the phonon's mean free path is $\Lambda_\nu(\omega) = 1/\rho R_\nu(\omega)$, and $L_\nu(\omega) \sim \Lambda_\nu(\omega)$ in the large-N (or small-dL) limit where the transmission probability of each small segment with length dL is close to one ($T_\nu(\omega) \sim 1$).

According to the above discussion, a general expression of thermal conductance is given as

$$\kappa = \sum_\nu \int_{\omega_\nu^{\min}}^{\omega_\nu^{\max}} \frac{d\omega}{2\pi} \hbar\omega \left[\frac{\partial f(\omega, T)}{\partial T}\right] \frac{\Lambda_\nu(\omega)}{L + \Lambda_\nu(\omega)} \tag{11}$$

For a short conductor ($L \ll \Lambda_\nu(\omega)$), Eq. (11) reproduces the Landauer formula [1, 6] for coherent phonon transport with perfect transmission. In the other limit ($L \gg \Lambda_\nu(\omega)$), it reduces to the Boltzmann-Peierls formula [41].

We now apply the developed formula (11) to thermal transport in SWCNTs at room temperature. Instead of estimating $\Lambda_\nu(\omega)$ from Eq. (9), we use an phenomenological expression $\Lambda_\nu(\omega) = c_\nu A/\omega^2 T$ for three-phonon Umklapp scattering events in the low-frequency limit $\hbar\omega/k_B T \ll 1$, where $A = 3.35 \times 10^{23}$ mK/s^2 is the coupling constant for graphene [42] and c_ν represents the curvature effect of a CNT ($c_\nu = 1$ corresponds to a graphene). By using this expression we can perform integration in Eq. (11) analytically. Strictly speaking, this expression can apply only to acoustic phonon modes with linear dispersion, but it has been shown to be useful to represent other modes as well [30]. Consequently, the thermal conductance is expressed simply as:

$$\kappa_{\text{CNT}} = \frac{k_B}{2\pi} \sum_\nu \Omega_\nu \left\{ \arctan\left(\frac{\omega_\nu^{\max}}{\Omega_\nu}\right) - \arctan\left(\frac{\omega_\nu^{\min}}{\Omega_\nu}\right) \right\} \tag{12}$$

where $\Omega_\nu(L) = \sqrt{c_\nu A/TL}$ is an L-dependent characteristic frequency, which is a key quantity for understanding the crossover between ballistic and diffusive phonon transport in the CNTs. The ν dependence of c_ν is neglected hereafter, i.e., the mode-dependent characteristic

frequency $\Omega_\nu(L)$ is replaced by $\Omega(L)$. In spite of the relative simplification, this works remarkably well to describe L dependence of thermal conductance in the quasi-ballistic regime, as will be discussed below.

In Eq. (10), effects of phonon scattering at interfaces between a CNT and the left/right leads were not included. One of simple treatments of the interfacial thermal resistance is to introduce it by the following way: $\kappa^{-1} = \kappa_{\rm CNT}^{-1} + \kappa_{\rm int}^{-1}$. The interfacial resistance $\kappa_{\rm int}^{-1}$ can be decided by fitting experimental or numerical calculation data.

Now, we estimate the thermal conductance of SWCNTs by performing the NEMD simulations [26, 28] with Brenner's bond-order potential [21], and compare the MD results to the above-described theory. The L-dependence of thermal conductance was quantified for various tube lengths, up to micrometers at $T = 300$ K ($T_{\rm hot} = 310$ K and $T_{\rm cold} = 290$ K). We refer the detailed simulation procedure to Ref. [26]. The thermal conductances for (3,3) and (5,5) SWCNTs obtained from the NEMD simulations are shown by blue and red circles in **Figure 12**, respectively. The solid curves representing theoretical curves given the proper choice of two parameters $\kappa_{\rm int}$ and c (e.g., $\kappa_{\rm int}^{-1} = 0.09$ K/nW and $c = 0.65$ for the (3,3) SWCNT) excellently agree with the MD data. Most recently, the L-dependent thermal conductance (or conductivity) of SWCNTs shown here has been measured in experiments [31, 44], although we cannot compare the theory with the experiments because the detailed information on tube structure such as number of walls and their chiralities was not described.

We return to discuss the ballistic-diffusive crossover. The relative position of $\Omega(L)$ with respect to the phonon dispersion relation determines the thermal-transport properties of SWCNTs. As illustrated in **Figure 13**, the dashed blue line indicates the position of $\Omega(L)$ relative to the

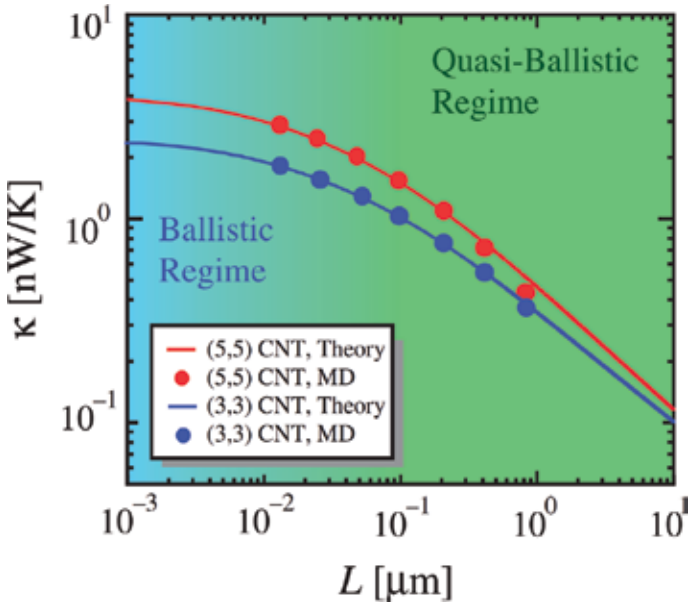

Figure 12. Length dependence of thermal conductance [43]. Copyright 2009 the Japan Society of Applied Physics.

http://dx.doi.org/10.5772/intechopen.81292

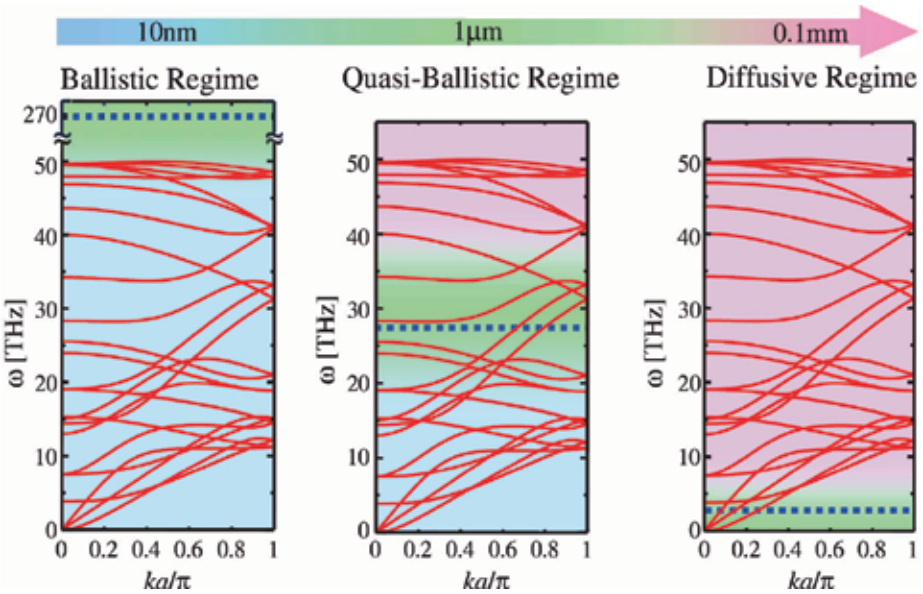

Figure 13. The relative position of the length dependent characteristic frequencies, 270 THz (left panel), 27 THz (middle panel), and 2.7 THz (right panel) [43]. Copyright 2009 the Japan Society of Applied Physics.

dispersion relation. As seen in **Figure 12**, nanometer-length SWCNTs display the thermal conductance independent of L, reflecting purely ballistic phonon transport. At nanometer length, $\Omega(L)$ is much larger than the energies of the phonons, as shown in the left panel of **Figure 13**.

With an increase in L, up to micrometer length, the value of $\Omega(L)$ decreases, lying in the middle of the phonon dispersion relation, as shown in the central panel of **Figure 13**. In this situation, low-frequency phonon modes ($\omega_\nu^{\max} \ll \Omega(L)$) give L-independent thermal conductance reflecting a ballistic nature, whereas the high-frequency modes $\left(\omega_\nu^{\min} \gg \Omega(L)\right)$ show $\kappa \propto 1/L$ reflecting a diffusive nature. The intermediate-frequency phonon modes ($\omega_\nu^{\min} < \Omega(L) < \omega_\nu^{\max}$) cannot be described in terms of both Landauer and Boltzmann-Peierls formulae, and the thermal conductance exhibits nonlinear L-dependence described by Eq. (12). Thus, it is concluded that micrometer-length SWCNTs belong to the quasi-ballistic thermal transport regime in which ballistic and diffusive phonons coexist.

Next, the case when $\Omega(L)$ is much lower than the excitation frequency of the lowest optical phonons is discussed, as shown in the right panel of **Figure 13**. In this case, the tube length$L$ reaches millimeters and the contribution of optical phonons to thermal conductance has a behavior as $\kappa \propto 1/L$, resulting in constant thermal conductivity, as $\lambda = (L/S)\kappa = \text{const}$. Here, S is the cross-sectional area of a SWCNT. On the other hand, the acoustic modes show $\kappa \propto L^{-1/2}$, leading to a power-law divergence $\lambda \propto L^{1/2}$ of thermal conductivity [29, 30]. This divergence closely relates to the long-standing problem pointed out by Pomeranchuk in the 1940s that the low-frequency acoustic phonon contribution to thermal conductivity diverges in the thermodynamic limit $L \to \infty$ [45]. However, it is known, in general, that the divergence disappears if

we take into account higher-order phonon-phonon scattering events, although the possibility of the above-stated long-time tail in low-dimensional materials remains an open problem [46, 47]. In either case, the agreement between the current theory and MD simulation results indicates that the higher-order effects are negligible in the current length regime. This consists with the previously reported observation from Boltzmann's kinetic approach [30].

4. Thermal properties of graphene modulated by strain

Finally, we shortly mention the recent theoretical work about the thermal property in another carbon material, a graphene [48]. In this work, the strain response of the phonon specific heat was investigated. The low temperature behavior of the specific heat is dominated by the three acoustic modes, i.e., the longitudinal acoustic (LA) mode, transverse acoustic (TA) mode, and out-of-plane acoustic (ZA) mode. It is well known that the LA and TA modes have a linear dispersion in the long wavelength region while the other has a quadratic one in the absence of the strain [49]. This means that the ZA mode is critical for low-temperature dependence of the specific heat. As a result, the specific heat has a linear dependence at low temperature. As the strain increases, the dispersion of the ZA mode drastically changes, so that this dispersion becomes linear in the same as the LA and TA modes [50, 51]. Due to the ZA mode linearized by the strain, the low-temperature dependence of the specific heat becomes quadratic. Therefore, since the specific heat directly relates the thermal conductivity, it is easily expected that the strain can also modulate the temperature dependence of the thermal conductivity.

5. Conclusion

This chapter reviewed recent progress of theoretical studies on phonon transport in SWCNTs focusing on the quantization of phonon thermal conductance, phonon Anderson localization, and so on. At low temperature, the phonon thermal conductance of SWCNTs has a quantized universal value of $4\kappa_0$, where the factor, 4 is the number of the acoustic modes in SWCNTs. As the temperature increases, the crossover from the ballistic transport to diffusive one occurs and the thermal conductance in the intermediate region between them indicates the non-linear dependence of tube length.

Acknowledgements

The authors would like to thank Kazuyuki Watanabe, Satoshi Watanabe, Shigeo Maruyama, Junichiro Shiomi, and Satoru Konabe for their useful discussions during this work. This work was supported, in part, by JSPS KAKENHI grants (nos. 19710083, 20048008, 22013004, 24681021, 15H03523 and 18H01816).

Author details

Kenji Sasaoka[1] and Takahiro Yamamoto[2]*

*Address all correspondence to: takahiro@rs.tus.ac.jp

1 W-FST Center, RIST, Tokyo University of Science, Tokyo, Japan

2 Department of Liberal Arts, Faculty of Engineering, Tokyo University of Science, Tokyo, Japan

References

[1] Rego LGC, Kirczenow G. Quantized thermal conductance of dielectric quantum wires. Physical Review Letters. 1998;**81**:232-235. DOI: 10.1103/Phys Rev Lett.81.232

[2] Angelescu DE, Cross MC, Roukes ML. Heat transport in mesoscopic systems. Superlattices and Microstructures. 1998;**23**:673-689. DOI: 10.1006/spmi.1997.0561

[3] Blencowe MP. Quantum energy flow in mesoscopic dielectric structures. Physical Review B. 1999;**59**:4992-4998. DOI: 10.1103/PhysRevB.59.4992

[4] Saito R, Takeya T, Kimura T, Dresselhaus G, Dresselhaus M S. Raman intensity of single-wall carbon nanotubes. Physical Review B. 1998;**57**:4145-4153. DOI: 10.1103/PhysRevB.57.4145

[5] Saito R, Dresselhaus G, Dresselhaus M S. Physical Properties of Carbon Nanotubes. London: Imperial College Press; 1998. DOI: 10.1016/S0921-5107(00)00444-X

[6] Yamamoto T, Watanabe S, Watanabe K. Universal features of quantized thermal conductance of carbon nanotubes. Physical Review Letters. 2004;**92**:075502. DOI: 10.1103/PhysRevLett.92.075502

[7] Dresselhaus M S, Dresselhaus G, Eklund P C. Science of Fullerenes and Carbon Nanotubes. New York: Academic; 1996

[8] Hone J, Llaguno MC, Biercuk MJ, Johnson AT, Batlogg B, Benes Z, et al. Thermal properties of carbon nanotubes and nanotube-based materials. Applied Physics A. 2002;**74**:339-343. DOI: 10.1007/s003390201277

[9] Hone J. Phonons and thermal properties of carbon nanotubes. In: Dresselhaus M S, Dresselhaus G, Avouris P, editors. Carbon Nanotubes: Synthesis, Structure, Properties, and Applications. Berlin: Springer-Verlag; 2001. pp. 273-287. DOI: 10.1007/3-540-39947-X

[10] Rego LGC, Kirczenow G. Fractional exclusion statistics and the universal quantum of thermal conductance: A unifying approach. Physical Review B. 1999;**59**:13080-13086. DOI: 10.1103/PhysRevB.59.13080

[11] Saito R, Fujita M, Dresselhaus G, Dresselhaus M S. Electronic structure of chiral graphene tubules. Applied Physics Letters. 1992;**60**:2204-2206. DOI: 10.1063/1.107080

[12] Hamada N, Sawada S, Oshiyama A. New one-dimensional conductors: Graphitic microtubules. Physical Review Letters. 1992;**68**:1579-1581. DOI: 10.1103/PhysRevLett.68.1579

[13] Dresselhaus MS, Jishi RA, Dresselhaus G, Inomata D, Nakano K, Saito R. Group theoretical concepts for carbon nanotubes. Molecular Materials. 1994;**4**:27-40

[14] Olk CH, Heremans JP. Scanning tunneling spectroscopy of carbon nanotubes. Journal of Materials Research. 1994;**9**:259-262. DOI: 10.1557/JMR.1994.0259

[15] Wildöer JWG, Venema LC, Rinzler AG, Smalley RE, Dekker C. Electronic structure of atomically resolved carbon nanotubes. Nature (London). 1998;**391**:59-62. DOI: 10.1038/34139

[16] Guttman GD, Ben-Jacob E, Bergman DJ. Thermoelectric properties of microstructures with four-probe versus two-probe setups. Physical Review B. 1996;**53**:15856. DOI: 10.1103/PhysRevB.53.15856-15862

[17] Greiner A, Reggiani L, Kuhn T, Varani L. Thermal conductivity and Lorenz number for one-dimensional ballistic transport. Physical Review Letters. 1997;**78**:1114-1117. DOI: 10.1103/PhysRevLett.78.1114

[18] Molenkamp LW, Gravier T, van Houten H, Buijk OJA, Mabesoone MAA, Foxon CT. Peltier coefficient and thermal conductance of a quantum point contact. Physical Review Letters. 2002;**68**:3765-3768. DOI: 10.1103/PhysRevLett.68.3765

[19] Rao AM, Richter E, Bandow S, Chase B, Eklund PC, Williams KA, et al. Dresselhaus diameter-selective Raman scattering from vibrational modes in carbon nanotubes. Science. 1997;**275**:187-191. DOI: 10.1126/science.275.5297.187

[20] Hone J, Whitney M, Piskoti C, Zettl A. Thermal conductivity of single-walled carbon nanotubes. Physical Review B. 1999;**59**:R2514-R2516. DOI: 10.1103/PhysRevB.59.R2514

[21] Brenner DW. Empirical potential for hydrocarbons for use in simulating the chemical vapor deposition of diamond films. Physical Review B. 1990;**42**:9458-9471. DOI: 10.1103/PhysRevB.42.9458

[22] Che J, Cagin T, Goddard WA III. Generalized extended empirical bond-order dependent force fields including nonbond interactions. Theoretical Chemistry Accounts. 1999;**102**:346-354. DOI: 10.1007/s002140050506

[23] Nishimura F, Takahashi T, Watanabe K, Yamamoto T. Bending robustness of thermal conductance of carbon nanotubes: Nonequilibrium molecular dynamics simulation. Applied Physics Express. 2009;**2**:035003. DOI: 10.1143/APEX.2.035004

[24] Nose S. A unified formulation of the constant temperature molecular dynamics methods. The Journal of Chemical Physics. 1984;**81**:511-519. DOI: 10.1063/1.447334

[25] Hoover WG. Canonical dynamics: Equilibrium phase-space distributions. Physical Review A. 1985;**31**:1695-1697. DOI: 10.1103/PhysRevA.31.1695

[26] Shiomi J, Maruyama S. Molecular dynamics of diffusive-ballistic heat conduction in single-walled carbon nanotubes. Japanese Journal of Applied Physics. 2008;**47**:2005-2009

[27] Tuckerman M, Berne BJ, Martyna GJ. Reversible multiple time scale molecular dynamics. The Journal of Chemical Physics. 1992;**97**:1990-2001. DOI: 10.1063/1.463137

[28] Maruyama S. A molecular dynamics simulation of heat conduction in finite length SWNTs. Physica B: Condensed Matter. 2002;**323**:193-195. DOI: 10.1016/S0921-4526(02)00898-0

[29] Wang J, Wang J–S. Carbon nanotube thermal transport: Ballistic to diffusive. Applied Physics Letters. 2006;**88**:111909. DOI: 10.1063/1.2185727

[30] Mingo N, Broid DA. Length dependence of carbon nanotube thermal conductivity and the problem of long waves. Nano Letters. 2005;**5**:1221-1225. DOI: 10.1021/nl050714d

[31] Chang CW, Okawa D, Garcia H, Majumdar A, Zettl A. Breakdown of Fourier's law in nanotube thermal conductors. Physical Review Letters. 2008;**101**:075903. DOI: 10.1103/PhysRevLett.101.075903

[32] Chang CW, Okawa D, Garcia H, Majumdar A, Zettl A. Nanotube phonon waveguide. Physical Review Letters. 2007;**99**:045901. DOI: 10.1103/PhysRevLett.99.045901

[33] Yamamoto T, Watanabe W. Nonequilibrium Green's function approach to phonon transport in defective carbon nanotubes. Physical Review Letters. 2006;**96**:255503. DOI: 10.1103/PhysRevLett.96.255503

[34] Mingo N. Anharmonic phonon flow through molecular-sized junctions. Physical Review B. 2006;**74**:125402. DOI: 10.1103/PhysRevB.74.125402

[35] Wang J-S, Wang J, Zeng N. Nonequilibrium Green's function approach to mesoscopic thermal transport. Physical Review B. 2006;**74**:033408. DOI: 10.1103/PhysRevB.74.033408

[36] Yamamoto T, Sasaoka K, Watanabe S. Universality and diversity in a phonon-transmission histogram of isotope-disordered carbon nanotubes. Physical Review Letters. 2011;**106**:215503. DOI: 10.1103/PhysRevLett.106.215503

[37] Savic´ I, Mingo N, Stewart DA. Phonon transport in isotope-disordered carbon and boron-nitride nanotubes: Is localization observable? Physical Review Letters. 2008;**101**:165502. DOI: 10.1103/PhysRevLett.101.165502

[38] Beenakker CW. Random-matrix theory of quantum transport. Review of Modern Physics. 1997;**69**:731-808. DOI: 10.1103/RevModPhys.69.731

[39] Imry Y. Active transmission channels and universal conductance fluctuations. Europhysics Letters. 1986;**1**:249-256. DOI: 10.1209/0295-5075/1/5/008

[40] Datta S. Electronic Transport in Mesoscopic Systems. Cambridge: Cambridge University Press; 1995

[41] Peierls RE, editor. Quantum Theory of Solid. New York: Oxford University Press; 1995

[42] Klemens PG, Pedraza DF. Thermal conductivity of graphite in the basal plane. Carbon. 1994;**32**:735-741. DOI: 10.1016/0008-6223(94)90096-5

[43] Yamamoto T, Konabe S, Shiomi J, Maruyama S. Crossover from ballistic to diffusive thermal transport in carbon nanotubes. Applied Physics Express. 2009;**2**:095003. DOI: 10.1143/APEX.2.095003

[44] Wang ZL, Tang DW, Li XB, Zheng XH, Zhang WG, Zheng LX, et al. Length-dependent thermal conductivity of an individual single-wall carbon nanotube. Applied Physics Letters. 2007;**91**:123119. DOI: 10.1063/1.2779850

[45] Pomeranchuk I. Heat conductivity of dielectrics at high temperatures. Journal of Physics (USSR). 1941;**4**:259

[46] Lepri S, Livi R, Politi A. Thermal conduction in classical low-dimensional lattices. Physics Report. 2003;**377**:1-80. DOI: 10.1016/S0370-1573(02)00558-6

[47] Livi R, Lepri S. Thermal physics: Heat in one dimension. Nature. 2003;**421**:327. DOI: 10.1038/421327a

[48] Tada K, Funatani T, Konabe S, Sasaoka K, Ogawa M, Souma S, et al. Modulations of thermal properties of graphene by strain-induced phonon engineering. Japanese Journal of Applied Physics. 2017;**56**:025102. DOI: 10.7567/JJAP.56.025102

[49] Carrete J, Li W, Lindsay L, Broido DA, Gallego LJ, Mingo N. Physically founded phonon dispersions of few- layer materials and the case of borophene. Materials Research Letters. 2016;**4**:204. DOI: 10.1080/21663831.2016.1174163

[50] Bonini N, Garg J, Marzari N. Acoustic phonon lifetimes and thermal transport in free-standing and strained graphene. Nano Letters. 2673;**2012**:12. DOI: 10.1021/nl202694m

[51] Ma F, Zheng HB, Sun YJ, Yang D, Xu KW. Strain effect on lattice vibration, heat capacity, and thermal conductivity of graphene. Applied Physics Letters. 2012;**101**:111904. DOI: 10.1063/1.4752010

Edited by Vasilios N. Stavrou

The field of low-dimensional structures has been experiencing rapid development in both theoretical and experimental research. *Phonons in Low Dimensional Structures* is a collection of chapters related to the properties of solid-state structures dependent on lattice vibrations. The book is divided into two parts. In the first part, research topics such as interface phonons and polaron states, carrier-phonon non-equilibrium dynamics, directional projection of elastic waves in parallel array of N elastically coupled waveguides, collective dynamics for longitudinal and transverse phonon modes, and elastic properties for bulk metallic glasses are related to semiconductor devices and metallic glasses devices. The second part of the book contains, among others, topics related to superconductor, phononic crystal carbon nanotube devices such as phonon dispersion calculations using density functional theory for a range of superconducting materials, phononic crystal-based MEMS resonators, absorption of acoustic phonons in the hyper-sound regime in fluorine-modified carbon nanotubes and single-walled nanotubes, phonon transport in carbon nanotubes, quantization of phonon thermal conductance, and phonon Anderson localization.

Published in London, UK

IntechOpen

ISBN 978-1-83881-803-6